

PRECISION MEASUREMENT OF ISOSPIN DIFFUSION IN PERIPHERAL SN+SN
COLLISIONS AT 70 MEV/U

By

Jack Robert Winkelbauer

A DISSERTATION

Submitted to
Michigan State University
in partial fulfillment of the requirements
for the degree of

Physics - Doctor of Philosophy

2015

ABSTRACT

PRECISION MEASUREMENT OF ISOSPIN DIFFUSION IN PERIPHERAL SN+SN COLLISIONS AT 70 MEV/U

By

Jack Robert Winkelbauer

Much effort has been undertaken recently to improve constraints on the symmetry energy term in the Nuclear Equation of State (EOS). Specifically, the behavior of the symmetry energy above and below nuclear saturation density plays a significant role in the properties of neutron stars, the structure of heavy nuclei, and the dynamics of nuclear reactions. The tendency for neutrons to drift from a neutron-rich region to a neutron-deficient region during a peripheral collision of heavy nuclei is known as isospin diffusion, and has been previously shown to be a sensitive observable for the study of the symmetry energy at sub-saturation densities.

Projectile fragmentation reactions with beams of $^{112,118,124}\text{Sn}$ at 70MeV/u on targets of $^{112,118,124}\text{Sn}$ have been measured at Michigan State University, in order to understand the effect of the isospin asymmetry on the reaction dynamics. Heavy fragments with $Z > 20$ were detected and isotopically identified using the S800 Spectrometer, and the momentum distributions of these fragments were reconstructed. Additionally, light charged particles and intermediate mass fragments were detected in an array of Si-CsI telescopes to simultaneously determine the isotopic distributions of fragments with $Z < 8$. The impact parameter of the collision was characterized by a measurement of the charged particle multiplicity in a 4π scintillator array. These data provide a detailed picture of the evolution of the projectile-like residue over a range of isospin asymmetries and impact parameter.

The measured yield ratios have been used to extract information about the diffusion of neutrons between the projectile and target during peripheral collisions. The validity of using isotopic yield ratios as a surrogate for the isospin asymmetry of the compound system are discussed, and the associated isospin diffusion results are presented.

ACKNOWLEDGMENTS

I would like to thank my advisor Betty Tsang for all of her advice, support, and insight over the past six years. She was always available to ask for help and I could always count on her to proofread an abstract or edit a Powerpoint presentation at a moments notice. I am grateful that she has had such patience with such a stubborn graduate student. Betty has always provided critical feedback about graduate school and my career path. I was also fortunate to have Bill Lynch as an additional source of advice and insight. I have learned a great deal from Bill over the years while working on many experiments, analyzing data, and in many hours of group meetings. I also enjoyed the many barbecues and group dinners that Bill and Betty hosted, which often seemed more like a gathering with family than with co-workers.

I am thankful to the other members of my committee: Ed Brown, Pengpeng Zhang, and Pawel Danielewicz. I appreciated all their advice and patience trying to understand my complex thesis project.

Our group had many graduate students who helped me along the way. Rachel Showalter's organization, discipline, and attention to detail was always a benchmark to strive for in my own work. Rachel was also indispensable in running my experiment, and provided useful feedback during our weekly analysis meetings. Dan Coupland taught me a great deal about data acquisition and programming. Mike Youngs taught me a lot about electronics, soldering, and he always knew who to talk to if he didn't know the answer. I also enjoyed working with Andy Rogers, Jenny Lee, Alisher Sanetullaev, and Micha Kilburn, albeit for a short time. Our groups two postdocs, Zibi Chajecki and Bec Shane were invaluable when running my experiment; the experiment would have been impossible without them.

The NSCL staff members also deserve a lot of credit. Among the many people who made this experiment possible, a few that stand out are Craig Snow, Ron Fox, Andy Thulin, Tom Ginter, Daniel Bazin, John Yurkon and Dave Sanderson.

While many people helped me do work, I am also grateful to the people who helped me not work. Adam Fritsch, Zach Meisel, Jayda Meisel, Mike Scott, Curt Rogers, and Adam Salois helped me make some great memories including bowling, tailgating, pontoon boating, camping, and hunting. Trips up north with my Mom and Dad were a much needed break from classes, experiments, and thesis writing.

I am also truly thankful to my wife Julie for her patience and understanding over the past six years of midnight shifts, extended travel, and all-nighters. Julie was supportive and encouraging, and always provided me with a sounding board for complicated problems. I really appreciate all of your help for all of these years.

TABLE OF CONTENTS

LIST OF TABLES	viii
LIST OF FIGURES	ix
Chapter 1 Introduction	1
1.1 The Nuclear Equation of State	3
1.2 Outline of Dissertation	4
Chapter 2 Motivation	6
2.1 Density Dependence of the Symmetry Energy	6
2.2 Physical Consequences of the Symmetry Energy	9
2.2.1 Nuclear Astrophysics	9
2.2.2 Nuclear Structure	11
2.2.3 Nuclear Reactions	13
2.3 Isospin Diffusion	15
2.3.1 Isoscaling in Statistical Processes	18
2.3.2 Previous measurement of Isospin Diffusion at NSCL	21
2.3.3 A New Measurement of Isospin Diffusion	23
2.4 Transport Calculations	24
Chapter 3 Experimental Setup	30
3.1 Overview of Experiment	30
3.2 S800 Spectrometer	34
3.3 Large Area Silicon Strip Array (LASSA)	38
3.4 Miniball/Miniwall Array	43
Chapter 4 Data Analysis	47
4.1 Detector Calibrations	47
4.1.1 Ionization Chamber	47
4.1.2 Hodoscope	49
4.1.3 Cathode Readout Drift Chambers (CRDC's)	50
4.1.4 Inverse Mapping	57
4.2 Particle Identification	59
4.2.1 Empirical Corrections	60
4.2.2 Absolute Determination of N,Z	71
4.3 Charge State Analysis	84
4.3.1 Calculation of Contamination using GLOBAL	86
4.4 Reconstructing Momentum Distributions	91
4.4.1 Combining Spectrometer Settings	91

4.4.2	Fitting Function	93
4.4.3	Simultaneous Fitting of Isobaric Velocity Distributions	94
4.5	Miniball Centrality Selection	99
Chapter 5	Results	110
5.1	Systematics of Velocity Distributions	110
5.2	Isotopic Distributions of Residue Fragments	121
5.3	Yield Ratios and Isoscaling	124
5.4	Isospin Transport Ratio	136
5.4.1	Linearity of Isoscaling Observables	139
5.4.2	Isospin Diffusion Results	146
Chapter 6	Conclusion	159
APPENDICES	162
Appendix A	Particle Identification Spectra	163
Appendix B	Hodoscope Analysis	171
Appendix C	Acceptance Correction	179
REFERENCES	191

LIST OF TABLES

Table 2.1	Neutron isoscaling parameter α and isospin transport ratio measured in the previous NSCL Isospin Diffusion experiment.	22
Table 2.2	Effective physical quantities resulting from the parameter sets used in this study. These quantities are calculated from the interaction at nuclear saturation density.	29
Table 3.1	Target thicknesses.	30
Table 3.2	Statistics obtained from each reaction system, combining the three magnetic settings of the S800 spectrometer.	33
Table 3.3	Geometric parameters of the Miniball-Miniwall array used in this experiment.	46
Table 4.1	Descriptions of the variables obtained from the S800 or calculated using the inverse maps.	58
Table 4.2	Maximum impact parameter and total integrated cross section measured in the for the six measured beam-target combinations.	102
Table 4.3	Mean impact parameter deduced from the miniball multiplicity tabulated by atomic number Z . The errors are the width (σ) of a gaussian fit to the impact parameter distribution for each Z	109
Table 5.1	Fitting parameters from the systematics of the velocity distributions.	120
Table 5.2	Isospin Transport Ratio and Modified Isospin Transport Ratio results, tabulated as a function of atomic number Z . These data are plotted in Figures 5.20 to 5.22.	150
Table B.1	Approximate thicknesses of the S800 focal plane detectors	172
Table B.2	Approximate energy loss as a function of Atomic Number Z , Starting from 60 MeV/u (near $B\rho = 2.51$)	172

LIST OF FIGURES

Figure 3.1	Schematic of the scattering chamber, showing the Miniball-Miniwall and the LASSA array. The beam enters from the left, and the heavy residues exit to the right into the S800 spectrometer.	31
Figure 3.2	Schematic drawing of the S800 focal plane. Figure is taken from [57].	35
Figure 3.3	Schematic drawing of the CRDC's in the S800 focal plane. Figure is taken from [58].	36
Figure 3.4	Schematic drawing of the LASSA array. Figure is taken from [61]. .	39
Figure 3.5	Photo of the LASSA array. The forward rings of the Miniball and Miniwall are shown on the left side, and the eight LASSA telescopes are shown on the right side.	40
Figure 3.6	Angles of each pixel for the eight LASSA telescopes, extrapolated from measurements with ROMER Arm. Angles are calculated with respect to the measured beamline.	42
Figure 3.7	Forward part of the Miniball-Miniwall array, in the configuration used for this experiment. The two most forward rings of the Miniwall are not used.	44
Figure 3.8	Fully assembled Miniball-Miniwall array, showing the backward rings. The beam is incident from the left, and the target is at the geometric center of the miniball.	45
Figure 3.9	Left: Schematic of a Miniball detector [65]. Right: Schematic showing the time structure of a Miniball signal [67]. The three shaded regions represent the time windows wherein the Fast, Slow, and Tail signals are integrated by the Charge ADC's.	45
Figure 4.1	Gas pressure in the S800 ionization chamber, as a function of time. The pressure deviated from the set pressure of 300 Torr throughout most of the experiment.	48
Figure 4.2	Left Panel: Uncorrected ionization chamber energy loss vs. gas pressure, gated on ^{75}Br . Several different reactions at $B\rho = 2.6$ are shown to sample the range of pressure from 300-335 Torr. Right Panel: Same as left, but with the correction from Equation 4.3 applied.	49

Figure 4.3	Top Panel: Raw hodoscope signals for each crystal, when scanning the ^{124}Sn beam across all detectors. Bottom Panel: Same as top, with all crystals gain matched.	50
Figure 4.4	Top Panel: Maximum raw pad signals vs. pad number for one run in the $^{112}\text{Sn}+^{112}\text{Sn}$ reaction system at $B\rho = 2.4$ Tm. Bottom Panel: Same as top, but pads are gain matched and corrected for non-linearity. Sloped cutoff at low channels corresponds to a threshold in the E1 scintillator, which is used as the S800 DAQ trigger.	52
Figure 4.5	Induced pad signal vs. pad number for one (typical) event in the $^{112}\text{Sn}+^{112}\text{Sn}$ reaction system at $B\rho = 2.4$ Tm. A gaussian fit to the data is shown, and the dotted line indicates the extracted centroid of the event.	53
Figure 4.6	Schematic drawing of the CRDC mask. The long edge corresponds to the dispersive direction.	55
Figure 4.7	Mask spectrum for CRDC1.	55
Figure 4.8	Top Panel: Raw CRDC1 drift time vs. run number, for all data runs. Bottom Panel: Calibrated and matched CRDC1 non-dispersive position vs. run number.	56
Figure 4.9	a.) Uncorrected TOF vs. uncorrected energy loss, measured in the $^{112}\text{Sn}+^{112}\text{Sn}$ reaction system at $B\rho = 2.4$ Tm. Solid line shows the two dimensional gate used to select an approximate Z b.) Uncorrected TOF vs. dispersive position at the focal plane, requiring the gate shown in panel a. Solid line shows the correlation between TOF and dispersive position. c.) Uncorrected TOF vs. dispersive angle at the focal plane, requiring the gate shown in panel a. Solid line shows the correlation between TOF and dispersive angle. d.) Corrected TOF (first iteration) vs. uncorrected energy loss.	62
Figure 4.10	a.) TOF (first iteration) vs. uncorrected energy loss, measured in the $^{112}\text{Sn}+^{112}\text{Sn}$ reaction system at $B\rho = 2.4$ Tm. b.) TOF (first iteration) vs. dispersive position at the focal plane, requiring the gate shown in panel a. c.) TOF (first iteration) vs. dispersive angle at the focal plane, requiring the gate shown in panel a. d.) TOF (second iteration) vs. uncorrected energy loss.	64

Figure 4.11	a.) <i>TOF</i> (second iteration) vs. uncorrected energy loss, measured in the $^{112}\text{Sn}+^{112}\text{Sn}$ reaction system at $B\rho = 2.4$ Tm. b.) Energy loss (uncorrected) vs. dispersive position at the focal plane, requiring the gate shown in panel a. c.) Energy loss (uncorrected) vs. dispersive angle at the focal plane, requiring the gate shown in panel a. d.) <i>TOF</i> (second iteration) vs. energy loss (first iteration).	65
Figure 4.12	a.) <i>TOF</i> (second iteration) vs. energy loss (first iteration), measured in the $^{112}\text{Sn}+^{112}\text{Sn}$ reaction system at $B\rho = 2.4$ Tm. b.) Energy loss (first iteration) vs. dispersive position at the focal plane, requiring the gate shown in panel a. c.) Energy loss (first iteration) vs. dispersive angle at the focal plane, requiring the gate shown in panel a. d.) <i>TOF</i> (second iteration) vs. energy loss (second iteration).	66
Figure 4.13	a.) <i>TOF</i> vs. ΔE , measured in the $^{112}\text{Sn}+^{112}\text{Sn}$ reaction system at $B\rho = 2.4$ Tm, showing gates for a fixed Z and $N - Z$. b.) Projection onto the <i>TOF</i> axis of the spectrum in panel a, gated on one isotope. c.) Projection onto the ΔE axis of the spectrum in panel a, gated on one isotope. d.) <i>TOF</i> vs. ΔE , showing an example of a gate resulting from this fitting procedure. The gate is an ellipse with the semimajor axes equal to 2σ , extracted from the fits in panels b and c.	68
Figure 4.14	Spectrum of <i>TOF</i> vs. ΔE , with the particle identification gates adopted in the $^{112}\text{Sn}+^{112}\text{Sn}$ reaction system at $B\rho = 2.4$ Tm.	69
Figure 4.15	a_1 coefficient, plotted as a function of <i>TOF</i> and ΔE , measured in the $^{112}\text{Sn}+^{112}\text{Sn}$ reaction system at $B\rho = 2.4$ Tm. The a_1 coefficient represents how strongly the <i>TOF</i> depends on the quantity $x_1 + x_2$. The black crosses represent the final locations of the isotopes of interest. The values of the correction coefficients are extrapolated outside this range of <i>TOF</i> and are used for the first step of the correction, which is approximate.	72
Figure 4.16	The centroid positions in <i>TOF</i> and ΔE for each isotope identified in the $^{112}\text{Sn}+^{112}\text{Sn}$ reaction system at $B\rho = 2.4$ Tm. Measured centroids for each isotope are shown as solid circles, while extrapolated positions are shown as open circles. A vertical line is drawn to indicate the location of the $N - Z = 0$ isotopes.	74
Figure 4.17	Isotopic spacing (ns/nucleon) vs. Z , measured in the $^{112}\text{Sn}+^{112}\text{Sn}$ reaction system at $B\rho = 2.4$ Tm. A fit of Equation 4.16, with $Z_{\text{offset}} = 0$ is shown in the main panel. In the inset, the χ^2 distribution for varying Z_{offset} is shown.	76

Figure 4.18	Particle Identification centroids, calculated using the cyclotron RF as the start time, measured in the $^{112}\text{Sn}+^{112}\text{Sn}$ reaction system at $B\rho = 2.51$ Tm. The solid circles represent a centroid extracted from data, while the open circles are extrapolated centroids. In addition, the particle identification spectrum for the degraded beam run is shown on the same plot, with its centroid shown as a solid circle. The solid line corresponds to an extrapolation of the location of the $Z = 50$ isotopes, and the dotted lines correspond to the extrapolations for $Z = 49$ and $Z = 51$	78
Figure 4.19	Odd-Even Staggering ratio, measured in the $^{112}\text{Sn}+^{112}\text{Sn}$ reaction system, using the integrated yields. Left panel shows even- A (even $N - Z$) fragments. Right panel shows odd- A (odd $N - Z$) fragments.	79
Figure 4.20	Uncorrected energy loss vs. magnetic rigidity, measured in the $^{112}\text{Sn}+^{112}\text{Sn}$ reaction system, with all three rigidity settings combined. The yields are scaled by the live-time and the normalization of the beam from the Miniball. These fragments shown have $N - Z = 5$, and a reference line is drawn at $Z = 30$	80
Figure 4.21	Particle identification centroids for the three symmetric reactions $^{112}\text{Sn}+^{112}\text{Sn}$, $^{118}\text{Sn}+^{118}\text{Sn}$, and $^{124}\text{Sn}+^{124}\text{Sn}$, for $B\rho = 2.4$ Tm. . .	81
Figure 4.22	Left Panel: Final particle identification, measured in the $^{112}\text{Sn}+^{112}\text{Sn}$ reaction system at $B\rho = 2.4$ Tm. Right Panel: Rectangularized particle identification variables. The sharp cutoffs are present because interpolation is used, and no attempt to extrapolate is made.	83
Figure 4.23	Calculated particle identification locations for a subset of the fragments of interest in the $^{112}\text{Sn}+^{112}\text{Sn}$ reaction system. The fully stripped fragments are represented by the black crosses and the primary contaminant from hydrogen-like fragments are represented by red crosses. The error bars represent one sigma resolution in the respective experimental quantities. The Z values for the contaminant are scaled by the ratio of the (slightly different) $\frac{m}{q}$ of the two overlapping fragments, which approximates the difference in their energy-loss measurements.	86
Figure 4.24	Charge state contribution (ratio of hydrogen-like ions to fully stripped ions) shown as a function of atomic number Z , as calculated by GLOBAL. Isotopes shown have $N - Z = 6$	88
Figure 4.25	Charge state correction (inverse of left side of Equation 4.21) shown as a function of atomic number Z . Isotopes shown have $N - Z = 6, 7, 8$.	90

Figure 4.26	Distribution in magnetic rigidity (momentum), for ^{88}Zr , measured in the $^{124}\text{Sn}+^{124}\text{Sn}$ reaction. The lower axis shows the rigidity, while the upper axis shows the linear momentum. The data are scaled by the live time and the miniball beam normalization.	92
Figure 4.27	Distribution in magnetic rigidity (momentum), for ^{88}Zr , measured in the $^{124}\text{Sn}+^{124}\text{Sn}$ reaction. Only data measured in the central region of the S800 spectrometer where the acceptance is constant are included in this figure, and in the final fitting procedure. The final fit result for this isotope is shown as a dotted line.	92
Figure 4.28	Fit result for distributions in velocity, for $A = 77$, measured in the $^{124}\text{Sn}+^{124}\text{Sn}$ reaction. The range of velocity that is covered by a fixed range of $B\rho$ is different for each isobar, and is shown by the dotted arrows.	94
Figure 4.29	Fit results for distributions in momentum, for $A = 77$, measured in the $^{124}\text{Sn}+^{124}\text{Sn}$ reaction. The fitting function is a normal gaussian function, with three free parameters, and the plotted curves are equally normalized. Each distribution is fit individually. Different isobars result in different fits because of the asymmetry of the distribution combined with the limited acceptance range.	95
Figure 4.30	Fit results for distributions in momentum, for $A = 77$, measured in the $^{124}\text{Sn}+^{124}\text{Sn}$ reaction. The fitting function is a skewed gaussian function (Equation 4.23, with four free parameters, and the plotted curves are equally normalized. The three distributions are fit individually.	96
Figure 4.31	Fit result for distributions in velocity, for $A = 77$, measured in the $^{124}\text{Sn}+^{124}\text{Sn}$ reaction. The three spectra are fit simultaneously with Equation 4.24, so that the shape is identical in each spectrum. . . .	97
Figure 4.32	Fit result for distributions in velocity, for $A = 77$, measured in the $^{118}\text{Sn}+^{118}\text{Sn}$ reaction. The three spectra are fit simultaneously with Equation 4.24, so that the shape is identical in each spectrum. . . .	97
Figure 4.33	Fit result for distributions in velocity, for $A = 77$, measured in the $^{112}\text{Sn}+^{112}\text{Sn}$ reaction. The three spectra are fit simultaneously with Equation 4.25. Contrary to Figures 4.31 and 4.32, the centroids of the distributions are allowed to vary between isobars.	98

Figure 4.34	Total reaction cross section vs. miniball multiplicity (left-side panels) and calculated impact parameter vs. miniball multiplicity (right-side panels). Shown for two targets each for ^{112}Sn (Top), ^{118}Sn (Middle), and ^{124}Sn (Bottom).	101
Figure 4.35	Reduced impact parameter vs. miniball multiplicity (right-side panels). Shown for the reactions $^{112}\text{Sn}+^{112}\text{Sn}$ and $^{124}\text{Sn}+^{124}\text{Sn}$	103
Figure 4.36	Two-dimensional spectrum showing the impact parameter extracted from the Miniball multiplicity vs. the atomic number Z of the fragment measured in the S800, plotted for the $^{112}\text{Sn}+^{112}\text{Sn}$ reaction data. The solid circles show the average impact parameter for each Z , where the errors are smaller than the data points.	104
Figure 4.37	Two-dimensional spectrum showing the impact parameter extracted from the Miniball multiplicity vs. the atomic number Z of the fragment measured in the S800, plotted for the $^{124}\text{Sn}+^{124}\text{Sn}$ reaction data. The solid circles show the average impact parameter for each Z , where the errors are smaller than the data points.	105
Figure 4.38	Difference between the impact parameter determined using a mean and fitting with a gaussian function vs. the atomic number Z of the fragment measured in the S800, plotted for the $^{112}\text{Sn}+^{112}\text{Sn}$ reaction data.	106
Figure 4.39	Measured correlation between the average Z of the heavy residue measured in the S800 and the impact parameter extracted from the charged particle multiplicity. Data points are shown for the $^{112}\text{Sn}+^{112}\text{Sn}$, $^{112}\text{Sn}+^{124}\text{Sn}$, $^{124}\text{Sn}+^{112}\text{Sn}$, and $^{124}\text{Sn}+^{124}\text{Sn}$ systems. The impact parameter is calculated as the mean impact parameter for events which yield a fragment with atomic number Z	107
Figure 5.1	Skew parameter vs. Mass Loss ($A_{\text{proj}} - A$). Top, middle, and bottom panels are the ^{112}Sn , ^{118}Sn , and ^{124}Sn projectiles, respectively. The ^{112}Sn , ^{118}Sn , and ^{124}Sn targets are represented by the blue, green, and red points, respectively. A horizontal dashed line is drawn for no skewing, or a symmetric gaussian. A negative value represents a longer tail extending to lower velocity.	112

Figure 5.2	Isobar velocity slope parameter vs. Mass Loss ($A_{\text{proj}} - A$). Top, middle, and bottom panels are the ^{112}Sn , ^{118}Sn , and ^{124}Sn projectiles, respectively. The ^{112}Sn , ^{118}Sn , and ^{124}Sn targets are represented by the blue, green, and red points, respectively. A horizontal dashed line is drawn for zero slope, which means that all isobars have identical velocity distributions, where a positive value means that higher Z isobars have higher velocity.	114
Figure 5.3	Isobar velocity slope parameter vs. Mass Loss ($A_{\text{proj}} - A$), for $^{40,48}\text{Ca}$ and $^{58,64}\text{Ni}$ projectiles with ^9Be and ^{181}Ta targets, at $140 \frac{\text{MeV}}{\text{u}}$. Data taken from [75]	115
Figure 5.4	Most-probable velocity vs. Mass Loss ($A_{\text{proj}} - A$). Top, middle, and bottom panels are the ^{112}Sn , ^{118}Sn , and ^{124}Sn projectiles, respectively. The ^{112}Sn , ^{118}Sn , and ^{124}Sn targets are represented by the blue, green, and red points, respectively. The data are corrected for the energy loss in the target and the timing scintillator. The beam velocity for all three projectiles is $\beta = .367$	116
Figure 5.5	Gaussian width parameter vs. Mass Loss ($A_{\text{proj}} - A$). Top, middle, and bottom panels are the ^{112}Sn , ^{118}Sn , and ^{124}Sn projectiles, respectively. The ^{112}Sn , ^{118}Sn , and ^{124}Sn targets are represented by the blue, green, and red points, respectively. The dashed lines indicate the fitting result of the modified Goldhaber description discussed in the text.	117
Figure 5.6	Isotopic yield distributions for five reaction systems, for $Z=30$ to $Z=35$. The data are corrected for the charge state contamination, but are not corrected for acceptance. Solid lines/filled circles represent symmetric reactions, and dotted lines/open circles represent the mixed reactions.	122
Figure 5.7	Isotopic yield distributions for five reaction systems, for $Z=35$ to $Z=41$. The data are corrected for the charge state contamination, but are not corrected for acceptance. Solid lines/filled circles represent symmetric reactions, and dotted lines/open circles represent the mixed reactions.	123
Figure 5.8	Neutron isoscaling ratio for $^{124}\text{Sn} + ^{124}\text{Sn}$ with respect to $^{112}\text{Sn} + ^{112}\text{Sn}$ for $Z=27$ to $Z=43$. The lines shown are linear fits to the data. Odd-Z are shown in blue, and even-Z are shown in red for clarity.	125

Figure 5.9	Neutron isoscaling ratio for $^{124}\text{Sn}+^{118}\text{Sn}$ with respect to $^{112}\text{Sn}+^{112}\text{Sn}$ for $Z=27$ to $Z=43$. The lines shown are linear fits to the data. Odd- Z are shown in blue, and even- Z are shown in red for clarity.	126
Figure 5.10	Neutron isoscaling ratio for $^{124}\text{Sn}+^{112}\text{Sn}$ with respect to $^{112}\text{Sn}+^{112}\text{Sn}$ for $Z=27$ to $Z=43$. The lines shown are linear fits to the data. Odd- Z are shown in blue, and even- Z are shown in red for clarity.	127
Figure 5.11	Neutron isoscaling ratio for $^{118}\text{Sn}+^{118}\text{Sn}$ with respect to $^{112}\text{Sn}+^{112}\text{Sn}$ for $Z=27$ to $Z=43$. The lines shown are linear fits to the data. Odd- Z are shown in blue, and even- Z are shown in red for clarity.	128
Figure 5.12	Neutron isoscaling ratio for $^{112}\text{Sn}+^{124}\text{Sn}$ with respect to $^{112}\text{Sn}+^{112}\text{Sn}$ for $Z=27$ to $Z=43$. The lines shown are linear fits to the data. Odd- Z are shown in blue in the lower panel, and even- Z are shown in red in the upper panel.	129
Figure 5.13	Neutron isoscaling parameter α for $^{112,124}\text{Sn}+^{112,124}\text{Sn}$ and $^{118}\text{Sn}+^{118}\text{Sn}$ for $Z=27$ to $Z=43$. No correction for charge state contamination is included.	130
Figure 5.14	Neutron isoscaling parameter α for $^{112,124}\text{Sn}+^{112,124}\text{Sn}$ and $^{118}\text{Sn}+^{118}\text{Sn}$ for $Z=27$ to $Z=43$. The calculated correction for charge state contamination has been applied to the data.	131
Figure 5.15	Neutron isoscaling parameter, α for $^{124}\text{Sn}+^{124}\text{Sn}$ and $^{118}\text{Sn}+^{118}\text{Sn}$ with respect to $^{112}\text{Sn}+^{112}\text{Sn}$, for $Z=27$ to $Z=43$, showing the effect of the choice of fit range. Solid symbols show the two symmetric reactions with the full fit range, while the open symbols show the result when one isotope is excluded at either end of the range. Excluding the lowest isotope increases the value of α , and excluding the highest isotope reduces the value of α . Only the two systems are shown for clarity.	133
Figure 5.16	Neutron isoscaling parameter, α for $^{124}\text{Sn}+^{124}\text{Sn}$, $^{118}\text{Sn}+^{118}\text{Sn}$, $^{124}\text{Sn}+^{112}\text{Sn}$, and $^{112}\text{Sn}+^{124}\text{Sn}$ with respect to $^{112}\text{Sn}+^{112}\text{Sn}$, for $Z=27$ to $Z=43$	134
Figure 5.17	Correction for charge state contamination to the isospin transport ratio, calculated using the isoscaling parameter α for the $^{118}\text{Sn}+^{118}\text{Sn}$ reaction. The filled circles represent the difference between the corrected and the uncorrected result.	138

Figure 5.18	Isospin transport ratio, calculated using the isoscaling parameter α for the $^{118}\text{Sn}+^{118}\text{Sn}$ reaction. Three different versions of the results are shown, with three different fit ranges used for the isoscaling ratio fitting. The green data points shows the result for the full fit range, while the red and blue lines indicate the result for removing the highest and lowest isotopes in the fit, respectively. The dashed line shows the value expected for R_i from the standard isoscaling relationships.	140
Figure 5.19	Primary residue asymmetry, calculated using ImQMD-Sky with the four parameter sets detailed in 2.4, plotted against the asymmetry of the projectile, for the three symmetric reactions $^{112}\text{Sn}+^{112}\text{Sn}$, $^{118}\text{Sn}+^{118}\text{Sn}$, $^{124}\text{Sn}+^{124}\text{Sn}$, for impact parameter $b = 10$ fm. The calculated asymmetry is the asymmetry for fragments with $Z > 20$, averaged over all events.	144
Figure 5.20	Isospin transport ratio, calculated using the isoscaling parameter α using 5 measured reactions.	147
Figure 5.21	Modified isospin transport ratio, calculated using the isoscaling parameter α using 5 measured reactions. The black open squares are the average of the two mixed systems.	148
Figure 5.22	Modified Isospin Transport Ratio vs. Atomic Number Z , for the two mixed reactions, $^{124}\text{Sn}+^{112}\text{Sn}$ and $^{112}\text{Sn}+^{124}\text{Sn}$.	149
Figure 5.23	Primary residue asymmetry, calculated using ImQMD-Sky with the SLy4 parameter set (soft symmetry energy), plotted against the average Z of the resulting projectile-like fragment, for the reactions $^{112}\text{Sn}+^{112}\text{Sn}$, $^{112}\text{Sn}+^{124}\text{Sn}$, $^{118}\text{Sn}+^{118}\text{Sn}$, $^{124}\text{Sn}+^{112}\text{Sn}$, $^{124}\text{Sn}+^{124}\text{Sn}$, for impact parameters $b = 10\text{fm}$ and $b = 6\text{fm}$.	153
Figure 5.24	Isospin Transport Ratio, calculated using ImQMD-Sky with the SLy4 parameter set (soft symmetry energy), plotted against the impact parameter. The reactions $^{112}\text{Sn}+^{112}\text{Sn}$, $^{112}\text{Sn}+^{124}\text{Sn}$, $^{124}\text{Sn}+^{112}\text{Sn}$, $^{124}\text{Sn}+^{124}\text{Sn}$ are shown. The solid lines are calculated using the average values of δ for a fixed b , and the dashed lines are calculated using the average values of δ for a fixed Z .	154
Figure 5.25	Isospin Transport Ratio, calculated using ImQMD-Sky with four Skyrme parameter sets, plotted against the impact parameter, for the $^{124}\text{Sn}+^{112}\text{Sn}$ reaction, for impact parameters $b = 10\text{fm}$ and $b = 6\text{fm}$.	155

Figure 5.26	Isospin Transport Ratio, calculated using ImQMD05 for $\gamma = 0.5, 1.0, 2.0$, plotted against the impact parameter, for the $^{112}\text{Sn}+^{124}\text{Sn}$ reaction, for impact parameters $b = 6\text{fm}$, $b = 9\text{fm}$, and $b = 10\text{fm}$. Only one mixed system is shown here and the vertical axis is focused on the calculated system.	157
Figure 5.27	Modified Isospin Transport Ratio vs. Atomic Number Z for the $^{112}\text{Sn}+^{124}\text{Sn}$ system. The solid region shows the experimental result, and the blue, green, and red crosses correspond to $\gamma = 0.5, 1.0$, and 2.0 , respectively. The calculations are done at $b = 6\text{ fm}$, $b = 9\text{ fm}$, and $b = 10\text{ fm}$	158
Figure A.1	Particle Identification for the $^{112}\text{Sn}+^{112}\text{Sn}$ reaction. The three panels show the three different momentum settings that were measured. See Section 4.2 for details.	164
Figure A.2	Particle Identification for the $^{112}\text{Sn}+^{124}\text{Sn}$ reaction. The three panels show the three different momentum settings that were measured. See Section 4.2 for details.	165
Figure A.3	Particle Identification for the $^{118}\text{Sn}+^{112}\text{Sn}$ reaction. The three panels show the three different momentum settings that were measured. See Section 4.2 for details.	166
Figure A.4	Particle Identification for the $^{118}\text{Sn}+^{118}\text{Sn}$ reaction. The three panels show the three different momentum settings that were measured. See Section 4.2 for details.	167
Figure A.5	Particle Identification for the $^{124}\text{Sn}+^{112}\text{Sn}$ reaction. The three panels show the three different momentum settings that were measured. See Section 4.2 for details.	168
Figure A.6	Particle Identification for the $^{124}\text{Sn}+^{118}\text{Sn}$ reaction. The three panels show the three different momentum settings that were measured. See Section 4.2 for details.	169
Figure A.7	Particle Identification for the $^{124}\text{Sn}+^{124}\text{Sn}$ reaction. The three panels show the three different momentum settings that were measured. See Section 4.2 for details.	170
Figure B.1	Overall detection efficiency of the CsI hodoscope for the $^{112}\text{Sn}+^{112}\text{Sn}$ reaction system, at $B\rho = 2.4, 2.51$, and 2.6 Tm . The efficiency is simply the fraction of particles which are otherwise detected and identified in the focal plane that also leave a signal in any hodoscope crystal.	173

Figure B.2	Energy measured in crystal #9, shown vs. Z , for the $^{112}\text{Sn}+^{112}\text{Sn}$ reaction system, at $B\rho = 2.51$ Tm. This figure requires that crystal #9 is the crystal with the largest signal amplitude for that event. . .	174
Figure B.3	Non-dispersive position spectra at the hodoscope, shown for the two different segments of the experiment. The dotted line shows the approximate position of the gap between the middle two columns of hodoscope elements. The spectra are arbitrarily normalized to be on the same scale. Because the acceptance was limited to the region near the gap, most of the data is corrupted by the position dependence of the crystal response.	175
Figure B.4	Hodoscope Energy from crystal #9 vs. Dispersive position spectra at the hodoscope, for the $^{112}\text{Sn}+^{112}\text{Sn}$ reaction system, at $B\rho = 2.4$. The dotted lines show the approximate positions of the edge of crystal #9.	176
Figure B.5	Hodoscope Energy from crystal #9 vs. Dispersive position spectra at the hodoscope, for the $^{112}\text{Sn}+^{112}\text{Sn}$ reaction system, at $B\rho = 2.4$. The dotted lines show the approximate positions of the edge of crystal #9. Only fragments identified as $Z > 30$ using the normal particle identification spectrum are included this figure, which should not reach the hodoscope. As a result, these signals come from either coincident light fragments or background from multiple hits.	177
Figure B.6	Hodoscope energy, measured in the $^{112}\text{Sn}+^{112}\text{Sn}$ reaction system, at $B\rho = 2.6$ Tm, empirically corrected for momentum, for $^{46}\text{Ti}^{22+}$. The solid line shows the approximate centroid of this peak, and the dotted line shows the estimated position of the primary contaminant, $^{44}\text{Ti}^{21+}$, when accounting for energy losses and assuming the energy scale is linear.	178
Figure C.1	Schematic diagram showing magnetic elements of the S800. Only the Optics in the Non-Dispersive Direction are shown. The S800 was tuned assuming the reaction target was at the normal target position (the pivot point), which resulted in over-Focusing the fragments from the actual target position. The dashed green curve represents the track of a fragment emitted at the maximum scattering angle from the optimal target position. The solid red curve represents the track of a fragment emitted at the maximum scattering angle from the actual target position, upstream of the pivot point.	180

Figure C.2	Scattering angles at the target position. The left panel shows the $^{124}\text{Sn}+^{124}\text{Sn}$ reaction at the 2.6 Tm magnetic rigidity setting as measured in June 2011 with the proper beam tuning. The right panel shows the $^{124}\text{Sn}+^{124}\text{Sn}$ reaction at the 2.6 Tm magnetic rigidity setting as measured in October 2011 with the incorrect beam tuning. Neither histogram requires a particle identification gate, but both require a timing signal in the timing start scintillator, which causes the square cut out in the center. (See Figure C.3)	181
Figure C.3	Scintillator used to measure the start time of the heavy fragments that are detected in the S800 focal plane. Notice the square hole cutout, which allows the unreacted beam to pass through.	181
Figure C.4	Scattering angles at the target position. The left pane shows the $^{112}\text{Sn}+^{112}\text{Sn}$ reaction at the 2.4 Tm magnetic rigidity setting. The right pane shows the $^{124}\text{Sn}+^{124}\text{Sn}$ reaction at the 2.4 Tm magnetic rigidity setting. The significant vertical offset in the left panel is due to miscalibration of the mechanical target drive used to move the scintillator.	182
Figure C.5	Dispersive angle at the target position versus fragment energy (<i>dta</i>) measured in the $^{124}\text{Sn}+^{124}\text{Sn}$ reaction at the 2.51 Tm magnetic rigidity setting. No PID gates or other requirements are applied, the sharp cutoffs are simply due to the acceptance of the S800 Spectrometer. The dotted line shows an example of the <i>ata</i> – <i>dta</i> gate used to calculate the acceptance.	184
Figure C.6	Non-dispersive position at the target versus Non-dispersive angle, measured in the $^{124}\text{Sn}+^{124}\text{Sn}$ reaction at the 2.51 Tm magnetic rigidity setting, with a gate requiring $-.03 < dta < .03$. The spectrum on the left shows the raw measured parameters, while the spectrum on the right shows <i>bta</i> corrected for the correlations with <i>ata</i> (approximated as quadratic), <i>dta</i> (approximated as linear), and <i>yta</i> (approximated as linear).	185
Figure C.7	Non-dispersive angle at the target versus fragment energy, measured in the $^{124}\text{Sn}+^{124}\text{Sn}$ reaction at the 2.51 Tm magnetic rigidity setting. The spectrum on the left shows the raw measured parameters, while the spectrum on the right shows <i>bta</i> corrected for the correlations with <i>ata</i> (approximated as quadratic), <i>dta</i> (approximated as linear), and <i>yta</i> (approximated as linear).	185

Figure C.8	Dispersive angle at the target versus Non-dispersive angle at the target, measured in the $^{124}\text{Sn}+^{124}\text{Sn}$ reaction at the 2.51 Tm magnetic rigidity setting. The spectrum on the left shows the raw measured parameters, while the spectrum on the right shows <i>bta</i> corrected for the correlations with <i>ata</i> (approximated as quadratic), <i>dta</i> (approximated as linear), and <i>yta</i> (approximated as linear).	186
Figure C.9	Corrections for acceptance calculation from cutout in timing scintillator, measured in the $^{124}\text{Sn}+^{124}\text{Sn}$ reaction at the 2.51 Tm magnetic rigidity setting. Top: Dispersive angle at the target versus Non-dispersive angle at the target; Middle: Non-dispersive angle at the target versus fragment energy; Bottom: Non-dispersive position at the target versus Non-dispersive angle. Spectra on the left show raw measured parameters, spectra on the right show parameters with correlations removed as discussed in the text. Dashed lines indicate cuts applied to the other spectra to demonstrate the boundary clearly. . .	187
Figure C.10	Monte Carlo efficiency calculated for the $^{124}\text{Sn}+^{124}\text{Sn}$ reaction, for the $B\rho = 2.51\text{Tm}$ magnetic setting. The efficiency is plotted as a two dimensional function of scattering angle θ and the measured <i>dta</i> . The color scale represents the fractional efficiency for each bin. . .	188

Chapter 1

Introduction

Since Rutherford first measured α particles scattering from atomic nuclei in 1907, [1] the field of nuclear physics advanced substantially in the description of the nucleus and the nuclear interaction. The discovery of the neutron by Chadwick in 1932 [2] indicated that the nucleus is comprised of two different types of nucleons. The shell model, which is still in use today, was proposed on this basis that protons and neutrons populate different orbitals [3]. The quark model [4, 5] successfully described each nucleon as three quarks bound together by the strong force, and nuclei are bound by the residual interaction from the quarks. Quantum chromodynamics (QCD) describes the strong interaction between the quarks that comprise the nucleus, but QCD is too complex for calculations of finite nuclei to be feasible with current theories. Consequently, much effort has been invested in the study of the structure of nuclei, the properties of nuclear matter, and the study of nuclear reactions with microscopic and macroscopic models.

As opposed to modeling all the constituent nucleons and their respective interactions, nuclear properties can be modeled macroscopically. The semi-empirical mass formula, which models the nucleus as an incompressible fluid (also known as the liquid drop model) is an early example of describing the bulk properties of the nucleus.

Due to complexities of the physics describing the interactions among many bodies, different theoretical approaches are used to describe nuclei of different mass scales. The advance of supercomputing techniques and many-body theories has allowed nuclei up to ($A \approx 12$)

to be described with ab initio (from first principles) calculations [6, 7]. These methods are limited by computing resources because the calculations grow exponentially with A .

Currently, properties of light nuclei up to ^{40}Ca and heavier nuclei close to magic numbers can be described by the shell model. The shell model describes the structure of the nucleus analogous to the electronic structure of the atom. The nucleons move in a common potential well and the neutrons and protons fill different sets of orbitals because of an additional quantum number called “isospin”. The neutron has an isospin projection of $T_z = +1/2$ and the proton $T_z = -1/2$. The shell model is notable for its explanation of magic numbers (2,8,20,28,50,82,126) of protons or neutrons, from strong spin-orbit coupling. Nuclei with magic numbers such as ^{40}Ca ($N=20$, $Z=20$) and ^{208}Pb ($N=126$, $Z=82$) are analogous to noble gases in atomic physics. Beyond nuclei with filled sd orbitals ($N, Z > 20$), approximations must be made where part of the nucleus is represented by an inert core with magic numbers of protons or neutrons. Then, the calculation is limited to one or a few nucleons that fill the orbitals just outside of this inert core. Because each nucleon can interact with all other nucleons including those in the core, precise calculations are limited to the region of the nuclear chart close to shell closures.

When describing medium and heavy mass nuclei, Energy Density Functional (EDF) methods are often used [8, 9]. EDF methods, also called Self-Consistent Mean Field¹ methods, use an effective interaction to approximate the interaction between nucleons. The effective interaction is normally tuned to reproduce relevant nuclear properties such as masses, binding energies, or the energy levels of excited states over a large range of nuclei. Commonly used interactions are the Skyrme interaction, the Gogny interaction, and the Relativistic

¹In a “self-consistent” mean field, the potential is calculated from the actual positions (and momenta) of the nucleons

Mean Field Theory [10, 11, 12]. EDF methods have the advantage that they can be utilized across the nuclear chart.

1.1 The Nuclear Equation of State

The goal of this work is to understand the equation of state for cold nuclear matter, which is important for nuclear astrophysics and nuclear structure. In this context the interesting relationship is how the energy or pressure changes with density. The nuclear equation of state is difficult to probe on earth, because it is impossible to create bulk nuclear matter in a laboratory. The best approximation is to study the dynamics in collisions of finite heavy nuclei at intermediate energy, where densities different from normal nuclear density can be created. Data from these heavy ion collisions can then be compared to a transport model that includes the important aspects of the EoS.

In central collisions above the fermi energy (the average energy of a nucleon in a nucleus), densities higher than nuclear saturation density can be reached. Light particles emitted during the expansion of the compressed nuclear system can provide a characterization of the expansion of this dense matter [13]. In some cases, the expansion results in a complete breakup of the system where many fragments of varying sizes (also known as Intermediate Mass Fragments, with $Z = 3$ to $Z = 20$) are emitted, a process called multifragmentation. In mid-peripheral collisions, a low-density neck can form between the target and projectile nuclei, which can also be a source of intermediate mass fragments. In all cases, the goal is to understand the dynamics of nuclear collisions, which are controlled by the Equation of State.

Much effort has been spent on constraining the EoS, because of its importance for many physical systems. The behavior of nuclear matter that is *symmetric*, i.e. the densities of protons and neutrons are equal, has largely been constrained in the laboratory using a variety of different experimental techniques using beams of heavy-ions [13]. The frontier of this research is in the understanding of *asymmetric* nuclear matter, specifically in the understanding of the density dependence of the symmetry energy.

Information about the EoS of asymmetric nuclear matter is essential to describing physical properties of a neutron star. One possible end point for a star with sufficient initial mass, neutron stars are compact objects that have collapsed gravitationally to the point where nuclear degeneracy pressure is in hydrostatic equilibrium with the gravitational force. To understand any of the properties of a neutron star, its Equation of State (EoS) must be known.

1.2 Outline of Dissertation

This dissertation is a study of the density dependence of the symmetry energy term in the nuclear EoS using heavy ion collisions at intermediate energy. First, in Chapter 2, the motivation for this experiment is described, as well as the experimental landscape leading up to this experiment. The theoretical framework that is used to interpret this data is also introduced and described here. Chapter 3 describes the physical setup of the experiment and the detectors used in this study. Chapter 4 presents all the critical steps in processing the raw data into physical observables. Chapter 5 discusses the physical observables that are extracted in this study. These physical observables are also compared to theoretical predictions. Chapter 6 talks about the physics insights drawn from the analysis of the data

from this experiment, and open issues regarding the density dependence of the symmetry energy. In the Appendices, several aspects of the experiment that were investigated in detail during the course of the data analysis are discussed.

Chapter 2

Motivation

2.1 Density Dependence of the Symmetry Energy

The liquid drop model and the semi-empirical mass formula provide some physical intuition regarding the nuclear EoS and the symmetry energy. The semi-empirical mass formula is used to describe the binding energy (mass) of nuclei using only the number of protons and neutrons [14, 15]. It is composed of several terms motivated by physics, and the coefficients of each term are normally obtained by fitting Equation 2.1 to the known masses of nuclei. A standard form for the binding energy per nucleon is

$$\frac{E}{A} = \underbrace{a_V}_{\text{Volume}} - \underbrace{\frac{a_S}{A^{1/3}}}_{\text{Surface}} - \underbrace{a_C \frac{Z^2}{A^{4/3}}}_{\text{Coulomb}} - \underbrace{a_{\text{sym}} \frac{(N-Z)^2}{A^2}}_{\text{Symmetry}} - \underbrace{\delta(A, Z)}_{\text{Pairing}} \quad (2.1)$$

The first three terms are easily visualized in terms of the liquid drop model. The volume term is simply the binding energy due to the cohesion of the nucleons in the nucleus. The nuclear force has a limited range, so each nucleon interacts only with the adjacent nucleons. Thus the volume binding energy per nucleon, a_V , is constant. For a finite nucleus, the surface nucleons are in contact with fewer nucleons than the core nucleons, so the binding energy is reduced. The surface term accounts for this reduction by subtracting a binding energy proportional to the surface area of the sphere. The coulomb force further reduces the binding energy due to the repulsion of the positively charged protons, and the approximate

magnitude can be calculated analytically. The last term is called the “pairing” energy and accounts for the extra stability for even-Z, even-N nuclei and the reduction of stability for nuclei with an unpaired proton or neutron. The remaining term is known as the “symmetry” energy. The symmetry term decreases the binding energy for nuclei with different numbers of protons (Z) and neutrons (N). Configurations with $N = Z$ minimize the binding energy because protons and neutrons fill two separate sets of orbitals. Stable heavy nuclei have $N > Z$ due to the competition between the coulomb term and the symmetry term. The symmetry term is parametrized by the isospin asymmetry, δ

$$\delta = \frac{(N - Z)}{(N + Z)} \tag{2.2}$$

The symmetry term is proportional to the square of the asymmetry, because the strong nuclear force should be equivalent for neutrons or protons, so only even powers of δ are allowed. The isospin asymmetry is a small number ($\delta < .25$) for most nuclei, and higher powers (e.g. δ^4) can normally be neglected. Using just this simple picture and a few free parameters, Equation 2.1 reproduces the mass of known nuclei, and provides estimates of the unmeasured masses of exotic nuclei. In fact, in many nuclear reaction simulations, variations of the liquid drop model formula have been used to calculate the masses for extremely proton-rich or neutron-rich nuclei.

The semi-empirical mass formula is a suitable conceptual starting point for realistic EoS, but it assumes that the system is at zero temperature and at fixed density. To further develop the EoS, the nuclear potential must be parametrized as a functional of the proton and neutron density, which is one of the primary goals of nuclear physics research today. The focus of this dissertation is on improving the understanding the symmetry energy part

of this energy functional. The symmetry energy part of the nuclear energy density can be separated from the symmetric matter equation of state in the following way

$$\epsilon(\rho, T, \delta) = \epsilon(\rho, T, \delta = 0) + S(\rho)\delta^2 \quad (2.3)$$

where the symmetry interaction $S(\rho)$ is a function of the nucleon density. $S(\rho)\delta^2$ is called the “symmetry energy”. This expression is an approximation for $\delta \ll 1$. While the temperature can play a role, the more important unknown behavior is the dependence of the symmetry energy on the density. Typically, formulations of $S(\rho)$ ignore any explicit temperature dependence. When describing the interaction in terms of the nucleon density, the asymmetry is defined by:

$$\delta = \frac{(\rho_n - \rho_p)}{(\rho_n + \rho_p)} \quad (2.4)$$

where ρ_p is the volume density of protons, ρ_n is the volume density of neutrons, and ρ is the total nucleon density $\rho_n + \rho_p$. The symmetry energy at saturation density is related to the symmetry term $a_{\text{sym}} \approx 24$ MeV in the semi-empirical mass formula, but $S(\rho)$ includes explicitly the density dependence.

The symmetry energy is modestly constrained at subsaturation densities, and mostly unconstrained for supersaturation densities. For example, the symmetry energy near nuclear saturation density has been constrained from the binding energy of stable nuclei [16]. A common energy functional used for calculations of nuclear matter and finite nuclei is the Skyrme-Hartree-Fock model, [10] which is described in further detail in Section 2.4. The Skyrme force is controlled by a set parameters that can be varied to optimize the model’s

ability to reproduce specific experimental observables for nuclei. Within this model, the density dependence of the symmetry energy is valid mainly around nuclear saturation density which describes the central density of most heavy nuclei. The nuclear interactions that are used in this work are derived from the general Skyrme-type interaction.

2.2 Physical Consequences of the Symmetry Energy

The symmetry energy has a large influence in many areas of nuclear physics and astrophysics. It dictates many properties of neutron stars, because neutron stars are dense, cold, and extremely asymmetric nuclear matter. It also influences nuclear structure; as the density decreases near the surface of a nucleus, a greater asymmetry of neutrons can be supported, creating a so-called neutron skin [16]. Furthermore, the symmetry energy affects the dynamics of nuclear reactions with neutron-rich heavy nuclei. These different areas of nuclear physics can provide information about the symmetry energy which can likewise assist in the interpretation of these physical processes.

2.2.1 Nuclear Astrophysics

A neutron star has collapsed to the point where the nuclear force is in hydrostatic equilibrium with the gravitational force. The intense pressure causes electron capture reactions to become energetically favorable and the matter can become dominated by neutrons. The situation is known as “beta equilibrium”, because the energy gained by an electron capture reaction is equal to the energy cost imposed by the symmetry energy, which is a function of the density. In this way, the proton fraction in a neutron star is completely determined by the density dependence of the symmetry energy. If the proton fraction is high enough, the

“direct Urca process” can occur, which cools neutron stars by allowing energy to be carried away by neutrinos [17]. If the direct Urca process can take place at some depth (density) in a neutron star, it will dominate the cooling of the neutron star and impact the evolution of the neutron star.

The bulk properties of a neutron star are also dictated by the symmetry energy, in the form of the mass-radius relationship. When the composition and equation of state are known, the mass and radius of a spherical body in hydrostatic equilibrium are related by:

$$\frac{dP(r)}{dr} = \frac{GM(r)\rho(r)}{r^2} \quad (2.5)$$

This is modified with general relativity to arrive at the Tolman-Oppenheimer-Volkov equation [18]:

$$\frac{dP(r)}{dr} = -\frac{G}{r^2} \left[\rho(r) + \frac{P(r)}{c^2} \right] \left[M(r) + 4\pi r^3 \frac{P(r)}{c^2} \right] \left[1 - \frac{2GM(r)}{c^2 r} \right]^{-1} \quad (2.6)$$

Once the equation of state (the relationship between $\rho(r)$ and $P(r)$) is specified, the mass-radius relationship can be determined. Conversely, if the mass and radius of a neutron star can be simultaneously and precisely measured, a constraint on the EoS can be determined.

The maximum mass in the mass-radius relationship allows observations of the mass alone to provide constraints on the neutron star EoS. Two recent measurements of neutron stars close to 2 solar masses [19, 20] are very informative for the study of the neutron star equation of state, because they rule out EoS’s with small symmetry energy at high density. Only an EoS with a stiffer asymmetry term at higher density is able to sustain a massive neutron star by providing the pressure needed to resist gravitational collapse. The location of the

transition between the heterogeneous, solid crust and the homogeneous, liquid outer core is also sensitive to the symmetry energy [21]. The density dependence of the symmetry energy determines the energy cost of separating uniform, isospin-asymmetric nuclear matter into regions of higher and lower density. For a stiffer symmetry energy term, the core-crust transition occurs at a lower density.

2.2.2 Nuclear Structure

Analogous to the example of neutron stars, the symmetry energy also plays a role in the structure of heavy nuclei. Although heavy nuclei have $\delta < 0.25$, the symmetry energy is a crucial uncertainty in mean field models of the nuclear interaction. When describing nuclear matter, $S(\rho)$ is often described with a quadratic Taylor series, expanded about $\rho = \rho_0$:

$$S(\rho) = S_0 + L \left(\frac{\rho - \rho_0}{3\rho_0} \right) + \frac{K_{\text{sym}}}{2} \left(\frac{\rho - \rho_0}{3\rho_0} \right)^2 \dots \quad (2.7)$$

Where S_0 is the symmetry energy at saturation density, L is the slope of the symmetry energy at saturation density, and K_{sym} is the curvature of the symmetry energy at saturation density. The linear term in 2.7 is the source of the “symmetry pressure” which can be obtained from the Helmholtz free energy for $T \approx 0$:

$$P = \rho^2 \frac{\partial \epsilon}{\partial \rho} \quad (2.8)$$

and so at nuclear saturation density ρ_0 the pressure of pure neutron matter is approximately:

$$P_0 = \rho_0 \frac{L}{3} \quad (2.9)$$

One example of the effect of the symmetry energy in nuclear structure is the existence of a “neutron skin” in neutron rich nuclei. Quantitatively, the neutron skin is described by the difference between the root-mean-square neutron and proton radii:

$$\Delta_{np} = \sqrt{r_n^2} - \sqrt{r_p^2} \quad (2.10)$$

The neutron skin of ^{208}Pb calculated in the Skyrme-Hartree-Fock model has been shown to be directly and tightly correlated with the slope of the symmetry energy L [16]. A stiffer symmetry energy (higher L) results in a lower value of the symmetry energy at subsaturation densities. Therefore, the energy cost of an asymmetric neutron skin (low density) is lower than the energy cost of spreading the asymmetry over the volume of the nucleus (normal nuclear density) result in a larger neutron skin thickness. Various techniques have been employed to measure the neutron distributions of heavy nuclei [22, 23, 24, 25]. Interpretation of these data is difficult because the results from hadronic probes are highly model dependent. Thus, large uncertainties exist in the neutron distributions while the charge distributions are precisely known.

Measuring the neutron skin thickness is a useful test for the isospin dependent part of the nuclear energy density functional. The most model independent method is a measurement of the neutron radius of ^{208}Pb using parity-violating electron scattering on a polarized Pb target. This experiment was completed, but had large error bars because it did not acquire enough statistics [26]. The measurement for ^{208}Pb will be repeated after installing radiation-hard electronics and vacuum systems, which were a large source of down-time during the first experiment [27]. A measurement for ^{48}Ca has been approved as well [28].

2.2.3 Nuclear Reactions

The symmetry energy also affects the dynamics of many types of nuclear reactions. For example, multifragmentation is the process by which an excited heavy nucleus decays when the excitation energy is too large for the nucleus to deexcite by emitting only nucleons and gamma rays. The process can be pictured as the formation of a region of hot nuclear matter shortly after collisions of two nuclei, which then expands to subsaturation density and breaks up into many smaller fragments. The fragments are distributed in mass and charge according to the free energy of a partition of fragments. The fragments can still have significant excitation energy, and realistic predictions require further evaporation of light particles. The Statistical Multifragmentation Model (SMM) treats this process in a simple, statistical, and semi-empirical way, and provides reasonable predictions of multifragmentation yields. [29] The symmetry energy in the form of the chemical potentials plays a critical role in multifragmentation, in particular the isotopic distributions. As will be discussed in Section 2.3.1, how the isotopic distributions change from one system to another is correlated to the strength of the symmetry energy. SMM-type models do not treat the nuclear interaction directly, instead they approximate the process into several instantaneous steps. Nonetheless, SMM requires assumptions about the EoS which can be informed by experimental constraints on the symmetry energy.

Another class of nuclear process that is partially tied to the symmetry energy and the EoS of nuclear matter are known as Giant Resonances. Important examples are the Giant Dipole Resonance (GDR) and the Giant Monopole Resonance (GMR). The GMR is also known as a *breathing mode*, and can be understood as a radial oscillation of the proton and neutron densities. The resonance energy of the GMR is directly related to the incompressibility

of nuclear matter, because the incompressibility provides the restoring force against the vibration. The incompressibility of bulk nuclear matter is defined to be

$$K_0 = 9\rho^2 \left. \frac{d^2 E/A}{d\rho^2} \right|_{\rho=\rho_0}, \quad (2.11)$$

but for finite nuclei, surface and coulomb effects must be included. A finite nucleus incompressibility can be extracted from the experimental energy of the GMR and the RMS nuclear radius by

$$E_{GMR} = \sqrt{\frac{\hbar^2 K_A}{m \langle r^2 \rangle}}. \quad (2.12)$$

K_A can be determined from experiment, but the relationship between K_A and K_0 is uncertain, which makes the determination of K_0 difficult.

The GDR is a dipole oscillation of proton and neutron densities along one axis of the nucleus. When the proton and neutron densities oscillate in phase, the excitation is called isoscalar, and when the proton and neutron densities oscillate out of phase it is called isovector. The isovector GDR is an oscillation where the restoring force is provided by the symmetry energy. Thus, studying the GDR provides information about the symmetry energy.

These oscillations of finite nuclei only provide information about densities close to normal nuclear density. In contrast, the Pygmy Dipole Resonance (PDR) is proposed to be an oscillation of the isospin symmetric core of the nucleus inside the asymmetric neutron skin. [30, 31] Because this would preferentially probe the surface of the nucleus, it could provide information about the low density behavior of the symmetry energy. The relative strength of the PDR has been shown to be related to the density dependence of the symmetry energy.

2.3 Isospin Diffusion

One concept that was developed in the study of the symmetry energy with heavy ion collisions is called isospin diffusion. This simple concept is a natural step in reaction dynamics: put a neutron-rich nucleus very close to a neutron-poor nucleus and see how fast the system reaches isospin equilibrium. The symmetry energy would drive the two nuclei to exchange protons or neutrons, until the isospin asymmetry of the two nuclei became equalized. In practice, the situation is more complicated.

To overcome the coulomb repulsion, the projectile and target nuclei must have large relative velocity. For isospin diffusion to occur, the reaction timescale should be comparable to the nucleon-nucleon collision timescale inside the nucleus. For this reason, the physics must be interpreted using a dynamical reaction model that describes the evolution of individual nucleons through the collision. To describe this many body problem, many approximations must be made. Nonetheless, by carefully choosing reliable observables and continuously improving the nuclear transport calculations, constraints on the symmetry energy have been obtained.

For the purposes of this dissertation, isospin diffusion will be discussed in the context of isotopes of Sn. This is a natural choice, as Sn has stable isotopes ranging from ^{112}Sn ($\delta = .1071$) to ^{124}Sn ($\delta = .1935$), and the Sn+Sn system is large enough to apply a macroscopic approach to the physics. With high-intensity radioactive beams at the Facility for Rare Isotope Beams (FRIB, under construction), the range of asymmetry can be increased using radioactive isotopes from ^{108}Sn to ^{132}Sn .

When ^{112}Sn and ^{124}Sn collide in a peripheral collision (large impact parameter b), an overlap region forms between the colliding nuclei and nucleons can be exchanged. On average,

neutrons would diffuse from the neutron-rich ^{124}Sn to the neutron-poor ^{112}Sn through the neck region. The densities of protons and neutrons can be described with a diffusion equation,

$$j_n = D_n^\rho \Delta \rho - D_n^\delta \Delta \delta \quad (2.13)$$

$$j_p = D_p^\rho \Delta \rho - D_p^\delta \Delta \delta, \quad (2.14)$$

where the $D_{n,p}^{\rho,\delta}$ are the diffusion coefficients for neutrons and protons for density and isospin.

Combining Equation 2.13 and 2.14 gives

$$j_\delta = j_n - j_p = \underbrace{\left(D_n^\delta - D_p^\delta \right) \Delta \delta}_{\text{Isospin Diffusion}} - \underbrace{\left(D_n^\rho - D_p^\rho \right) \Delta \rho}_{\text{Isospin Migration}} \quad (2.15)$$

which indicates that two mechanisms drive the diffusion of isospin between the projectile and the target. The isospin gradient drives a diffusion of isospin directly. A separate effect known as ‘‘isospin migration’’ also influences the equilibration. Isospin migration is a net flux of isospin because the density diffusion coefficient D_n^ρ for neutrons is different from the density diffusion coefficient D_p^ρ for protons. Because the symmetry energy decreases with decreasing density, a low density region can support a bigger isospin asymmetry so neutrons diffuse faster into the neck region than protons [32]. Isospin migration would be present in both the symmetric and mixed collisions.

The observable that would constitute a direct measurement of isospin diffusion would be a measurement of the isospin asymmetry of the excited projectile-like fragment at the moment of the separation between projectile and target, which happens on the timescale of $\approx 10^{-22}\text{s}$. Unfortunately the reaction products are measured on a timescale that is many

orders of magnitude longer, and the detected fragments have deexcited by particle emission. Because of this deexcitation, the composition of the primary excited fragment is obscured.

When simulating the reaction with a dynamical transport model, the asymmetry of the primary source can be calculated directly. In an experiment, the measured observables must be related to this observable in a quantitative way. For the purpose, the “isospin transport ratio” has been constructed (in this case for the mixed reaction $^{112}\text{Sn}+^{124}\text{Sn}^1$) to quantify the amount of diffusion.:

$$R_I(X_{112+124}) = \frac{2X_{112+124} - (X_{124+124} + X_{112+112})}{X_{124+124} - X_{112+112}} \quad (2.16)$$

where X is an observable that is related to the isospin asymmetry achieved in the reaction.

This observable has several useful properties. If an experimental observable X is identified where $\delta = aX + b$, then $R_I(\delta) = R_I(X)$. This is critical because the theoretical calculations produce the isospin asymmetry δ , which cannot be measured directly in the experiment. If $X_{112+124} = X_{112+112}$ then $R_I = -1$, and if $X_{124+112} = X_{124+124}$ then $R_I = +1$. $R_I = \pm 1$ indicates that no diffusion occurred. If diffusion drives the system to isospin equilibrium, then $R_I(X) = 0$ in either mixed reaction.²

If an observable which meets the linearity condition is identified, then the measured observable can be compared to the calculated isospin asymmetry. This is an experimental question independent from the measurement of isospin diffusion. Previously [33] and for this purposes of this study, the observable that is explored is the isotopic scaling (denoted by α) of fragments which is the topic of the next section. It was shown in [34] that $\delta = a\alpha + b$ for central collisions, but this linearity should be measured for peripheral collisions as well.

¹The convention for reaction notation throughout the dissertation will be: (projectile)+(target)

²Because of the mass asymmetry of the projectiles, $R_I(\delta)=0.0507$ at equilibrium, see Section 5.4.

2.3.1 Isoscaling in Statistical Processes

“Isoscaling” describes the way that an isotopic yield ratio of fragments emitted in a statistical process follows an exponential function of the neutron and proton number of the fragment. When plotted as a logarithm, the trend is linear. This behavior was first described in [35], and was identified in many physical systems including multifragmentation, evaporation, and deeply inelastic reaction mechanisms. Since that time, isoscaling has been observed in many other physical systems such as fission and projectile fragmentation. [36, 37] The isoscaling trend is generally described with a three parameter relation:

$$R_{21}(N, Z) = \frac{Y_2(N, Z)}{Y_1(N, Z)} = C e^{(\alpha N + \beta Z)} \quad (2.17)$$

where $Y_i(N, Z)$ is the yield of the isotope with atomic number Z and neutron number N , measured in the reaction i . By convention the more neutron-rich system is in the numerator, which results in $\alpha > 1$ and $\beta < 1$. This is a useful way to describe how the isotopic distribution changes when the isospin content of the emitting system is changed. In practice, forming yield ratios between different reactions eliminates the dependence on absolute normalizations, detector acceptance, and the structure of the emitted fragments, as well as reduces the effects of sequential decays. Isoscaling is fundamentally related to the symmetry energy, and various statistical models predict that the magnitude of the isoscaling slope α (or β) should be proportional to the symmetry energy part of the nuclear binding energy $\frac{C_{\text{sym}}}{T}$. [38] The description most often used, which keeps the leading order terms in N and

Z , and assumes the temperature to be the same in the two systems being compared, is:

$$\alpha = \frac{\Delta\mu_n}{T} \approx \frac{4C_{\text{sym}}}{T} \left[\left(\frac{Z_1}{A_1} \right)^2 - \left(\frac{Z_2}{A_2} \right)^2 \right] \quad (2.18)$$

$$\beta = \frac{\Delta\mu_p}{T} \approx \frac{4C_{\text{sym}}}{T} \left[\left(\frac{N_1}{A_1} \right)^2 - \left(\frac{N_2}{A_2} \right)^2 \right] \quad (2.19)$$

$\Delta\mu_n$ ($\Delta\mu_p$) refers to the difference of the neutron (proton) chemical potential between the two emitting sources, and are approximated by the neutron and proton separation energies. These expressions are produced in the context of several statistical models [35], but experimentally, some ambiguity remains. Equations 2.18 and 2.19 show that α and β do not depend linearly on the isospin asymmetry of the emitting source. In the previous study of isospin diffusion, [33], it was assumed that this expression might be linear with the asymmetry of the composite system as it is difficult to determine the asymmetry of the emitting system.

An alternative picture can be described in terms of scaling with the mass and neutron excess as opposed to the neutron and proton number. It is a simple transformation, but has some useful features. In this case α and β are replaced with α' and β' , which are the scaling coefficients for mass and neutron excess, respectively:

$$R'_{21}(A, N - Z) = \frac{Y_2(A, N - Z)}{Y_1(A, N - Z)} = C' e^{\left(\alpha' A + \beta' (N - Z) \right)} \quad (2.20)$$

where

$$\alpha' = \frac{(\alpha + \beta)}{2} \quad (2.21)$$

$$\beta' = \frac{(\alpha - \beta)}{2} \quad (2.22)$$

and in this alternative point of view, the results are related to the isospin composition by:

$$\alpha' = \frac{\Delta(\mu_n + \mu_p)}{2T} \approx \frac{-C_{\text{sym}}}{T} (\delta_2^2 - \delta_1^2) \quad (2.23)$$

$$\beta' = \frac{\Delta(\mu_n - \mu_p)}{2T} \approx \frac{2C_{\text{sym}}}{T} (\delta_2 - \delta_1) \quad (2.24)$$

This alternative isoscaling was suggested originally in [39] where isoscaling (of light fragments) was studied with multifragmentation reactions induced by light ions. In that study, it was noted that the absolute magnitudes of α and β were similar, so α' was small although was measureably positive. In [40], “isobaric scaling” was studied, where the yield for a constant A was fit as a function of $N - Z$ when measuring heavy residues from projectile fragmentation. In this study, β' was shown to have similar behavior to α , but α' was assumed to be negligible. The choice may seem simply notational, but one method may have advantages. For instance, when studying projectile fragmentation the temperature could be approximated by a linear function of the fragment mass:[41]

$$T(A) = T_o + T_1 \left(\frac{A}{A_{\text{proj}}} \right) \quad (2.25)$$

From the point of view of measuring isoscaling of heavy residue yields from projectile fragmentation, especially over a large range of Z and A , a varying temperature would result in a systematically varying α and β . When fitting the isobaric yield ratios as a function of $N - Z$, because isotopes of a fixed mass likely come from a single temperature, the isoscaling trend may be more reliable. It is possible to extract a slope for each fragment mass, $\beta'(A)$, and a slope for for each neutron excess, $\alpha'(N - Z)$. With the “normal” isoscaling

variables, $\alpha(Z)$ and $\beta(N)$ can be extracted. In the ideal case, the formulations are identical and interchangeable. In the experiment, both are potentially useful.

Another consideration is that of the possible isoscaling variables, only $\beta' = (\alpha - \beta)/2$ has a linear dependence on δ , which makes it appealing for use with the isospin transport ratio. Also, one very interesting relationship appears when taking the ratio of the α' and β' from 2.23 and 2.24:

$$\frac{\alpha'}{\beta'} = \frac{\alpha + \beta}{\alpha - \beta} = \frac{\delta_1 + \delta_2}{2} = \bar{\delta} \quad (2.26)$$

Since the T and C_{sym} cancel, this ratio would probe the average asymmetry between the two reactions directly, without relying on a calibration of the temperature. Since in this experiment the reference reaction (reaction “1”) is $^{112}\text{Sn} + ^{112}\text{Sn}$, the average asymmetry is a measure of the asymmetry of the compared reaction (reaction “2”). The isospin transport ratio calculated with this observable is useful to understand the systematics of the isoscaling behavior in projectile fragmentation.

This dissertation seeks to use isoscaling as an observable for the isospin transport ratio to measure isospin diffusion between ^{112}Sn and ^{124}Sn . In addition, a secondary goal is to verify the relations with α and β with δ .

2.3.2 Previous measurement of Isospin Diffusion at NSCL

The present study is a continuation of a long program at NSCL to constrain the symmetry energy part of the nuclear EoS. [42] Isospin diffusion was used successfully for this purpose in [33]. In that experiment, the four reactions $^{112}\text{Sn} + ^{112}\text{Sn}$, $^{112}\text{Sn} + ^{124}\text{Sn}$, $^{124}\text{Sn} + ^{112}\text{Sn}$, and $^{124}\text{Sn} + ^{124}\text{Sn}$ at 50 MeV/u were studied. The experiment combined the Miniball-Miniwall

Reaction	α	$R_I(\alpha)$
$^{112}\text{Sn}+^{112}\text{Sn}$	0	-1
$^{112}\text{Sn}+^{124}\text{Sn}$	0.16 ± 0.02	-0.45 ± 0.05
$^{124}\text{Sn}+^{112}\text{Sn}$	0.42 ± 0.02	0.47 ± 0.05
$^{124}\text{Sn}+^{124}\text{Sn}$	0.57 ± 0.02	+1

Table 2.1 Neutron isoscaling parameter α and isospin transport ratio measured in the previous NSCL Isospin Diffusion experiment.

array with the Large Area Silicon Strip Array (LASSA) (both described in Chapter 3) and an additional annular Silicon-CsI detector at very forward angles, and the purpose was to measure isoscaling of intermediate mass fragments (IMF’s) from the the Sn+Sn collisions.

The data that was used to form these isoscaling ratios was selected to be “mid-peripheral”, by requiring $b/b_{\text{max}} > 0.8$ and $y/y_{\text{beam}} > 0.7$ where b is the scattering impact parameter and y is the rapidity. The purpose of this impact parameter selection is to select collisions where the nucleons can be exchanged between the target and the projectile. If more central collisions were included, the data would contain fragments emitted from multifragmentation of the entire combined Sn+Sn system, which would represent isospin equilibrium.

IMF yields were measured for $3 \leq Z \leq 8$, and the fragments were fit using the standard three parameter isoscaling formula. Results are published in [34, 33]. For example, the isoscaling parameter α that was extracted is listed in Table 2.1. The result obtained was $R_I(\alpha) = +0.47 \pm 0.05$ for the $^{124}\text{Sn}+^{112}\text{Sn}$ system and $R_I(\alpha) = -0.45 \pm 0.05$ for the $^{112}\text{Sn}+^{124}\text{Sn}$ system. The interpretation of this result is that the system evolved roughly halfway to isospin equilibrium during the collision.

2.3.3 A New Measurement of Isospin Diffusion

The focus of this dissertation is a new measurement of isospin diffusion using the isoscaling parameters extracted from heavy projectile-like fragment yields. The experiment is described in detail in Chapter 3.

There were several shortcomings in the previous isospin diffusion experiment that are meant to be addressed in this study. One issue with measuring isoscaling of IMF's is that the yields for these fragments are relatively low. Because the LASSA array only covers a small portion of the possible scattering angles, the efficiency for detecting these fragments is quite low as well. As an alternative way of probing the isospin asymmetry of the projectile like fragment, heavy projectile-like fragments can be measured at very forward angles. Projectile fragmentation cross sections are high; a semi-peripheral collision will very likely result in producing a heavy fragment. Higher cross sections (as well as many more data points) will allow for much higher statistics. The properties of the heavy fragments are also more directly connected to those of the excited primary source. The yields of IMF's can be influenced by various reaction mechanisms which can obscure the isospin diffusion signal. Various measurements [37, 43, 44] of isoscaling from heavy projectile-like fragments also provide some confidence that this type of study can be used with good precision. In addition to logistical advantages, theoretical calculations suggest that the heavy residues may have a different sensitivity to the symmetry energy than the IMF's [45].

Another nice feature of the measurement of heavy residues is that heavy fragments only result from peripheral collisions. This will allow for an additional measure of the centrality of the collision: higher Z fragments come from more peripheral collisions. In addition, the measurement of the impact parameter will be more reliable, with an improved method for

normalizing the beam current and total reaction cross sections. A reliable extraction of the impact parameter being probed in the experiment is important in the comparison to theoretical calculations.

Finally, this experiment will attempt to verify the relationships of the isoscaling parameters α and β with the $\frac{N}{Z}$ or δ of the emitting source. This will be accomplished by measuring a data set for the $^{118}\text{Sn}+^{118}\text{Sn}$ in addition to the $^{112}\text{Sn}+^{112}\text{Sn}$ and $^{124}\text{Sn}+^{124}\text{Sn}$ reactions. The $^{118}\text{Sn}+^{118}\text{Sn}$ system represents a data point approximately midway between the other two symmetric systems, and should give an independent measure of “isospin equilibrium”. In other words, by examining the trend of the isoscaling observables with the increasing asymmetry of the different Sn isotopes, the isoscaling relationships described in this chapter can be tested. Measuring additional combinations with the ^{118}Sn isotope may also help to constrain other effects that affect the isospin content, such as isospin migration.

2.4 Transport Calculations

When studying the nuclear equation of state, physical quantities are rarely probed directly. Normally, an observable is measured in the laboratory and the results are then compared to a realistic simulation. The input parameters of the model calculation are varied to find the best agreement with the data before drawing any physical conclusions. This requires a model that can not only reliably reproduce experimental quantities, but has physically motivated input parameters. A phenomenological model is less useful because some model parameters may not be physically meaningful, and the models may not contain all of the physics involved in the collisions. When using heavy ion collisions to study the EoS, the collision process has a large number of degrees of freedom so the calculations are computationally demanding.

Nonetheless, the models must be sufficiently complex so that the microscopic physics is treated realistically.

For this study, the ImQMD model is used [46, 47, 48]. This is a variation in the class of Quantum Molecular Dynamics (QMD) models. Molecular Dynamics models were developed to describe molecular systems, but the method has been adopted in nuclear physics as well. In QMD, each nucleon is represented by a gaussian wave packet which moves semi-classically subject to a self-consistent mean field. The width of the gaussian wave packet is an important parameter in the simulations, and its value is fixed during the reaction. For system with different sizes, a phenomenological formula was proposed to parametrize the width of wave packet:

$$\sigma_r^2 = \frac{\sigma_{r,Approj}^2 + \sigma_{r,Atarget}^2}{2} \quad (2.27)$$

where

$$\sigma_{r,A}^2 = \left(0.16A^{1/3} + 0.49\right)^2 \text{ fm}^2. \quad (2.28)$$

QMD keeps track of the correlations between N nucleons, compared to BUU-type models [49]. As a result, it is more computationally demanding than BUU. The single particle phase space distribution function is given by:

$$f_i(\vec{r}, \vec{p}) = \frac{1}{(\pi\hbar)^3} \exp\left(-\frac{(\vec{r} - \vec{r}_i)^2}{2\sigma_r^2} - \frac{(\vec{p} - \vec{p}_i)^2}{2\sigma_p^2}\right) \quad (2.29)$$

where σ_r and σ_p are the position and momentum wave packet widths. The specific details of the QMD model are well documented elsewhere [46, 47, 48] and are not critical to this study.

Because the models are semi-classical, the Pauli exclusion principle has to be included at least in an approximate way, which is referred to as “Pauli blocking”. There are many different versions based on the QMD model, which usually differ by the method that they handle “Pauli blocking”. In Antisymmetrized Molecular Dynamics [50, 51], each nuclear system is represented by a Slater determinant of gaussian wave packets, which satisfies the Pauli principle. This leads to a much more computationally intensive model, so AMD calculations for very large systems are not commonly performed. The CoMD formulation [52] addresses Pauli blocking by placing a limit on the phase space occupation density; if a particle travels into occupied phase space, the particle is scattered. If Pauli blocking is ignored in the model, the system will evolve towards a classical thermodynamic limit, which is not applicable to finite nuclei.

The Improved Quantum Molecular Dynamics Model (ImQMD) was originally developed for the description of fusion processes near the coulomb barrier [46]. ImQMD uses isospin dependent nucleon-nucleon scattering cross sections; the cross section for protons is different than for neutrons. The critical input to ImQMD is the form of the mean field potential that dictates the evolution of the nucleonic wave packets. Recently, ImQMD05 [47] has been modified to study the Nuclear EoS using heavy ion collisions. In ImQMD05, the symmetric part of the nuclear potential can be taken from the Skyrme force [10]:

$$V_{loc} = \frac{\alpha \rho^2}{2 \rho_0} + \frac{\beta}{\eta + 1} \frac{\rho^{\eta+1}}{\rho_0^\eta} + \frac{g_{sur}}{2\rho_0} (\nabla \rho)^2 \quad (2.30)$$

where α , β , η , ρ_0 , and g_{sur} are parameters of the model and are related to the standard Skyrme parameters. In the case of ImQMD05, the goal is to study the density dependence of the symmetry energy, so a simple power law dependence is adopted for the potential energy part of the symmetry energy density:

$$\epsilon_{sym} = \frac{C_{sym}}{2} \left(\frac{\rho}{\rho_0} \right)^\gamma \rho \delta^2 \quad (2.31)$$

which allows for simple control of the symmetry energy. High values of γ ($\gamma > 1$) are labeled “stiff” and lower values ($\gamma < 1$) are labeled “soft”.

ImQMD05 was used successfully in determining constraints on the symmetry energy from heavy ion collisions. Measurements of isospin diffusion using isoscaling of intermediate mass fragments and ${}^7\text{Li}/{}^7\text{Be}$ yield ratios were reproduced by ImQMD calculations of the average isospin asymmetry in collisions at several impact parameters [34]. The “double-ratio” of neutrons to protons in central collisions of ${}^{112}\text{Sn}+{}^{112}\text{Sn}$ and ${}^{124}\text{Sn}+{}^{124}\text{Sn}$ presented in [53] was also reproduced by calculations with ImQMD05 in [54]. The extracted constraints on the density dependence of the nuclear symmetry energy are summarized in [42].

A newer version of the ImQMD model, ImQMD-Sky, was developed to utilize an even more realistic nuclear interaction [48]. A more detailed Skyrme potential is used, but the spin-dependent part of the potential is neglected because this is thought to be a minor contribution. The momentum dependence of the nuclear mean field is included as:

$$V_{md} = \int d^3p d^3p' \left[C_o f(\vec{r}, \vec{p}) f(\vec{r}, \vec{p}') (\vec{p} - \vec{p}')^2 \right] \quad (2.32)$$

$$+ \int d^3p d^3p' \left[D_o \left(f_n(\vec{r}, \vec{p}) f_n(\vec{r}, \vec{p}') (\vec{p} - \vec{p}')^2 + f_p(\vec{r}, \vec{p}) f_p(\vec{r}, \vec{p}') (\vec{p} - \vec{p}')^2 \right) \right]$$

where C_0 and D_0 are each directly a function of the parameters of the Skyrme force and the local part of the nucleonic energy density is

$$\begin{aligned}
 V_{loc} = & \underbrace{\frac{\alpha}{2} \frac{\rho^2}{\rho_0} + \frac{\beta}{\eta+1} \frac{\rho^{\eta+1}}{\rho_0^\eta} + \frac{g_{sur}}{2\rho_0} (\nabla\rho)^2}_{\text{Symmetric Matter}} \\
 & + \underbrace{\frac{g_{sur,iso}}{\rho_0} [\nabla(\rho_n - \rho_p)]^2 + (A_{sym}\rho^2 + B_{sym}\rho^{\gamma+1}) \delta^2}_{\text{Asymmetric Matter}}
 \end{aligned} \tag{2.33}$$

and the parameters $\alpha, \beta, \eta, \gamma, g_{sur}, g_{sur,iso}, A_{sym}, B_{sym}$ can be obtained from the normal Skyrme interaction parameters. The benefit of using the Skyrme interaction is that the Skyrme potential has been developed to describe nuclear structure properties, which provides some confidence that the physics is properly treated. In addition, the Skyrme parameter sets are easily interchanged and a different interaction can be used. Using the Skyrme interaction allows more degrees of freedom in describing the interaction, but these effects can be hard to understand intuitively. One way to picture the momentum dependent interaction is with the concept of an effective mass. The effective mass can be introduced to describe how the potential energy depends on the momentum. This can be pictured by writing down Hamilton's equation:

$$\dot{x} = \frac{\partial H}{\partial p} = \frac{\partial T}{\partial p} + \frac{\partial V}{\partial p} \tag{2.34}$$

$$= \frac{p}{m} + \frac{\partial U}{\partial p} \tag{2.35}$$

$$= \frac{p}{m} \left(1 + \frac{m}{p} \frac{\partial U}{\partial p} \right) \equiv \frac{p}{m^*}$$

Name	ρ_0 (fm^{-3})	E_0	K_0	S_0	L	K_{sym}	m^*/m	m_n^*/m	m_p^*/m
SLy4	0.160	-15.97	230	32	46	-120	0.69	0.68	0.71
SkI2	0.158	-15.78	241	33	104	71	0.68	0.66	0.71
SkM*	0.160	-15.77	217	30	46	-156	0.79	0.82	0.76
Gs	0.158	-15.59	237	31	93	14	0.78	0.81	0.76

Table 2.2 Effective physical quantities resulting from the parameter sets used in this study. These quantities are calculated from the interaction at nuclear saturation density.

where m^* is the effective mass. $\frac{m^*}{m}$ represents the overall effect of the momentum dependence of the nuclear potential. m_n^* and m_p^* are not free parameters of the interaction, but result from the choice of the Skyrme parameter set. It is also a function of the local nucleon density. The effective mass at saturation density is approximately 30% lower than the free nucleon mass. This “effective mass splitting” is a measure of how the momentum dependence can affect the symmetry energy part of the nuclear interaction, and therefore can affect isospin-sensitive observables.

In this dissertation, calculations with both versions ImQMD05 and ImQMD-Sky have been performed. For ImQMD05, γ 's from 0.5 to 2.0 were used. For ImQMD-Sky, the four parameter sets that will be shown are **SLy4**, **SkI2**, **SkM***, and **Gs**. The saturation parameters for the four Skyrme parameter sets are shown in Table 2.2.

Although isospin diffusion is mainly influenced by the density dependence of the symmetry energy, the momentum dependence of the nuclear interaction (reflected in the effective mass splitting) can also affect the isospin transport ratio [45]. By examining calculations with a varying symmetry energy density dependence (ImQMD05), as well as calculations with several accepted Skyrme parameter sets (ImQMD-Sky), the best picture of the isospin dynamics can be obtained. The results of the calculations will be shown in Chapter 5.

Chapter 3

Experimental Setup

3.1 Overview of Experiment

This experiment was performed at the Coupled Cyclotron Facility (CCF) at the National Superconducting Cyclotron Laboratory (NSCL) at Michigan State University (MSU). The experiment utilized primary beams of ^{112}Sn , ^{118}Sn , and ^{124}Sn from the K1200 Cyclotron at 120 MeV/u. The energy of the primary beam was degraded using the A1900 fragment separator, which resulted in beams with an energy of 70 MeV/u with a momentum width of $\pm 0.125\%$. These beams were transported from the A1900 to the target position in the S3 vault at the pivot point of the S800 Spectrometer. The beams were impinged on isotopically enriched ($> 99.5\%$ purity) targets of ^{112}Sn , ^{118}Sn , and ^{124}Sn . The thicknesses of the targets used are shown in Table 3.1. Using the Miniball-Miniwall array as an indirect beam monitor, the beam rate on target was determined to be between $2 \times 10^7 \text{s}^{-1}$ and $6 \times 10^7 \text{s}^{-1}$.

Target	Thickness $\left(\frac{\text{mg}}{\text{cm}^2}\right)$	Number Density $\left(10^{19} \frac{\text{atoms}}{\text{cm}^2}\right)$
^{112}Sn	5.940	3.19
^{118}Sn	6.316	3.22
^{124}Sn	5.512	2.68

Table 3.1 Target thicknesses.

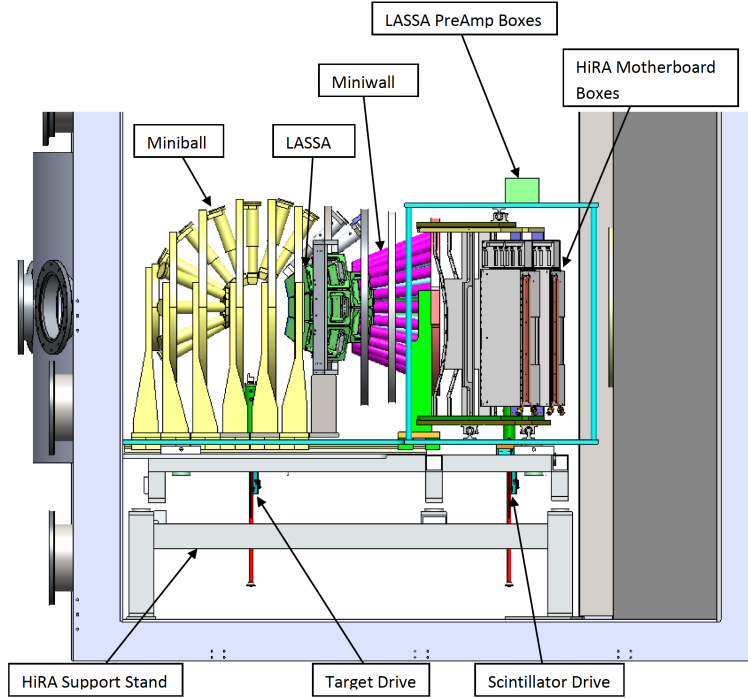


Figure 3.1 Schematic of the scattering chamber, showing the Miniball-Miniwall and the LASSA array. The beam enters from the left, and the heavy residues exit to the right into the S800 spectrometer.

The experimental apparatus included three separate detector systems: the MSU Miniball-WashU Miniwall array, the LASSA array, and the S800 spectrometer. A schematic drawing of the target chamber is shown in Figure 3.1.

The reaction targets were located at the center of the Miniball, and charged particles from reactions in the target were detected in the Miniball and in the LASSA array, while heavy residues passed through the scattering chamber to be detected in the S800 spectrometer. Additionally, a thin scintillator (made from BC-408 scintillator material) was located approximately 0.75 meters from the target position. This thin scintillator was used to measure the time-of-flight (TOF) of heavy fragments through the S800.

The combination of several complex detector systems poses unique challenges. The experiment uses stable beams and the reactions of interest have large cross sections, so the

rate limiting factor was the throughput of the data acquisition system. To help limit the dead-time associated with each event, the electronics were separated into three distinct data acquisition systems (LASSA, Miniball-Miniwall, S800). Each event was time-stamped and the resulting data files were merged offline. This allowed each system to digitize signals in parallel, which decreased the dead-time. In this configuration, the dead-time is dictated by the dead-time of the slowest system. The resulting live-time was 70% or greater when reading up to 500 events/second.

To record the timestamp for each event, each of the three systems contained an XLM72 configured as a 64-bit scaler. This scaler was incremented by a signal from a 100MHz clock module which was reset at the beginning of each run. To combine the data offline, the timestamp of the event recorded in each detector system were matched up event-by-event. A negligible number of events were lost in this merging procedure. In order to verify that the three systems were timestamped correctly online, certain reference signals were recorded in each system, which could be compared directly without merging the data.

During the experiment, the trigger for the data acquisition system was a coincidence of the S800 spectrometer (derived from the E1 timing signal), with the multiplicity trigger from the Miniball-Miniwall array (multiplicity ≥ 2). The LASSA array was not part of the trigger, and its data was only taken along with the S800 and the Miniball-Miniwall. In the end, seven different Sn+Sn reaction systems were measured, and the amount of events recorded in each system are shown in Table 3.2.

Reaction System	Events (Millions)
$^{112}\text{Sn}+^{112}\text{Sn}$	11.4
$^{112}\text{Sn}+^{124}\text{Sn}$	8.7
$^{118}\text{Sn}+^{112}\text{Sn}$	3.8
$^{118}\text{Sn}+^{118}\text{Sn}$	10.7
$^{124}\text{Sn}+^{112}\text{Sn}$	12.3
$^{124}\text{Sn}+^{118}\text{Sn}$	10.1
$^{124}\text{Sn}+^{124}\text{Sn}$	15.2

Table 3.2 Statistics obtained from each reaction system, combining the three magnetic settings of the S800 spectrometer.

3.2 S800 Spectrometer

The S800 spectrometer [55] was used in this experiment to measure the heavy residual fragments from $^{112,118,124}\text{Sn}+^{112,118,124}\text{Sn}$ collisions. The S800 consists of two dipole magnets that are capable of bending fragments up to 4.0 T·m. The momentum acceptance is $\approx 5\%$ and the angular acceptance is about 20 msr. In this experiment, the S800 is operated in focused mode, where the beam is focused at the target position, and the fragments are dispersed by their magnetic rigidity in the focal plane. The S800 can identify the mass and charge of these fragments by using the ΔE -TOF- $B\rho$ method, described in Section 4.2.

The measurement of the heavy fragments begins when the fragments pass through a $100\mu\text{m}$ plastic scintillator located about 0.75m downstream of the target. A rectangular hole was cut out of the center of the scintillator to allow the beam to pass through, undegraded. Otherwise, the ^{112}Sn beam would have been deflected into the S800 focal plane. If the full beam intensity entered the focal plane, the focal plane detectors would have been damaged. The scintillator itself would also deteriorate quickly if the beam was impinged on it. The effect of this hole on the results is discussed in more detail in Appendix C.

The focal plane consists of several detectors that are used to provide kinematical information about the detected fragments. A schematic drawing of the focal plane is shown in Figure 3.2. First, the fragments pass through two Cathode Readout Drift Chambers (CRDC's) [56]. Each provides a position measurement in two dimensions. Each CRDC is approximately 30 cm by 59 cm wide, and is about 1.5 cm thick in the beam direction. They are filled with a gas mixture that is 80% CF_4 and 20% C_4H_{10} at 140 Torr. The gas volume is isolated from the vacuum by thin windows made from $12\mu\text{m}$ thick PPTA, a polymer similar to kevlar. When a particle passes through the gas volume, the gas is ionized and the ionization electrons are

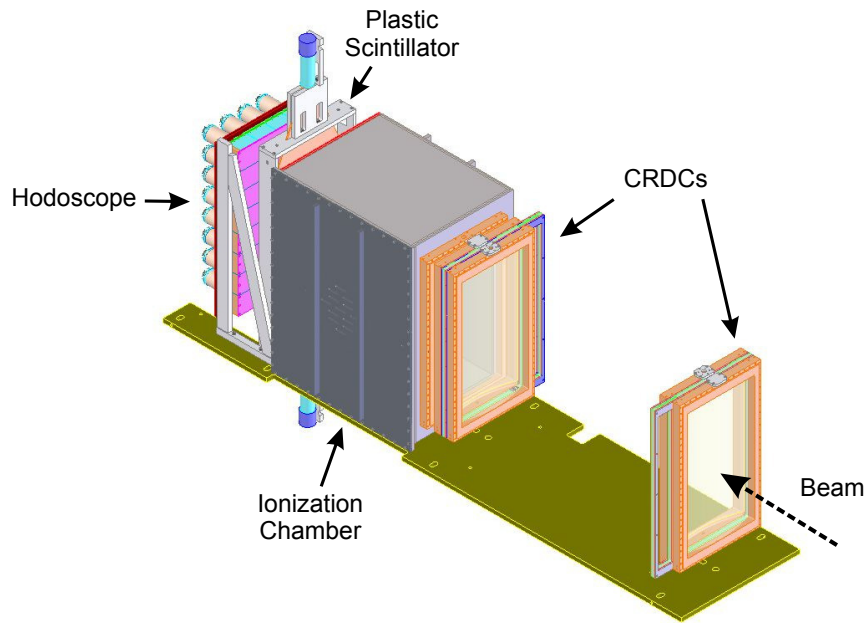


Figure 3.2 Schematic drawing of the S800 focal plane. Figure is taken from [57].

drifted by an electric field. They are avalanched on anode wires that run perpendicular to the beam direction, which induces a charge on the cathode pads. Each CRDC has 224 pads that register the induced charge from the avalanching electrons. The induced charge is spread over about 10 pads in a roughly gaussian distribution. By fitting the charge distribution, the position in this dimension (the “dispersive” direction) can be determined with a resolution of $\sigma < .5$ mm. By comparing the time that the signal arrives to a fixed reference, the position in the non-dispersive direction can be determined. A schematic drawing of the CRDC’s is shown in Figure 3.3.

After the CRDC’s, the fragment enters the ionization chamber, where they lose a significant portion of their energy. The atomic charge Z of the heavy fragment is determined using the energy loss measured in this detector. Like the CRDC’s, the S800 ionization chamber

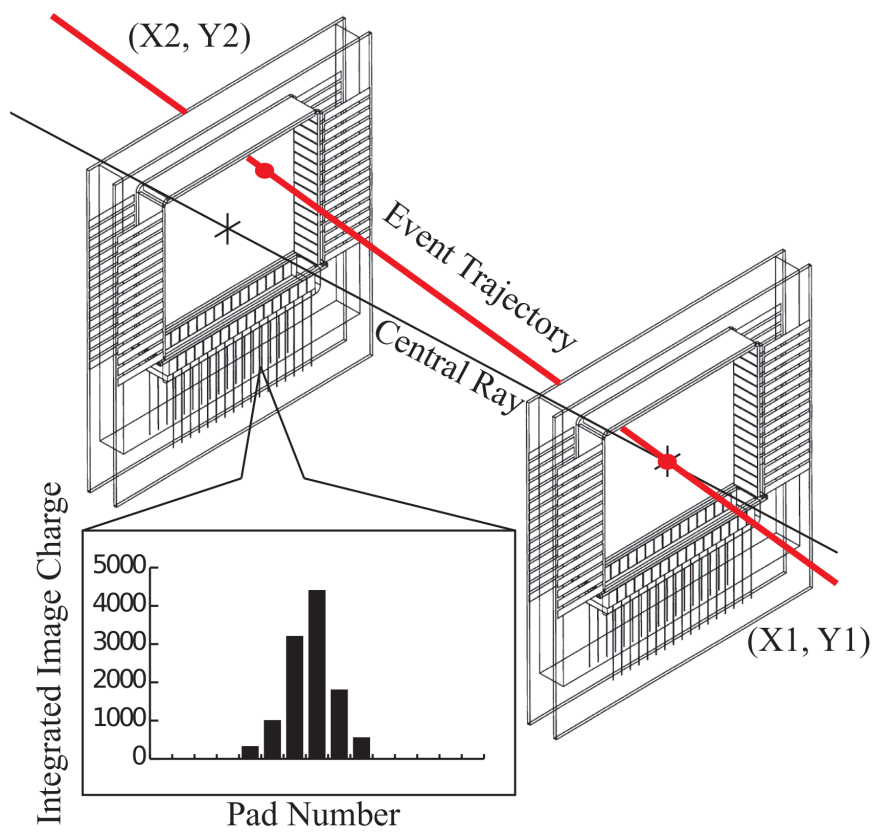


Figure 3.3 Schematic drawing of the CRDC's in the S800 focal plane. Figure is taken from [58].

is a gas-filled detector, filled with 300 Torr of P10 gas. (90% Ar, 10% Methane). It is segmented into 16 separate volumes, and the ionization in each volume is measured individually. The ionization chamber is segmented to decrease the overall noise in the combined signal. Each segment has $1/16^{\text{th}}$ of the electronic noise of the total volume, but the noise adds in quadrature and not additively.

The fragments then deposit most or all of their remaining energy in a 30cm by 59cm wide, 1mm thick scintillator, called the E1 scintillator. The timing signal from the E1 scintillator is subtracted from the timing signal from the scintillator in the target chamber to give the time-of-flight through the S800. The time-of-flight is used to identify the heavy fragments by their mass-to-charge ratio. The scintillator has an EMI 9807B photomultiplier tube at each end. In this experiment, only information from the high-momentum side was used, because this side provided the experimental trigger.

Finally, the highest energy fragments deposit any remaining energy in a 4 by 8 array of 32 CsI(Na) scintillators, which are each read out with a Hamamatsu model R1307 photomultiplier tube [59]. It can be seen at the end of the focal plane in Figure 3.2. The hodoscope was commissioned shortly before this experiment. Its purpose is to provide an additional measurement of the fragment energy. The total energy is needed to distinguish fragments that are not fully stripped of electrons. The analysis of the data from the hodoscope is described separately in Appendix B.

In order to reconstruct the full momentum distribution of the heavy fragments, three different magnetic settings were used in the S800. The range of isotopes that are measured in this experiment was determined by the choice of magnetic rigidity. For a given velocity, very neutron-rich fragments have high magnetic rigidity, and neutron-poor fragments have low magnetic rigidity. The least rigid beam species is ^{112}Sn , with $B\rho = 2.745 \text{ T}\cdot\text{m}$. To

prevent any charge states of the primary beam from entering the focal plane, measurements were made at 2.40, 2.51, and 2.60 T·m. This also means that the fragments that were measured are more neutron-poor than ^{112}Sn , because the fragments will all have similar velocity.

3.3 Large Area Silicon Strip Array (LASSA)

The Large Area Silicon Strip Array (LASSA) was used to detect and identify light particles and intermediate mass fragments (IMF's) up to Carbon [60]. The LASSA array, for this experiment, was made up of eight telescopes, each consisting of a 500 μm double-sided silicon strip detector in front of a group of four CsI(Tl) crystals. A schematic of the LASSA array is shown in Figure 3.4. The silicon DSSD is segmented into 16 strips on each side, with the front strips orthogonal to the back strips. When a charged particle passes through the silicon wafer, a signal is induced in one back strip and one front strip. The overlap between the triggered front and back strip defines a pixel, a 3mm by 3mm square. The position of the pixel can be used to determine the scattering angle of the detected particle. The identity of the particle can be determined by comparing the signal measured in the silicon detector with the signal measured in the CsI crystal. Using this method, isotopic identification can be obtained up to oxygen isotopes, but in this experiment the dynamic range of the electronics was chosen to measure through Carbon.

The LASSA array, with 8 telescopes, contains 256 individual silicon detector strips. Each detector strip was connected to a charge sensitive amplifier (CSA), which was located near the detectors inside the vacuum chamber. The CSA's were built specifically for the LASSA array, and are described in detail in [60]. The electronics used to process the signals from

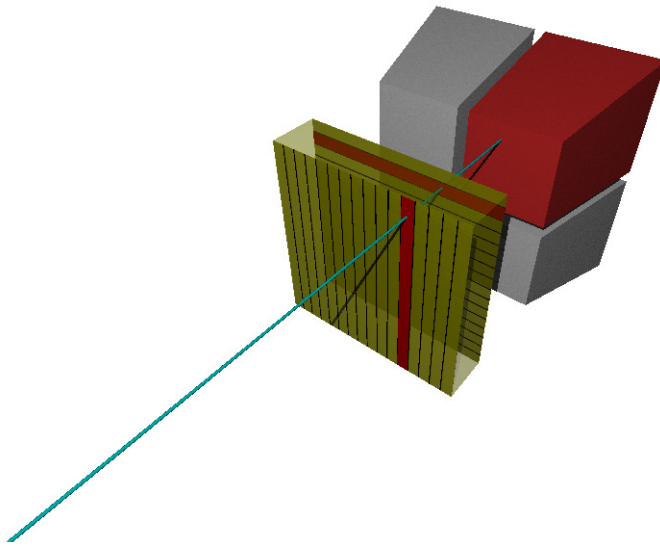


Figure 3.4 Schematic drawing of the LASSA array. Figure is taken from [61].

the LASSA silicon detectors were Application-Specific Integrated Circuits (ASIC) [62], which were specifically developed for use with silicon strip detectors such as LASSA (or HiRA [63]). The advantages of using these high-density ASIC electronics are their relatively low cost and the low space requirements for instrumenting the array. Because the ASIC's are designed for sparse readout (only channels which are above threshold are recorded), many channels can be instrumented without drastically increasing the dead-time of the system.

The dynamic range of the ASIC electronics is limited, which limits the range of elements that could be isotopically identified. To solve this problem, the signals were recorded with two gain stages. The signal from the high-gain charge-sensitive preamplifier was resistively split and one signal was attenuated by a factor of four. The high gain setting was optimized for distinguishing isotopes of hydrogen and helium, and the low gain setting was chosen to identify isotopes through carbon. This method has since been used in several experiments

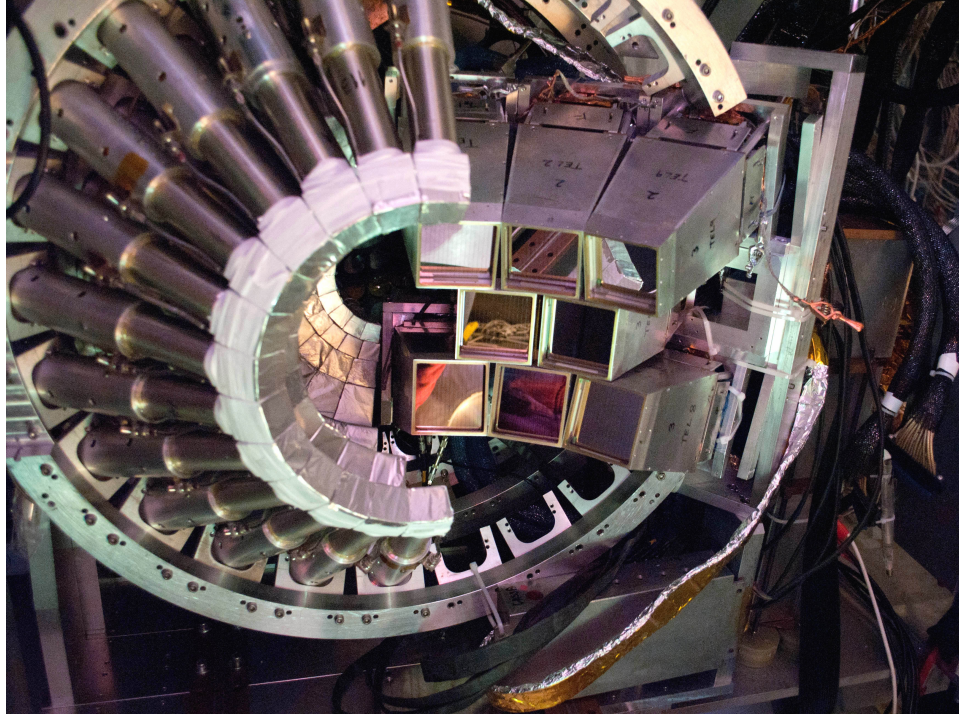


Figure 3.5 Photo of the LASSA array. The forward rings of the Miniball and Miniwall are shown on the left side, and the eight LASSA telescopes are shown on the right side.

with the HiRA array [64]. The number of channels (512) was manageable compared to the full suite of HiRA detectors which requires nearly 2000 channels.

The LASSA array took the place of the right side of the forward part of the Miniball-Miniwall Array. A photo of the LASSA in the experimental configuration is shown in Figure 3.5. During the experiment, the silicon detectors were covered with a thin Mylar foil to prevent light leaks as well as several layers of Sn-Pb foil to absorb electrons ejected from the target.

An important feature of DSSD's is the pixel structure that results from the perpendicular front and back strips. The position of the pixel determines the scattering angle of a particle if the position of the detector relative to the target is measured. The position of the LASSA array was measured using a portable coordinate measuring machine (CMM) arm, commercially available under the brand name ROMER. This arm is capable of measuring positions in

three dimensions in an approximately 1m radius with a precision of $< 100\mu\text{m}$. The ROMER arm measures the position of a probe tipped with a 3mm ruby sphere. By measuring data points along a surface, 3 dimensional features (planes, spheres, cylinders, etc.) can be constructed. Because the ROMER arm requires physical contact with a surface, the position of the silicon detectors was determined by measuring the position of the aluminum housing of the telescope. The pixel positions were then found using the CAD design parameters of the LASSA telescope. The positions are first measured in the local coordinate system of the ROMER arm, and are then transformed into the NSCL global coordinate system. The beamline and S800 are aligned to this reference frame, so the angles with respect to the beamline can be determined. The measured positions are shown in Figure 3.6.

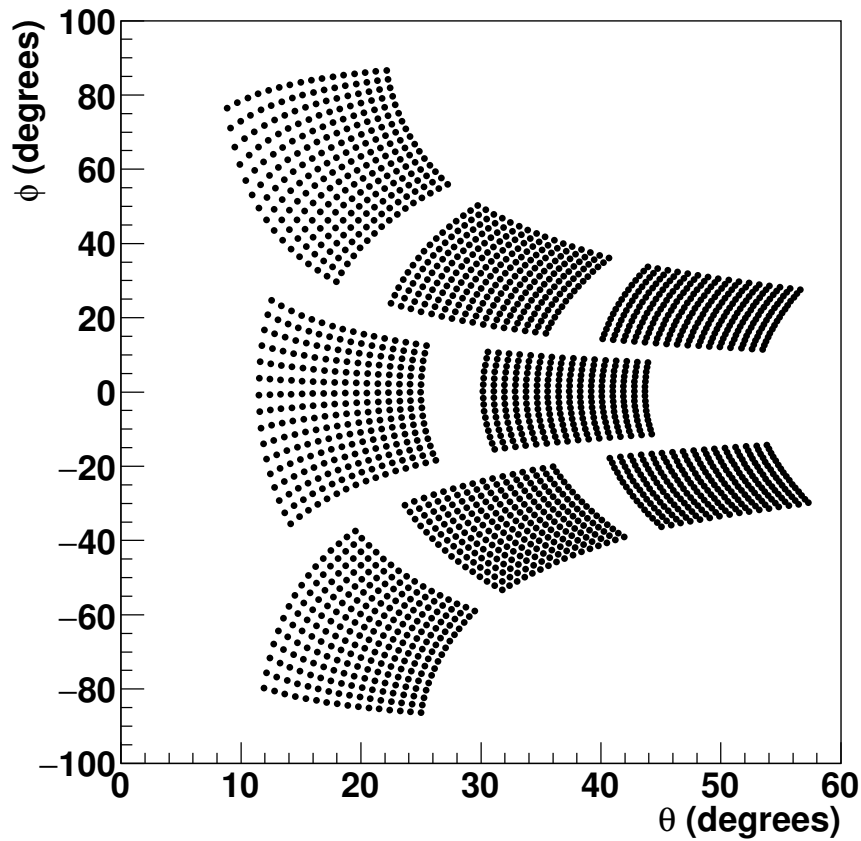


Figure 3.6 Angles of each pixel for the eight LASSA telescopes, extrapolated from measurements with ROMER Arm. Angles are calculated with respect to the measured beamline.

3.4 Miniball/Miniwall Array

The MSU-Miniball [65] was developed to study multifragmentation induced by heavy ion collisions. In its original configuration, it consisted of 188 individual detectors, covering 89% of 4π . It consisted of 11 azimuthally symmetric rings of detectors, and each ring is mounted separately on a pair of rails along the beam direction. Heavy ion collisions at intermediate energies require high granularity at forward angles, because the reactions produce high charged particle multiplicity at forward directions. To address this, the Miniwall array was built at Washington University [66]. The Miniwall replaced the forward two rings of the Miniball with 6 new rings. The Miniwall detectors are functionally similar to the Miniball detectors. As opposed to being mounted on individual ring structures, the Miniwall detectors are all mounted from a single metal base. The Miniwall detectors are significantly further from the target, and are more densely packed, which allows for a significant increase in granularity. The Miniwall is shown, with the first two miniball rings, in Figure 3.7, and the full Miniball-Miniwall assembly is shown in Figure 3.8.

Each detector has two active elements: a thin, fast plastic scintillator in front of a 2cm thick CsI(Tl) scintillator crystal. This configuration is called a phoswich (“phosphor sandwich”), and the light produced in the scintillators is measured by a photomultiplier tube. A schematic of a single detector is shown in the left side of Figure 3.9. The two scintillating elements have different time responses, so that signals in the fast scintillator can be disentangled from the CsI by comparing the signal at different regions in time. The right side of Figure 3.9 shows the structure of the output of a Miniball-Miniwall detector. Specifically, elements with higher Z will lose a larger portion of their energy in the fast scintillator compared to the CsI, and so the ratio of Fast:Slow will be larger. In addition,

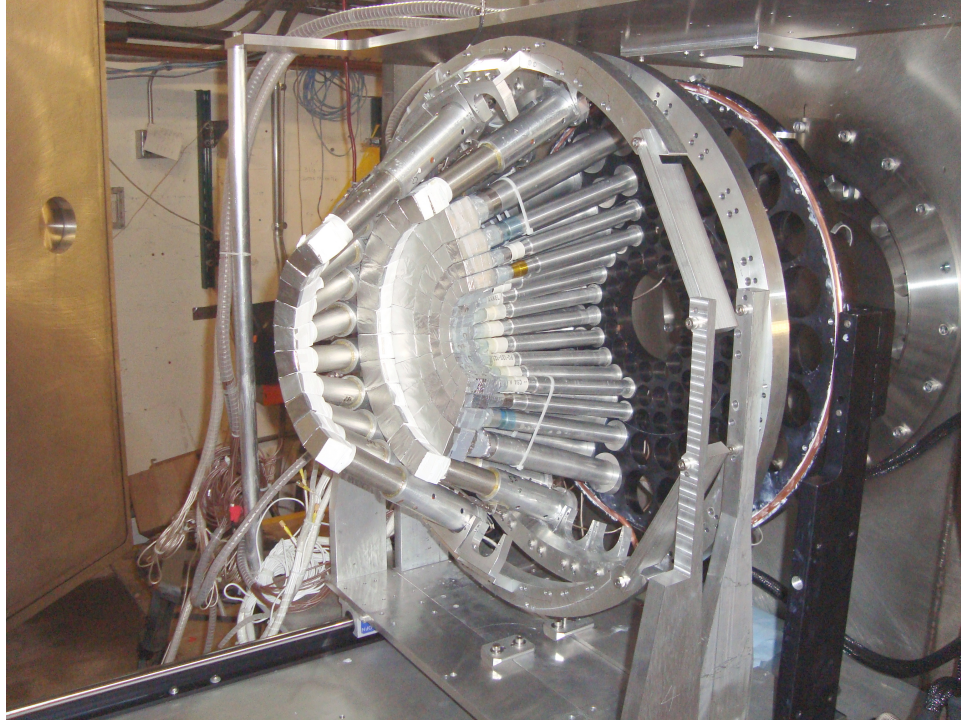


Figure 3.7 Forward part of the Miniball-Miniwall array, in the configuration used for this experiment. The two most forward rings of the Miniwall are not used.

for light particles (H and He), the shape of the pulse depends weakly on the Z and A of the incident particle. By comparing the Slow and Tail signals, the shape can be used to identify isotopes of H and He.

The Miniball-Miniwall electronics, for this experiment, consisted of 12 banks of 16 channels (192 channels), and for each channel, four signals needed to be digitized. (Fast, Slow, Tail, and Time). Detailed diagrams of the Miniball electronics are shown in [61] and [68], and the electronics used in this experiment were designed in the same way. Table 3.3 shows the geometric coverage of the Miniball-Miniwall array that was used during this experiment. Because many detectors had to be removed to allow the LASSA array to be mounted, the coverage of the remaining array adds up to 77% of 4π .

For the purposes of this dissertation, the Miniball-Miniwall array functions as a charged particle counter. By simply counting the number of detectors that are above threshold,



Figure 3.8 Fully assembled Miniball-Miniwall array, showing the backward rings. The beam is incident from the left, and the target is at the geometric center of the miniball.

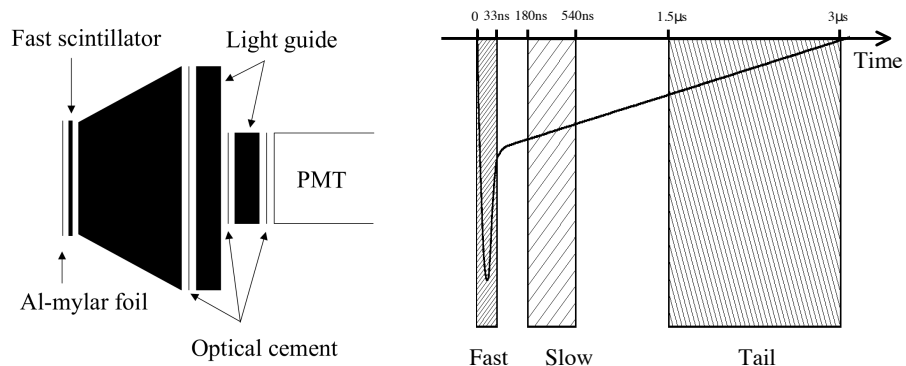


Figure 3.9 Left: Schematic of a Miniball detector [65]. Right: Schematic showing the time structure of a Miniball signal [67]. The three shaded regions represent the time windows wherein the Fast, Slow, and Tail signals are integrated by the Charge ADC's.

Ring #	# of Detectors	θ°	$\Delta\Omega$ (msr)
3(MW)	10/22	10	2.59
4(MW)	12/26	13	2.85
5(MW)	11/24	16.625	5.56
6(MW)	11/24	21.875	10.64
3'	13/28	28	11.02
4	10/24	35.5	22.9
5	13/24	45	30.8
6	15/20	57.5	64.8
7	20/20	72.5	74
8	16/18	90	113.3
9	14/14	110	135.1
10	12/12	130	128.3
11	8/8	150	125.7
Total	165/264	-	9712 (77% of 4π)

Table 3.3 Geometric parameters of the Miniball-Miniwall array used in this experiment.

the approximate charged particle multiplicity can be determined. The charged particle multiplicity can be related to the impact parameter, which is described in detail in Section 4.5. The more complex functions of the Miniball, like the particle identification or energy calibration, are not used in this dissertation, but can be used in the future for further analysis. For example, the total transverse energy can be used as a measure of the centrality of the collision as well [69].

Chapter 4

Data Analysis

4.1 Detector Calibrations

4.1.1 Ionization Chamber

The purpose of the S800 ionization chamber is to provide a measure of the energy loss that a fragment experiences, which gives information about the atomic number of the fragment. (see Section 4.2) The ionization chamber is segmented [56] into sixteen separate sections, which reduces the overall signal resolution. The 16 signals are gain matched so that the signal from the primary beam is equal in each segment. To combine the signals from 16 anodes, the signals are simply summed (and divided by 16, to keep the numbers on the same scale).

$$\Delta E_{\text{sum}} = \frac{1}{16} \sum_{i=0}^{16} \Delta E_{\text{raw},i} \quad (4.1)$$

The main calibration that needed to be applied to the ionization chamber was a correction for the drift of the gain, due to a systematic shift of the gas pressure during the experiment. The pressure of the P10 gas was nominally set at 300 Torr, but due to a problem in the gas handling system, the gas pressure drifted between 300 and 330 Torr. The pressure was

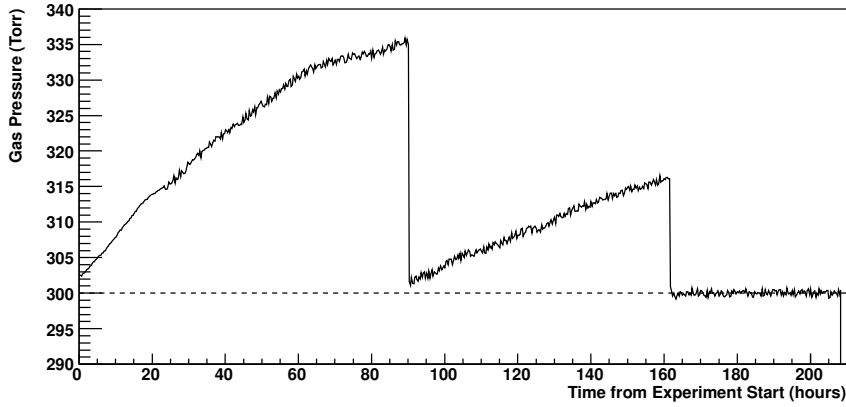


Figure 4.1 Gas pressure in the S800 ionization chamber, as a function of time. The pressure deviated from the set pressure of 300 Torr throughout most of the experiment.

recorded by the gas handling system so an empirical correction is made run-by-run. The trend of the pressure as a function of time is shown in Figure 4.1.

The drift of the gas pressure would affect the resolution of the particle identification spectrum in a given beam-target- $B\rho$ setting, since the gain would drift proportionally. The effect is particularly problematic during the data taken with the ^{112}Sn beam, since each $B\rho$ setting was measured in two segments, with appreciably different gas pressures. The correction is based on the concept that the amount of ionization will depend on the volume number density in the gas, which is directly proportional to the gas pressure. A first order correction can be obtained by simply scaling the energy loss with the fractional change in the pressure:

$$\Delta E = \frac{\Delta E_{\text{sum}}}{1 + \frac{P-300}{300}} \quad (4.2)$$

but an empirical scaling factor for the pressure was determined, so that the resulting correction was

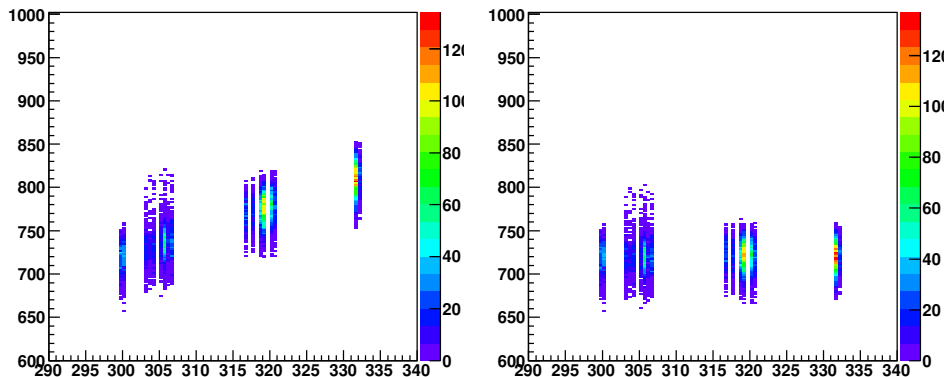


Figure 4.2 Left Panel: Uncorrected ionization chamber energy loss vs. gas pressure, gated on ^{75}Br . Several different reactions at $B\rho = 2.6$ are shown to sample the range of pressure from 300-335 Torr. Right Panel: Same as left, but with the correction from Equation 4.3 applied.

$$\Delta E = \frac{\Delta E_{\text{sum}}}{1 + (.00394) \cdot (P - 300)} \quad (4.3)$$

The correction was found by fitting the trend of the energy loss with the measured pressure. Since any one setting only sampled a small range of pressure, many settings had to be used. The result of the correction for pressure is shown in Figure 4.2. This energy loss, corrected for pressure, is the quantity used for particle identification in Section 4.2.

4.1.2 Hodoscope

The hodoscope at the end of the S800 focal plane consists of 32 CsI(Na) scintillator crystals, arranged in a 4x8 array, and is used to measure the total kinetic energy of the fragment detected in the focal plane. During the experiment, the gas was removed from the CRDC's and the ionization chamber, and the beam was scanned across the face of the detectors. This supplied a monoenergetic signal to match the gain of all the crystals. Since only one

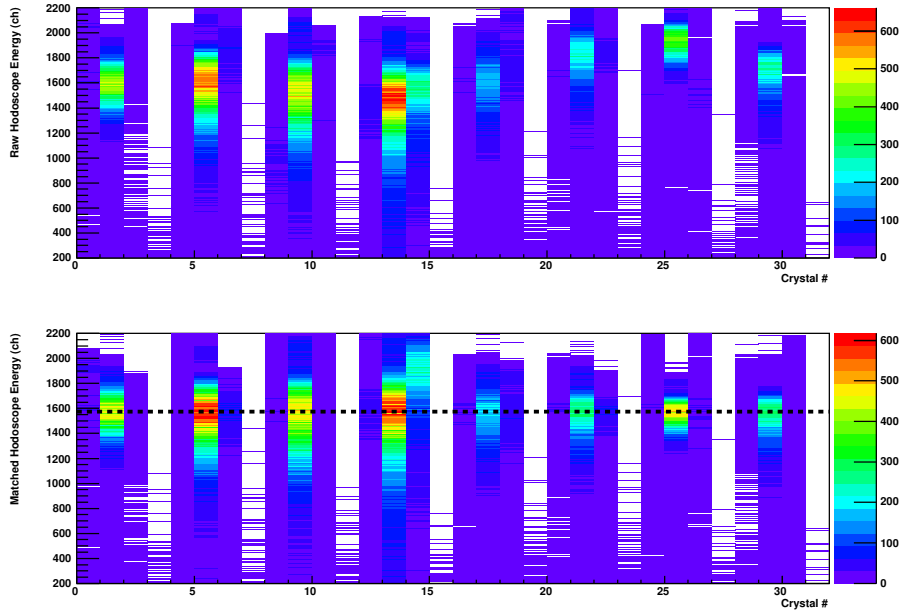


Figure 4.3 Top Panel: Raw hodoscope signals for each crystal, when scanning the ^{124}Sn beam across all detectors. Bottom Panel: Same as top, with all crystals gain matched.

calibration point was possible, and the light output of CsI depends on the species of the fragment, all channels are simply scaled to have the same peak value. This calibration is shown in Figure 4.3. When calibrating to a true energy scale, a non-linear function must be applied, as described in [70]. The hodoscope did not perform as expected during this experiment so the hodoscope data were not used. Further analysis with the hodoscope is described in Appendix B.

4.1.3 Cathode Readout Drift Chambers (CRDC's)

The S800 spectrometer has a dispersive focal plane: a fragment's position in the focal plane determines its magnetic rigidity, or momentum. Two CRDC's are used to measure the position of the incoming fragment in two dimensions, at two planes separated by about 1m. These detectors provide critical information about the detected fragments, because these position measurements allow for the particles trajectory to be traced back to the target

position. The inverse mapping is described in Section 4.1.4. This section describes the calibration of the position information from the CRDC's.

The x (dispersive) positions are measured by analyzing the charge induced on an array of 224 pads. Pads which are missing, have saturated signals, or otherwise marginal performance are excluded. Charge is induced on many pads, and the corresponding position can be extracted with a resolution that is better than the pad pitch. This position can be extracted either by using the center-of-gravity of the charge distribution or by fitting. Since both of these methods involve comparing the amplitudes of neighboring pads, a procedure was implemented to match the gain of all the pads. For each pad, the charge induced on the pad was compared to the energy loss in the ionization chamber. Each pad signal was matched to the energy loss in the ionization chamber, actually using a non-linear function to fix the saturation of some pads. The result of this, for the first CRDC, is shown in Figure 4.4. Although the linearity correction is probably unnecessary for the precision needed in this experiment, this procedure may be useful for experiments requiring very high precision angular resolution.

Fitting the charge distribution as opposed to using center-of-gravity was found to be much more precise when commissioning the CRDC's, so that method is used in this analysis [56]. This distribution is sampled for each event, and an example of this fitting for a single event is shown in Figure 4.5. The fit yields a pad value, which is converted into an x position using the pad pitch (2.54mm/pad).

The exact calibration of the dispersive position can be verified using data from mask runs, but in general, the calibration of this dimension does not change, since the CRDC pads are fixed in space from one experiment to the next. The calibration of the non-dispersive position does change from one experiment to the next, and even throughout an experiment.

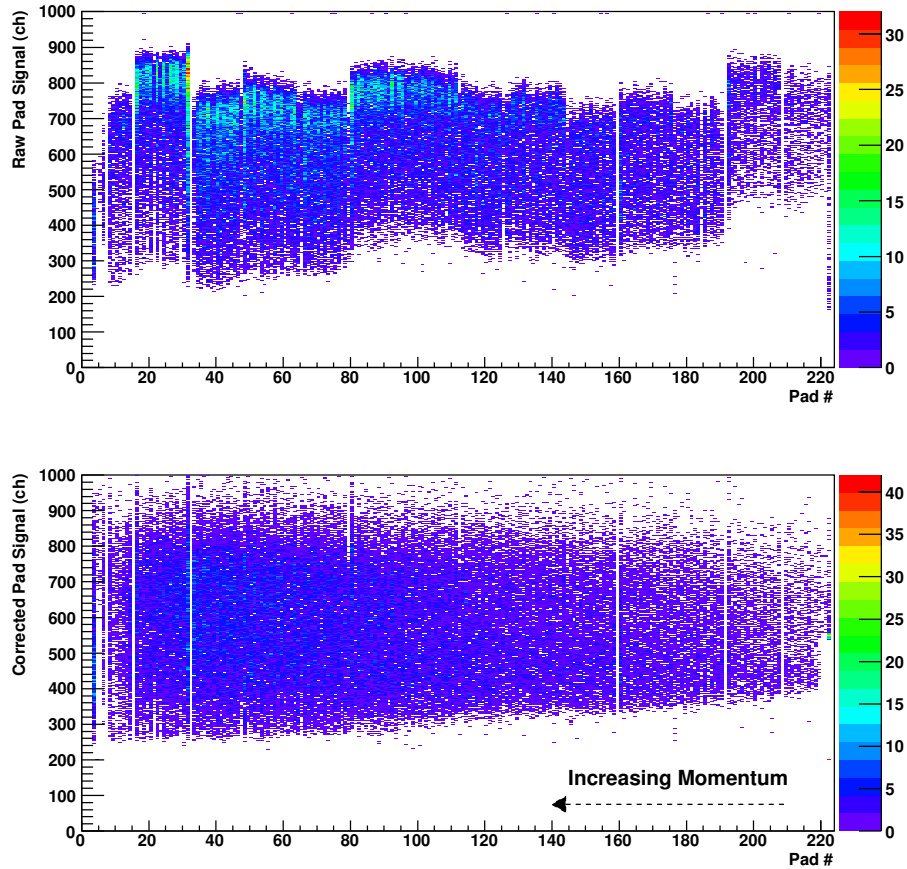


Figure 4.4 Top Panel: Maximum raw pad signals vs. pad number for one run in the $^{112}\text{Sn}+^{112}\text{Sn}$ reaction system at $B\rho = 2.4$ Tm. Bottom Panel: Same as top, but pads are gain matched and corrected for non-linearity. Sloped cutoff at low channels corresponds to a threshold in the E1 scintillator, which is used as the S800 DAQ trigger.

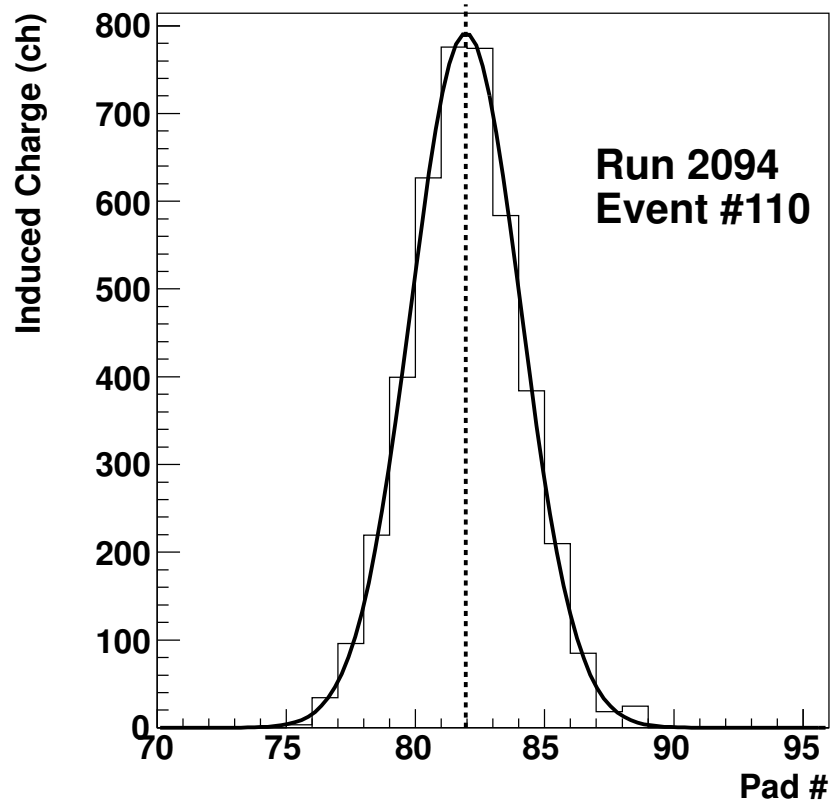


Figure 4.5 Induced pad signal vs. pad number for one (typical) event in the $^{112}\text{Sn}+^{112}\text{Sn}$ reaction system at $B\rho = 2.4$ Tm. A gaussian fit to the data is shown, and the dotted line indicates the extracted centroid of the event.

The non-dispersive position is obtained by using the drift time of the electrons from the ionization track along an electric field in the non-dispersive direction. This measurement is sensitive to variables such as the gas pressure and the purity of the detector gas, which vary with time. The calibration is obtained by inserting a tungsten mask into the path of the fragments. The mask was located approximately 10 cm in front of each CRDC. The mask was machined with precise holes and slots to allow fragments to pass through at specific positions. A CAD drawing of the CRDC mask is shown in Figure 4.6. When the mask is in place, only fragment which travel through the holes/slots will be detected.

When calibrating the position, there are two minor complications. One complication comes from the finite spacing between the CRDC and its mask. For fragments which transit at an appreciable angle, the position measured in the spectrum will be offset from the design position of the hole. Because reaction fragments are used to populate the mask run, there is a large spread of angles, which significantly decreases the precision of the calibration. To account for this, the information from both CRDCs can be combined to utilize this angle information. This procedure causes the second complication, because it causes the calibration of CRDC1 to depend on the calibration of CRDC2. The two CRDC's must be then corrected iteratively, one at a time, until the calibration converges. The intermediate steps are not shown here, but the resulting CRDC1 mask spectrum is shown in Figure 4.7.

The last step in calibrating the CRDC's is to make a correction to the calibration in the non-dispersive direction, to account for the changing electron drift velocity over time. By simply extracting the centroid in the non-dispersive direction run by run, and then scaling that calibration, the variation from run to run is eliminated. The matched, calibrated non-dispersive position is shown in Figure 4.8

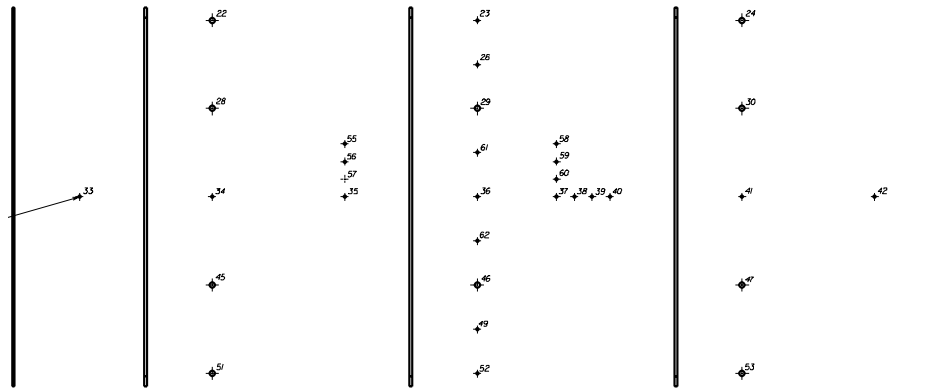


Figure 4.6 Schematic drawing of the CRDC mask. The long edge corresponds to the dispersive direction.

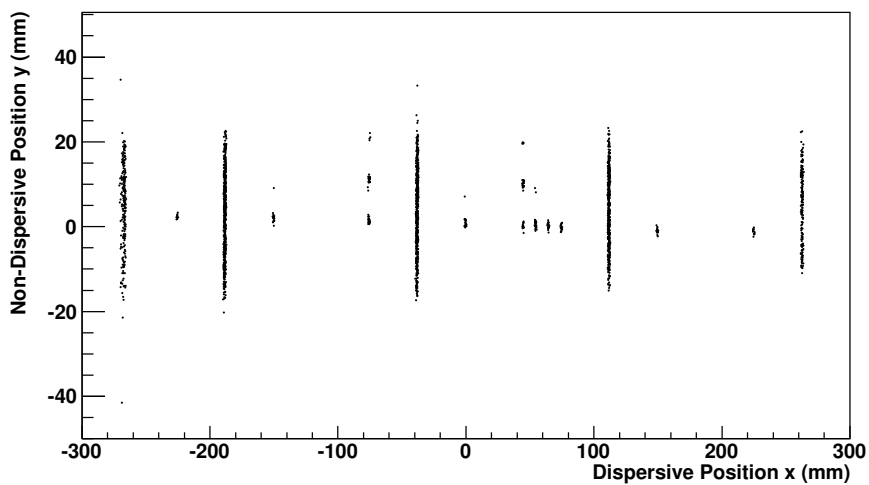


Figure 4.7 Mask spectrum for CRDC1.

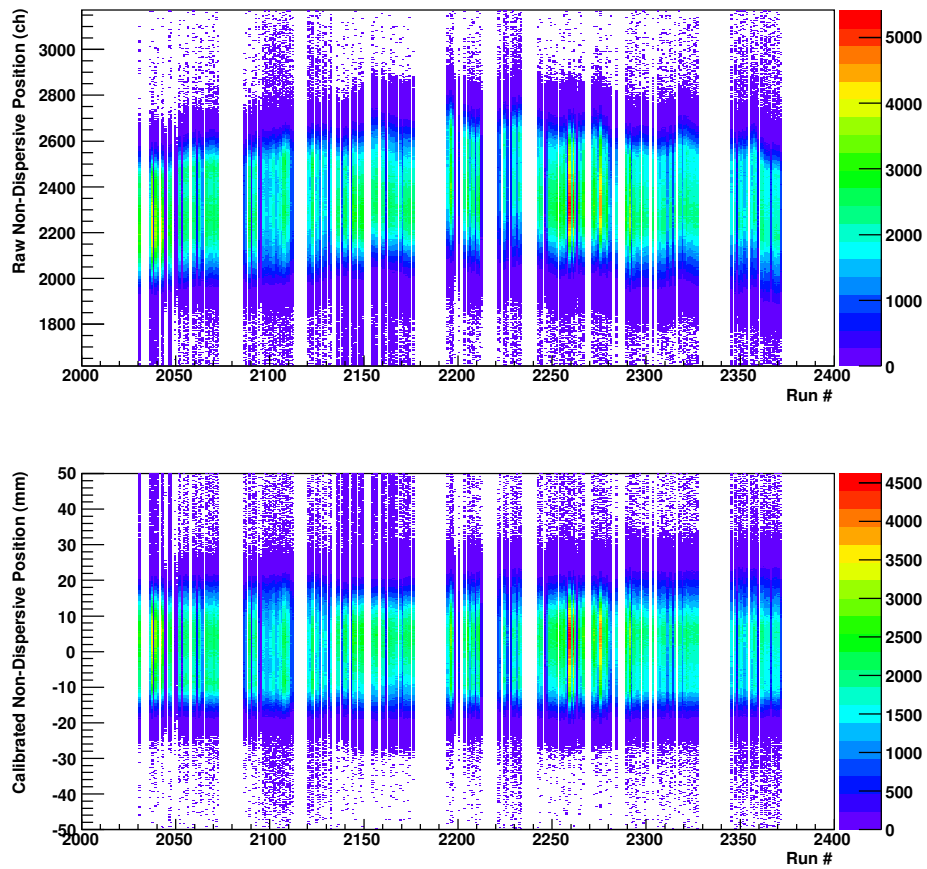


Figure 4.8 Top Panel: Raw CRDC1 drift time vs. run number, for all data runs. Bottom Panel: Calibrated and matched CRDC1 non-dispersive position vs. run number.

4.1.4 Inverse Mapping

The measured positions in focal plane can be transformed into corresponding quantities at the target position by use of an inverse map [71]. These inverse maps are available publicly, and are utilized in most experiments with the S800. The magnetic field of the S800 magnets was mapped and the data were incorporated into a simulation using COSY INFINITY, which is then used to extract an empirical transformation between the incoming (target) and outgoing (focal plane) positions and angles. This transformation is then inverted, and can be used in the analysis to reconstruct the reaction at the target position.

The inverse map can be described with a matrix equation:

$$\begin{pmatrix} dta \\ yta \\ ata \\ bta \end{pmatrix} = \underbrace{\begin{pmatrix} (dta|xfp) & (dta|yfp) & (dta|afp) & (dta|bfp) \\ (yta|xfp) & (yta|yfp) & (yta|afp) & (yta|bfp) \\ (ata|xfp) & (ata|yfp) & (ata|afp) & (ata|bfp) \\ (bta|xfp) & (bta|yfp) & (bta|afp) & (bta|bfp) \end{pmatrix}}_{\text{Inverse Map Matrix}} \cdot \begin{pmatrix} xfp \\ yfp \\ afp \\ bfp \end{pmatrix} \quad (4.4)$$

where the variables are described in Table 4.1. To fully account for the measured magnetic field profiles, each element in the inverse map matrix is a nonlinear function of the four measured parameters. The non-dispersive position at the target, yta , can be obtained through the inverse map, while the dispersive position at the target, xta , cannot. This is simply due to the fact that the x direction has dispersion in the magnetic field, so that ata and dta are convoluted.

Variable	Description	Definition
x_{fp}	Dispersive position at the focal plane	$crdc1.x$
y_{fp}	Non-dispersive position at the focal plane	$crdc1.y$
a_{fp}	Dispersive angle at the focal plane	$\frac{crdc2.x - crdc1.x}{1.073m}$
b_{fp}	Non-dispersive angle at the focal plane	$\frac{crdc2.y - crdc1.y}{1.073m}$
dta	Fragment Energy (Fractional)	Output from Map $\left(\frac{E - E_0}{E_0}\right)$
yta	Non-dispersive position at the target	Output from Map
ata	Dispersive angle at the target	Output from Map
bta	Non-dispersive angle at the target	Output from Map
E_0	Central energy of magnetic setting	Constant for an experimental setting

Table 4.1 Descriptions of the variables obtained from the S800 or calculated using the inverse maps.

Using the inverse map allows for the determination of the energy (with high precision) of the outgoing fragment, as well as provides angular information. The angular acceptance in this experiment was too limited to provide useful information about the systematics of the angular distributions produced in projectile fragmentation, although the angular information can be used to make corrections for acceptance, which is described in more detail in Appendix C.

The last step involves applying offsets to the target angles (ata and bta) to correct for the incoming angle of the beam. For each beam, the beam was degraded into the focal plane using varying thicknesses of aluminum foil. These calibration runs provide the outgoing target angles that are then defined as zero angle. If there were an offset in the dispersive position at the target, that would result in a miscalibration of the energy of the fragment detected in the focal plane. This could be addressed using the energy of the primary beam into the S800 focal plane as a calibration point, but a precise, absolute energy calibration is not critical for the physics in this experiment.

4.2 Particle Identification

One of the main advantages of the S800 Spectrometer is its ability to isotopically identify heavy reaction products. To analyze the data, the TOF- ΔE - $B\rho$ method is used. First, the mass-to-charge ratio can be related (for motion through a magnetic field) to the Time-Of-Flight (TOF) and magnetic rigidity ($B\rho$) by:

$$\frac{m}{q} \propto \frac{B\rho}{\beta\gamma} \propto B\rho \cdot TOF \quad (4.5)$$

Where m is the fragment mass, q is the charge of the fragment, $B\rho$ is the magnetic rigidity of the particle, β is velocity of the fragment in units of the speed of light, and γ is the Lorentz factor. The atomic number can be related to the energy loss in the ionization chamber by the Bethe-Bloch formula:

$$-\frac{dE}{dx} = \frac{4\pi e^4 Z^2}{m_0 c^2 \beta^2} N z \left[\ln \left(\frac{2m_0 c^2 \beta^2}{I} \right) - \ln (1 - \beta^2) - \beta^2 \right] \quad (4.6)$$

which gives the stopping power $\frac{dE}{dx}$ in a medium of atomic number z , atomic number density N and ionization potential I . Where e and m_0 are the charge and mass of an electron, Z is the atomic number of the fragment. Finally, since both the energy loss (ΔE) and TOF have some non-trivial dependencies on the velocity, these numbers are corrected empirically using the measured $B\rho$. In addition, dependencies of the ΔE and TOF on the measured

trajectories in the focal plane can be removed as well. Finally, the corrected ΔE and TOF can be converted into Z and A . This process is described in detail in this section.

4.2.1 Empirical Corrections

There are several quantities that obviously affect the TOF and ΔE . For instance, there will be a spread in the raw TOF associated with the spread in the fragment momentum, because the S800 has a 5% momentum acceptance at a given rigidity setting. As a concrete example, ^{75}Br in the $B\rho = 2.51$ rigidity setting travels approximately 15 m from the target to the S800 focal plane in between 138.7 and 144.9 ns (assuming only the momentum spread is affecting the TOF), but the separation between ^{75}Br and ^{76}Br is only 1.65 ns at $B\rho = 2.51$. This also would assume that the flight path has a fixed length, which is only true for fragments that travel along the optical axis of the S800. For example, fragments of a fixed momentum that are scattered to the inside of the bend of the S800 dipoles would experience a shorter flight path than particles which travel on the outside of the bend. In addition to physical differences in TOF , there can be effects due to the detection systems. For example, the measured TOF would be affected by propagation time of the light created in the E1 timing scintillator, since it is a very large scintillator and the timing signal is collected at the ends. Fragments that hit the timing scintillator close to the photomultiplier tube will have a shorter measured TOF than fragments that hit the middle of the scintillator. Instead of trying to understand each of these effects separately, the TOF and ΔE are simply corrected empirically using the measured positions in the focal plane. Because the method for applying these corrections is of general interest, the steps for one case are shown in detail in this section. Usually, the

TOF and ΔE are corrected the following way:

$$TOF_{corr} = TOF_{raw} - \left(\frac{d(TOF)}{d(x1)} \right) crdc1.x - \left(\frac{d(TOF)}{d(afp)} \right) afp - \left(\frac{d(TOF)}{d(y1)} \right) crdc1.y - \left(\frac{d(TOF)}{d(bfp)} \right) bfp \quad (4.7)$$

$$\Delta E_{corr} = \Delta E_{raw} - \left(\frac{d(\Delta E)}{d(x1)} \right) crdc1.x - \left(\frac{d(\Delta E)}{d(afp)} \right) afp - \left(\frac{d(\Delta E)}{d(y1)} \right) crdc1.y - \left(\frac{d(\Delta E)}{d(bfp)} \right) bfp \quad (4.8)$$

where the linear corrections are obtained empirically from the data. For a better description of the variables used, see Section 4.1.4.

The general goal of the corrections is to simply subtract the dependence of the TOF and ΔE on the focal plane coordinates. Ideally, this dependence would be extracted after the particle identification is done, but in practice, this must be done iteratively. In Figure 4.9a, the TOF and ΔE are shown with no corrections. In this case, slanted lines corresponding to fragments of a given element are seen, although with inadequate resolution. Because the TOF changes continuously with Z as well as with m/q , it is necessary to require a selection on Z to extract the correction for the TOF . The two dimensional gate which selects one Z is shown as a solid line on Figure 4.9a. Figures 4.9b and 4.9c show the correlation between the raw TOF and the dispersive position at CRDC1 (corresponds roughly to the fragment momentum) and the correlation between the raw TOF and the dispersive angle measured at the focal plane, respectively. To obtain the approximate trend, a line is drawn and the linear function is extracted. These approximate linear functions are shown in Figures 4.9b and 4.9c as a solid line. This linear trend with both variables is subtracted from the TOF

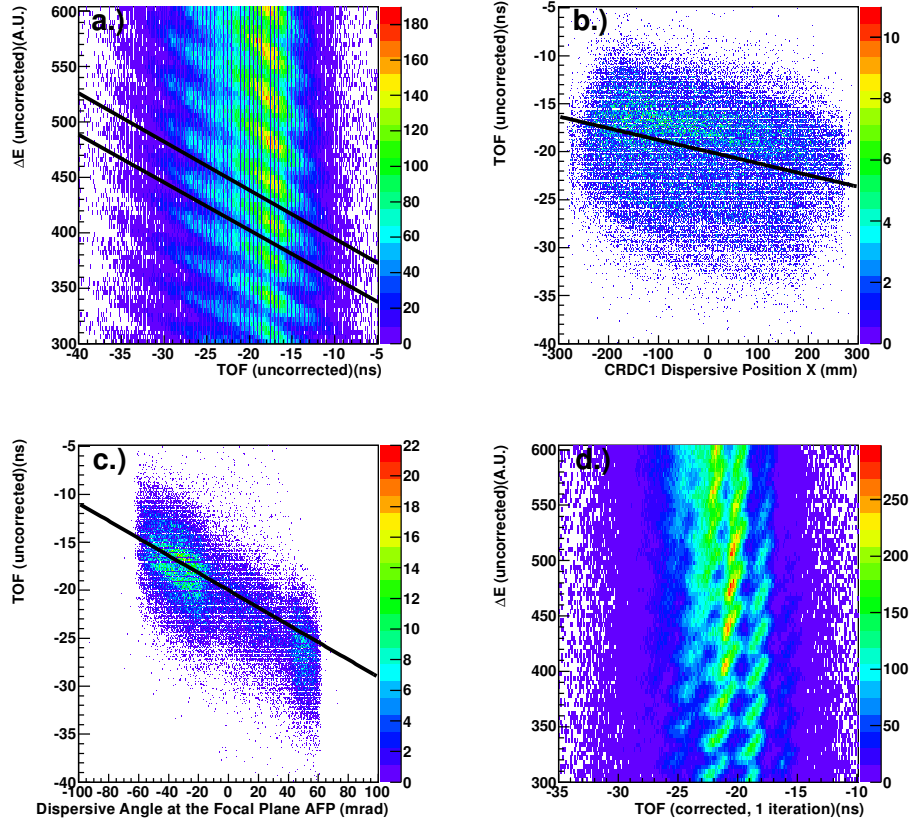


Figure 4.9 a.) Uncorrected TOF vs. uncorrected energy loss, measured in the $^{112}\text{Sn}+^{112}\text{Sn}$ reaction system at $B\rho = 2.4$ Tm. Solid line shows the two dimensional gate used to select an approximate Z b.) Uncorrected TOF vs. dispersive position at the focal plane, requiring the gate shown in panel a. Solid line shows the correlation between TOF and dispersive position. c.) Uncorrected TOF vs. dispersive angle at the focal plane, requiring the gate shown in panel a. Solid line shows the correlation between TOF and dispersive angle. d.) Corrected TOF (first iteration) vs. uncorrected energy loss.

and the result is shown in Figure 4.9d, and the isotopic structure starts to become apparent. As a note, Figure 4.9 shows a lower efficiency between $-20\text{mrad} < \text{afp} < 40\text{mrad}$, which is caused by the rectangular cutout in the start timing scintillator, discussed in more detail in Appendix C.

Applying the same procedure again, yields the results shown in Figure 4.10. In this step, the correlation between the TOF and the focal plane variables is much more apparent, and is again shown as a black line in Figures 4.10b and 4.10c. The horizontal line structures in

Figures 4.10b and 4.10c correspond (approximately) to different isotopes for the selection of an element Z shown in Figure 4.9a. After applying the second iteration of the correction, there is reasonable separation of all isotopes, shown in Figure 4.10d. Comparison of Figure 4.9a and 4.10d shows a dramatic improvement in the isotopic resolutions. In Figure 4.10d, the well-separated vertical bands correspond to a fixed $N - Z$, while no isotopic separation is seen in Figure 4.9a.

Once the corrections for the dispersive focal plane position and angle are applied, corrections for the non-dispersive position and angle can be extracted exactly the same way, although these are smaller corrections. In Figure 4.9a, each vertical band is composed of many isotopes with equal $N - Z$, but with different atomic number Z . To achieve this separation, the energy loss must be corrected as well.

The measured energy loss is influenced by the focal plane trajectories in a similar way to the *TOF*. For a given isotope, fragments with higher momentum will have a lower energy loss (Eq. 4.6). In addition, fragments with a different incident angle through the ionization chamber will deposit a different amount of energy. As with the *TOF*, the correlations are simply extracted empirically and are subtracted from the energy loss.

The first iteration of the energy loss correction is shown in Figure 4.11. The goal is to separate different elements, so the best way to visualize this is to select fragments with a fixed neutron excess (the nearly vertical lines shown in Figure 4.11a). The correlation of the energy loss with the dispersive focal plane position and angle are shown in Figures 4.11b and 4.11c. As with the *TOF*, the first iteration only needs to extract the general trend, so the line drawn in Figure 4.11a is simply a guess. The corrected particle identification spectrum is shown in Figure 4.11d. Even after the first iteration, separation of isotopes by atomic number is apparent.

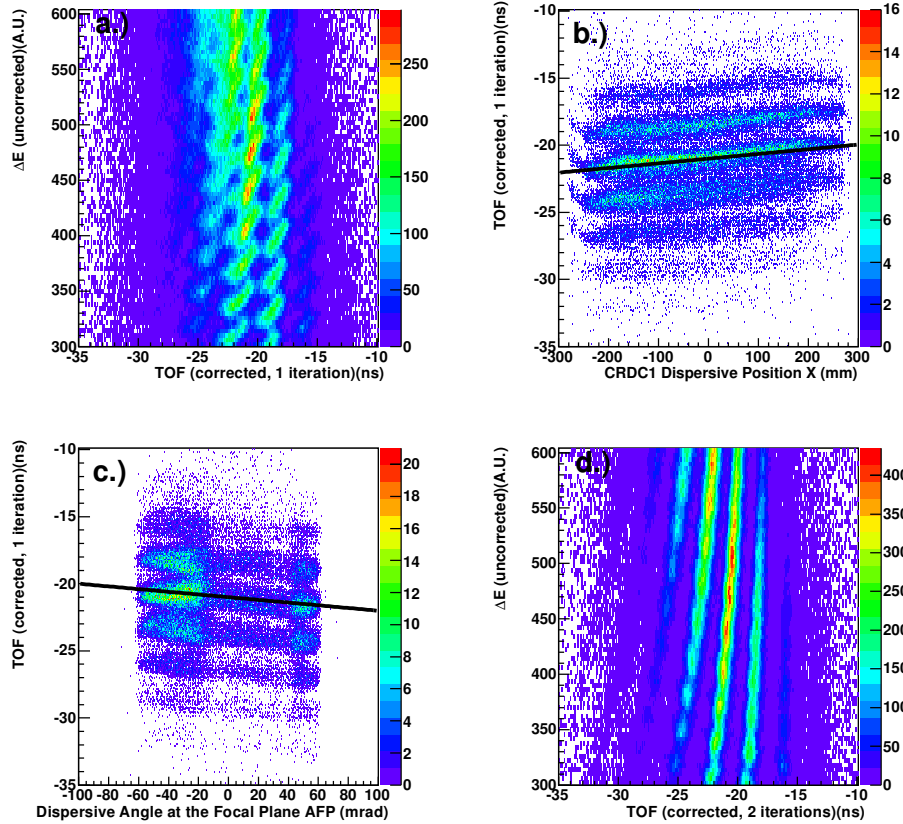


Figure 4.10 a.) TOF (first iteration) vs. uncorrected energy loss, measured in the $^{112}\text{Sn}+^{112}\text{Sn}$ reaction system at $B\rho = 2.4$ Tm. b.) TOF (first iteration) vs. dispersive position at the focal plane, requiring the gate shown in panel a. c.) TOF (first iteration) vs. dispersive angle at the focal plane, requiring the gate shown in panel a. d.) TOF (second iteration) vs. uncorrected energy loss.

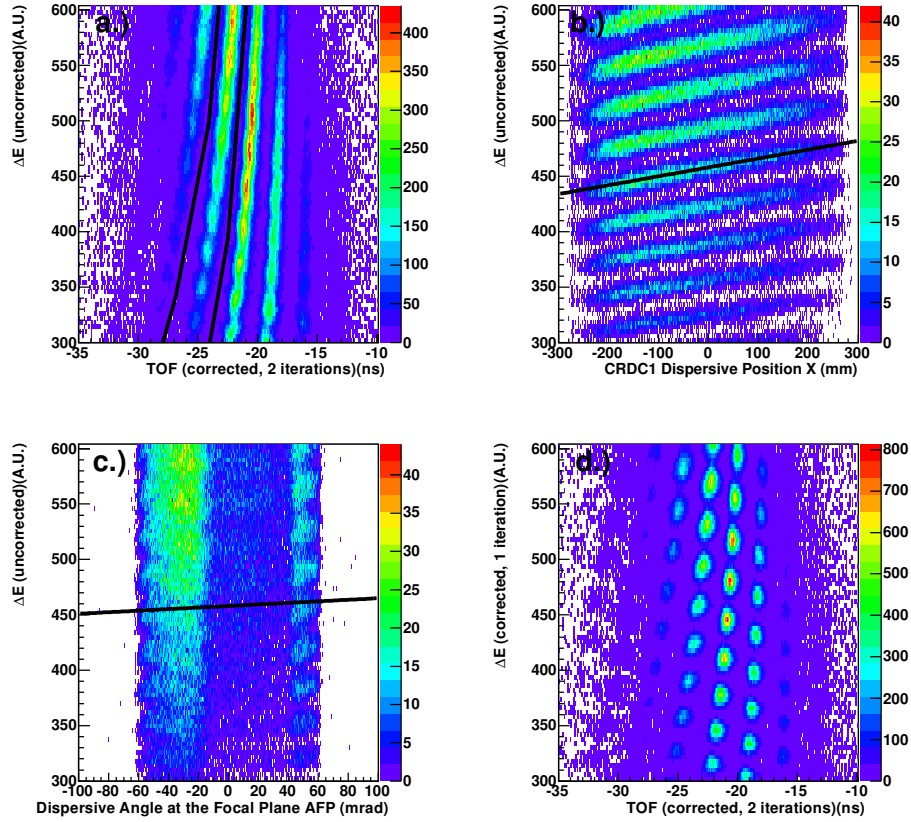


Figure 4.11 a.) TOF (second iteration) vs. uncorrected energy loss, measured in the $^{112}\text{Sn}+^{112}\text{Sn}$ reaction system at $B\rho = 2.4$ Tm. b.) Energy loss (uncorrected) vs. dispersive position at the focal plane, requiring the gate shown in panel a. c.) Energy loss (uncorrected) vs. dispersive angle at the focal plane, requiring the gate shown in panel a. d.) TOF (second iteration) vs. energy loss (first iteration).

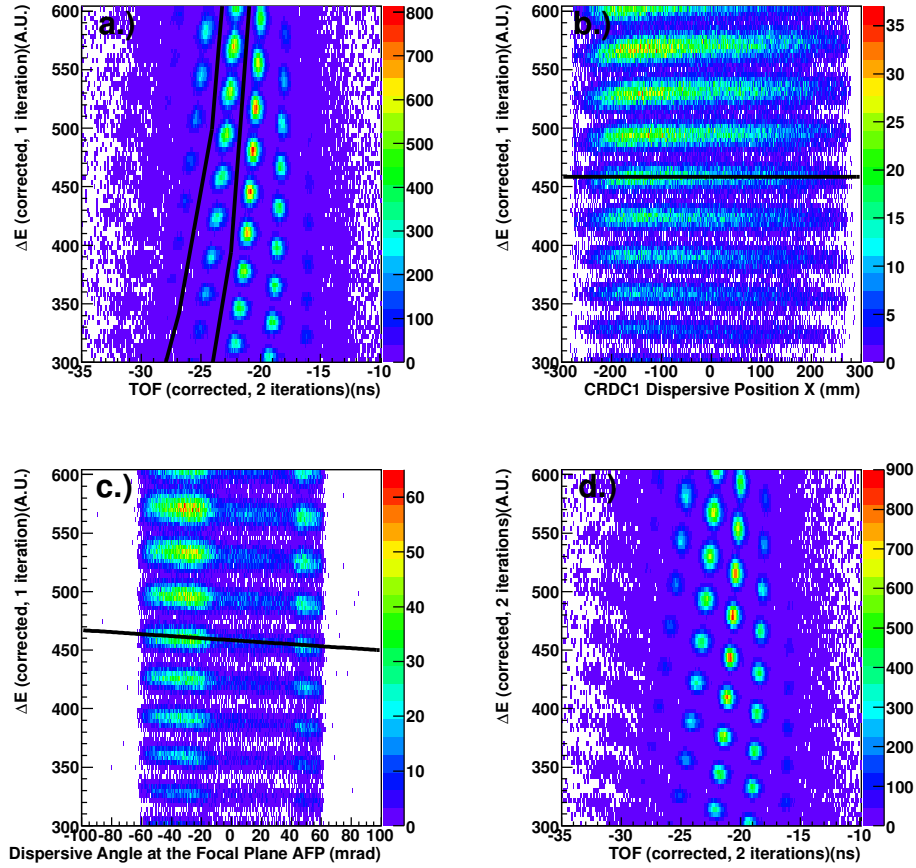


Figure 4.12 a.) TOF (second iteration) vs. energy loss (first iteration), measured in the $^{112}\text{Sn}+^{112}\text{Sn}$ reaction system at $B\rho = 2.4$ Tm. b.) Energy loss (first iteration) vs. dispersive position at the focal plane, requiring the gate shown in panel a. c.) Energy loss (first iteration) vs. dispersive angle at the focal plane, requiring the gate shown in panel a. d.) TOF (second iteration) vs. energy loss (second iteration).

After applying this same procedure again, the results for the second iteration of the correction to the energy loss are shown in Figure 4.12. In the second iteration, the correlation with the dispersive focal plane angle is much clearer, shown in (Figure 4.12c). The particle identification spectrum, shown in Figure 4.12d shows both isotopic and elemental resolution over this range of fragments for this system. In these figures, only the correction for the dispersive focal plane variables are being applied for clarity. In the case of the $B\rho = 2.51$ Tm and $B\rho = 2.60$ Tm settings, for higher- Z fragments, it is necessary to apply corrections for the non-dispersive variables as well.

The procedure detailed above allows for optimization of the TOF and ΔE for a single isotope, or a region of isotopes. In this experiment, it is necessary to achieve good resolution over a wide range of isotopes and elements, and to develop a procedure to do this consistently for many reaction systems and unit settings. The corrections applied above diverge from the true corrections when moving away from the isotopes used to optimize the correction. Once the TOF and ΔE are corrected enough to draw gates around individual isotopes, a correction can be determined locally for each isotope. Also, since the corrections described previously relied on less robust iterative multidimensional fitting, these local corrections can improve on the consistency of the corrections between reaction systems.

The first step is to create a set of gates for the isotopes which have adequate statistics. First, gates are drawn for each Z and $N - Z$ line, and then the intersection of these two gates roughly defines an isotope. To find the gates in a consistent repeatable way, a gaussian function is fit to a projection of the data for that isotope onto the TOF and ΔE axes. An example of this procedure is shown in Figure 4.13. This procedure allows for straightforward automation for generation of gates for all reaction systems. These gates are used for calculation of the final, local corrections, but the final particle identification determination

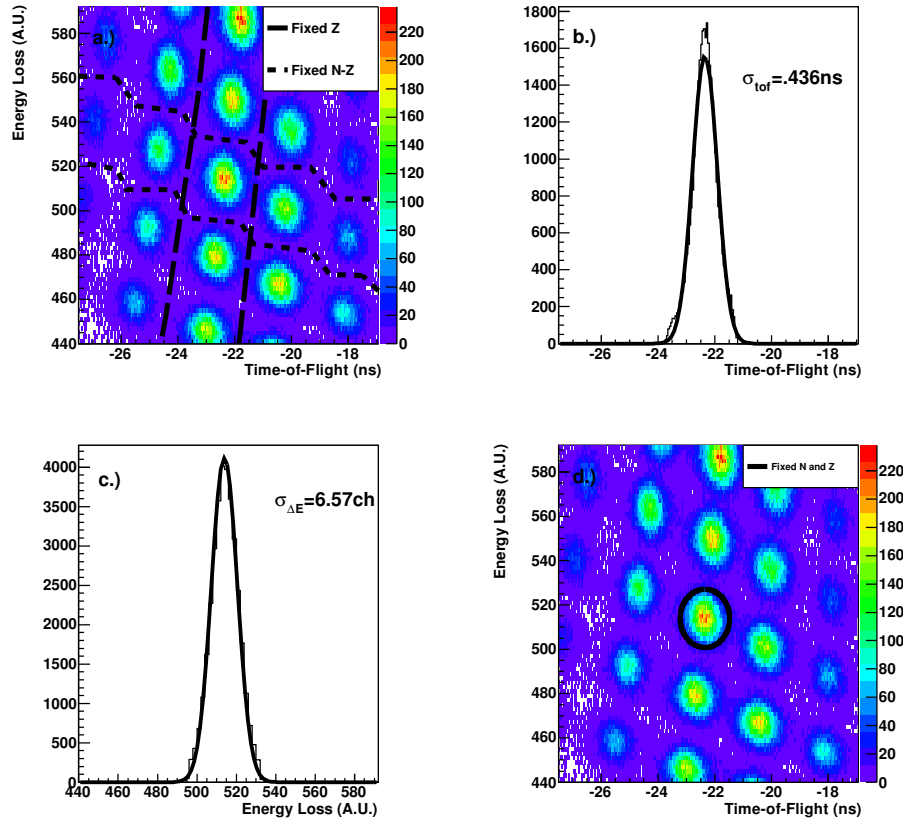


Figure 4.13 a.) TOF vs. ΔE , measured in the $^{112}\text{Sn}+^{112}\text{Sn}$ reaction system at $B\rho = 2.4$ Tm, showing gates for a fixed Z and $N - Z$. b.) Projection onto the TOF axis of the spectrum in panel a, gated on one isotope. c.) Projection onto the ΔE axis of the spectrum in panel a, gated on one isotope. d.) TOF vs. ΔE , showing an example of a gate resulting from this fitting procedure. The gate is an ellipse with the semimajor axes equal to 2σ , extracted from the fits in panels b and c.

is based on a rectangularized matrix of variables which is described later in this section. An example of the complete set of gates for one reaction system is shown in Figure 4.14.

The next step is to extract corrections for the TOF and the ΔE on an isotope-by-isotope basis. Since there is typically several hundred isotopes in a given beam-target- $B\rho$ setting, and 21 different settings were measured, this procedure cannot be done iteratively as described above. Instead, a similar procedure is used with a few differences. First, the variables used in the fit are slightly different. Also, the corrections here are multiplicative factors, as opposed

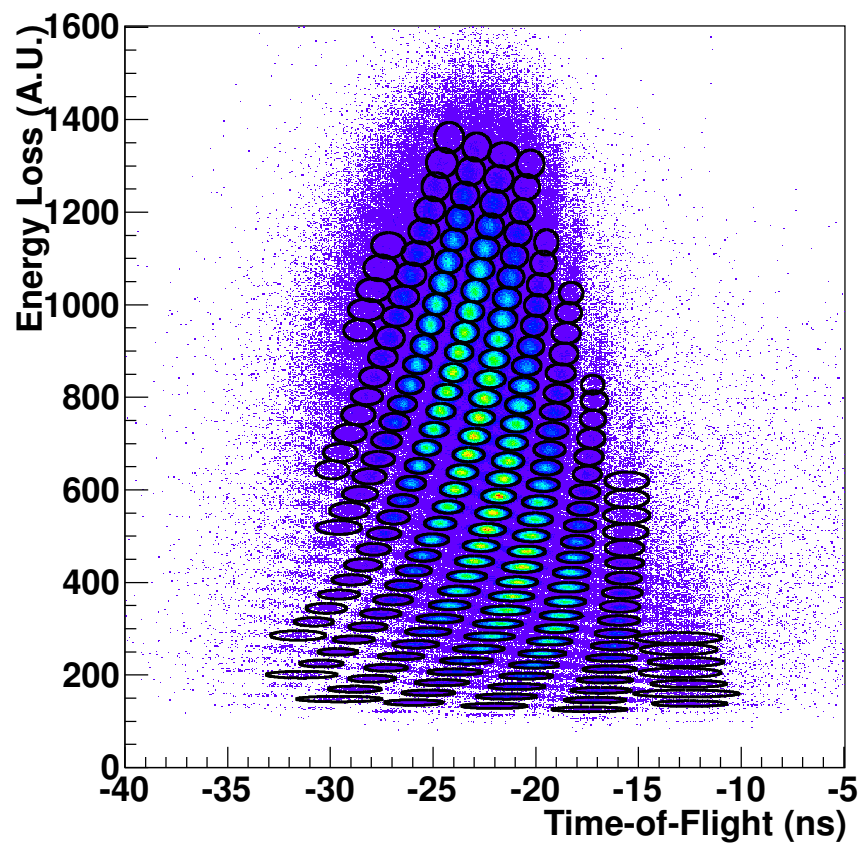


Figure 4.14 Spectrum of TOF vs. ΔE , with the particle identification gates adopted in the $^{112}\text{Sn}+^{112}\text{Sn}$ reaction system at $B\rho = 2.4$ Tm.

to subtractions. This is physically motivated, because many of the correlations (for instance, how ΔE depends on the fragment momentum) are direct proportionalities. The functional forms used for the correction are:

$$TOF_{corr} = TOF_{raw} / (1 + a_1 (x1 + x2) + a_2 (x2 - x1) + a_3 (y1 + y2) + a_4 (y2 - y1)) \quad (4.9)$$

$$\Delta E_{corr} = \Delta E_{raw} / (1 + b_1 (x1 + x2) + b_2 (x2 - x1) + b_3 (y1 + y2) + b_4 (y2 - y1)) \quad (4.10)$$

where the coefficients a_i, b_i are obtained from fitting directly a four-dimensional hyperplane for each isotope for both TOF and ΔE . Since these coefficients are extracted for each isotope, technically, $a_i = a_i(N, Z)$. Since N, Z are not known until after applying this correction, the coefficients can be parametrized as $a_i = a_i(TOF_0, \Delta E_0)$ where TOF_0 and ΔE_0 are simply the centroid for each isotope using the initial set of corrections. An example of the dependence of a_1 on TOF and ΔE is shown in Figure 4.15. The measured positions of the centroids (using the initial correction) are overlaid for reference as black crosses. For a given event, the final correction is calculated in two steps. The global correction must be used in the first step to interpolate the value of the correction. This correction yields a TOF and a ΔE that are approximately correct, which are in turn used to interpolate a new correction, which is then used to calculate the final TOF and a ΔE . This is necessary to ensure that the final correction depends only on the final location of the TOF and ΔE , which is the quantity used to parametrize the correction. This is shown in Equations 4.11 to 4.14.

$$TOF_{step1} = TOF_{raw} / \left(1 + \sum_i a_i (TOF_{global}, \Delta E_{global}) f_i(x1, x2, y1, y2) \right) \quad (4.11)$$

$$TOF_{final} = TOF_{raw} / \left(1 + \sum_i a_i (TOF_{step1}, \Delta E_{step1}) f_i(x1, x2, y1, y2) \right) \quad (4.12)$$

$$\Delta E_{step1} = \Delta E_{raw} / \left(1 + \sum_i b_i (TOF_{global}, \Delta E_{global}) f_i(x1, x2, y1, y2) \right) \quad (4.13)$$

$$\Delta E_{final} = \Delta E_{raw} / \left(1 + \sum_i b_i (TOF_{step1}, \Delta E_{step1}) f_i(x1, x2, y1, y2) \right) \quad (4.14)$$

The end result of these corrections is that the TOF and ΔE for a given isotope collapse into a single point. This is equivalent to the situation that all the fragments travelled at the central rigidity of the S800 and along the central ray of the S800. The vertical and horizontal widths of these structures are only influenced by the experimental detector resolutions.

4.2.2 Absolute Determination of N,Z

After the particle identification spectra are properly corrected, there is still some ambiguity in the absolute determination of N and Z . However if the N and Z of one isotope is identified, the remaining isotopes can be found by simply counting from the known isotope as a function of Z or $N - Z$. This can be achieved in several ways. Some experiments measure the beam directly in the production data. This was not done in this case because the range of fragments was chosen to avoid illuminating the focal plane detectors with different charge states of the beam, so the fragments in the data have much lower magnetic rigidity than the three beam species used. Another useful method is to use the fact that ${}^8\text{Be}$ is unbound and count isotopes up from there. This would involve changing the voltages and pressures in the CRDC's and

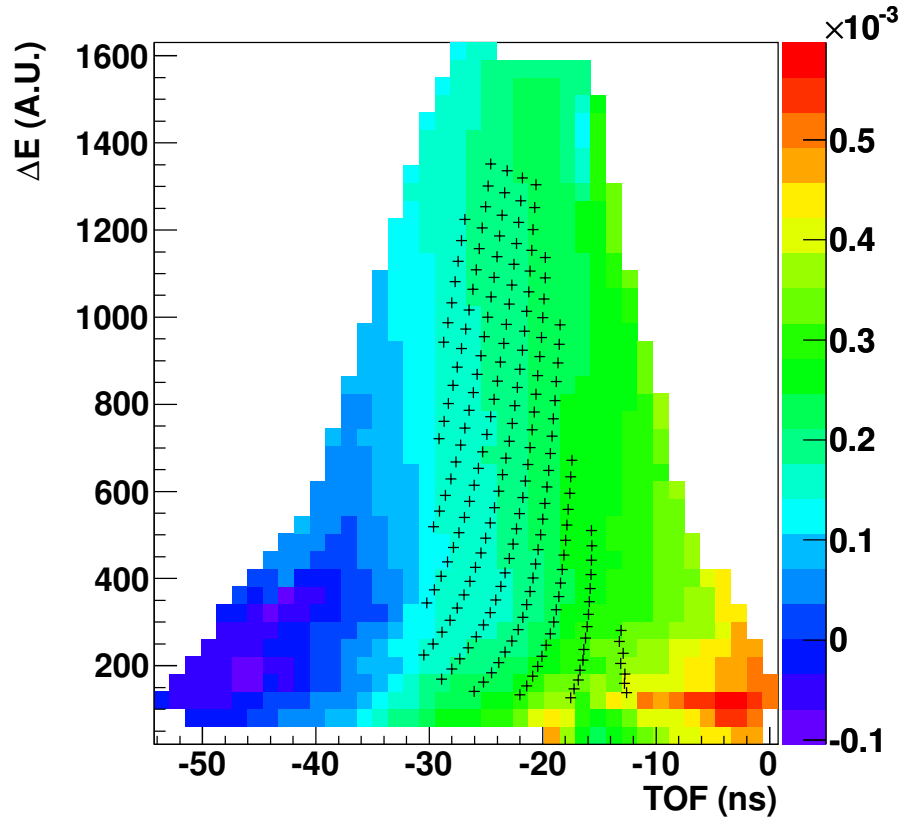


Figure 4.15 a_1 coefficient, plotted as a function of TOF and ΔE , measured in the $^{112}\text{Sn}+^{112}\text{Sn}$ reaction system at $B\rho = 2.4$ Tm. The a_1 coefficient represents how strongly the TOF depends on the quantity $x_1 + x_2$. The black crosses represent the final locations of the isotopes of interest. The values of the correction coefficients are extrapolated outside this range of TOF and are used for the first step of the correction, which is approximate.

the Ionization chamber, and would waste valuable beam time. This was not realistic to do for the many reaction systems measured in this experiment.

The proposed method in this experiment was to degrade the beam into the focal plane using varying thicknesses of aluminum foil. While it was simple to degrade the beam into the focal plane, the method also requires that sufficient fragments are produced in the range between the beam and the fragments of interest. Unfortunately, the statistics in each case were insufficient. Also, in order to degrade the beam with varying amounts of material, a degrader was placed at the target position as well as on the drive that held the scintillator used as a start time for the S800 particle identification. Since this scintillator couldn't be used while degrading the beam, it is difficult to compare the degraded beam data to the measured fragment data. In the end, a combination of methods is used to achieve a reliable determination of the particle identification.

First, the absolute $N - Z$ can be determined from the shape of the constant $N - Z$ lines. For $N - Z = 0$, the time of flight does not change with Z . Unfortunately, the data generally does not contain fragments this neutron-deficient. In the case of $^{112}\text{Sn}+^{112}\text{Sn}$, the data does extend into this region, but with very low statistics. However, By extrapolating from data that is measured with good statistics, the vertical line of isotopes for $N - Z = 0$ can be easily determined. The extrapolation used is linear, and done separately for each Z . This is shown in Figure 4.16.

The determination of the absolute atomic number can also be extracted from the behavior of the TOF . Assuming that the TOF is linearly related to the m/q of the fragment, and that $m/q = A/Z$ (assuming $q = Z$), the isotopic spacing in TOF is inversely proportional to Z :

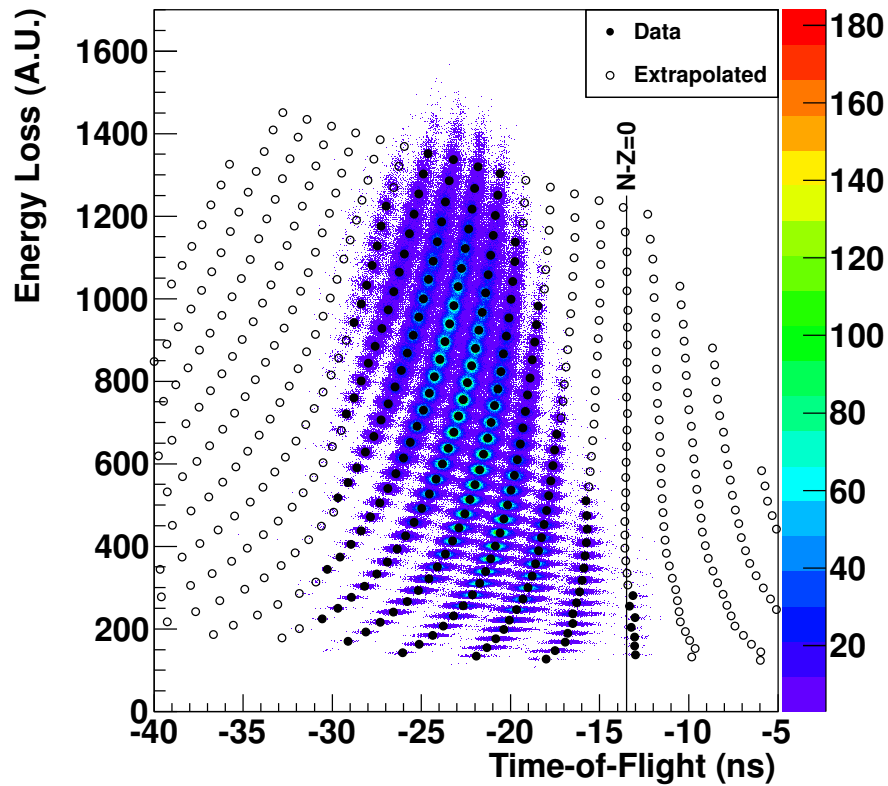


Figure 4.16 The centroid positions in TOF and ΔE for each isotope identified in the $^{112}\text{Sn}+^{112}\text{Sn}$ reaction system at $B\rho = 2.4 \text{ Tm}$. Measured centroids for each isotope are shown as solid circles, while extrapolated positions are shown as open circles. A vertical line is drawn to indicate the location of the $N - Z = 0$ isotopes.

$$\begin{aligned}
TOF &= a \cdot \frac{A}{Z} + b \\
\frac{\Delta TOF}{\Delta A} &= a \cdot \frac{1}{Z}
\end{aligned}
\tag{4.15}$$

This isotopic spacing is found from the linear extrapolation that is also used in Figure 4.16. This spacing can be fit by a function, using a guess for Z , allowing for an integer offset of Z , and using the χ^2 to choose the best fit. The fitting function is:

$$\frac{\Delta TOF}{\Delta A} = a \cdot \frac{1}{Z - Z_{\text{offset}}}
\tag{4.16}$$

An example of the fit to find the absolute Z is shown in Figure 4.17. Using this procedure, with the stated assumptions, gives a best fit for Z . Since the χ^2 distribution does not have a sharp minimum, the determination is not exact. The value of Z extracted in this way may be off by ± 1 charge unit, but it is not likely off by two units. To further solidify this determination, there is several more pieces of information that can be used.

The best case for comparing the degraded beam to the reaction fragments (As described on Page 73) is when the ^{112}Sn beam was degraded into the focal plane, because its magnetic rigidity was closest to the magnetic rigidity of the measured fragments. Because the start timing scintillator was not in place during this data, a different timing signal had to be used. In this case, the start time is provided by the RF signal from the coupled cyclotrons, which is basically the time that the beam pulse is generated. The disadvantage of this method is that the timing resolution of the RF signal is $\sigma = 1.5\text{ns}$, too large to distinguish isotopes. To deal

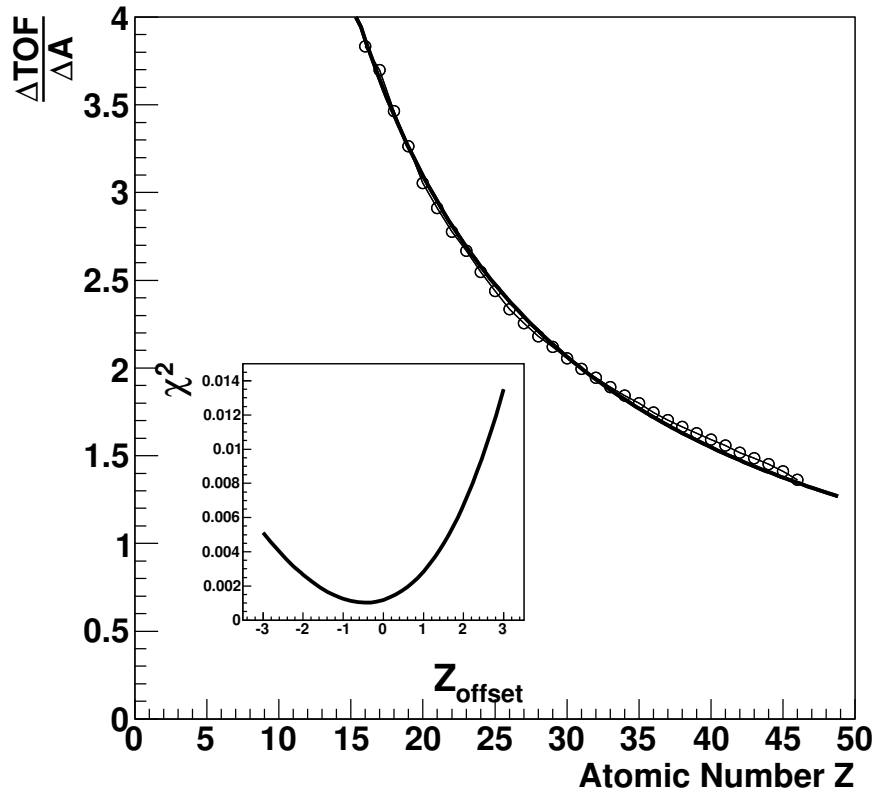


Figure 4.17 Isotopic spacing (ns/nucleon) vs. Z , measured in the $^{112}\text{Sn}+^{112}\text{Sn}$ reaction system at $B\rho = 2.4$ Tm. A fit of Equation 4.16, with $Z_{\text{offset}} = 0$ is shown in the main panel. In the inset, the χ^2 distribution for varying Z_{offset} is shown.

with the resolution problem, the normal particle identification using the timing scintillator is applied first. Then, for each selected isotope, the centroid of the particle identification spectrum using the RF as the start time can be determined. These centroids are shown in Figure 4.18. Since there is gap in coverage between the beam and the measured fragments, some extrapolation must be made, as shown in the solid and dashed lines. The highest Z shown in Figure 4.18 is $Z = 47$, which is not used in the extrapolation because of edge effects. The position of the degraded beam is consistent with the previous determination of the atomic number. Again, this gives an absolute determination of the atomic number.

Another test that can be applied relies on a phenomenon known as Odd-Even Staggering (OES). In many nuclear reactions, in this case projectile fragmentation, there is an overproduction of fragments with even- Z , when compared to the neighboring odd- Z nuclei. Recent studies have shown that the staggering is more complicated; there is staggering in both the neutron number N and in the atomic number Z , and these effects can compete with each other [72, 73]. The effect has been associated with nucleon pairing, which becomes important during the final stages of the de-excitation process. One clear message of these studies is that one can expect overproduction of even- Z fragments, especially for even- A fragments, and especially in the case of neutron-poor fragments. When using the procedures described above, the particle identification may be ambiguous by one unit, but the OES can be used to validate the choice made. The OES is calculated by dividing the yields by a smooth function that is defined by a polynomial fit to several points above and below that point. This procedure clearly shows only the fluctuations around the smooth behavior of the yields. In this case, the integrated yields are used to calculate the ratio, described more in Section 4.4. Figure 4.19 shows this ratio, calculated for both the even and odd mass fragments measured in the $^{112}\text{Sn}+^{112}\text{Sn}$ reaction system at $B\rho = 2.4$ Tm. It is clear in the case of the even

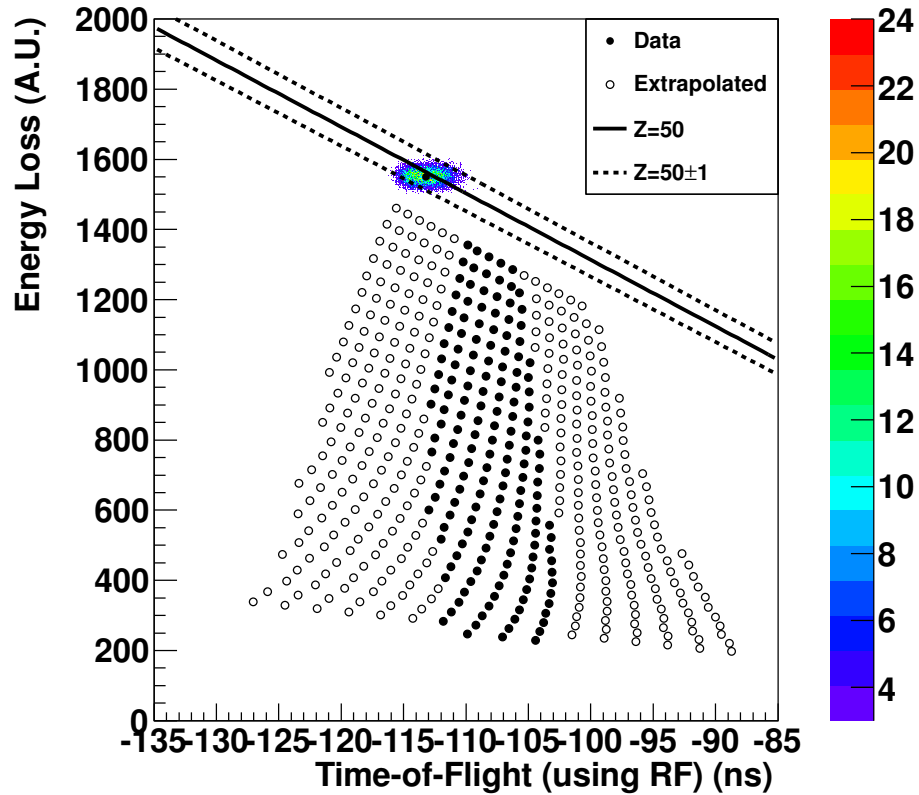


Figure 4.18 Particle Identification centroids, calculated using the cyclotron RF as the start time, measured in the $^{112}\text{Sn}+^{112}\text{Sn}$ reaction system at $B\rho = 2.51$ Tm. The solid circles represent a centroid extracted from data, while the open circles are extrapolated centroids. In addition, the particle identification spectrum for the degraded beam run is shown on the same plot, with its centroid shown as a solid circle. The solid line corresponds to an extrapolation of the location of the $Z = 50$ isotopes, and the dotted lines correspond to the extrapolations for $Z = 49$ and $Z = 51$.

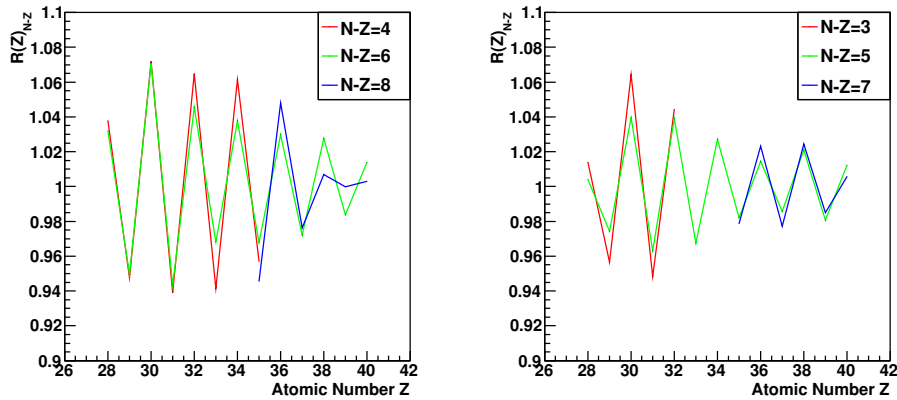


Figure 4.19 Odd-Even Staggering ratio, measured in the $^{112}\text{Sn}+^{112}\text{Sn}$ reaction system, using the integrated yields. Left panel shows even- A (even $N - Z$) fragments. Right panel shows odd- A (odd $N - Z$) fragments.

$N - Z$ (even A) fragments that there is overproduction for even values of Z , which means that the determination of Z cannot be offset by only one unit. The odd masses are shown as well, to address the case where both Z and $N - Z$ are offset by one unit. In this case, the staggering is still as expected, which implies that even if $N - Z$ was also shifted by one, the staggering should still be present as normal.

Once the determination is made for one system, the other systems can be calibrated the same way. If there were some miscalibration of the particle identification, there are some tests to verify that particle identification matches between reaction systems. The first test is to verify that, for one reaction, the three $B\rho$ settings are identified the same way. Since the determination of $N - Z$ is done fairly confidently, the main concern is the determination of Z . This can be verified by comparing the energy loss without corrections between the three $B\rho$ settings. When the correction for momentum is not applied, the energy loss should be a continuous function of rigidity over the three overlapping rigidity settings. This is shown in Figure 4.20. Following this process allows very confident matching between rigidity settings.

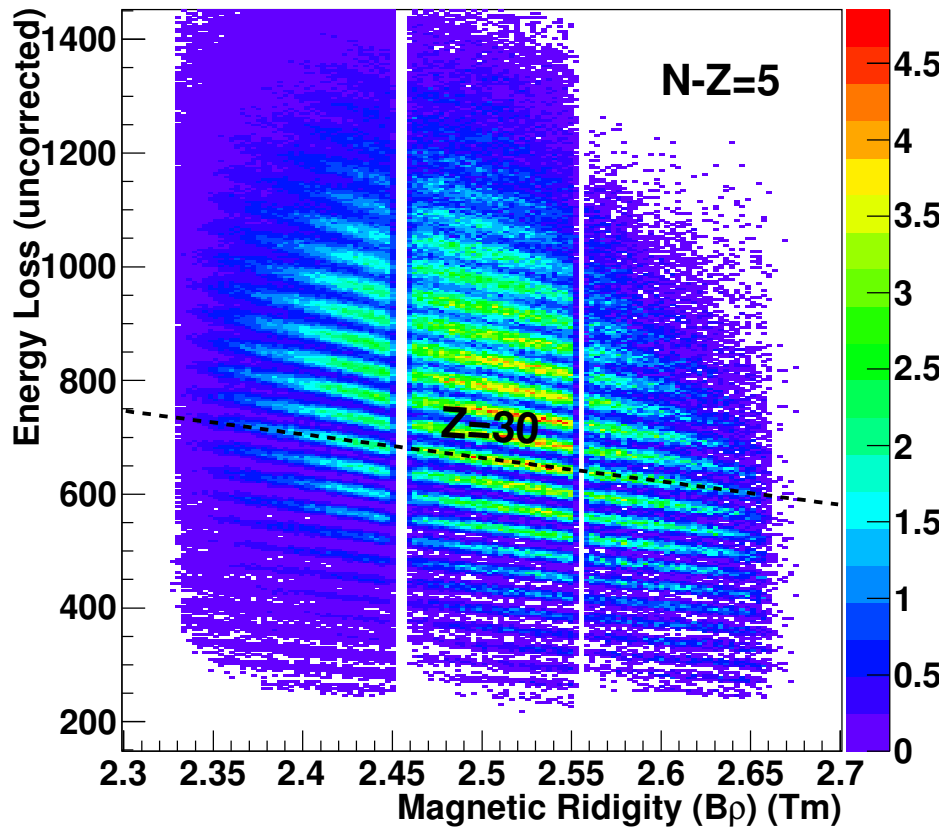


Figure 4.20 Uncorrected energy loss vs. magnetic rigidity, measured in the $^{112}\text{Sn}+^{112}\text{Sn}$ reaction system, with all three rigidity settings combined. The yields are scaled by the live-time and the normalization of the beam from the Miniball. These fragments shown have $N - Z = 5$, and a reference line is drawn at $Z = 30$.

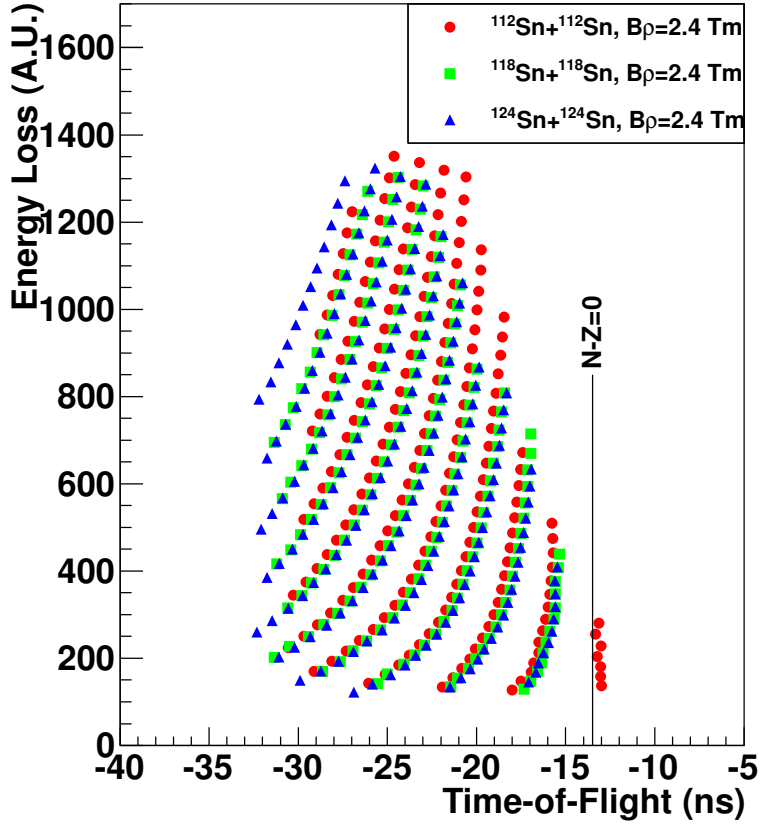


Figure 4.21 Particle identification centroids for the three symmetric reactions $^{112}\text{Sn}+^{112}\text{Sn}$, $^{118}\text{Sn}+^{118}\text{Sn}$, and $^{124}\text{Sn}+^{124}\text{Sn}$, for $B\rho = 2.4 \text{ Tm}$.

Finally, once the determination of Z and $N - Z$ are made for all beam-target-rigidity combinations, the particle identification from the three systems can be compared. Ideally, the positions of isotopes in the corrected particle identification plots should be the same from one system to another, but because of minor differences in magnetic settings, calibrations, and corrections, there can be some small differences. The particle identification centroids for the three symmetric reactions are shown in Figure 4.21. The figure shows that basically the same isotopes are measured in all three reactions, and the locations of those isotopes only shift slightly between reactions.

Once the particle identification spectrum is understood, the continuous variables TOF and ΔE can be converted into discrete Z and $N - Z$. Instead of drawing gates for each isotope, the TOF and ΔE are converted directly into Z and $N - Z$ by creating a two dimensional transformation. The transformation is done by assigning a Z and $N - Z$ to each TOF_0 and ΔE_0 (the centroid in the particle identification plot), and then directly interpolating the points in between. The result is a rectangularization of the particle identification variables, which can then be used for the final isotope selection. The actual cuts used to determine Z and $N - Z$ are $Z_0 - .5 < Z < Z_0 + .5$ and $(N - Z)_0 - .5 < N - Z < (N - Z)_0 + .5$. The transformation of the particle identification plot is shown in Figure 4.22.

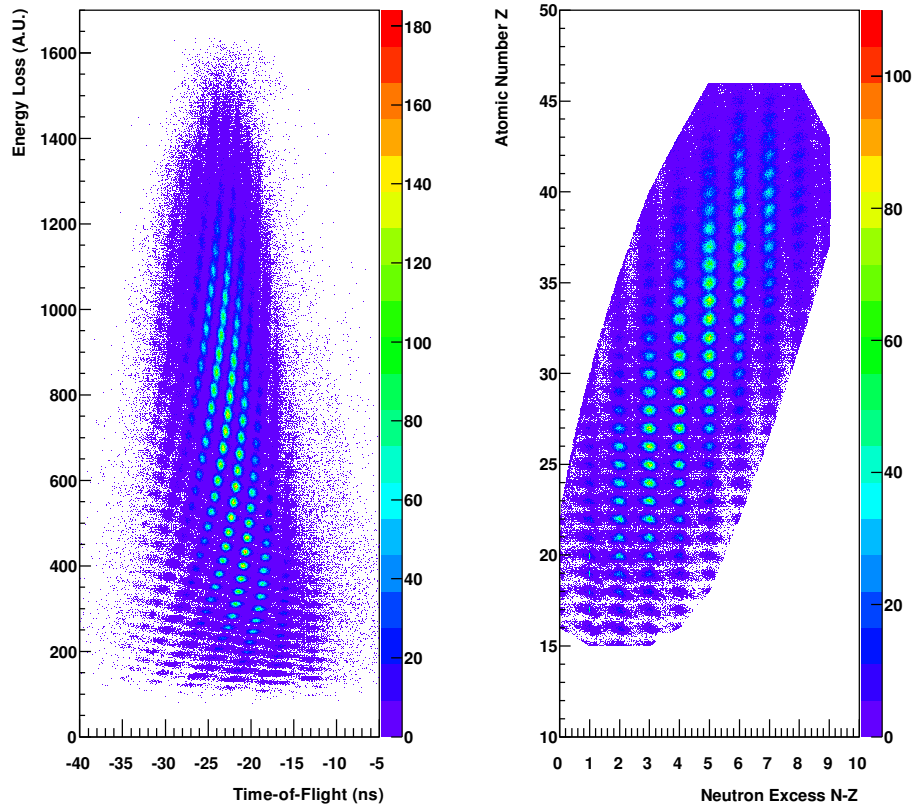


Figure 4.22 Left Panel: Final particle identification, measured in the $^{112}\text{Sn}+^{112}\text{Sn}$ reaction system at $B\rho = 2.4$ Tm. Right Panel: Rectangularized particle identification variables. The sharp cutoffs are present because interpolation is used, and no attempt to extrapolate is made.

4.3 Charge State Analysis

The procedure outlined in the previous section allows for determination of Z and A/q , and so far it is assumed that $Z = q$. However, some fragments may pick up electrons from the target or the timing scintillator, which causes $q \neq Z$. To measure the actual value of q , the Total Kinetic Energy (TKE) of the fragments is measured at the end of the focal plane. The CsI hodoscope was not part of the original proposal, but the array had been commissioned shortly before this experiment. As explained in Appendix B, the hodoscope did not prove to be useful for high- Z fragments in the energy domain of the current experiment. This section will describe the problems that were found, as well as a procedure adopted to calculate the magnitude of the correction for this effect.

To understand how the problem would manifest itself in the data, some assumptions can be made. First, for the fragments of interest, assume that the primary contamination in the spectrum is from fragments that have picked up only one electron. The predicted location that these hydrogen-like ions would enter the particle identification spectrum is shown in Figure 4.23. This figure is consistent with the fact that the particle identification seems to still resolve isotopes above $Z=40$, as the contamination is indistinguishable from the main fragments. This figure also shows that these hydrogen-like ions would enter the data set identified with the correct Z , but would be identified as the isotope with two more neutrons. The reason that the contamination follows such a simple pattern is that the region of isotopes being measured is close to the $N - Z = 0$ line, so $\frac{m}{q} \approx 2.0$. The result is that removing one unit of charge and two units of mass only slightly alters the $\frac{m}{q}$ of the hydrogen-like fragment. The hydrogen-like fragments also have nearly the same energy loss as the isotope

with two more neutrons because, for a fixed $B\rho$ and $\frac{m}{q}$, the velocity is fixed, which means the stopping power is the same. (See Equation 4.6).

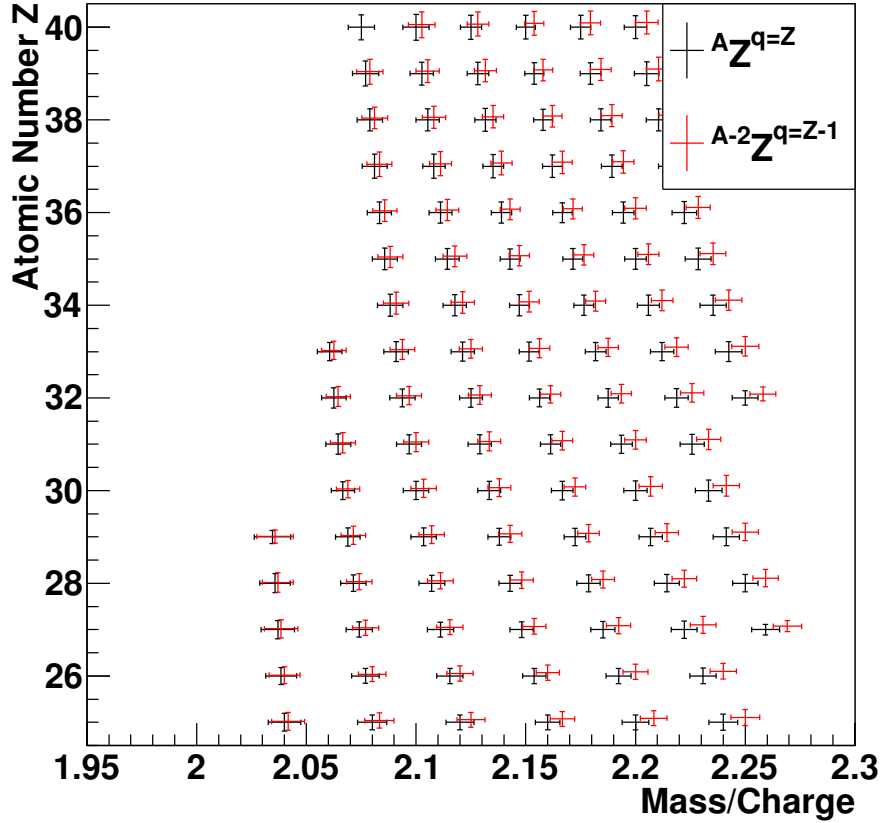


Figure 4.23 Calculated particle identification locations for a subset of the fragments of interest in the $^{112}\text{Sn}+^{112}\text{Sn}$ reaction system. The fully stripped fragments are represented by the black crosses and the primary contaminant from hydrogen-like fragments are represented by red crosses. The error bars represent one sigma resolution in the respective experimental quantities. The Z values for the contaminant are scaled by the ratio of the (slightly different) $\frac{m}{q}$ of the two overlapping fragments, which approximates the difference in their energy-loss measurements.

4.3.1 Calculation of Contamination using GLOBAL

To understand the magnitude of the charge state contamination, the empirical code GLOBAL is used [74].

The use of this code is well justified by [75], where the predicted charge state distributions agree with the measured charge state distributions from the fragmentation cross sections of

a ^{86}Kr ($Z=36$) beam at 64 MeV/u with complete A, Z, q identification. It was found that the experimental charge state distributions reasonably agreed with the predictions of GLOBAL, certainly within a factor of 2 for the single electron charge state. GLOBAL provides charge state information for projectile energies from 30 MeV/u to 2 GeV/u, and although it was designed for $Z > 28$, it provides reasonable results for lower Z as well. The version of GLOBAL that is packaged with LISE++ is used, which has minor improvements over the published algorithm. The results of a calculation for isotopes with fixed $N - Z$ at fixed $B\rho$ are shown in Figure 4.24. For the purposes of this study, the equilibrium charge state distribution is used, and the distribution comes from the timing scintillator, which is modeled as simply carbon. For the fixed isotopes shown, the charge state contamination decreases with increasing velocity, as expected. To properly account for the velocity dependence, a linear fit to three data points (at $B\rho = 2.4, 2.51, 2.6$) is used to calculate the correction as a function of $B\rho$.

To simplify the process of correcting the data, it is assumed that only the first charge state contributes, which should be reliable as long as this contribution is small ($< 20\%$). Also, it is assumed that the particle identification previously contains only the fully stripped fragment and the one contaminant isotope. With this assumption, the correction for isotope (N, Z) depends on four variables: the yield of isotope (N, Z) , the charge state fraction of isotope (N, Z) , the yield of isotope $(N - 2, Z)$, and the charge state fraction of isotope $(N - 2, Z)$. Since the measured yield Y_{exp} is a combination of the fully stripped ions and the contaminant ions:

$$Y_{exp}(N, Z) = \underbrace{Y(N, Z, q = Z)}_{\text{fully stripped}} + \underbrace{Y(N - 2, Z, q = Z - 1)}_{\text{contaminant}} \quad (4.17)$$

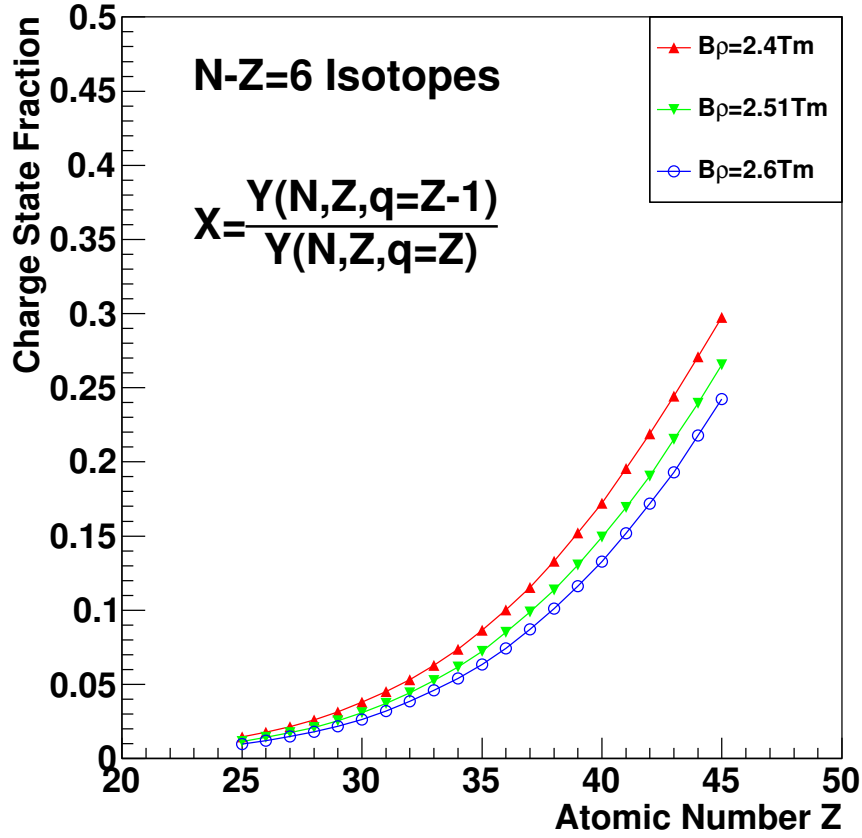


Figure 4.24 Charge state contribution (ratio of hydrogen-like ions to fully stripped ions) shown as a function of atomic number Z , as calculated by GLOBAL. Isotopes shown have $N - Z = 6$.

and the desired yield is:

$$Y(N, Z) = Y(N, Z, q = Z) + Y(N, Z, q = Z - 1) \quad (4.18)$$

which means that the measured yield is related to the desired yield by:

$$\begin{aligned} Y_{exp}(N, Z) &= Y(N, Z) + a \cdot Y(N - 2, Z) - b \cdot Y(N, Z) \\ &= (1 - b) \cdot Y(N, Z) + a \cdot Y(N - 2, Z) \end{aligned} \quad (4.19)$$

where

$$\begin{aligned}
 a &= \frac{Y(N-2, Z, q = Z-1)}{Y(N-2, Z)} \\
 b &= \frac{Y(N, Z, q = Z-1)}{Y(N, Z)}
 \end{aligned}
 \tag{4.20}$$

and a and b are the fractions calculated using GLOBAL. a represents the contamination of the isotope of interest from $N-2$, and b represents the loss of the isotope of interest to $N+2$. To get a correction factor, just divide by $Y(N, Z)$:

$$\frac{Y_{exp}(N, Z)}{Y(N, Z)} = (1-b) + a \cdot \frac{Y(N-2, Z)}{Y(N, Z)}
 \tag{4.21}$$

But the yield ratio on the right side involves the desired yields, which are unknown. Since the results from GLOBAL are approximate, the ratio of the uncorrected experimental yields can be used:

$$\frac{Y_{exp}(N-2, Z)}{Y_{exp}(N, Z)} \approx \frac{Y(N-2, Z)}{Y(N, Z)}
 \tag{4.22}$$

The procedure is slightly more complicated than is described above, since the yields are broadly distributed in $B\rho$ and the charge state fractions depend on $B\rho$ (velocity) as well. In that case the yields, $Y(N, Z)$, would be replaced by distributions in rigidity, $y(N, Z, B\rho)$. This is handled appropriately in the analysis, but for clarity, the description here only refers to the total integrated yields. Since the correction depends on the ratio, $\frac{Y(N-2, Z)}{Y(N, Z)}$, the correction must be calculated separately for each system. The correction, calculated using

the integrated yields for $^{112}\text{Sn}+^{112}\text{Sn}$ and $^{124}\text{Sn}+^{124}\text{Sn}$, is shown in Figure 4.25. The effect that this correction would have on the isoscaling observables is shown in Section 5.3.

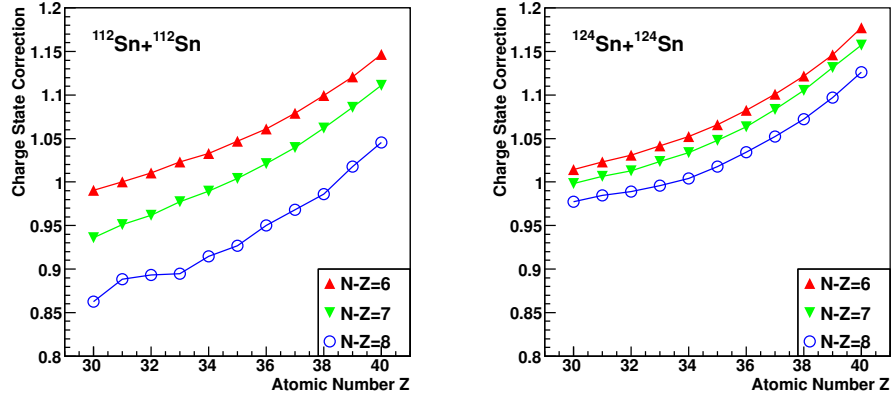


Figure 4.25 Charge state correction (inverse of left side of Equation 4.21) shown as a function of atomic number Z . Isotopes shown have $N - Z = 6, 7, 8$.

4.4 Reconstructing Momentum Distributions

4.4.1 Combining Spectrometer Settings

In this experiment, the data were measured in several settings, each covering about 5% in magnetic rigidity or momentum. The three rigidity settings had central values of 2.4, 2.51, and 2.6 Tm. The width of the distribution in momentum is on the order of 0.2 Tm (FWHM), depending on the A and Z of the species, so each momentum distributions spanned all three momentum settings. These settings were chosen such that there would be at least three isotopes with a majority of their momentum distribution measured. To combine the three different settings, each setting was scaled by the live time (measured using a clock scaler in the S800 DAQ) and scaled by the raw miniball scaler (proportional to the number of beam particles). The distribution (no correction for acceptance or charge states) for one isotope is shown in Figure 4.26, with the three settings shown as separate colors. It is apparent that the acceptance drops off near the minimum and maximum momentum measured in each setting. This effect is discussed more in Appendix C.

Although there are some differences in the acceptance from one setting to another, this effect was most pronounced for systems using the ^{112}Sn beam, at the beginning of the experiment. During the systems using the ^{124}Sn beam, the acceptance was more stable between rigidity settings. Assuming the acceptance is a function of $B\rho$ which is flat near the central rigidity, the central region can be used to obtain a rigidity (momentum) distribution that is accurate up to a scaling factor related to the angular acceptance. Based on the information in Appendix C, specifically Figure C.5, the central region with flat acceptance corresponds to $-.025 < dta < .025$, which corresponds to $B\rho \approx B\rho_0 \pm .03$ Tm.

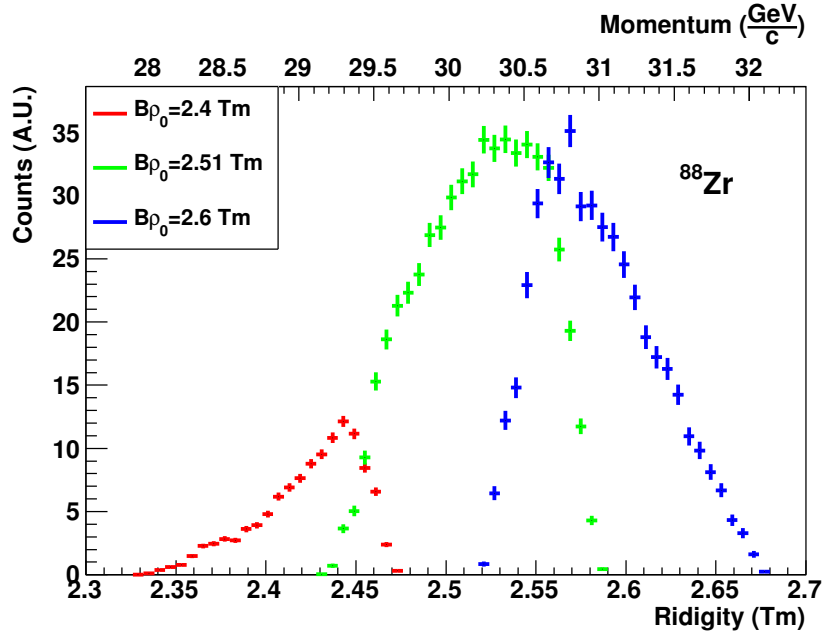


Figure 4.26 Distribution in magnetic rigidity (momentum), for ^{88}Zr , measured in the $^{124}\text{Sn}+^{124}\text{Sn}$ reaction. The lower axis shows the rigidity, while the upper axis shows the linear momentum. The data are scaled by the live time and the miniball beam normalization.

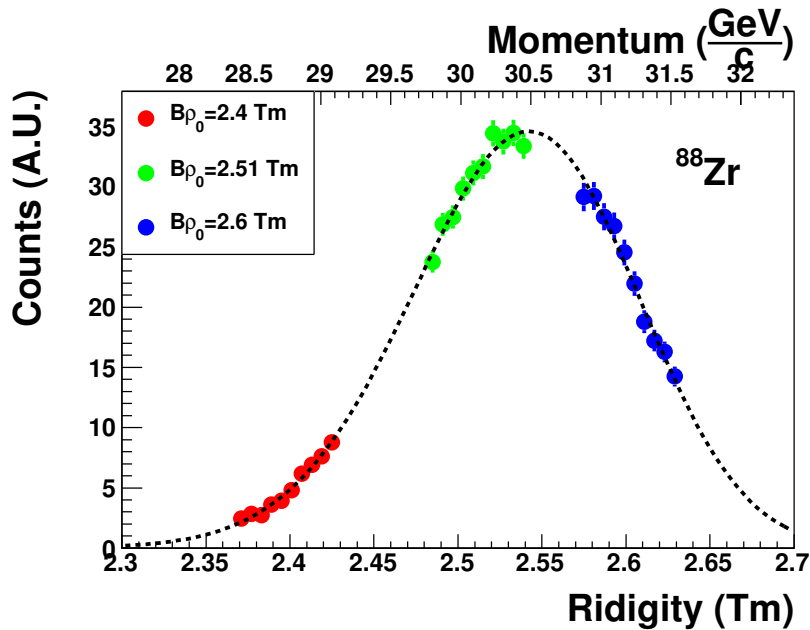


Figure 4.27 Distribution in magnetic rigidity (momentum), for ^{88}Zr , measured in the $^{124}\text{Sn}+^{124}\text{Sn}$ reaction. Only data measured in the central region of the S800 spectrometer where the acceptance is constant are included in this figure, and in the final fitting procedure. The final fit result for this isotope is shown as a dotted line.

4.4.2 Fitting Function

After removing the edge regions from the data in Figure 4.26, information about the rigidity (momentum) distributions can be extracted. An example of this is shown in Figure 4.27. The goal is to extract the integral of the rigidity (momentum) distribution, since different isotopes have different coverage in rigidity as shown in Figure 4.28. The simplest way to describe the distribution is with a Gaussian function, although this would not account for any asymmetries between the low momentum and high momentum sides of the distributions. This has been addressed previously by using a gaussian function which is asymmetric about the peak value [75]. This description can be rationalized by attributing the high momentum events to pure fragmentation and the low momentum events to a mixed reaction mechanism. In this experiment, the coverage is limited such that most rigidity (momentum) distributions are not precisely measured in their tails. It is reasonable to expect some asymmetry in the distributions, but extracting this information is difficult. The function described in [75] is two half gaussians with different widths, joined at the center. The data from this experiment should not be fit with this type of function, because one side of the distribution would be relatively unconstrained, due to limited acceptance. An alternative would be to use a skewed gaussian function, where the constant width is replaced with a linear function of the rigidity (momentum):

$$f(x) = a_0 \cdot \exp\left(\frac{(x - a_1)^2}{2(a_2 + a_3(x - a_1))^2}\right) \quad (4.23)$$

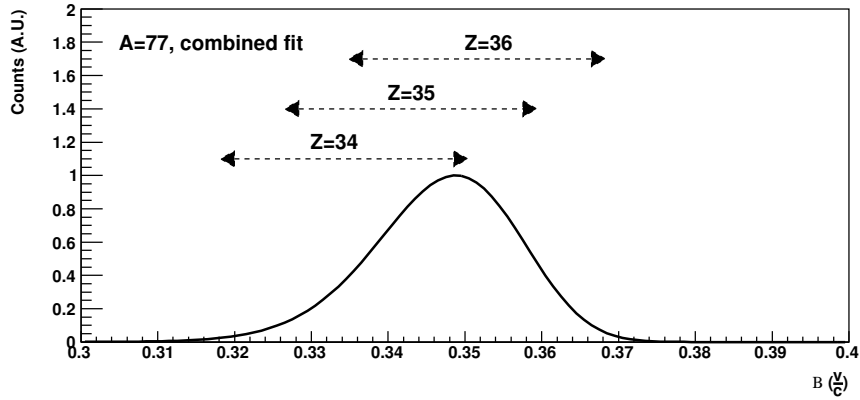


Figure 4.28 Fit result for distributions in velocity, for $A = 77$, measured in the $^{124}\text{Sn}+^{124}\text{Sn}$ reaction. The range of velocity that is covered by a fixed range of $B\rho$ is different for each isobar, and is shown by the dotted arrows.

The benefit of such a function would be that the asymmetry would be applied to both sides, so the fitting routine would be more robust when fitting partial distributions. To illustrate this effect, Figures 4.29 and 4.30 show the resulting distributions in momentum when using either a normal gaussian fit compared to a skewed gaussian, when comparing two isotopes of the same mass. For equal A , the momentum (or velocity) distributions are expected to be approximately equal [75]. The figure shows that, with a normal gaussian, there is a systematic shift due to the different rigidity acceptances of the two isotopes. (This is observed systematically in all isotopes) When fitting each isotope with the skewed gaussian, the distributions become identical. This indicates that fitting with a simple gaussian would introduce a systematic effect in the extrapolation for certain isotopes and that a skewed gaussian is more reflective of the full distribution.

4.4.3 Simultaneous Fitting of Isobaric Velocity Distributions

Since the goal is to extract ratios of fragment production cross sections, any fitting procedure must not introduce an effect that is systematic with the rigidity (momentum), because the

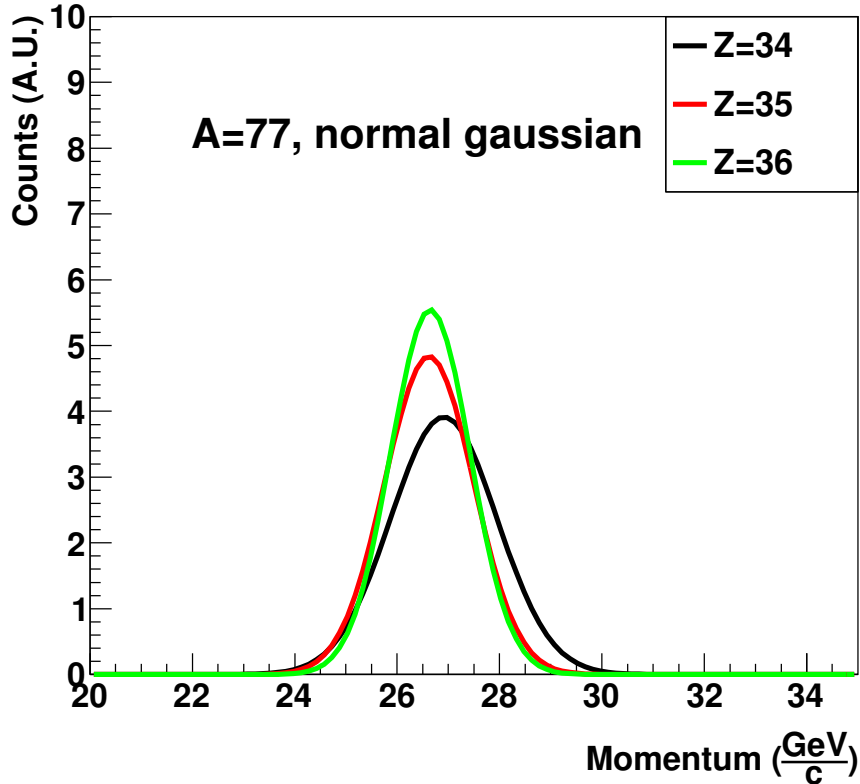


Figure 4.29 Fit results for distributions in momentum, for $A = 77$, measured in the $^{124}\text{Sn}+^{124}\text{Sn}$ reaction. The fitting function is a normal gaussian function, with three free parameters, and the plotted curves are equally normalized. Each distribution is fit individually. Different isobars result in different fits because of the asymmetry of the distribution combined with the limited acceptance range.

rigidity is correlated with the neutron excess of the fragment. Higher mass isotopes have the high momentum side cut off and lower mass isotopes have the low momentum side cut off. To improve the reliability of these fitting functions, a fit can be done using multiple isobars that are expected to have the same shape (in momentum or velocity space). As opposed to a fixed Z , which contains around 5 isotopes, a fixed A only has 2-3 isobars in the experimental acceptance. Isobars have different rigidity distributions so they sample different parts of their (presumably identical) momentum distributions. Enforcing these systematics involves fitting the distributions (in momentum space, or velocity space) simultaneously using the

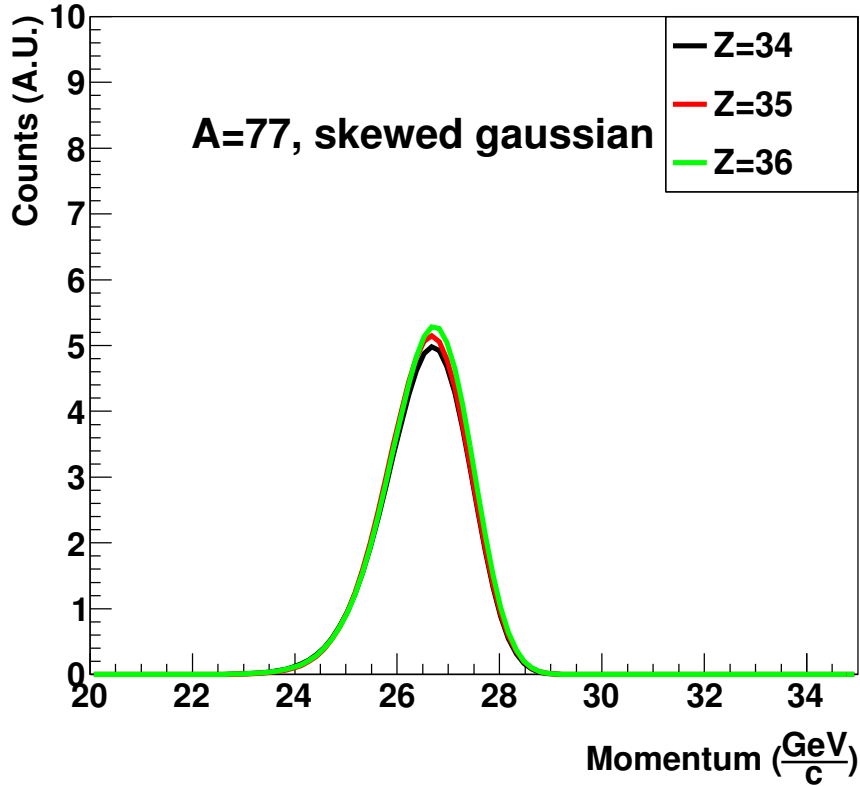


Figure 4.30 Fit results for distributions in momentum, for $A = 77$, measured in the $^{124}\text{Sn}+^{124}\text{Sn}$ reaction. The fitting function is a skewed gaussian function (Equation 4.23, with four free parameters, and the plotted curves are equally normalized. The three distributions are fit individually.

same shape parameters for the skewed gaussian while keeping the normalization parameters separate for each. For example, in the case shown for Figure 4.30, the fitting function would be:

$$f(x) = \begin{cases} a_{34} * \exp\left(\frac{(x-a_1)^2}{2(a_2+a_3(x-a_1))^2}\right) & : A = 34 \\ a_{35} * \exp\left(\frac{(x-a_1)^2}{2(a_2+a_3(x-a_1))^2}\right) & : A = 35 \\ a_{36} * \exp\left(\frac{(x-a_1)^2}{2(a_2+a_3(x-a_1))^2}\right) & : A = 36 \end{cases} \quad (4.24)$$

where the six parameters $a_1, a_2, a_3, a_{34}, a_{35},$ and a_{36} are optimized simultaneously, and $a_{34}, a_{35},$ and a_{36} are the relative normalizations for each isobar. When this simultaneous fit is applied, a single velocity distribution reasonably describes the data from the ^{124}Sn beam and for the ^{118}Sn beam. This result for the $A = 77$ isobars is shown for $^{124}\text{Sn}+^{124}\text{Sn}$ in Figure 4.31 and $^{118}\text{Sn}+^{118}\text{Sn}$ in Figure 4.32.

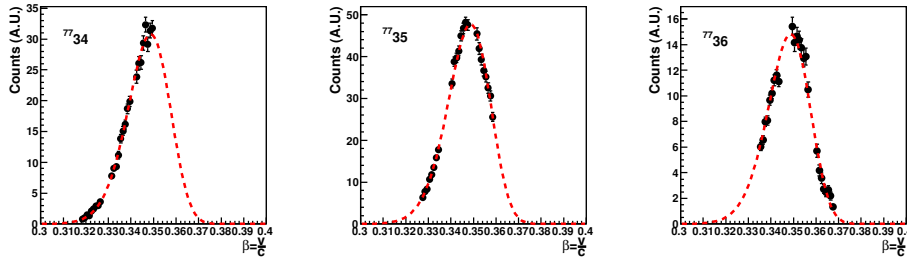


Figure 4.31 Fit result for distributions in velocity, for $A = 77$, measured in the $^{124}\text{Sn}+^{124}\text{Sn}$ reaction. The three spectra are fit simultaneously with Equation 4.24, so that the shape is identical in each spectrum.

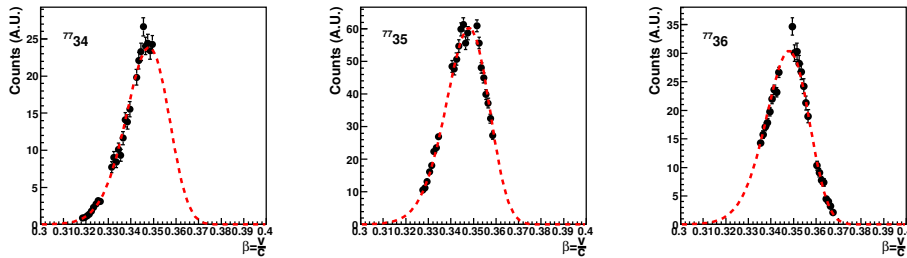


Figure 4.32 Fit result for distributions in velocity, for $A = 77$, measured in the $^{118}\text{Sn}+^{118}\text{Sn}$ reaction. The three spectra are fit simultaneously with Equation 4.24, so that the shape is identical in each spectrum.

To illustrate the advantage of fitting the isobars simultaneously, Figure 4.28 shows a fit distribution from the $^{124}\text{Sn}+^{124}\text{Sn}$ reaction, with the range in rigidity covered by each isobar shown by dotted arrows. Fitting the distributions simultaneously allows for more consistent fitting for the isobars where only one side of the distribution is given, which is necessary for extrapolation of the integrated yield.

In the data using the ^{112}Sn beam, the situation is somewhat more complicated. When fitting the three distributions simultaneously, there is a systematic shift in the peak value of the distribution for different isobars, so that fitting with a common distribution is not possible. To fit these distributions, an additional parameter can be added so that the peak centroid has a linear dependence on the Z of the isobars. This effect was also seen in the data from Ref. [75], where a similar linear dependence was used when fitting isotopes at the edge of the acceptance. More details of these systematics will be discussed in Section 5.1. To allow for this additional parameter, the fitting function becomes:

$$f(x) = \begin{cases} a_{34} * \exp\left(\frac{(x-a_1)^2}{2((a_2+a_4i)+a_3(x-a_1))^2}\right) & : A = 34 \\ a_{35} * \exp\left(\frac{(x-a_1)^2}{2((a_2+a_4i)+a_3(x-a_1))^2}\right) & : A = 35 \\ a_{36} * \exp\left(\frac{(x-a_1)^2}{2((a_2+a_4i)+a_3(x-a_1))^2}\right) & : A = 36 \end{cases} \quad (4.25)$$

where i is an index over the isobars. The parameter a_4 allows the centroid to shift across a chain of isobars, and for this example changes the peak of the velocity distribution by about 0.5% between each isobar. The result for this new fitting function for the $^{112}\text{Sn}+^{112}\text{Sn}$ system is shown in Figure 4.33. For consistency, all systems are fit allowing this parameter to vary. The systematic trends of the velocity distributions are presented in Section 5.1.

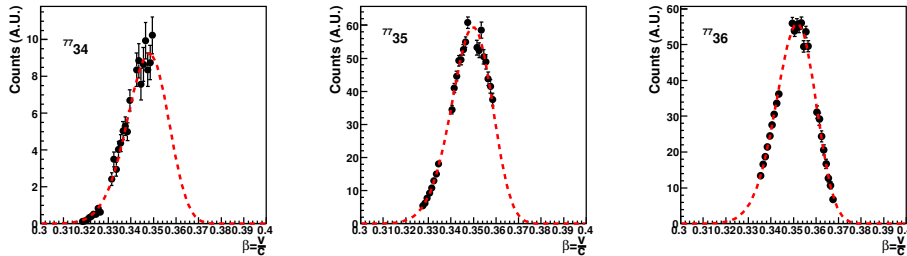


Figure 4.33 Fit result for distributions in velocity, for $A = 77$, measured in the $^{112}\text{Sn}+^{112}\text{Sn}$ reaction. The three spectra are fit simultaneously with Equation 4.25. Contrary to Figures 4.31 and 4.32, the centroids of the distributions are allowed to vary between isobars.

4.5 Miniball Centrality Selection

The Miniball allows for characterization of the impact parameters probed in the measured data set. The parameters of the Miniball are described in Section 3.4. The miniball multiplicity, which is close to the total charged particle multiplicity, is calculated simply by counting the number of miniball detectors with signals above threshold in an event. Although each miniball detector measures 4 quantities (fast, slow, tail, and time), only the energy in the slow gate is used for this calculation. This choice is made both for convenience, and because the electronics for the slow branch were the most reliable.

Once the multiplicity is extracted, this information can be transformed into a measurement of the impact parameter. This procedure has been used in the previously published results with heavy ion collisions, and is detailed in [76]. The calculation relies on the simple concept of a geometrical cross section for a collision with a sphere with radius r :

$$\sigma = \pi r^2 \tag{4.26}$$

This cross section can be parametrized using the scattering impact parameter b , so that the cross section of a collision that has an impact parameter of b or less is:

$$\int_0^b \sigma(b') db' = \pi b^2 \tag{4.27}$$

and the miniball multiplicity (N_c) should be anticorrelated with the impact parameter:

$$\int_0^b \sigma(b') db' = \int_{N_c}^{\infty} \sigma(N'_c) dN'_c \quad (4.28)$$

where $\sigma(N_c)$ is a quantity that is actually measurable in experiment. An important consideration in this measurement is that the experimental apparatus measures *any* reaction between the beam and target, and so the data acquisition system is triggered using only the Miniball, requiring a multiplicity of $N_c \geq 1$. This is different from the experimental trigger condition, so these normalization runs were measured for each beam-target combination separately from the fragment production data. In these runs, the beam was attenuated and the downstream timing scintillator was moved to the normalization position so that the beam rate can be counted directly. This procedure was done with the target in to measure the total reaction cross section, as well as with the target out (through a blank target frame) to measure the amount of background not coming from the reaction target. The spectra in each configuration are normalized by the number of incident beam particles (measured directly by the scintillator), as well as the areal atomic number density of the respective target. Then, the target-out spectra are subtracted from the target-in spectra. The resulting spectra are shown in the left-hand panels of Figure 4.34.

The total reaction cross section, and in turn b_{max} are defined by:

$$\pi b_{max}^2 = \int_1^{\infty} \sigma(N'_c) dN'_c \quad (4.29)$$

and these results are shown in Table 4.2

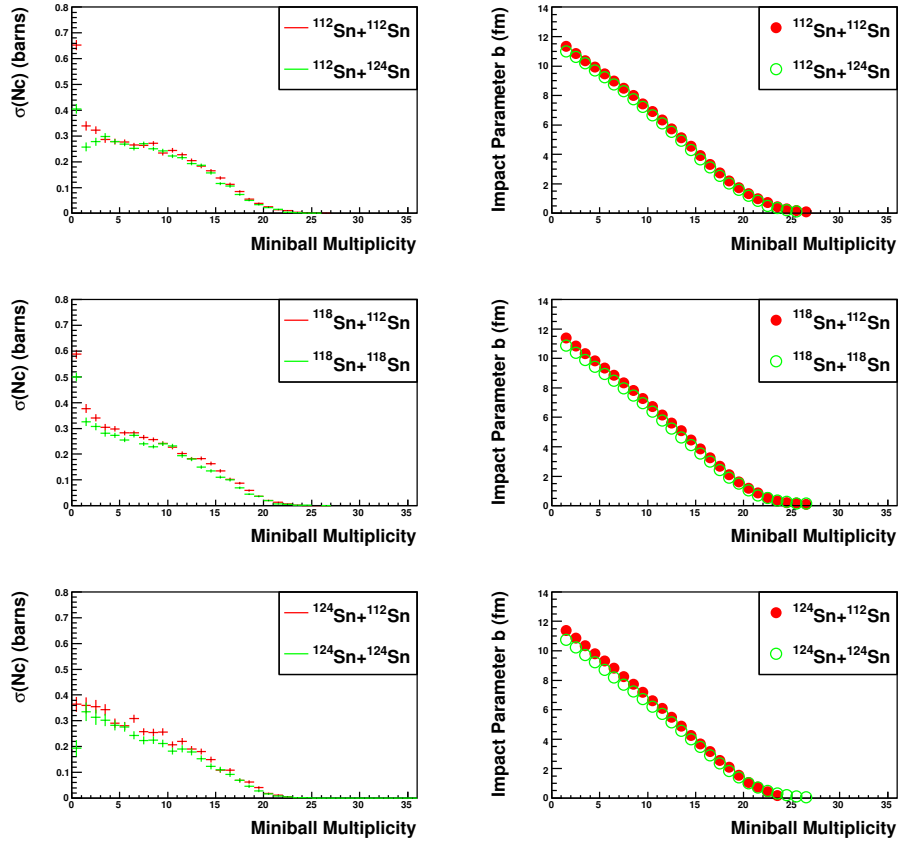


Figure 4.34 Total reaction cross section vs. miniball multiplicity (left-side panels) and calculated impact parameter vs. miniball multiplicity (right-side panels). Shown for two targets each for ^{112}Sn (Top), ^{118}Sn (Middle), and ^{124}Sn (Bottom).

The extracted b_{max} for the $^{124}\text{Sn}+^{124}\text{Sn}$ reaction is smaller than for the $^{112}\text{Sn}+^{112}\text{Sn}$ reaction, even though the radii of the neutron rich ^{124}Sn would be larger. This suggests that the multiplicity is influenced by the neutron-richness of the system as well as the impact parameter, since emitted neutrons are not detected.

When comparing systems which have different size, it is convenient to use the reduced impact parameter:

$$\hat{b} = \frac{b}{b_{\text{max}}} \quad (4.30)$$

Reaction	σ_{total} (barn)	b_{max} (fm)
$^{112}\text{Sn}+^{112}\text{Sn}$	4.04	11.34
$^{112}\text{Sn}+^{124}\text{Sn}$	3.79	10.98
$^{118}\text{Sn}+^{112}\text{Sn}$	4.07	11.38
$^{118}\text{Sn}+^{118}\text{Sn}$	3.71	10.86
$^{124}\text{Sn}+^{112}\text{Sn}$	4.07	11.38
$^{124}\text{Sn}+^{124}\text{Sn}$	3.62	10.73

Table 4.2 Maximum impact parameter and total integrated cross section measured in the for the six measured beam-target combinations.

which gives a dimensionless variable which scales with the centrality of the collision, event by event. The relationship between \hat{b} and N_c is shown in Figure 4.35.

The experimental data is averaged over a range of impact parameters, while theoretical calculations have a fixed impact parameter. The amount of isospin diffusion that will occur is correlated with time when the projectile and target are in contact. This contact time increases with increasing centrality of the collision. Thus, the impact parameter must be characterized to compare the simulation to the data. The experimental observable (isoscaling) is most conveniently measured as a function of Z , so a relationship between the measured Z and the impact parameter must be determined.

Because the data are measured in three different momentum settings, it is impossible to have a “minimum bias” normalization as was done with the Miniball. The relationship between the measured Z and the deduced impact parameter is shown in Figures 4.36 and 4.37 for the $^{112}\text{Sn}+^{112}\text{Sn}$ and $^{124}\text{Sn}+^{124}\text{Sn}$ reactions, respectively. These figures are made by combining all the data from the three $B\rho$ settings, with the appropriate normalizations for each setting. These spectra have a cutoff due to the acceptance at low Z , because the gain of the S800 focal plane detectors was not high enough to detect low Z fragments. At

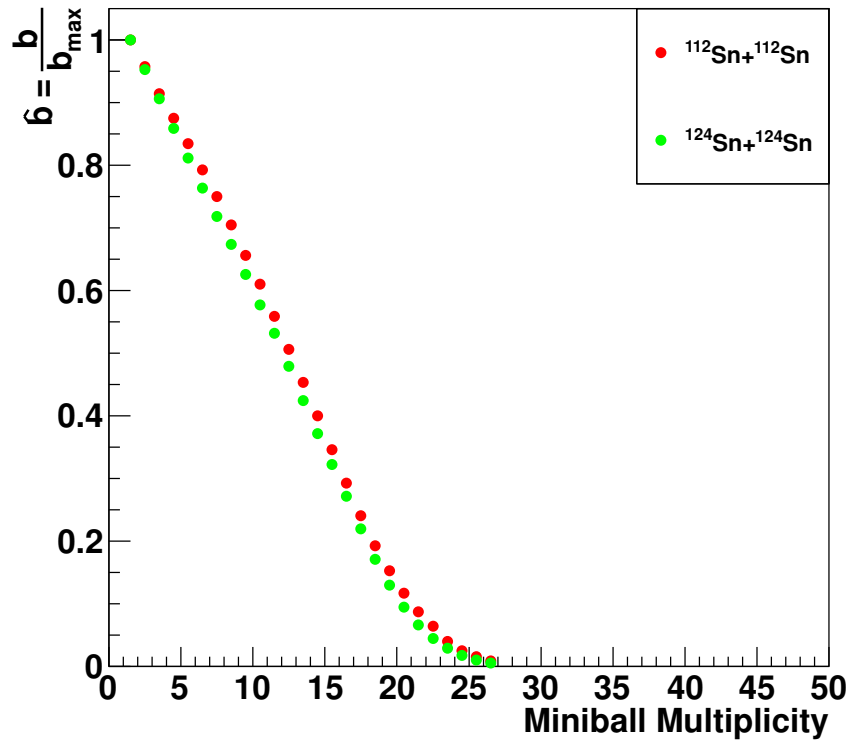


Figure 4.35 Reduced impact parameter vs. miniball multiplicity (right-side panels). Shown for the reactions $^{112}\text{Sn}+^{112}\text{Sn}$ and $^{124}\text{Sn}+^{124}\text{Sn}$.

high Z , there are low statistics near $Z=50$ because the entire isotopic distribution was not measured, only the more neutron-poor fragments were measured.

In Figures 4.36 and 4.37, the black circles represent the mean impact parameter for all events that result in a heavy fragment of charge Z . Alternatively, the most probable impact parameter could be used. Figure 4.38 shows the difference in the deduced impact parameter when calculating the mean compared to extracting the peak from a gaussian fit to the distribution. The difference is less than 0.1 fm, which is negligible. Since the isospin diffusion data is measured as an average over impact parameter for a fixed Z , the mean impact parameter will be used in all further analysis.

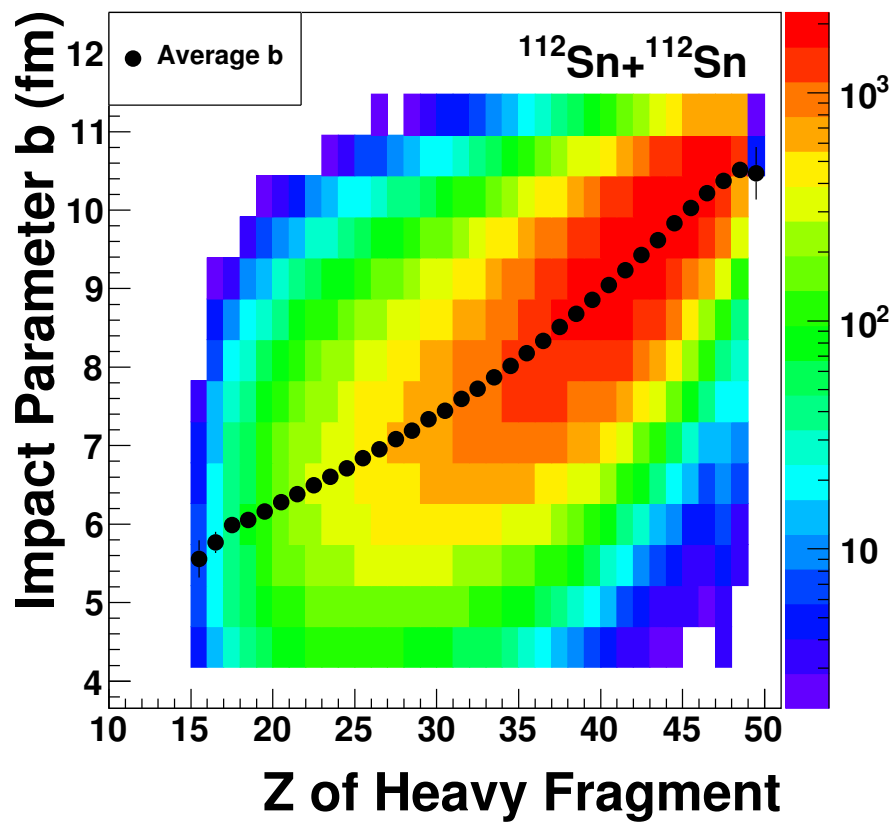


Figure 4.36 Two-dimensional spectrum showing the impact parameter extracted from the Miniball multiplicity vs. the atomic number Z of the fragment measured in the S800, plotted for the $^{112}\text{Sn} + ^{112}\text{Sn}$ reaction data. The solid circles show the average impact parameter for each Z , where the errors are smaller than the data points.

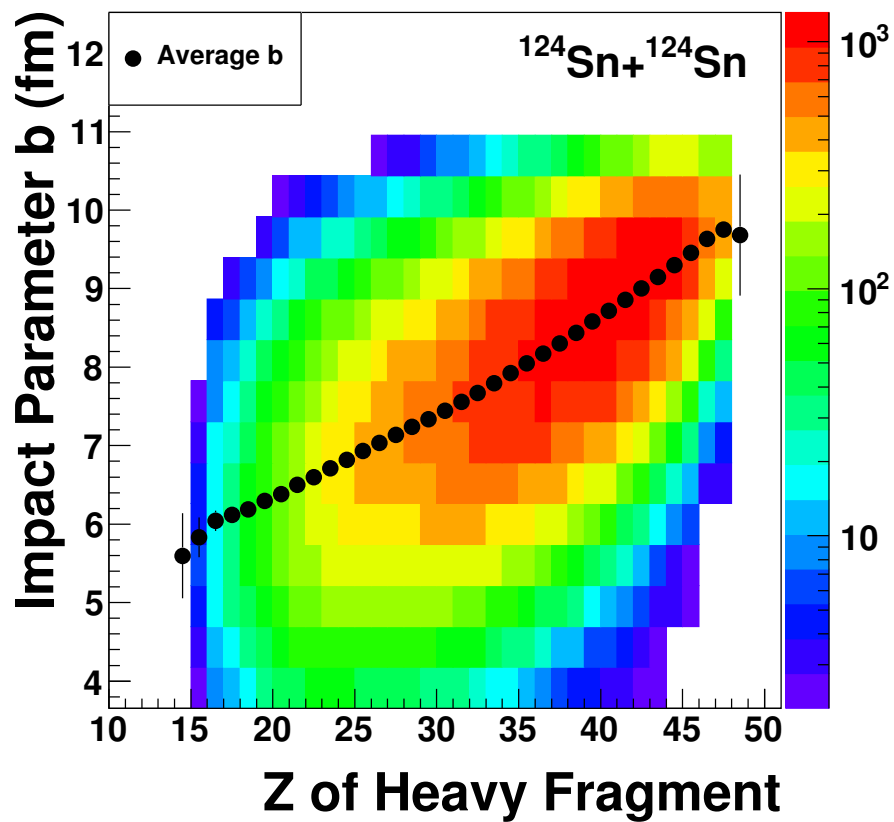


Figure 4.37 Two-dimensional spectrum showing the impact parameter extracted from the Miniball multiplicity vs. the atomic number Z of the fragment measured in the S800, plotted for the $^{124}\text{Sn}+^{124}\text{Sn}$ reaction data. The solid circles show the average impact parameter for each Z , where the errors are smaller than the data points.

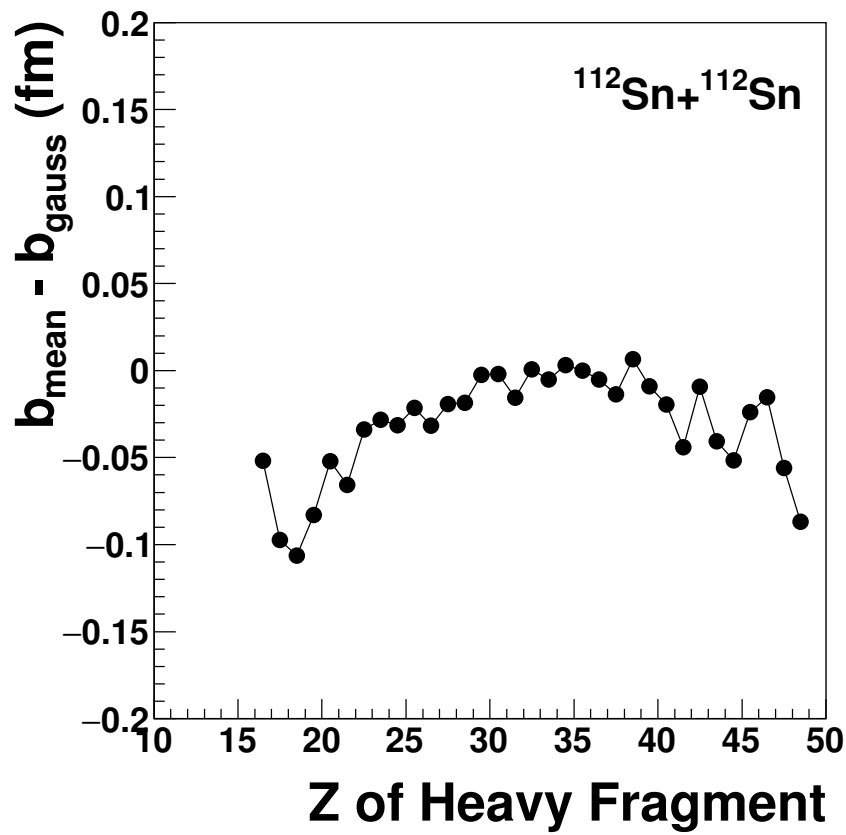


Figure 4.38 Difference between the impact parameter determined using a mean and fitting with a gaussian function vs. the atomic number Z of the fragment measured in the S800, plotted for the $^{112}\text{Sn} + ^{112}\text{Sn}$ reaction data.

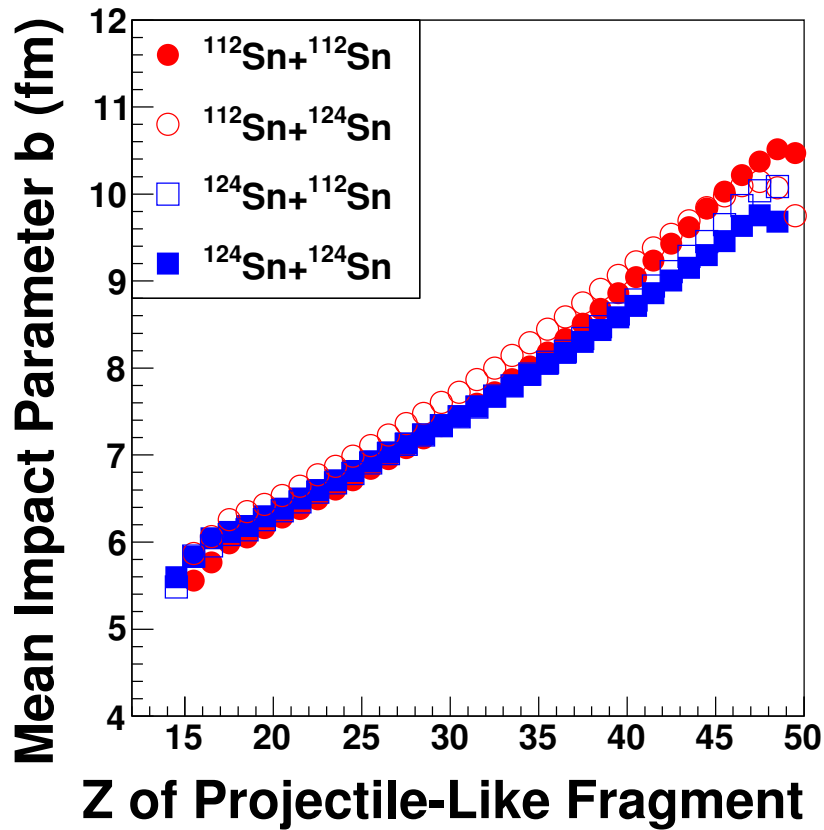


Figure 4.39 Measured correlation between the average Z of the heavy residue measured in the S800 and the impact parameter extracted from the charged particle multiplicity. Data points are shown for the $^{112}\text{Sn}+^{112}\text{Sn}$, $^{112}\text{Sn}+^{124}\text{Sn}$, $^{124}\text{Sn}+^{112}\text{Sn}$, and $^{124}\text{Sn}+^{124}\text{Sn}$ systems. The impact parameter is calculated as the mean impact parameter for events which yield a fragment with atomic number Z .

The relationship between the mean impact parameter and the fragment Z is shown for the four main reaction systems in Figure 4.39. Overall, the trend is similar between all four systems. For smaller Z , the deduced impact parameter does not strongly depend on the system, but for larger b there is a small difference between the four systems. The similarity of these trends gives some confidence that the charged particle multiplicity is a reliable measure of the impact parameter. The discrepancy at high Z between the different systems may be caused by the experimental acceptance, because only the more neutron-poor fragments are measured in each reaction.

Because the impact parameter distribution is sharply peaked, no cut on the impact parameter is made before extracting the isoscaling information. This allows the use of the full measured statistics, and the relationship between Z and b can be used to measure isospin diffusion as a function of impact parameter. From the measured relationship, the measured data from about $Z = 27$ to $Z = 43$ spans a range of impact parameters between $b \approx 7$ fm and $b \approx 10$ fm. The results for the four main reaction systems are shown in Table 4.3. The errors quoted in this table are obtained from a gaussian fit to the impact parameter distribution for each Z . These results will be used in Section 5.4 to connect the measured data with theoretical calculations.

Z	b (fm) $^{112}\text{Sn}+^{112}\text{Sn}$	b (fm) $^{112}\text{Sn}+^{124}\text{Sn}$	b (fm) $^{124}\text{Sn}+^{112}\text{Sn}$	b (fm) $^{124}\text{Sn}+^{124}\text{Sn}$
27	7.1±1.5	7.4±1.4	7.1±1.5	7.1±1.3
28	7.2±1.5	7.5±1.4	7.2±1.5	7.2±1.3
29	7.3±1.4	7.6±1.4	7.3±1.5	7.3±1.3
30	7.4±1.4	7.7±1.3	7.4±1.4	7.4±1.3
31	7.6±1.3	7.9±1.3	7.6±1.4	7.6±1.2
32	7.7±1.4	8±1.2	7.7±1.4	7.7±1.2
33	7.9±1.4	8.1±1.2	7.8±1.4	7.8±1.2
34	8±1.3	8.3±1.2	7.9±1.3	7.9±1.2
35	8.2±1.3	8.4±1.1	8.1±1.3	8±1.1
36	8.3±1.3	8.6±1.1	8.2±1.3	8.2±1.1
37	8.5±1.2	8.7±1.1	8.3±1.3	8.3±1.1
38	8.7±1.1	8.9±1.1	8.5±1.2	8.4±1
39	8.9±1.1	9.1±0.93	8.6±1.2	8.6±1
40	9±1.1	9.2±0.91	8.8±1.1	8.7±1
41	9.2±1.1	9.4±0.82	8.9±1.1	8.9±0.93
42	9.4±0.97	9.5±0.8	9.1±1.1	9±0.91
43	9.6±0.88	9.7±0.76	9.3±1.1	9.2±0.83

Table 4.3 Mean impact parameter deduced from the miniball multiplicity tabulated by atomic number Z . The errors are the width (σ) of a gaussian fit to the impact parameter distribution for each Z .

Chapter 5

Results

5.1 Systematics of Velocity Distributions

In this section, the measured fragment velocity distributions are discussed. By comparing the velocity distributions to established trends, the systematics may provide information about the reaction dynamics which may explain the isoscaling and isospin diffusion results in Sections 5.3 and 5.4. Many experiments focus on providing production cross sections for exotic nuclei, in order to improve models used to predict properties of exotic beams. Accurate predictions of projectile fragmentation cross sections are practically useful because fast fragmentation is the primary method for producing very exotic beams. The data measured in this experiment may be useful to improve models used to predict the purities and intensities of radioactive beams. In particular, this experiment measures how the projectile and target N/Z affects the fragmentation dynamics, because of the wide range of isospin asymmetry that was probed.

Since the dynamics of projectile fragmentation are dictated by the mass loss of the fragment, $\Delta A = A_{\text{proj}} - A$, so all parameters will be plotted in this chapter vs. ΔA . Although secondary decay alters the mass of the detected fragments, the mass loss can be related to the impact parameter and the energy dissipation during the collision. Plotting a variable vs. the mass loss then can give some insight into how that parameter is varying with the centrality and dissipation of the collision, which is useful for comparison to theory.

The parameter that accounts for the “skewing” of the distributions, γ_{skew} , is shown in Figure 5.1. The magnitude of this parameter reflects how asymmetric the velocity distributions is; a smaller magnitude of γ_{skew} means closer to a normal gaussian distribution. Many studies of projectile fragmentation [75, 77, 78] have shown that the momentum distribution is asymmetric. Semi-empirical models have been put forward to explain why this might be, but is beyond the scope of this work. The trend of the measured data shows that γ_{skew} does not seem to vary with the target mass at all. There is a weak dependence on the mass of the projectile. For all systems, the magnitude of γ_{skew} increases with increasing mass loss. If the process proceeded by “pure fragmentation”, the gaussian distribution would be more symmetric with $\gamma_{\text{skew}} \approx 0$. The experimental result that $\gamma_{\text{skew}} \neq 0$ is a signature of the increasing importance of non-fragmentation effects.

Another systematic trend which is not simply understood is how the velocity of isobars changes. Simple models of projectile fragmentation do not predict an isospin dependence for the velocity distributions [79, 80]. Most of the measured reactions demonstrate a velocity that depends only on the mass loss of the measured fragment. However, the neutron deficient reactions $^{112}\text{Sn}+^{112}\text{Sn}$ and $^{112}\text{Sn}+^{124}\text{Sn}$ have a clear dependence on the neutron excess of the isobars. When simultaneously fitting the velocity distributions, (see Section 4.4) the centroid β_0 of the skewed gaussian distribution is described as a linear function of the charge of the isobar:

$$\beta_0(A, Z) = \beta_0(A, Z_0) \left(1 + \frac{d\beta_0}{dZ} (Z - Z_0) \right) \quad (5.1)$$

$\frac{d\beta_0}{dZ}$ is a parameter of the fit and is plotted in Figure 5.2. For the reactions with the ^{112}Sn projectile, the effect of changing Z by one while holding A constant is an approximately 0.5%

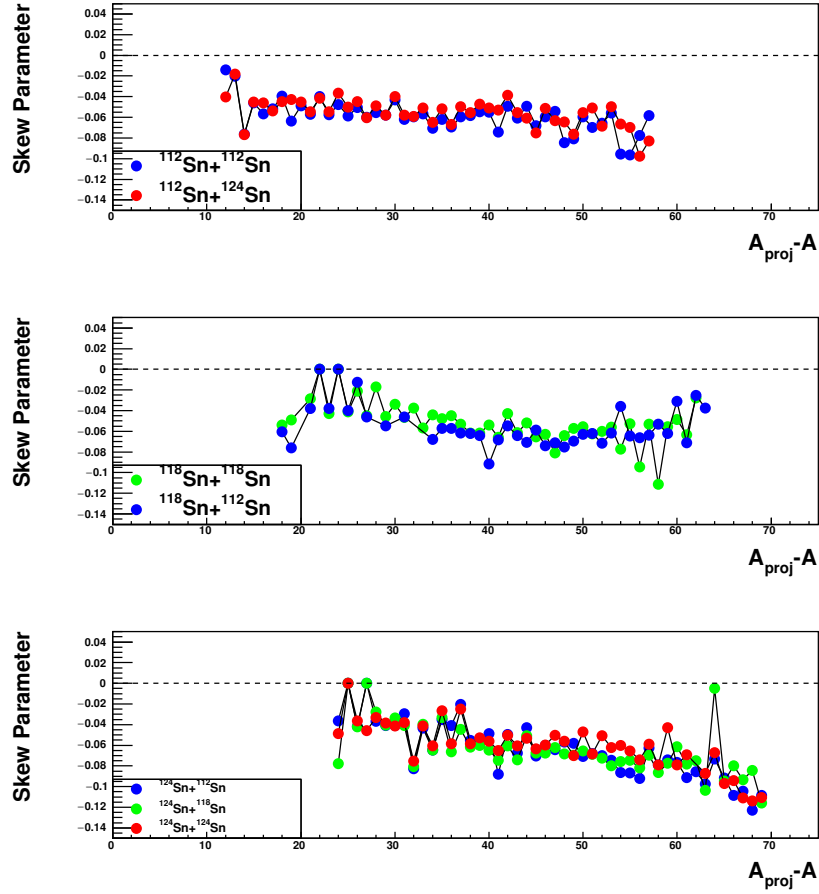


Figure 5.1 Skew parameter vs. Mass Loss ($A_{\text{proj}} - A$). Top, middle, and bottom panels are the ^{112}Sn , ^{118}Sn , and ^{124}Sn projectiles, respectively. The ^{112}Sn , ^{118}Sn , and ^{124}Sn targets are represented by the blue, green, and red points, respectively. A horizontal dashed line is drawn for no skewing, or a symmetric gaussian. A negative value represents a longer tail extending to lower velocity.

shift in the velocity. For comparison, the shift from the beam velocity ($\beta = .367$) is $< 5\%$, and the average velocity only shifts by about 2% over the whole range of $20 < \Delta A < 60$. This means that for the most neutron-poor projectile, changing Z between isobars has a significantly larger effect than does changing A between isotopes. For the more neutron-rich projectiles, $\frac{d\beta_0}{dZ}$ has a smaller magnitude and changes with target mass.

In this experiment, there is limited angular acceptance (see Appendix C, and there are other effects such as charge state contamination which could potentially create this effect, so data from [75] was investigated for this same effect. In that experiment performed at the NSCL, beams of $^{40,48}\text{Ca}$ and $^{58,64}\text{Ni}$ were impinged on Be and Ta targets and the reaction products were measured and identified by the A1900 fragment separator. For the neutron-poor reactions, $\frac{d\beta_0}{dZ}$ is again measurably positive and has a similar magnitude as results from the Sn+Sn collisions. This result is shown in Figure 5.3. In [75], the neutron-rich projectiles show the shift in the velocity distributions, but with $\frac{d\beta_0}{dZ} < 0$. For the neutron rich projectiles, $\frac{d\beta_0}{dZ}$ also shows a strong dependence on the target. These changes in the velocity distribution follow a clear trend, and suggests further study to investigate the cause.

The peak of the velocity distribution β_0 also exhibits a very regular trend, shown in Figure 5.4. For small mass loss, β_0 decreases with increasing mass loss. As the mass loss becomes larger, the trend becomes flat. In the reactions with ^{118}Sn and ^{124}Sn projectiles the trends are flatter simply because more nucleons must be removed to produce the same isotopes. [81] showed a similar trend for β_0 and suggested that β_0 can be used a tracer of the dissipation in the reaction. That experiment measured reactions with a ^{86}Kr beam and $^{112,124}\text{Sn}$ and $^{58,64}\text{Ni}$ targets at $15 \frac{\text{MeV}}{\text{u}}$.

This trend in the velocity is very useful in the interpretation of the reaction dynamics, because the isoscaling relations require that the temperature be equal in the systems being

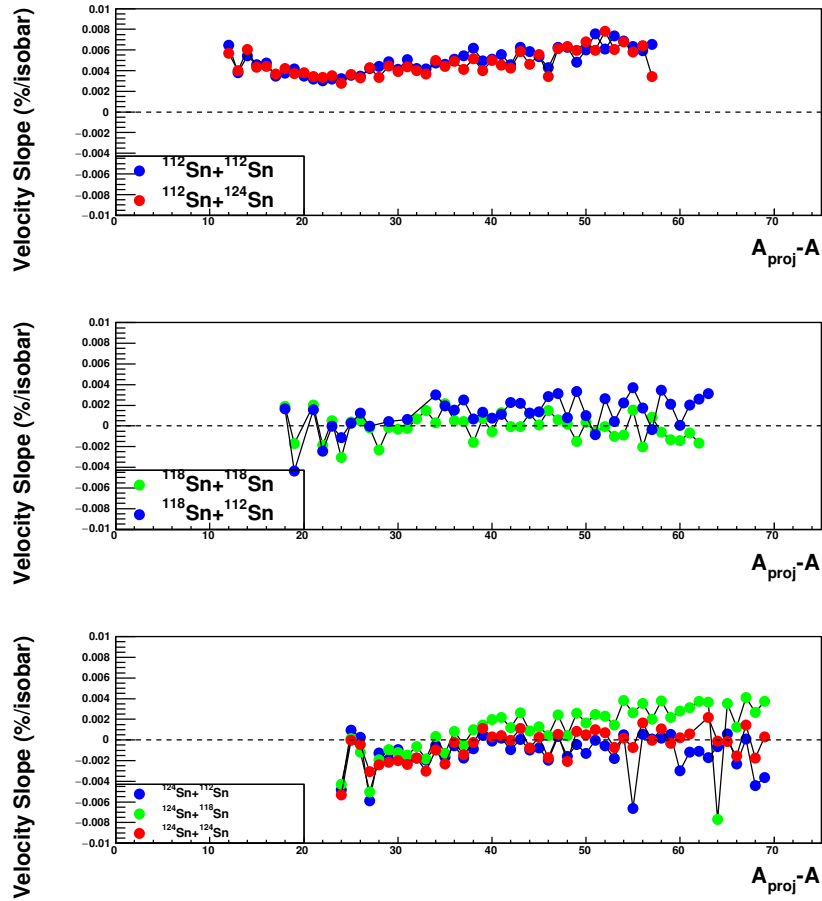


Figure 5.2 Isobar velocity slope parameter vs. Mass Loss ($A_{\text{proj}} - A$). Top, middle, and bottom panels are the ^{112}Sn , ^{118}Sn , and ^{124}Sn projectiles, respectively. The ^{112}Sn , ^{118}Sn , and ^{124}Sn targets are represented by the blue, green, and red points, respectively. A horizontal dashed line is drawn for zero slope, which means that all isobars have identical velocity distributions, where a positive value means that higher Z isobars have higher velocity.

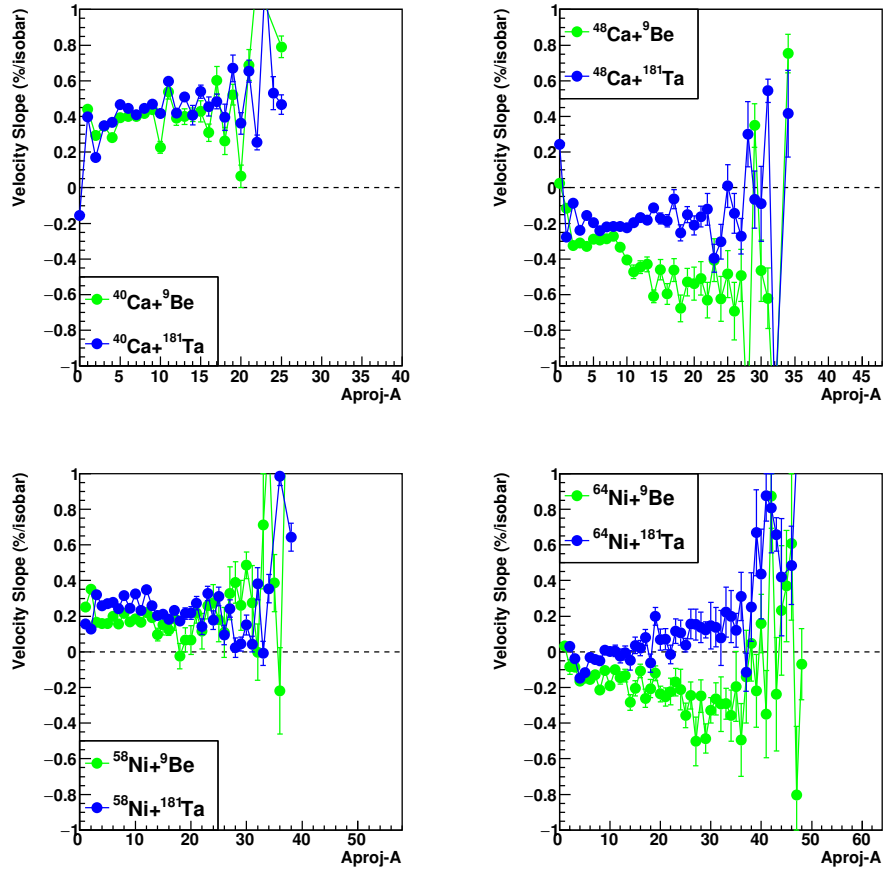


Figure 5.3 Isobar velocity slope parameter vs. Mass Loss ($A_{\text{proj}} - A$), for $^{40,48}\text{Ca}$ and $^{58,64}\text{Ni}$ projectiles with ^9Be and ^{181}Ta targets, at $140 \frac{\text{MeV}}{\text{u}}$. Data taken from [75]

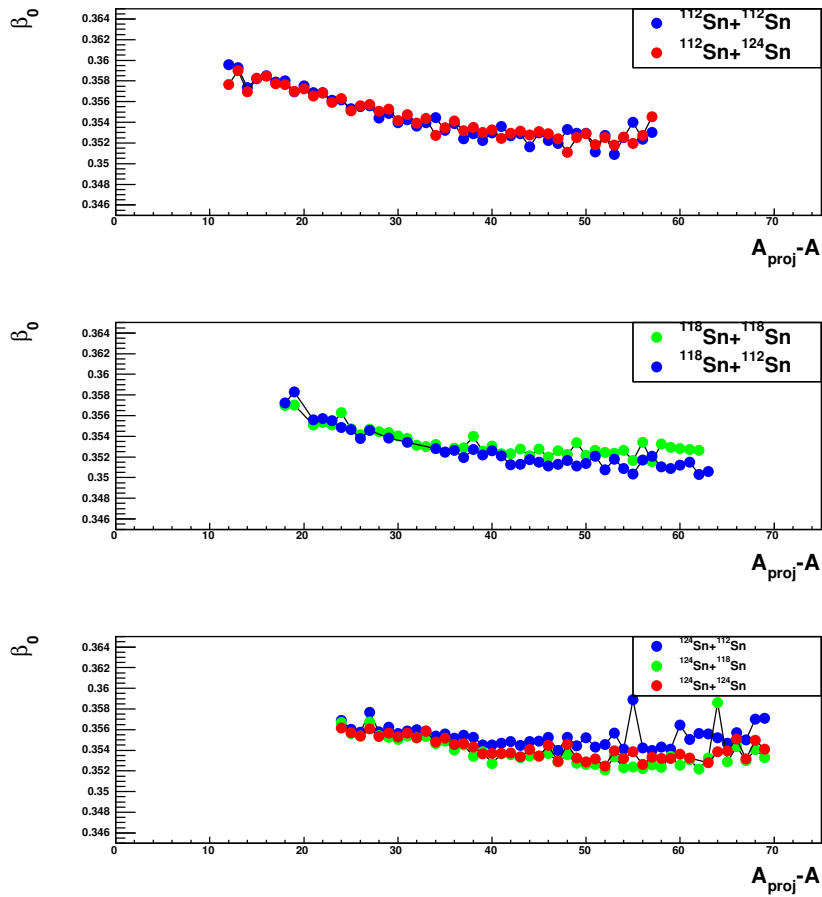


Figure 5.4 Most-probable velocity vs. Mass Loss ($A_{\text{proj}} - A$). Top, middle, and bottom panels are the ^{112}Sn , ^{118}Sn , and ^{124}Sn projectiles, respectively. The ^{112}Sn , ^{118}Sn , and ^{124}Sn targets are represented by the blue, green, and red points, respectively. The data are corrected for the energy loss in the target and the timing scintillator. The beam velocity for all three projectiles is $\beta = .367$.

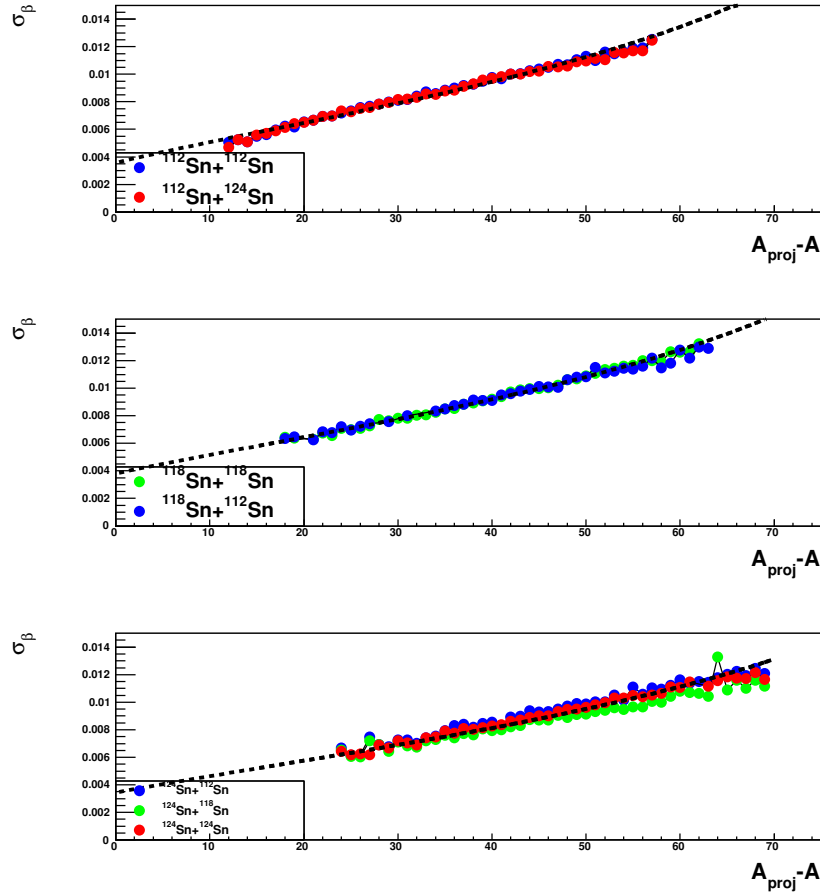


Figure 5.5 Gaussian width parameter vs. Mass Loss ($A_{\text{proj}} - A$). Top, middle, and bottom panels are the ^{112}Sn , ^{118}Sn , and ^{124}Sn projectiles, respectively. The ^{112}Sn , ^{118}Sn , and ^{124}Sn targets are represented by the blue, green, and red points, respectively. The dashed lines indicate the fitting result of the modified Goldhaber description discussed in the text.

compared. The systematic trend and the magnitude of β_0 are quite similar, which suggest that these reactions have a similar degree of dissipation. In addition, because the velocity flattens out with increasing mass loss, it can be assumed that for these fragments (i.e. $\Delta A \gtrsim 35$ for $^{112}\text{Sn}+^{112}\text{Sn}$), the excitation energy (and temperature) is not changing significantly.

The final parameter of interest in the velocity distributions is the width of the distributions. Goldhaber proposed a model for the systematics of the width [80], and this was further modified by Morrissey [79]. It is still an active area of research, [57, 82, 75] because it is critical in the production of radioactive beams via fast fragmentation. Goldhaber expanded

on the work by Feshbach and Huang [83] to explain the trends in many fragmentation data sets, and showed that the momentum distributions follow a common trend regardless of many assumptions made about the fragmentation process. The Goldhaber formulation can be simply derived by assuming that the system comes to equilibrium with a temperature T . Because the projectile separates into two fragments, the system has one degree of freedom, and so the average thermal kinetic energy is $kT/2$. Assuming that the projectile is separated into two fragments with masses A and $A_{\text{proj}} - A$ which have equal and opposite momenta, the energy in the center of mass can be written as

$$\frac{kT}{2} = \frac{\langle p_0^2 \rangle}{2m_n A} + \frac{\langle p_0^2 \rangle}{2m_n (A_{\text{proj}} - A)} \quad (5.2)$$

where m_n is the nucleon mass and $\langle p_0^2 \rangle$ is the mean squared momentum in the center of mass frame. Recognizing that $\langle p_0^2 \rangle = \sigma_0^2$, Equation 5.2 can be rearranged to give

$$\sigma^2 = mkT \frac{A(A_{\text{proj}} - A)}{(A_{\text{proj}})}. \quad (5.3)$$

These simple assumptions do not reproduce a factor of $A_{\text{proj}}/(A_{\text{proj}} - 1)$ which is seen in the data, but this is a negligible factor for large A_{proj} . The form of Goldhaber's systematics is usually written as:

$$\sigma^2 = \sigma_0^2 \frac{A(A_{\text{proj}} - A)}{(A_{\text{proj}} - 1)} \quad (5.4)$$

for a fragment A and a projectile A_{proj} , where σ_0 is approximately 90 MeV/c and can be related to the nucleon fermi energy.

Because the data from this experiment does not include fragments close to the projectile, distinguishing between different models is not possible. But, comparing the measured systematics to these models can indicate the robustness of the fitting procedure for the velocity distributions. To this end, the data is only compared to the Goldhaber systematics.

The actual measured width, shown in Figure 5.5, is a convolution of the fragmentation process, the straggling in the energy loss in the target and the timing scintillator, the beam spot size in the dispersive direction, and the intrinsic momentum width of the incoming beam. The beams used in this experiment are degraded from $120 \frac{\text{MeV}}{u}$, to $70 \frac{\text{MeV}}{u}$ using the A1900 fragment separator to select the appropriate portion of the beam. This results in an approximately 0.25% spread in the incoming beam momentum. Because this spread was not measured directly for each beam, a constant term σ_{proj} is added to the Goldhaber formula, and is allowed to vary in the fitting procedure. Since velocity distributions and not momentum distributions are used in the present results, the Goldhaber formula must be described in terms of velocity and mass loss ΔA :

$$\sigma_{\beta}^2 = \frac{\sigma_0^2(\Delta A)}{(A_{\text{proj}} - \Delta A)(A_{\text{proj}} - 1)} + \frac{\sigma_{\text{proj}}^2}{(A_{\text{proj}} - \Delta A)^2} \quad (5.5)$$

The fits of this function to the data (for the three symmetric systems) are shown in Figure 5.5. The fitting parameters are listed in Table 5.1. In order to fit the data, the constant additive factor must be on the order of 1% (of the total momentum), which is much larger than the 0.25% momentum width of the beam. This discrepancy implies that there is more complicated dynamics than the simple Goldhaber description. Nonetheless, the conclusion of this fitting procedure is that the reduced width σ_0 is similar to the Goldhaber description,

Reaction System	σ_0 (MeV/c)	σ_{proj} (MeV/c)
$^{112}\text{Sn}+^{112}\text{Sn}$	94.6	416
$^{118}\text{Sn}+^{118}\text{Sn}$	101	410
$^{124}\text{Sn}+^{124}\text{Sn}$	95.3	397

Table 5.1 Fitting parameters from the systematics of the velocity distributions.

which gives some confidence in the consistency of the data from one reaction system to another.

5.2 Isotopic Distributions of Residue Fragments

One goal of this experiment is to use isoscaling observables to infer information about the isospin content of the heavy projectile-like fragment distributions. This requires measuring precisely the *shape* of the isotopic distributions, which are used to make the isoscaling ratios in the next section. The relative yields, for a given element, are shown in Figure 5.6 and 5.7, where five different reaction systems are shown for each element. Although only relative yields are measured in this experiment, the shapes of the isotopic distributions should be preserved.

Comparing the dotted and solid lines in Figures 5.6 and 5.7 clearly indicates that changing the system asymmetry changes the isotopic distributions, albeit a small effect. For the higher Z fragments, the peak of the distributions are shifted to the right simply because fragments of a larger mass can support a larger neutron excess. To isolate that effect, isoscaling ratios are constructed in Section 5.3.

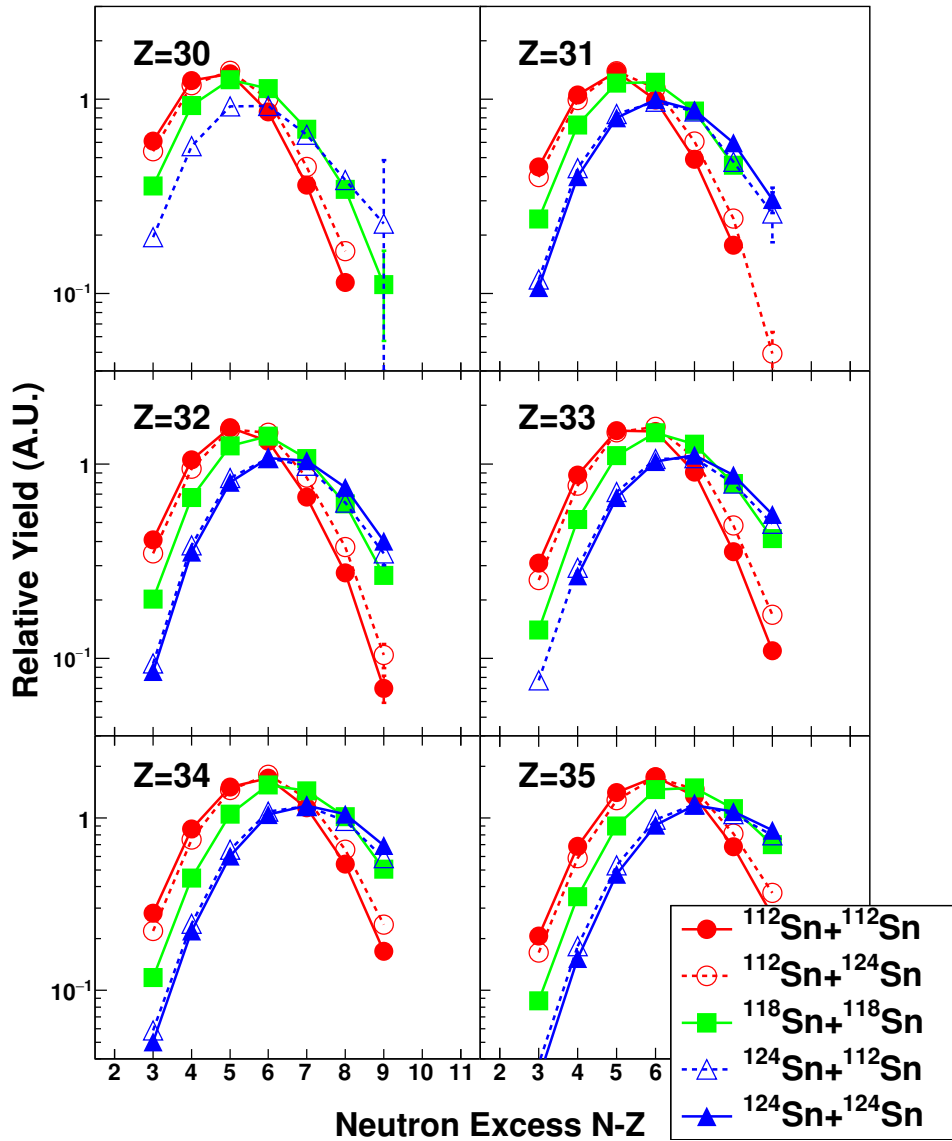


Figure 5.6 Isotopic yield distributions for five reaction systems, for $Z=30$ to $Z=35$. The data are corrected for the charge state contamination, but are not corrected for acceptance. Solid lines/filled circles represent symmetric reactions, and dotted lines/open circles represent the mixed reactions.

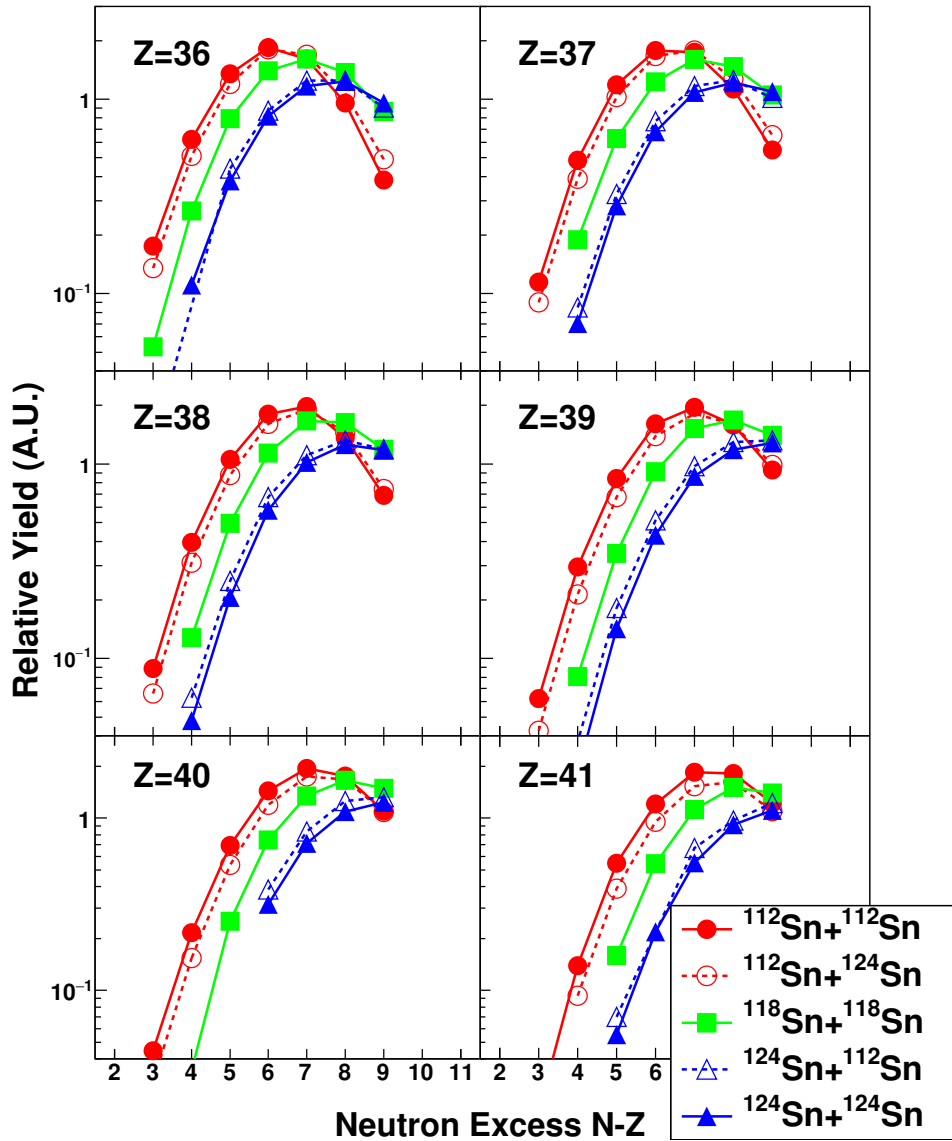


Figure 5.7 Isotopic yield distributions for five reaction systems, for $Z=35$ to $Z=41$. The data are corrected for the charge state contamination, but are not corrected for acceptance. Solid lines/filled circles represent symmetric reactions, and dotted lines/open circles represent the mixed reactions.

5.3 Yield Ratios and Isoscaling

To quantify the differences in the isotopic distributions between reaction systems, isoscaling can be used to condense the information from many data points into a single, physically meaningful quantity. In particular, the parameter that will be extracted for this analysis is the slope of the isotopic yield ratios, known as the “neutron isoscaling parameter”. (Defined in more detail in Section 2.3.1) By making a ratio of the isotopic distributions, microscopic effects such as binding energies and level densities are cancelled. The measured isoscaling ratios, with a fit to extract the slope for each individual element is shown in Figures 5.8 to 5.12. The last of these figures, for the $^{112}\text{Sn}+^{124}\text{Sn}$ reaction, is plotted in two panels for clarity because the slope of the yield ratios are small so neighboring elements would overlap.

The quantity that is important to extract is the slope of the lines shown in each figure. To extract a precise number it is important to address the non-linearities in the isoscaling ratio. In all the systems, when fitting a line to more than three isotopes, there is an obvious curvature so that the slope increases with higher N . The effect seems to be more pronounced for the lower mass fragments than for the higher mass fragments. Other studies of isoscaling have seen a similar effect. The non-linearity does affect the interpretation of the value of the isoscaling parameter α , as well as affecting the associated error bars, but the isospin transport ratio may not be affected, as is discussed in the next section.

The trend of the isoscaling parameter α with atomic number Z is shown in Figure 5.13. The data plotted in this figure are the fit parameters from the individual fits in Figures 5.8 to 5.12. The data for the $^{112}\text{Sn}+^{124}\text{Sn}$ system is divided into even and odd Z for clarity, because the values of α are small. These figures have not been corrected for the contamination due to charge states. To see the effect of the charge state correction, the isoscaling parameters

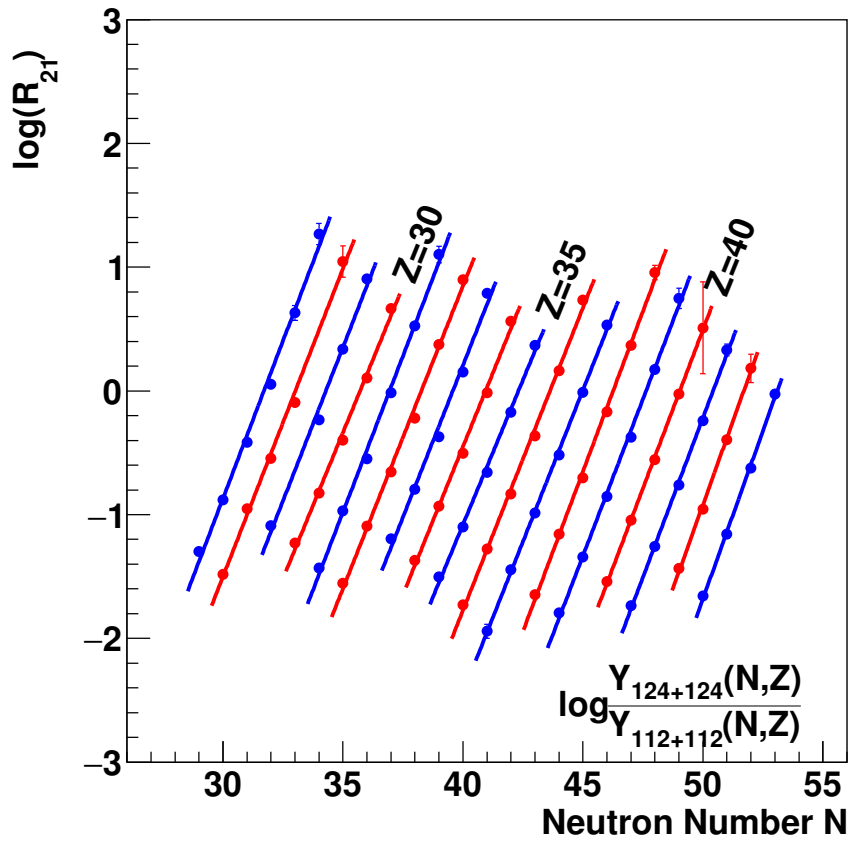


Figure 5.8 Neutron isoscaling ratio for $^{124}\text{Sn}+^{124}\text{Sn}$ with respect to $^{112}\text{Sn}+^{112}\text{Sn}$ for $Z=27$ to $Z=43$. The lines shown are linear fits to the data. Odd- Z are shown in blue, and even- Z are shown in red for clarity.

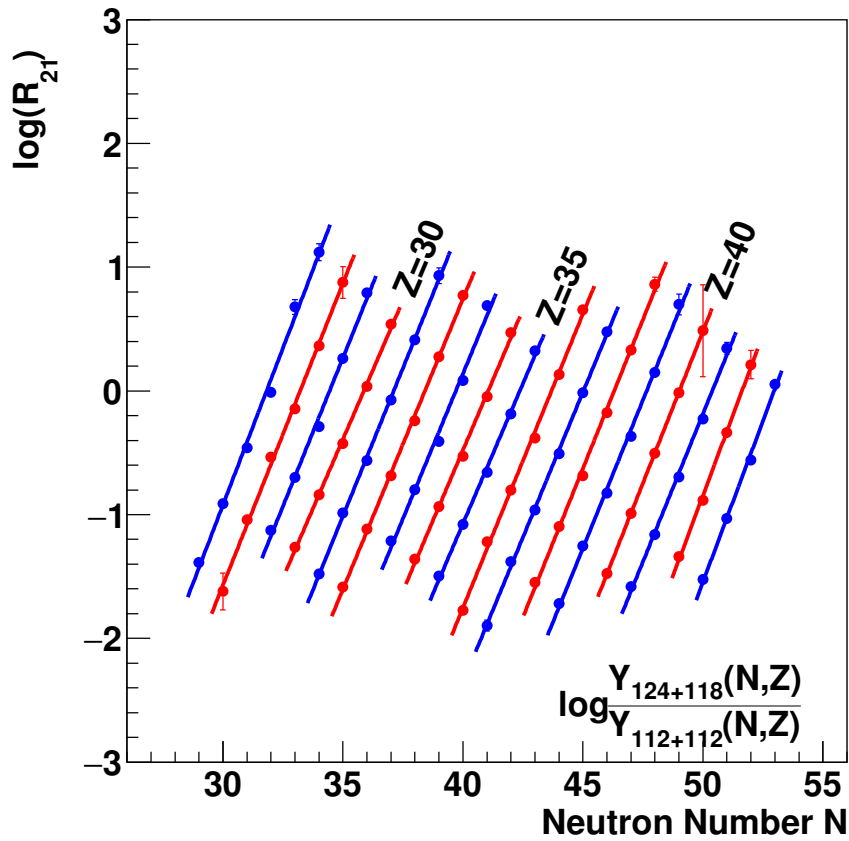


Figure 5.9 Neutron isoscaling ratio for $^{124}\text{Sn}+^{118}\text{Sn}$ with respect to $^{112}\text{Sn}+^{112}\text{Sn}$ for $Z=27$ to $Z=43$. The lines shown are linear fits to the data. Odd- Z are shown in blue, and even- Z are shown in red for clarity.

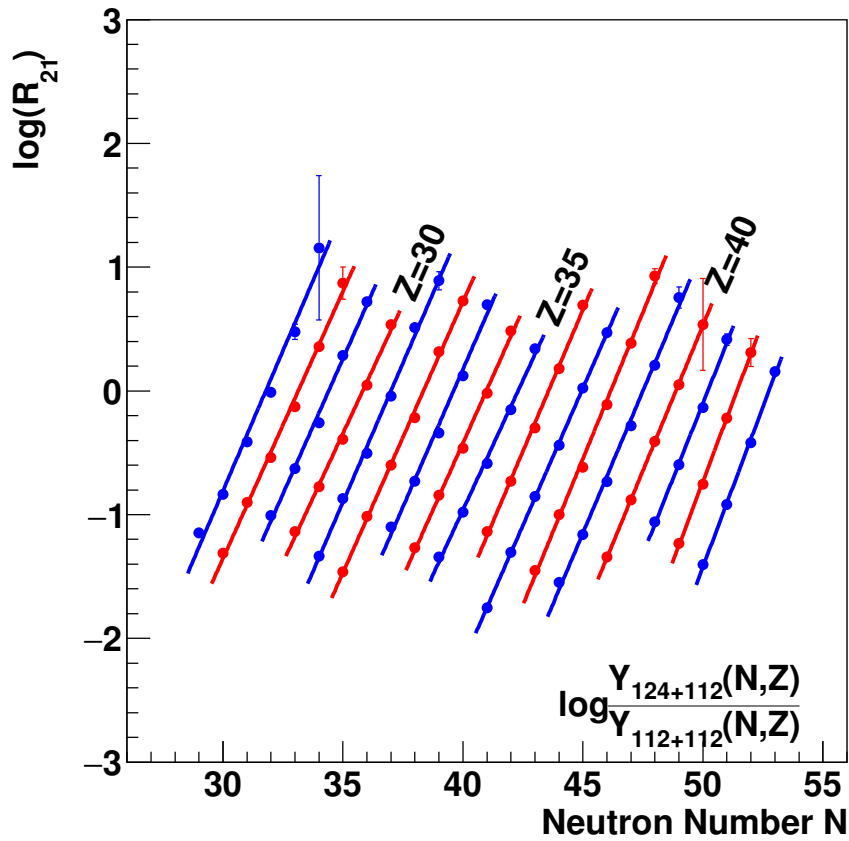


Figure 5.10 Neutron isoscaling ratio for $^{124}\text{Sn}+^{112}\text{Sn}$ with respect to $^{112}\text{Sn}+^{112}\text{Sn}$ for $Z=27$ to $Z=43$. The lines shown are linear fits to the data. Odd- Z are shown in blue, and even- Z are shown in red for clarity.

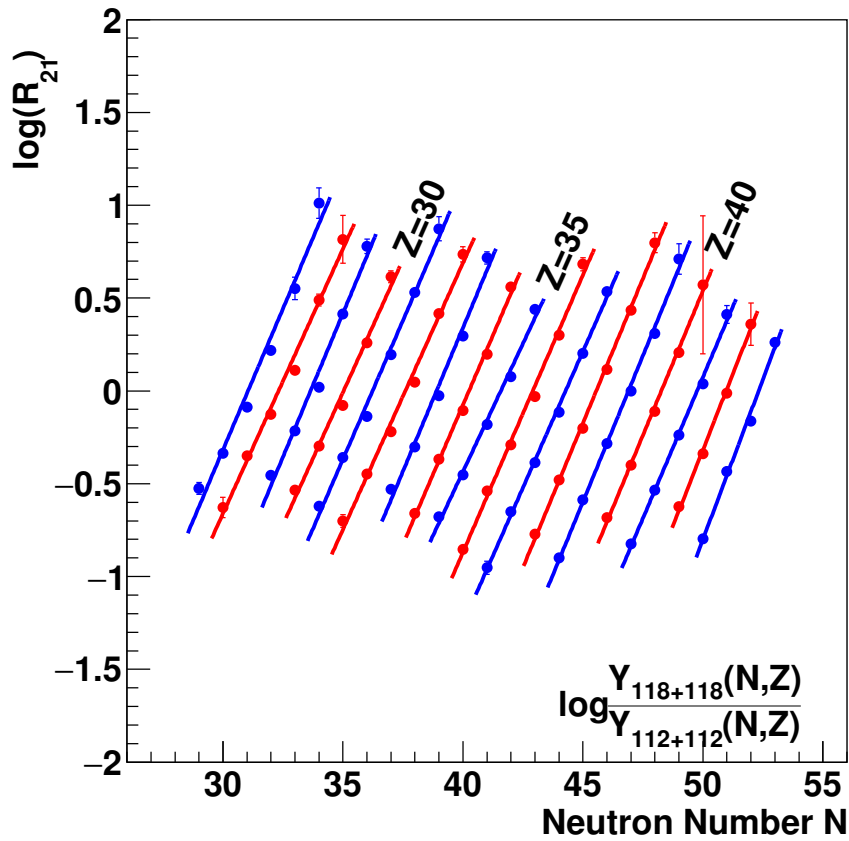


Figure 5.11 Neutron isoscaling ratio for $^{118}\text{Sn}+^{118}\text{Sn}$ with respect to $^{112}\text{Sn}+^{112}\text{Sn}$ for $Z=27$ to $Z=43$. The lines shown are linear fits to the data. Odd- Z are shown in blue, and even- Z are shown in red for clarity.

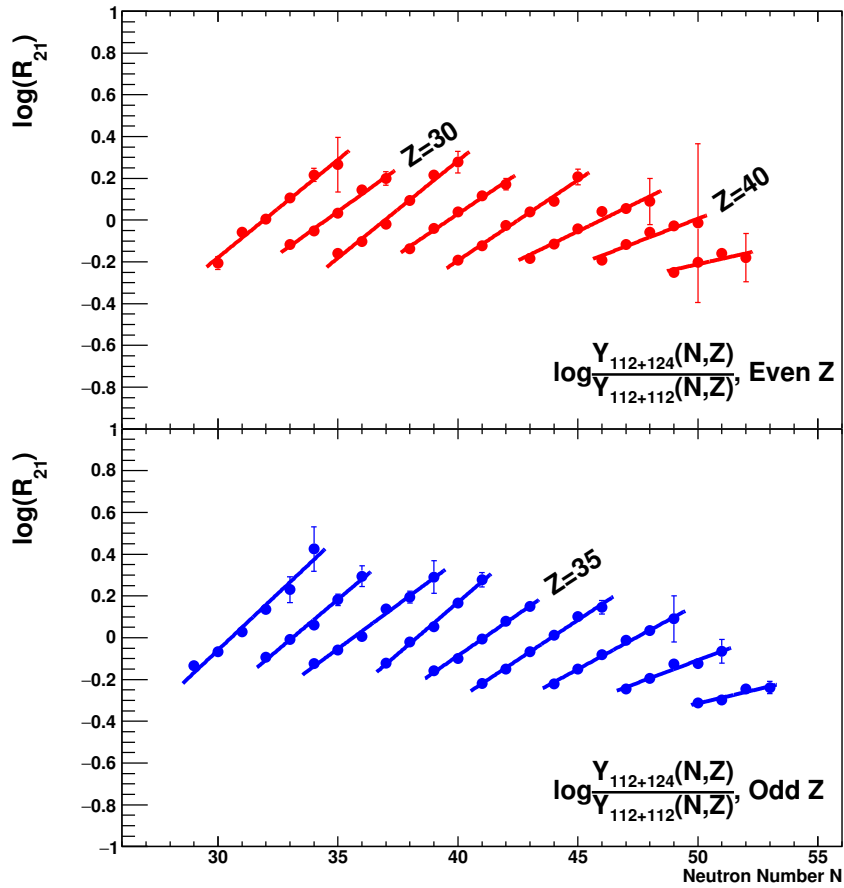


Figure 5.12 Neutron isoscaling ratio for $^{112}\text{Sn}+^{124}\text{Sn}$ with respect to $^{112}\text{Sn}+^{112}\text{Sn}$ for $Z=27$ to $Z=43$. The lines shown are linear fits to the data. Odd- Z are shown in blue in the lower panel, and even- Z are shown in red in the upper panel.

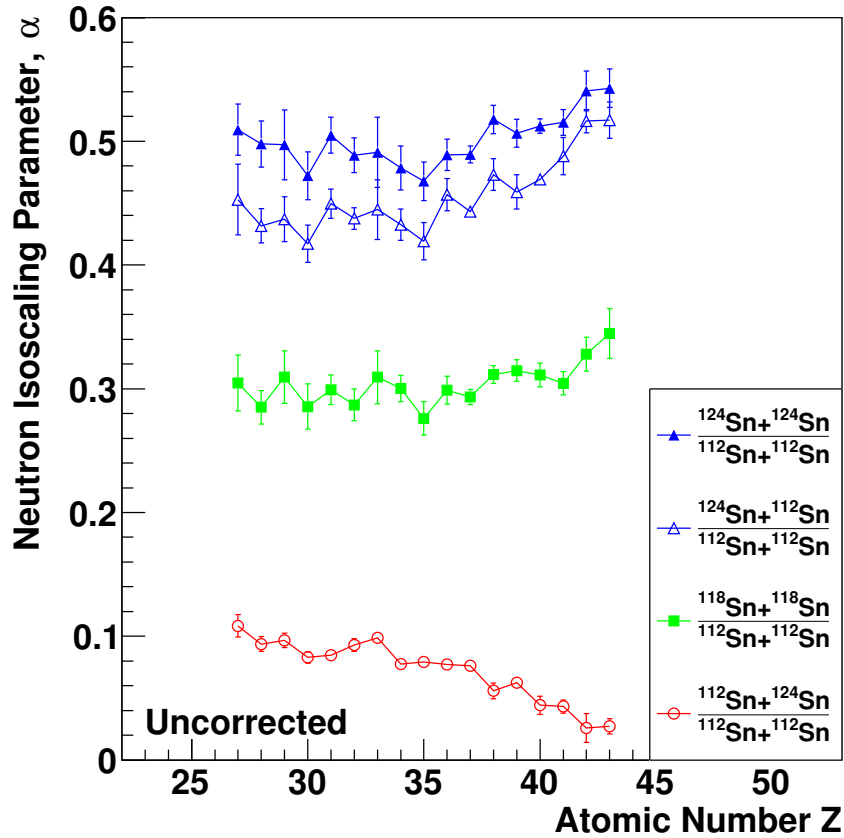


Figure 5.13 Neutron isoscaling parameter α for $^{112,124}\text{Sn}+^{112,124}\text{Sn}$ and $^{118}\text{Sn}+^{118}\text{Sn}$ for $Z=27$ to $Z=43$. No correction for charge state contamination is included.

obtained with corrected data are shown in Figure 5.14. The charge state correction causes an increase of α up to 10%. Because the charge state correction relies on an empirical calculation of the charge state effect, the correction introduces some systematic error into the absolute value of α . Fortunately, the correction has very little effect on the isospin transport ratio, which is discussed in Section 5.4.

The main source of error in the determination of α comes from the non-linear trend in the isoscaling ratios. Because of the non-linear trend, the slope is highly correlated with the choice of fit range. Sharp variations in the value of α as a function of Z are simply caused by changes in the range of isotopes that are measured. To demonstrate this effect,

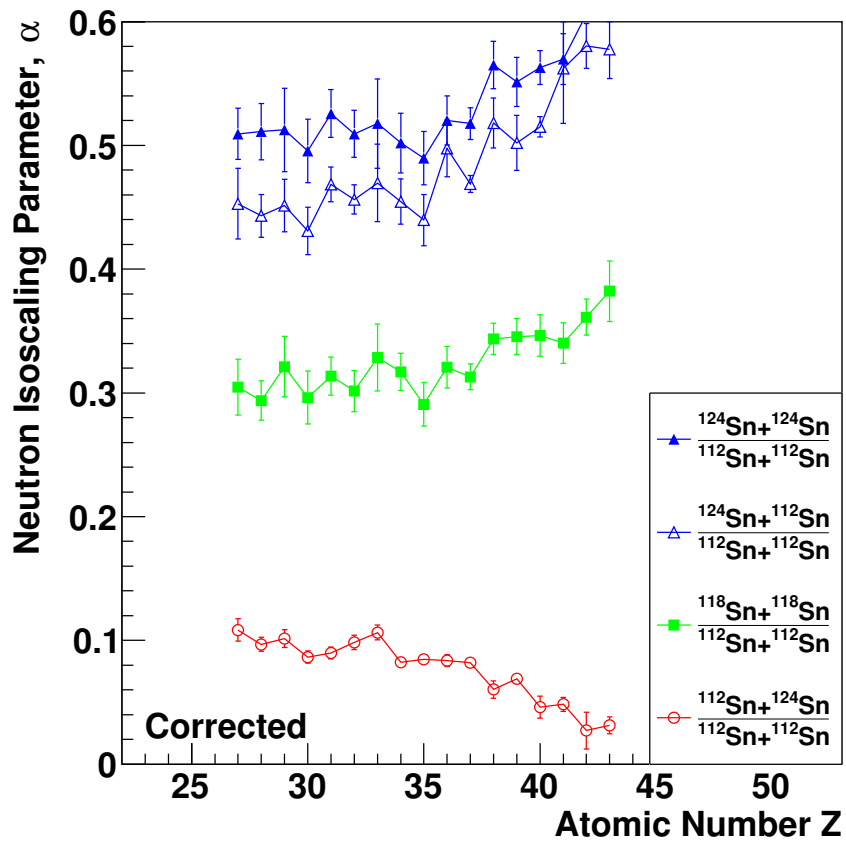


Figure 5.14 Neutron isoscaling parameter α for $^{112,124}\text{Sn}+^{112,124}\text{Sn}$ and $^{118}\text{Sn}+^{118}\text{Sn}$ for $Z=27$ to $Z=43$. The calculated correction for charge state contamination has been applied to the data.

in terms of α , the fit range can be modified by excluding a data point on either end of the fit range. Figure 5.15 shows how the choice of fit range affects the determination of alpha. Removing only one isotope changes the extracted value of alpha by as much as 5-10%. It is also clear from this figure that there is a similar effect for both reaction systems. This suggests that there is some systematic error (due to the non-linearity of the isoscaling ratio) that is similar for each system. One way this can be interpreted is that the primary emitting source has a range of different asymmetries that are correlated with the neutron excess, which is a probable consequence of measuring a system which has not reached complete equilibrium. Another possibility is that the effective temperature of these sources is slightly different. This is the claim made in [85], which suggests that the source temperature should be linearly dependent on the source asymmetry. Whether or not this is the case, fitting to a fixed range of isotopes would choose a certain temperature range, and this choice should be the same for each system. Section 5.4 will show that this choice does not significantly affect the isospin transport ratio.

Although there are several effects that can cause some change to the isoscaling parameter that is extracted from the data, the isospin diffusion effect can be clearly seen in the mixed systems, $^{112}\text{Sn}+^{124}\text{Sn}$ and $^{124}\text{Sn}+^{112}\text{Sn}$, shown in Figure 5.16. The general trend upward as a function of Z can be interpreted as the effect of a decreasing temperature for more peripheral collisions, because it is observed in the symmetric systems as well. In the more peripheral collisions, less nucleons are abraded from the projectile, resulting in a less excited nucleus. The fine structure, especially for the ^{124}Sn projectile, is a result of the effects of the different fit ranges for different Z. It will be shown that this fine structure, and the overall trend with Z is mostly canceled in the isospin transport ratio.

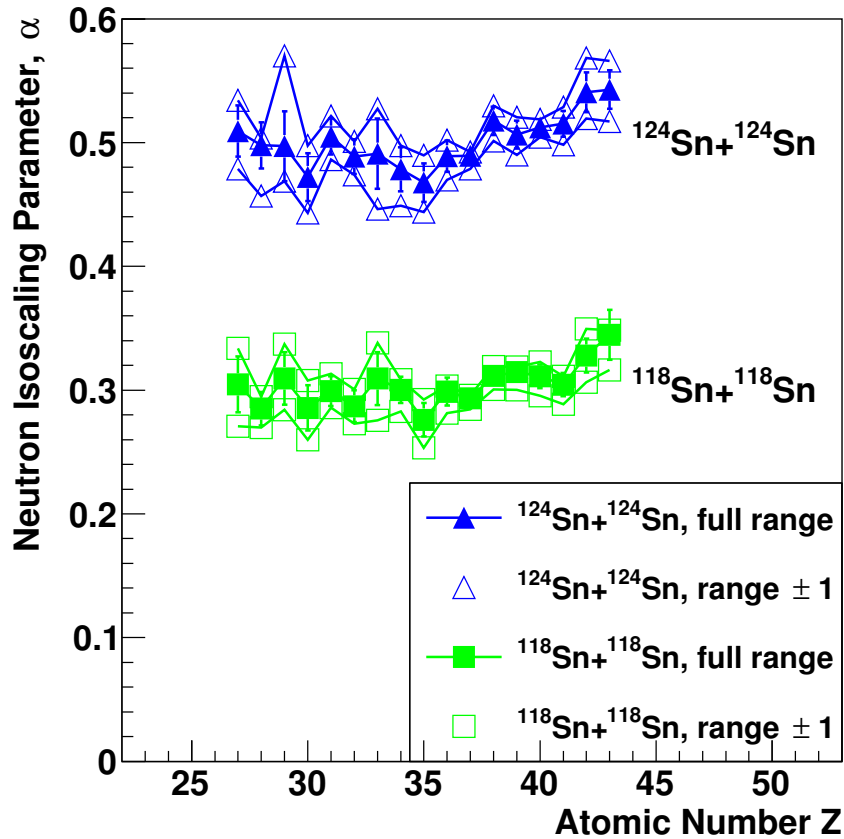


Figure 5.15 Neutron isoscaling parameter, α for $^{124}\text{Sn}+^{124}\text{Sn}$ and $^{118}\text{Sn}+^{118}\text{Sn}$ with respect to $^{112}\text{Sn}+^{112}\text{Sn}$, for $Z=27$ to $Z=43$, showing the effect of the choice of fit range. Solid symbols show the two symmetric reactions with the full fit range, while the open symbols show the result when one isotope is excluded at either end of the range. Excluding the lowest isotope increases the value of α , and excluding the highest isotope reduces the value of α . Only the two systems are shown for clarity.

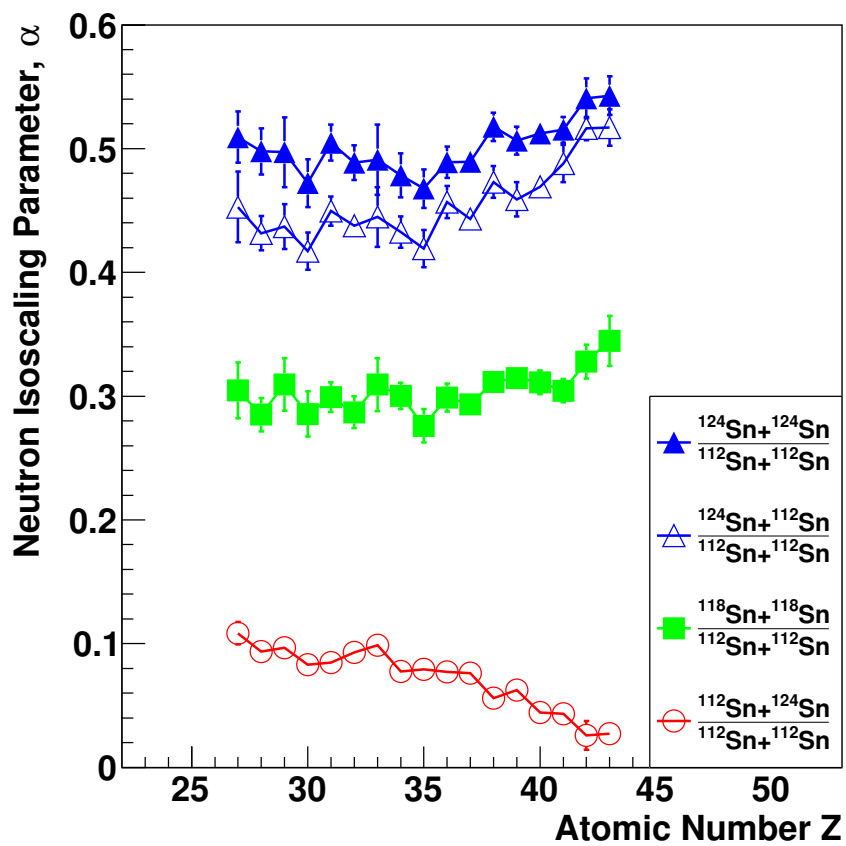


Figure 5.16 Neutron isoscaling parameter, α for $^{124}\text{Sn}+^{124}\text{Sn}$, $^{118}\text{Sn}+^{118}\text{Sn}$, $^{124}\text{Sn}+^{112}\text{Sn}$, and $^{112}\text{Sn}+^{124}\text{Sn}$ with respect to $^{112}\text{Sn}+^{112}\text{Sn}$, for $Z=27$ to $Z=43$.

Clearly, the isoscaling parameter α is sensitive to the isospin content of the system, but the precision of α alone is not adequate for this study. Although isoscaling is a phenomenon that is reproduced by many statistical models, the present study requires a dynamical transport model to understand the diffusion. Because of the computational difficulties with microscopic transport models, models such as ImQMD cannot be used to generate accurate isotopic distributions for heavy nuclei, so the isoscaling results cannot be compared to theory, directly. The next section will discuss how the parameter α can be used to form an isospin transport ratio, which is critical for a realistic comparison to theory.

5.4 Isospin Transport Ratio

The isospin transport ratio combines information (from isoscaling, in this case) from two symmetric systems and one mixed system to describe the degree of isospin equilibrium that the mixed system reached during the collision. In particular, the end goal is to understand the dynamics in the reaction between ^{112}Sn and ^{124}Sn , and how their differing isospin asymmetry affects the dynamics. In this experiment, the $^{118}\text{Sn}+^{118}\text{Sn}$ reaction is measured as well, which is relevant for the interpretation of the isospin diffusion data. Using the isospin transport ratio allows for a direct connection between physical observables and theoretical quantities, and is a simple, intuitive quantity. The isospin transport ratio is defined for the purposes of this experiment as:

$$R_I(X_{(112+124 \text{ or } 124+112)}) = \frac{2X_{(112+124 \text{ or } 124+112)} - (X_{(124+124)} + X_{(112+112)})}{X_{(124+124)} - X_{(112+112)}} \quad (5.6)$$

where the observable X is quantity that is either measured experimentally or calculated theoretically. In this case, the observable X is the isoscaling parameter α . Because isoscaling is a quantity that is determined from two reaction systems, this expression must be modified. The $^{112}\text{Sn}+^{112}\text{Sn}$ system is used as the reference, so dividing numerator and denominator by $X_{(112+112)}$ gives:

$$R_I(X_{(112+124 \text{ or } 124+112)}) = \frac{2\frac{X_{(112+124 \text{ or } 124+112)}}{X_{(112+112)}} - \left(\frac{X_{(124+124)}}{X_{(112+112)}} + 1\right)}{\frac{X_{(124+124)}}{X_{(112+112)}} - 1} \quad (5.7)$$

and recalling that the isoscaling parameter involves the logarithm of the yield ratios, the fractions on the right hand side can be replaced with the isoscaling parameter (and $\log(1) = 0$), giving:

$$R_I(X_{(112+124 \text{ or } 124+112)}) = \frac{2\alpha \left(\frac{112+124 \text{ or } 124+112}{112+112} \right) - \alpha \left(\frac{124+124}{112+112} \right)}{\alpha \left(\frac{124+124}{112+112} \right)} \quad (5.8)$$

which gives the expected values of -1 when the mixed reaction behaves like the $^{112}\text{Sn}+^{112}\text{Sn}$ reaction, and +1 when the mixed reaction behaves like the $^{124}\text{Sn}+^{124}\text{Sn}$. Practically, the isospin transport ratio is simply a linear transformation of an observable. There are other advantages that will be discussed further in this section.

There are several advantages to using the isospin transport ratio, that help to minimize the effect of several experimental problems. First, because the effect of charge state contamination has been calculated approximately, its effect on the isospin transport ratio can be estimated. As discussed in the previous section, the contamination amounts to a correction to α of up to 10%. Because the correction affects the different systems in a linear way, the correction has little effect on the isospin transport ratio. Figure 5.17 shows this effect, for the $^{118}\text{Sn}+^{118}\text{Sn}$ reaction. The correction to the isotopic yields is a smooth function and is mostly cancelled in constructing the isospin transport ratio. Because the main uncertainty in the charge state correction is the calculation from GLOBAL, which is the same for all systems and elements, so there is no indication that anything would change the cancellation of the correction. The correction is less than 0.02 for all Z , and because of the limited reliability of GLOBAL, this result is simply included as a systematic uncertainty of ± 0.02 .

In general, the biggest source of uncertainty in the determination of α is the non-linearity of the isoscaling ratio. There are various explanations for this non-linearity such as secondary

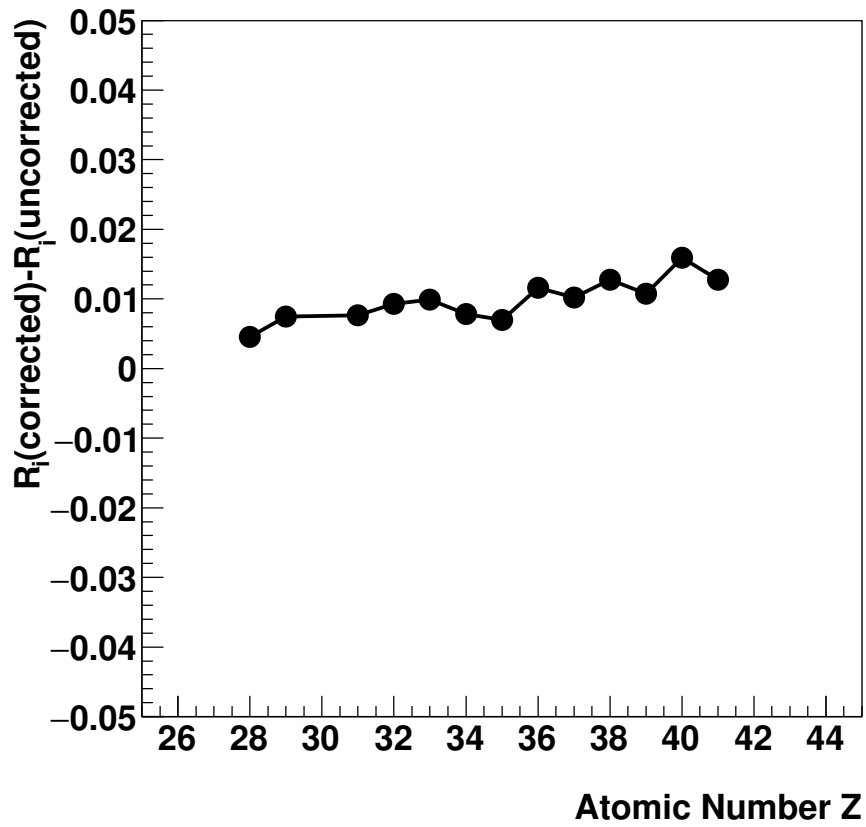


Figure 5.17 Correction for charge state contamination to the isospin transport ratio, calculated using the isoscaling parameter α for the $^{118}\text{Sn}+^{118}\text{Sn}$ reaction. The filled circles represent the difference between the corrected and the uncorrected result.

decay or differences in temperature of the emitting source. The non-linearity of the isoscaling ratio $\log(R_{21})$ is actually minor, but because it is systematically non-linear, there can be a systematic effect on the determined value of α . Although the systematic error in the determination of α is large, (see Figure 5.15) the effect on the isospin transport ratio is more subtle. Figure 5.18 shows the effect that the isoscaling fit range can have on the isospin transport ratio. Removing one isotope from the fit has an effect on the extracted R_i which is smaller than the propagated statistical error bars. Only the result for $^{118}\text{Sn}+^{118}\text{Sn}$ is shown, because the result does not depend strongly on the atomic number of the fragments used in the isoscaling fits. The effect on the isospin transport ratio is much smaller than the effect on the isoscaling parameter itself. The three options shown are for the full range of isotopes, and for removing one isotope from each end of the fit range. The variation between the three choices is less than the statistical error for each element, so there is no indication that the choice of fit range affects the isospin transport ratio, as long as the fit range is kept the same for each system. This is fortunate; it indicates that this observable is not very sensitive to the selection of fragments measured in the the experiment. More quantitatively, when taking an average of the points, the fit of the full range gives $R_i = 0.207 \pm 0.013$, while the sub-ranges give $R_i = 0.214 \pm 0.015$ and $R_i = 0.187 \pm 0.009$. Thus, the uncertainties that arise from the fit range are negligible.

5.4.1 Linearity of Isoscaling Observables

The measurement of the $^{118}\text{Sn}+^{118}\text{Sn}$ system gives important information about the validity of the isoscaling parameter as an isospin observable. In the simplest assumption, the $^{118}\text{Sn}+^{118}\text{Sn}$ system represents when the $^{124}\text{Sn}+^{112}\text{Sn}$ system has reached isospin equilibrium; if the ^{112}Sn and ^{124}Sn nuclei simply exchanged neutrons and no nucleons are lost. This

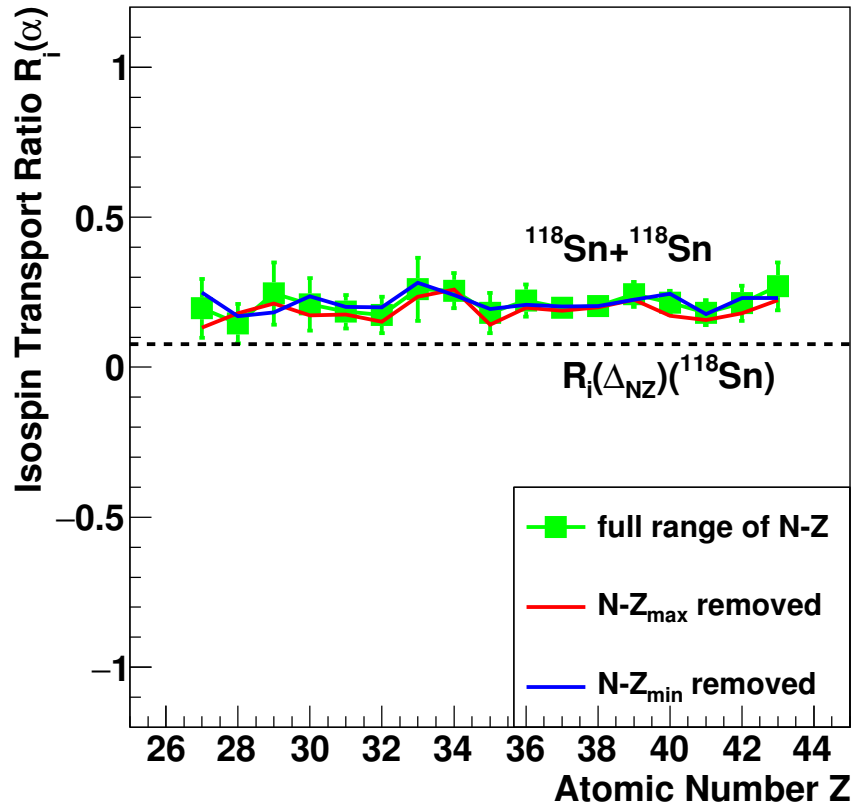


Figure 5.18 Isospin transport ratio, calculated using the isoscaling parameter α for the $^{118}\text{Sn} + ^{118}\text{Sn}$ reaction. Three different versions of the results are shown, with three different fit ranges used for the isoscaling ratio fitting. The green data points shows the result for the full fit range, while the red and blue lines indicate the result for removing the highest and lowest isotopes in the fit, respectively. The dashed line shows the value expected for R_i from the standard isoscaling relationships.

measurement helps to verify the important assumption: *does the isoscaling parameter have a linear relationship with the isospin asymmetry of the emitting source?* The isospin asymmetry of the primary fragments can be calculated in the ImQMD framework, but cannot be measured in experiment. The isoscaling parameter can be measured in the experiment, but cannot be easily calculated in the ImQMD framework. The isospin transport ratio allows these two variables to be compared directly, but only if they are linearly related to each other.

One consideration is the mass asymmetry of the different Sn isotopes. Because exchanging neutrons between the projectile and the target also changes the mass, the $^{118}\text{Sn}+^{118}\text{Sn}$ system is actually not halfway between $^{112}\text{Sn}+^{112}\text{Sn}$ and $^{124}\text{Sn}+^{124}\text{Sn}$, in terms of $\delta = \frac{N-Z}{A}$. In fact, when calculating R_i using only the δ of the Sn isotopes, the $^{118}\text{Sn}+^{118}\text{Sn}$ system would yield a value of $R_i = .051$ [45]. The value found in this study has been shown to be appreciably higher, $R_i = 0.207 \pm 0.013$. Actually, the isoscaling parameter has been assumed to have the following form, as derived in several statistical-type model frameworks [38]

$$\alpha_{21} = \frac{4C_{sym}}{T} \left(\left(\frac{Z_1}{A_1} \right)^2 - \left(\frac{Z_2}{A_2} \right)^2 \right) = \frac{4C_{sym}}{T} \Delta_{NZ} \quad (5.9)$$

where T is the temperature of the emitting source, and C_{sym} is the strength of the symmetry energy. No attempt is made here to deduce the temperature and extract C_{sym} , but this equation can give some insight into the dependence of α on the isospin content of the emitting source. The temperature confuses the situation until the isospin transport ratio is used, which cancels the T and C_{sym} , assuming that the temperatures reached in the different collisions are similar. However, α still depends on the difference of the square of Z/A between the two systems. Assuming this to be exactly true, the R_i that is obtained using Equation 5.9 should

be $R_i = 0.0762$. This expected quantity is shown as a dashed line in Figure 5.18. Although the discrepancy is outside of the error range for the experimental result, the relation between α and Δ_{NZ} is remarkably similar to expectations given the myriad of assumptions that must be made to derive Equation 5.9. This discrepancy must be addressed in order to compare the isospin diffusion results to ImQMD calculations.

One possibility is that the assumptions made when deriving Equation 5.9 do not hold. The first assumption was that the symmetry energy provided the main contribution to the neutron (proton) separation energy difference between the two systems. Assuming a statistical process created these fragments, the isoscaling parameter α (β) is equal to the difference in the neutron (proton) chemical potential between the two reactions, divided by the temperature. While different fragments detected in this study could come from different temperature, (removing more nucleons from the projectile results in higher excitation energy) the regular linear trend of the isoscaling ratios $\log(R_{21})$ implies that the temperature difference between the two reactions is small. Equation 5.9 was derived by taking the derivative of the binding energy with respect to neutron (proton) number assuming the symmetry energy is the main contribution. When comparing the symmetry, surface, and coulomb terms, the symmetry term makes up 98% of this neutron separation energy difference. More importantly, the separation energy difference is still linear with Δ_{NZ} when including the surface and coulomb terms. In the case of the proton isoscaling parameter β , the contributions from coulomb and surface effects are slightly larger, but the trend is still mostly linear as well. This part of the analysis does not seem to be the cause of this non-linearity.

Another possibility is that the preequilibrium emission strongly affects the asymmetry of the projectile-like fragment in the early part of the reaction. The isoscaling parameter reflects the asymmetry of the primary fragment at the point that the reaction becomes

a statistical thermodynamic process. Nucleons that are emitted early during the collision would not affect this observable. Because neutrons are not measured, this effect can only be predicted by calculations.

A third possibility is that the α measured for $^{124}\text{Sn}+^{124}\text{Sn}$ with respect to $^{112}\text{Sn}+^{112}\text{Sn}$ is modified by secondary decay of fragments more strongly than the alpha for $^{118}\text{Sn}+^{118}\text{Sn}$ with respect to $^{112}\text{Sn}+^{112}\text{Sn}$. This would happen, for instance, if secondary decay affected the yields for $^{124}\text{Sn}+^{124}\text{Sn}$ more than the other two reactions. Because secondary decay brings the final isotopic distributions closer together, it decreases the magnitude of α and β .

This effect can be examined in the ImQMD framework as well. ImQMD does not include the effects of secondary decay, the results only give insight into the primary fragment yields. The isospin asymmetry, averaged over all fragments with $Z > 20$, is plotted in Figure 5.19. The calculation shown is with ImQMD-Sky with four parameter sets, and the impact parameter is $b = 10$ fm. This result shows that the average asymmetry of the primary fragments is predicted (in ImQMD-Sky) to be linearly correlated with the projectile asymmetry for the symmetric reactions, regardless of the interaction used. The requirement of $Z > 20$ does not much affect the result in this case, because for such a peripheral reaction, very few large fragments are created with $Z < 30$.

While the effects of secondary decay are not included in ImQMD, and are not calculated here, the effect can be understood in a qualitative way. When measuring isoscaling, the yield of a specific isotope is compared to the same isotope in another reaction. The events that result in this certain isotope being measured have very different histories in one reaction versus another. There are two main effects that would cause the reaction to progress differently, but arrive at the same measured fragment. First, the mass of the Sn projectiles are different; to form a primary fragment of mass number 85 requires removing 27 nucleons from ^{112}Sn

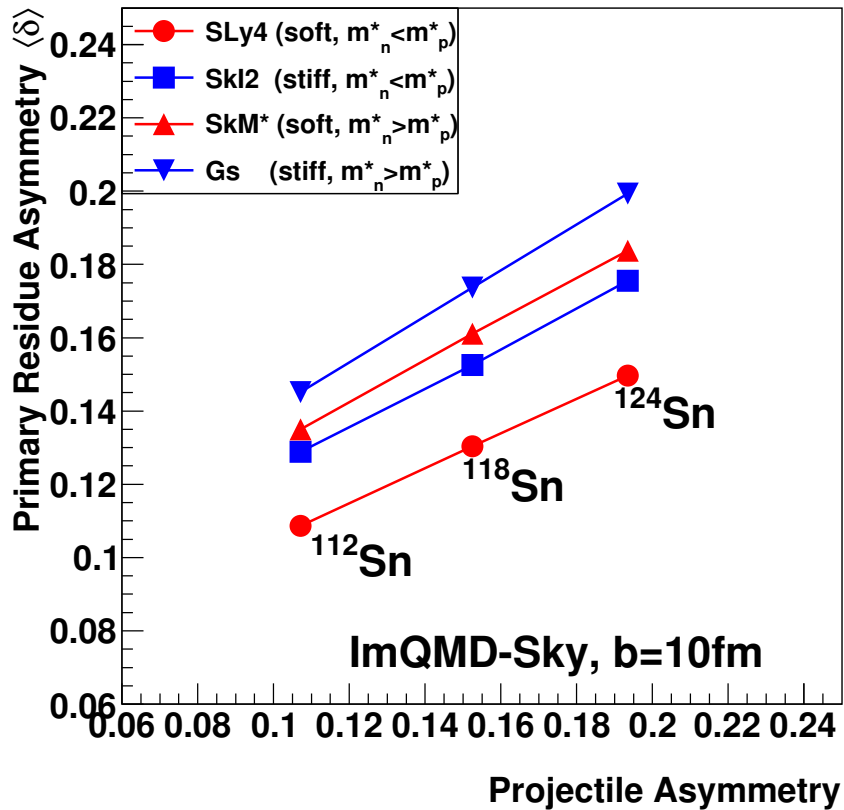


Figure 5.19 Primary residue asymmetry, calculated using ImQMD-Sky with the four parameter sets detailed in 2.4, plotted against the asymmetry of the projectile, for the three symmetric reactions $^{112}\text{Sn}+^{112}\text{Sn}$, $^{118}\text{Sn}+^{118}\text{Sn}$, $^{124}\text{Sn}+^{124}\text{Sn}$, for impact parameter $b = 10$ fm. The calculated asymmetry is the asymmetry for fragments with $Z > 20$, averaged over all events.

but requires removing 39 nucleons from ^{124}Sn . Therefore, the higher mass projectile would create a larger temperature and excitation energy. Then, the nucleus with a higher temperature would require more particle emission to decay to its final state. This would affect the comparison between the $^{118}\text{Sn}+^{118}\text{Sn}$ and $^{112}\text{Sn}+^{112}\text{Sn}$ reactions to a similar degree that it would affect the comparison between the $^{124}\text{Sn}+^{124}\text{Sn}$ and $^{118}\text{Sn}+^{118}\text{Sn}$ reactions, so the temperature difference alone would not lead to this non-linearity.

Once it is established that the different systems require different amounts of secondary decay, it follows that to measure fragments of the same (N,Z) in the different reactions, they must have originated from different primary fragments. In general, evaporation of nucleons has been shown to cause the system to approach an “Evaporation Attractor Line” (EAL), where the decay widths of protons and neutrons become equal [86]. As the decay process brings the system closer to the EAL, the driving force decreases, and the system approaches the EAL asymptotically. In general, how close the system gets to the EAL is directly related to the excitation energy. Because the higher-mass projectile would begin with hotter, more massive primary fragments to get to the same final isotope, the average asymmetry would be pushed more towards the EAL. This will be investigated in the future by using a decay model to study the de-excitation of the residues.

The result of this examination of the results from the $^{118}\text{Sn}+^{118}\text{Sn}$ system shows that the information from the third symmetric system is very helpful to understand the isoscaling parameter obtained in the mixed systems. The R_i obtained from the $^{118}\text{Sn}+^{118}\text{Sn}$ reaction in both experiment and in the calculations is nonzero, so some correction should be made before comparing the isospin transport ratios. Although the precise functional form of the relationship between α and δ is unknown, assuming the effect is smooth and continuous, a

quadratic correction can be used. A modified isospin transport ratio R_i^* can be defined as:

$$R_i^*(X) = R_i(X) + R_i(X_{eq}) \left(R_i(X)^2 - 1 \right) \quad (5.10)$$

where X_{eq} is the observable measured in the $^{118}\text{Sn}+^{118}\text{Sn}$ reaction. This expression still yields \pm for the $^{124}\text{Sn}+^{124}\text{Sn}$ and $^{112}\text{Sn}+^{112}\text{Sn}$ reactions, but uses the freedom in the quadratic term to put $^{118}\text{Sn}+^{118}\text{Sn}$ at $R_i^*(X_{eq}) = 0$. The purpose of developing the isospin transport ratio was to allow for a more direct comparison between experiment and theory. One result of this experiment, shown in this section, was to investigate how the isoscaling parameter depends on the asymmetry of the emitting source. This assumption turns out to be approximately true, although there is a non-linear effect on the order of 10%, which is remarkable considering the many assumptions made. To attempt to make a more precise measurement, the modified isospin transport ratio will be described in the next section.

5.4.2 Isospin Diffusion Results

One purpose of this measurement was to understand how the dynamics during collisions of heavy ions at intermediate energies are affected by changing the isospin asymmetry of the reaction system. In particular, *how does the isotopic distribution of heavy fragments change?* In Section 5.2, the isotopic distributions are shown, and there is a clear shift in the peaks of the isotopic distribution between the symmetric systems and the mixed systems. This is shown more clearly using the isospin transport ratio in Figure 5.20. The magnitude of the difference between the symmetric system and the mixed system, describes how much “diffusion” has occurred. As discussed in the previous section, the isoscaling parameter has some non-linear behavior with respect to the isospin asymmetry. For the same reason that

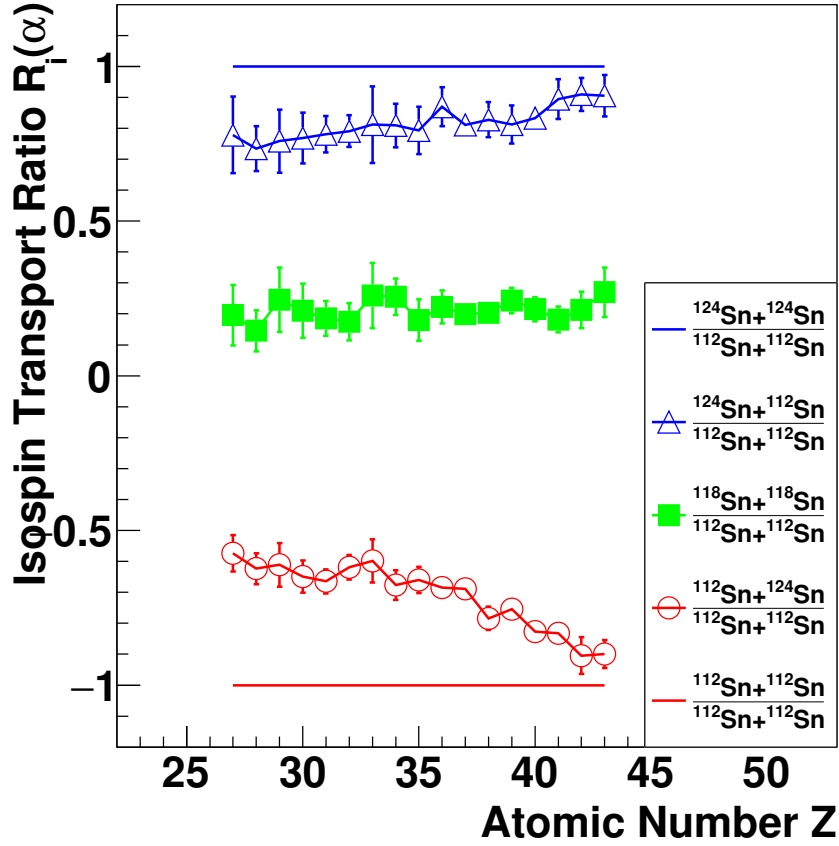


Figure 5.20 Isospin transport ratio, calculated using the isoscaling parameter α using 5 measured reactions.

the $^{118}\text{Sn}+^{118}\text{Sn}$ system gives $R_i > 0$, the two mixed systems in Figure 5.20 give results that are asymmetric about zero.

The striking feature of this result is that the absolute value of $R_i(\alpha)$ increases for increasing Z , meaning that the diffusion decreases for increasing Z . This is an expected feature, because larger Z fragments result from more peripheral collisions where the projectile and target will be in contact for a shorter time, resulting in less diffusion. The ImQMD simulations predict that the amount of diffusion should be at least similar in the two mixed reactions, so before comparing to the calculations, the nonlinearity of $R_i(\alpha)$ must be removed. Using the average value of R_i for the $^{118}\text{Sn}+^{118}\text{Sn}$ system, the modified isospin

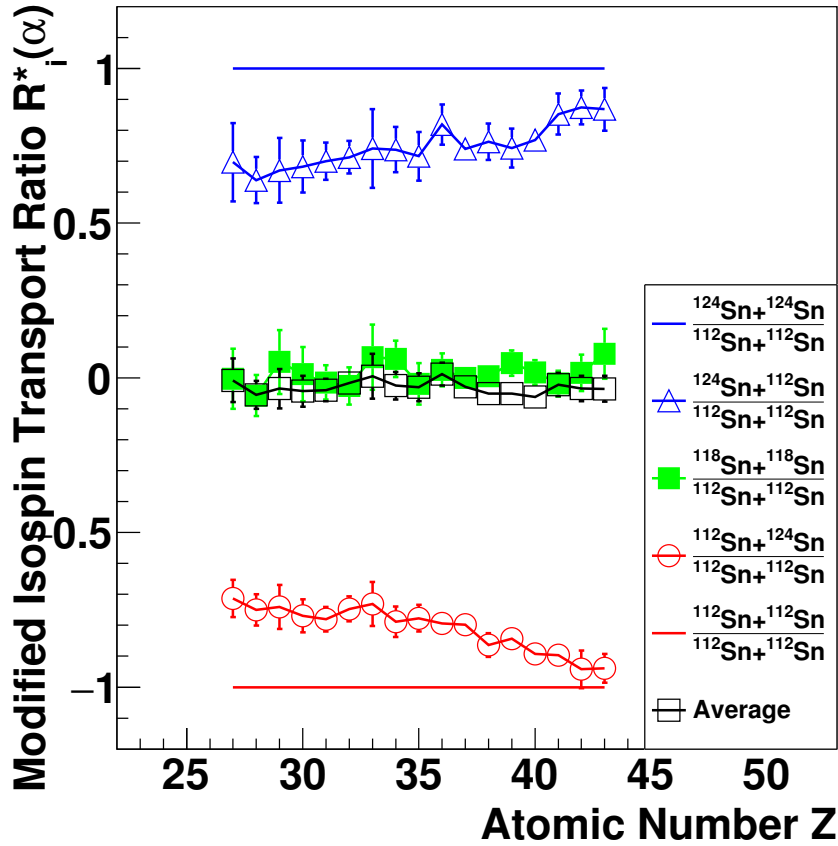


Figure 5.21 Modified isospin transport ratio, calculated using the isoscaling parameter α using 5 measured reactions. The black open squares are the average of the two mixed systems.

transport ratio establishes the expected symmetry, shown in Figure 5.21. The values are transformed from the standard isospin transport ratio using the average value of $R_i(\alpha)$ for $^{118}\text{Sn}+^{118}\text{Sn}$, so the green squares are centered at $R_i^*(\alpha) = 0$ by design. The average of the two mixed systems is shown as well. The average is close to $R_i^*(\alpha) = 0$, but is measurably lower, $R_i^*(\alpha) = -0.036 \pm 0.008$. This is either an indication that the correction being made does not have the simple quadratic form that is assumed for R_i^* , or that the two mixed systems exhibit a different amount of isospin diffusion. Either of those explanations is possible, so this difference is a measure of the systematic error in the final results.

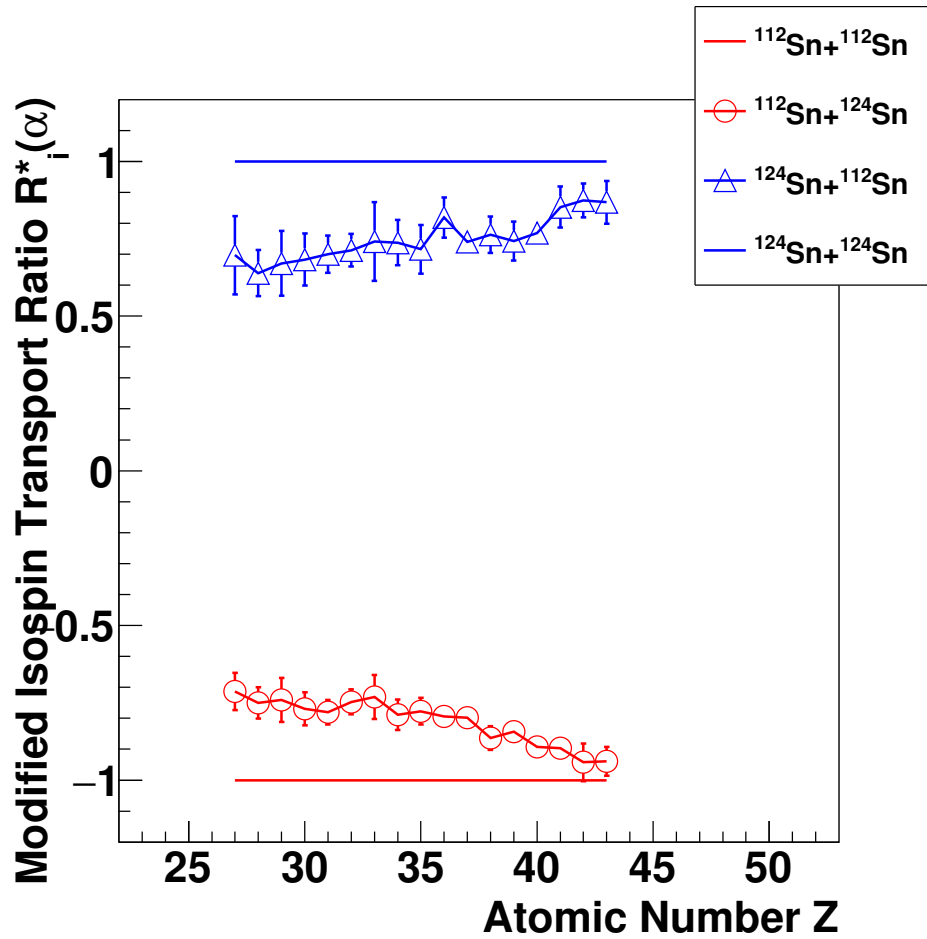


Figure 5.22 Modified Isospin Transport Ratio vs. Atomic Number Z, for the two mixed reactions, $^{124}\text{Sn}+^{112}\text{Sn}$ and $^{112}\text{Sn}+^{124}\text{Sn}$.

The final isospin diffusion result using the modified isospin transport ratio is shown in Figure 5.22. The $^{124}\text{Sn}+^{112}\text{Sn}$ system shows a slightly larger extent of isospin diffusion than the $^{112}\text{Sn}+^{124}\text{Sn}$ system. This dependence could result from the simple correction applied for the nonlinearity of α . This asymmetry could also result from the two systems having slightly different impact parameters.

Z	R_i $^{112}\text{Sn}+^{124}\text{Sn}$	R_i $^{118}\text{Sn}+^{118}\text{Sn}$	R_i $^{124}\text{Sn}+^{112}\text{Sn}$	R_i^* $^{112}\text{Sn}+^{124}\text{Sn}$	R_i^* $^{118}\text{Sn}+^{118}\text{Sn}$	R_i^* $^{124}\text{Sn}+^{112}\text{Sn}$
27	-0.57±0.059	0.2±0.097	0.78±0.12	-0.71±0.06	-0.0033±0.098	0.7±0.13
28	-0.62±0.05	0.15±0.066	0.73±0.072	-0.75±0.051	-0.057±0.066	0.64±0.074
29	-0.61±0.07	0.25±0.1	0.76±0.1	-0.74±0.072	0.051±0.1	0.67±0.1
30	-0.65±0.053	0.21±0.088	0.77±0.082	-0.77±0.054	0.012±0.088	0.68±0.084
31	-0.66±0.039	0.19±0.056	0.78±0.059	-0.78±0.039	-0.015±0.056	0.7±0.061
32	-0.62±0.04	0.17±0.06	0.79±0.051	-0.75±0.04	-0.027±0.06	0.71±0.053
33	-0.6±0.07	0.26±0.11	0.81±0.12	-0.73±0.071	0.067±0.11	0.74±0.13
34	-0.68±0.048	0.26±0.058	0.81±0.071	-0.79±0.049	0.061±0.059	0.74±0.073
35	-0.66±0.042	0.18±0.067	0.79±0.077	-0.78±0.043	-0.02±0.067	0.72±0.079
36	-0.68±0.035	0.22±0.053	0.87±0.063	-0.79±0.035	0.025±0.053	0.82±0.065
37	-0.69±0.02	0.2±0.029	0.81±0.021	-0.8±0.021	-0.00031±0.029	0.74±0.021
38	-0.78±0.037	0.2±0.036	0.83±0.057	-0.86±0.038	0.005±0.036	0.76±0.059
39	-0.75±0.03	0.24±0.041	0.81±0.062	-0.84±0.03	0.048±0.041	0.74±0.063
40	-0.83±0.032	0.22±0.039	0.83±0.017	-0.89±0.033	0.017±0.039	0.77±0.018
41	-0.83±0.034	0.18±0.042	0.89±0.065	-0.9±0.035	-0.019±0.042	0.85±0.067
42	-0.9±0.059	0.21±0.059	0.91±0.053	-0.94±0.061	0.015±0.059	0.87±0.055
43	-0.9±0.045	0.27±0.08	0.91±0.067	-0.94±0.046	0.078±0.08	0.87±0.069

Table 5.2 Isospin Transport Ratio and Modified Isospin Transport Ratio results, tabulated as a function of atomic number Z . These data are plotted in Figures 5.20 to 5.22.

When constructing a comparable observable from the ImQMD calculations, the biggest uncertainty is the ambiguity in reproducing the impact parameter dependence. When simulating these collisions with ImQMD, computing resources are a limiting factor. As a result, these calculations were only done for impact parameters of $b = 6$ fm, $b = 9$ fm, and $b = 10$ fm. A more thorough study would be to generate collisions with a weighted distribution of impact parameter. This would allow for a more detailed comparison of how the observables depend on the impact parameter selection, or equivalently, which range of Z a calculation should be compared to. More calculations are being done to establish this dependence, but are not available for this study.

Since the experimental R_i is formed by comparing results with a constant Z , the calculation must be constructed the same way. Fortunately, a fixed impact parameter results in similar range of Z in each system, because the projectiles have equal charge. Figure 5.23 shows an example of the results for the SLy4 skyrme parameter set, for two impact parameters. For a fixed b , the mixed systems have a different average Z than the symmetric system of the same projectile by about 1 unit of charge. This may be explained by the difference in the radii of the different isotopes of Sn; a bigger target abrades more nucleons. Another important trend is that the slope of the asymmetry in the mixed systems with Z is different from the symmetric systems. This is also expected, because the amount of diffusion should increase with decreasing impact parameter. The combination of these two trends results in a systematic shrinking of the isospin transport ratio so that $\Delta < \delta > \neq \Delta\delta_Z$ for both mixed systems and for any Z . The data compare the same Z in two reactions, whereas the calculations compare same impact parameter in two reactions. This effect should be addressed when comparing the ImQMD results to the data. Although the detailed observables, such

as the Z distribution may not be reproduced by ImQMD, there will be a similar effect in the real data.

Figure 5.24 shows how different R_i result from using either the average asymmetry, $\langle \delta \rangle$, for a fixed impact parameter or using the asymmetry for a fixed Z, δ_Z . The difference is largest ($\approx 15\%$ more diffusion) for the SLy4 parameter set, which predicts the largest isospin diffusion signal. To accurately account for this effect, more ImQMD calculations are needed at impact parameters from 7fm to 12fm. The result using only the calculations at 6fm and 10fm shows the behavior qualitatively, but is not robust enough to form a constraint on the symmetry energy.

Figure 5.25 shows the resulting $R_i(\delta_Z)$ when the impact parameter dependence is included, for the four skyrme parameter sets used in this study. Only the calculation for the $^{124}\text{Sn}+^{112}\text{Sn}$ reaction is shown for clarity. The effect of the density dependence of the symmetry energy is clearly demonstrated. SkI2 has a “stiff” density dependence of the symmetry energy, which means that the symmetry energy is smaller at subsaturation density. A smaller symmetry energy results in less diffusion because the driving force in the low density neck region would be weaker. A skyrme set with a “soft” symmetry energy produces more diffusion. The SLy4 interaction has a soft symmetry energy but a similar momentum dependence as the SkI2 interaction, and the diffusion is accordingly larger for SLy4. The effect of the different momentum dependent interactions used is shown, reflected by the different effective mass splitting. Because the skyrme parameter sets have many parameters which are simultaneously fit to data, it is difficult to isolate the effect of one aspect of the physics. The different effective mass splitting is obscured by the fact that the isoscalar effective mass is simultaneously changing. To understand the relationships between the various interaction properties, the covariance analysis is described in [87].

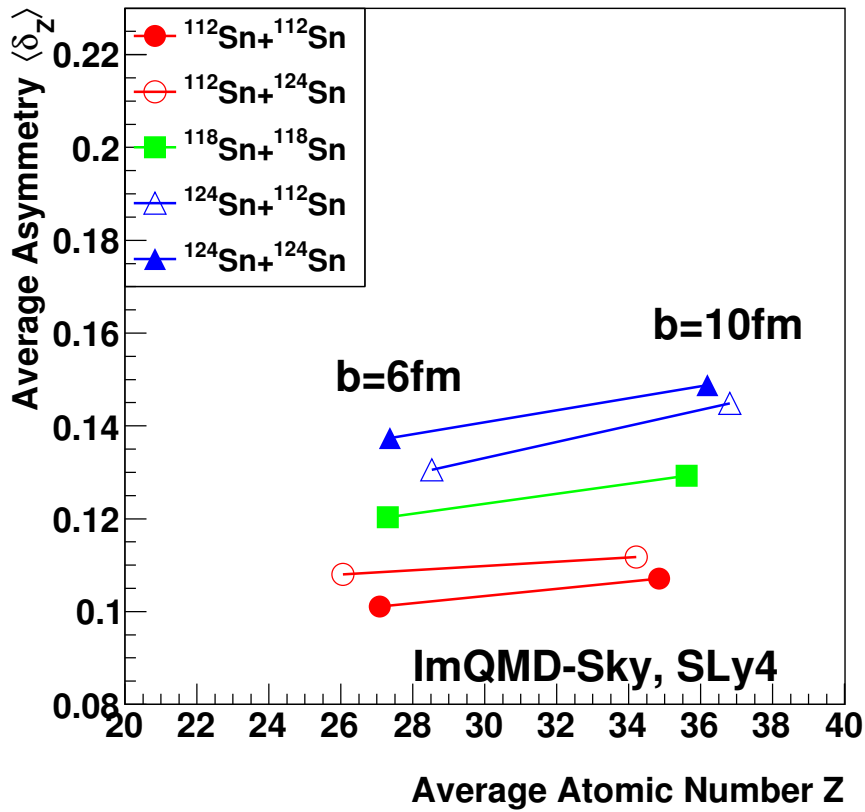


Figure 5.23 Primary residue asymmetry, calculated using ImQMD-Sky with the SLy4 parameter set (soft symmetry energy), plotted against the average Z of the resulting projectile-like fragment, for the reactions $^{112}\text{Sn} + ^{112}\text{Sn}$, $^{112}\text{Sn} + ^{124}\text{Sn}$, $^{118}\text{Sn} + ^{118}\text{Sn}$, $^{124}\text{Sn} + ^{112}\text{Sn}$, $^{124}\text{Sn} + ^{124}\text{Sn}$, for impact parameters $b = 10\text{fm}$ and $b = 6\text{fm}$.

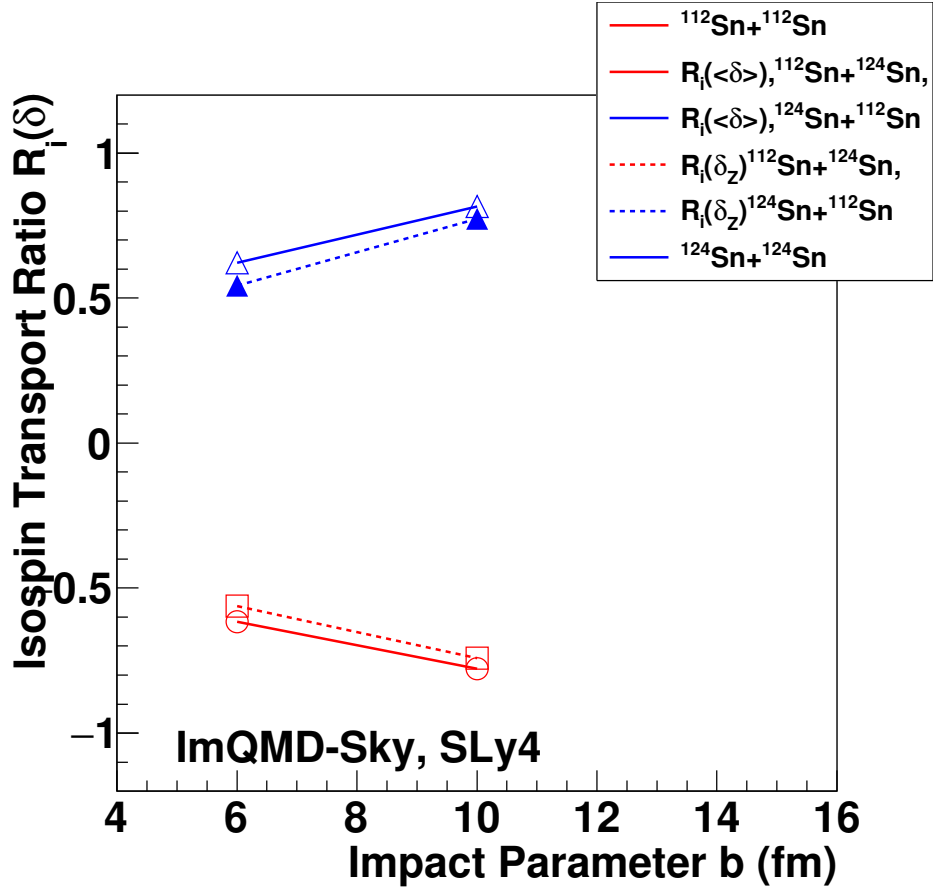


Figure 5.24 Isospin Transport Ratio, calculated using ImQMD-Sky with the SLy4 parameter set (soft symmetry energy), plotted against the impact parameter. The reactions ${}^{112}\text{Sn}+{}^{112}\text{Sn}$, ${}^{112}\text{Sn}+{}^{124}\text{Sn}$, ${}^{124}\text{Sn}+{}^{112}\text{Sn}$, ${}^{124}\text{Sn}+{}^{124}\text{Sn}$ are shown. The solid lines are calculated using the average values of δ for a fixed b , and the dashed lines are calculated using the average values of δ for a fixed Z .

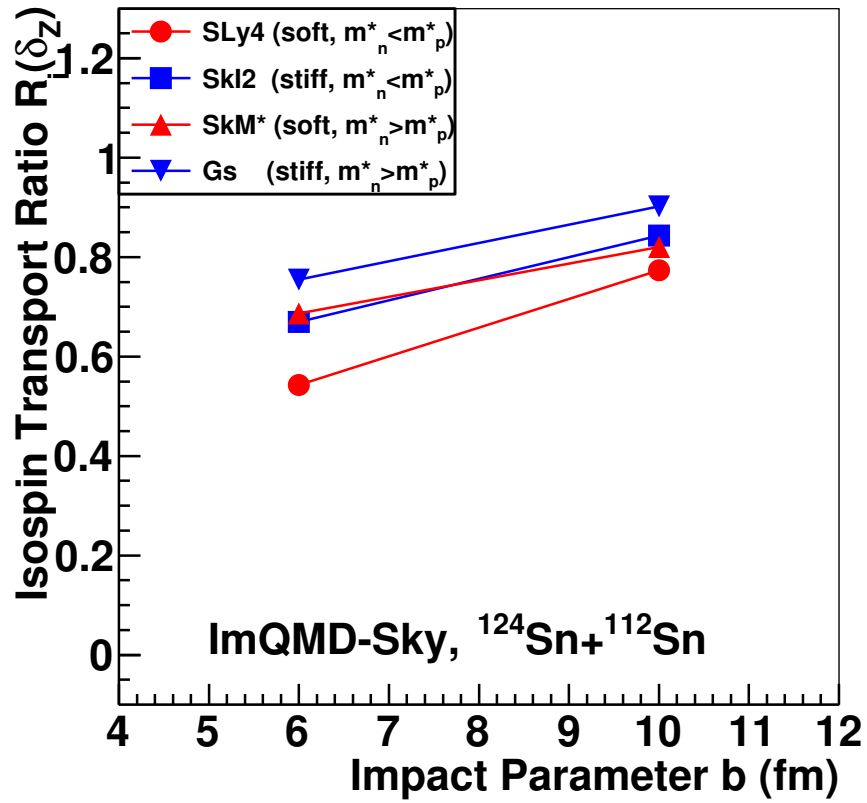


Figure 5.25 Isospin Transport Ratio, calculated using ImQMD-Sky with four Skyrme parameter sets, plotted against the impact parameter, for the $^{124}\text{Sn}+^{112}\text{Sn}$ reaction, for impact parameters $b = 10\text{fm}$ and $b = 6\text{fm}$.

The ImQMD-Sky model provides some insight into the physics, but to isolate the effect of the density dependence of the symmetry energy, ImQMD05 is used. For ImQMD05, the interaction portion of the nuclear symmetry energy is described by a simple power law, $S_i(\rho) = S_{i,0} \left(\frac{\rho}{\rho_0}\right)^\gamma$. These calculations were done for $b = 6$ fm, $b = 9$ fm, and $b = 10$ fm, but only the $^{112}\text{Sn}+^{124}\text{Sn}$ mixed system was calculated for $b = 6$ fm. Using this limited number of impact parameters, a linear dependence on Z for R_i can be generated from the model calculations. This is shown in Figure 5.26. There is a dependence of R_i on the stiffness of the symmetry energy term, so the experimental R_i should allow for a constraint on the exponent γ .

This diffusion result can be compared to the calculations, although a detailed comparison will be done when more calculations are available. The available calculations (shown in Figure 5.26) are plotted with the data for the $^{112}\text{Sn}+^{124}\text{Sn}$ system in Figure 5.27. The impact parameter calibration for the $^{112}\text{Sn}+^{112}\text{Sn}$ system is used, and the error region corresponds to an error in the average Z of ± 2.5 units.

The preliminary comparison suggests a density dependence of $\gamma \approx 1.0$. The previously measured constraints from isospin diffusion were $\gamma = 0.75 \pm 0.25$. The preliminary results may be consistent with these previous studies. Until more theoretical calculations can be done at the appropriate impact parameters and the results understood, no conclusions can be made. Also, work is currently underway to study the covariance relationship between the extracted γ , the strength of the symmetry energy at saturation density S_0 , and other transport model input parameters. A similar χ^2 analysis as in [42] will be done with additional ImQMD05 calculations, in order to obtain a confidence interval for γ . Nonetheless, the isospin diffusion result using heavy residue projectile fragmentation is a viable observable for constraining the density dependence of the symmetry energy.

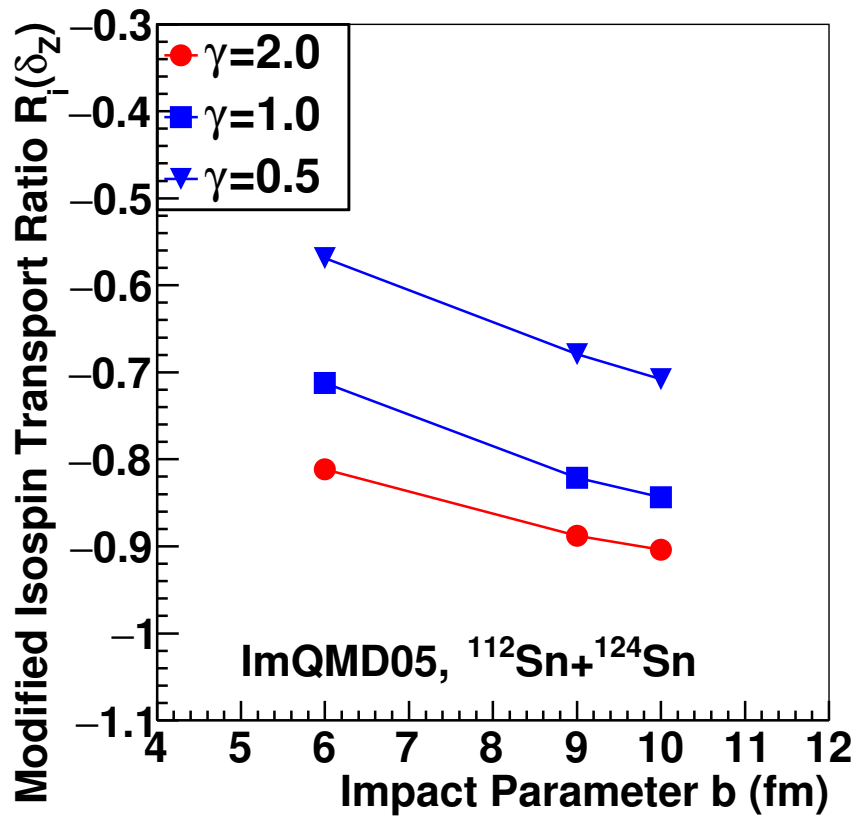


Figure 5.26 Isospin Transport Ratio, calculated using ImQMD05 for $\gamma = 0.5, 1.0, 2.0$, plotted against the impact parameter, for the $^{112}\text{Sn}+^{124}\text{Sn}$ reaction, for impact parameters $b = 6\text{fm}$, $b = 9\text{fm}$, and $b = 10\text{fm}$. Only one mixed system is shown here and the vertical axis is focused on the calculated system.

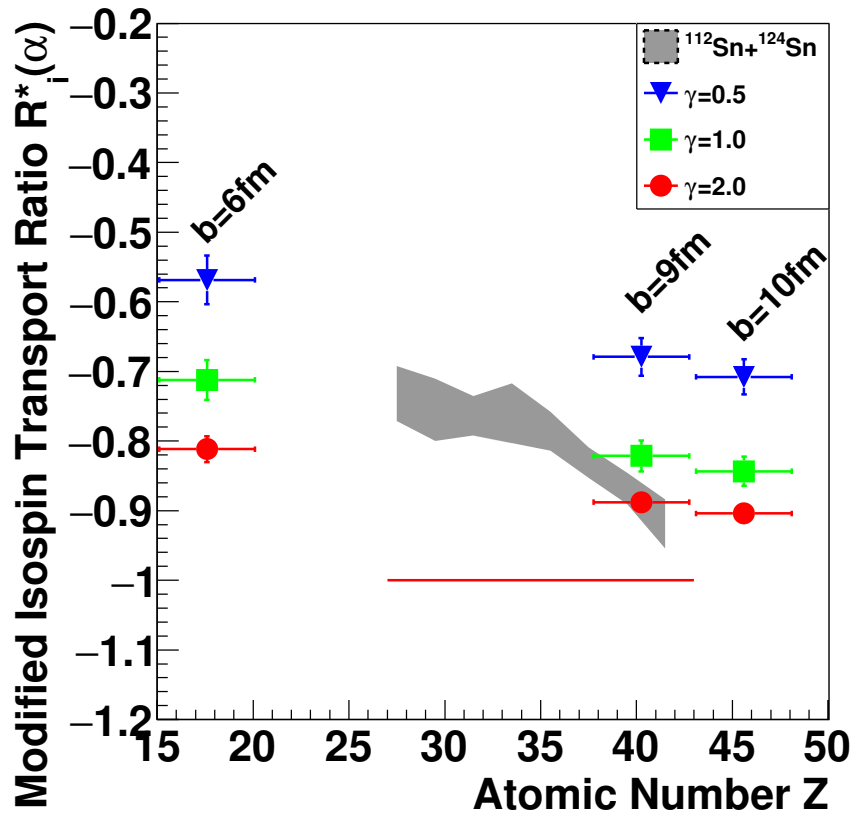


Figure 5.27 Modified Isospin Transport Ratio vs. Atomic Number Z for the $^{112}\text{Sn} + ^{124}\text{Sn}$ system. The solid region shows the experimental result, and the blue, green, and red crosses correspond to $\gamma = 0.5, 1.0,$ and $2.0,$ respectively. The calculations are done at $b = 6$ fm, $b = 9$ fm, and $b = 10$ fm.

Chapter 6

Conclusion

In this dissertation, the dynamics of nuclear reactions at intermediate energies were investigated by measuring heavy residues from collisions of $^{112,118,124}\text{Sn}$ beams with $^{112,118,124}\text{Sn}$ targets. Isotopic yield ratios of heavy fragments with $Z > 25$ were used to determine the extent of isospin diffusion that occurred in these reaction systems. By measuring a larger matrix of reactions than in previous isospin diffusion studies, a non-linear relationship between the isoscaling parameter α and the isospin asymmetry of the excited fragments was identified. These results will be used to improve the current experimental constraints on the density dependence of the nuclear symmetry energy.

The relative yields of heavy residues were measured using the S800 spectrometer. Isotopic and elemental identification was determined using time-of-flight and energy loss, which were corrected event-by-event using the measured fragment trajectories. An approximate correction was derived for the contamination due to multiple charge states of fragments being detected in the S800. Seven different reactions were measured using three magnetic rigidity settings, and the velocity distribution of each isotope was reconstructed. The relative yields were obtained by integrating these velocity distributions.

The MSU Miniball was used to measure the impact parameter event-by-event using the charged particle multiplicity and by measuring the total reaction cross section. The reduced impact parameter extracted from the charged particle multiplicity was shown to have an approximately linear relationship with the atomic number of the fragment measured in the

S800. An approximate relationship between the impact parameter and the atomic number Z of the heavy residue was determined.

The relative isotopic distributions measured by the S800 were used to form isotopic yield ratios to compare the isospin asymmetry obtained in each system. The data were shown to follow established isoscaling relationships, and the neutron isoscaling parameter was extracted as a function of atomic number for all systems. The neutron isoscaling parameter was shown to be positively correlated with atomic number, which can be attributed to an increasing temperature with increasing mass loss. The neutron isoscaling parameter was also found to vary with the range of isotopes used for the fit, so that fitting more neutron rich fragments resulted in a larger α .

The isoscaling parameter was used to form an isospin transport ratio to compare the $^{118}\text{Sn}+^{118}\text{Sn}$ system to the $^{112}\text{Sn}+^{112}\text{Sn}$ and $^{124}\text{Sn}+^{124}\text{Sn}$ systems. The isospin transport ratio for this system was shown to be insensitive to the systematic effects that caused variations in the isoscaling parameter, and was approximately constant over the range of Z measured in this experiment. This system yielded an isospin transport ratio which is larger than zero, indicating that the isoscaling parameter is not exactly linearly related to the isospin asymmetry of the initial compound system.

The isospin transport ratio was also used to quantify the amount of isospin diffusion that occurred in the mixed $^{124}\text{Sn}+^{112}\text{Sn}$ and $^{112}\text{Sn}+^{124}\text{Sn}$ systems. The isospin transport ratio for the $^{124}\text{Sn}+^{112}\text{Sn}$ system had a larger absolute value than for the $^{112}\text{Sn}+^{124}\text{Sn}$. This asymmetry is consistent with the positive isospin transport ratio measured for the $^{118}\text{Sn}+^{118}\text{Sn}$ system.

To account for the non-linearity of the isoscaling parameter, a modified isospin transport ratio was proposed which incorporated the measurement of the $^{118}\text{Sn}+^{118}\text{Sn}$ system. This

correction largely removed the asymmetry of the two mixed reactions. It was found that the amount of diffusion increased as the atomic number Z of the measured fragment decreased, which was interpreted as a dependence on the impact parameter in the collision.

The Improved Quantum Molecular Dynamics (ImQMD) transport simulation was used to interpret the isospin diffusion results. The collisions were simulated at several impact parameters, and with several different forms of the density dependence of the symmetry energy. The result was shown to be sensitive to the impact parameter, which qualitatively agrees with the experimental results.

Both the ImQMD-Sky and ImQMD05 results show a correlation between the isospin transport ratio with the density dependence of the symmetry energy. The data and the calculation show a strong dependence on the impact parameter. Because of computational limitations, calculations were completed for a limited set of impact parameters. To better account for the impact parameter dependence more calculations are needed, so a precise constraint on the impact parameter is not produced at this time. Calculations with other transport models such as the Boltzmann-Uehling-Uhlenbeck (BUU) model are underway as well.

The experiment also measured the yields of light particles and intermediate mass fragments in the LASSA array. Isoscaling information will be extracted from the intermediate mass fragment yields, and this information will be compared to the results presented here. The intermediate mass fragments should give a second independent measurement of isospin diffusion, which will improve the reliability of these results.

APPENDICES

Appendix A

Particle Identification Spectra

This section shows the final corrected particle identification spectra obtained using the S800 Spectrometer. Each figure shows the three magnetic rigidity settings measured for a single reaction. Seven different reaction systems are shown.

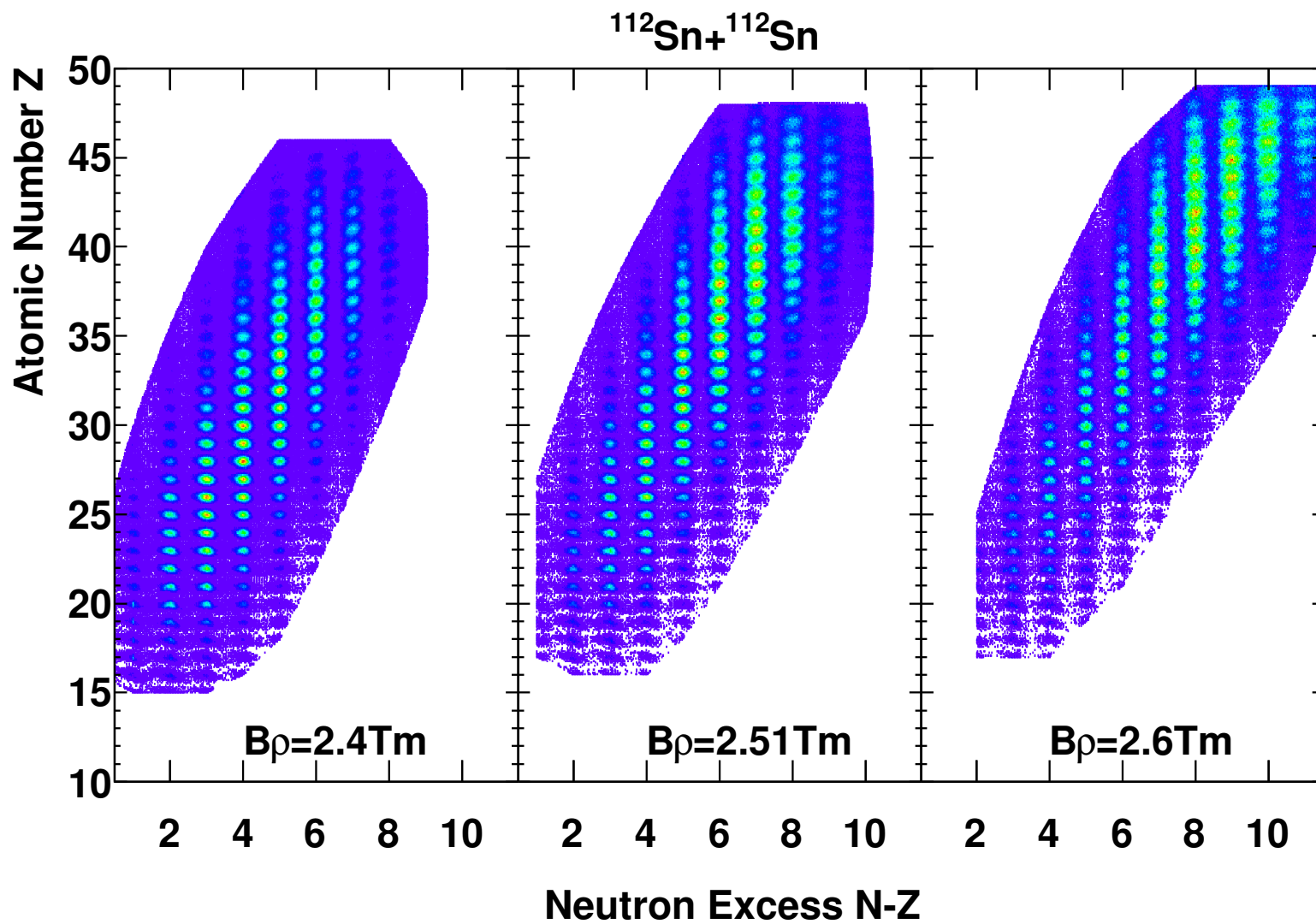


Figure A.1 Particle Identification for the $^{112}\text{Sn} + ^{112}\text{Sn}$ reaction. The three panels show the three different momentum settings that were measured. See Section 4.2 for details.

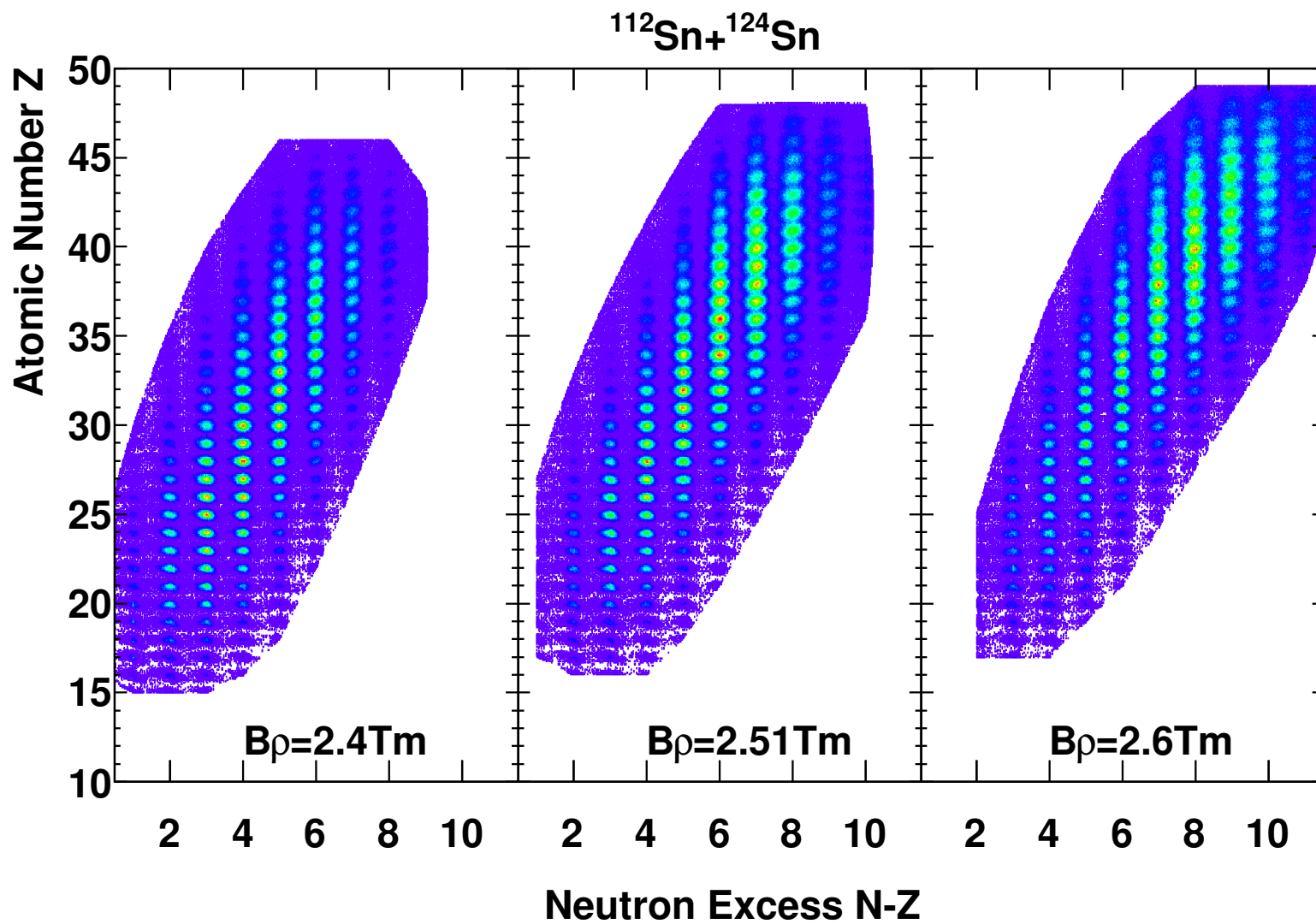


Figure A.2 Particle Identification for the $^{112}\text{Sn} + ^{124}\text{Sn}$ reaction. The three panels show the three different momentum settings that were measured. See Section 4.2 for details.

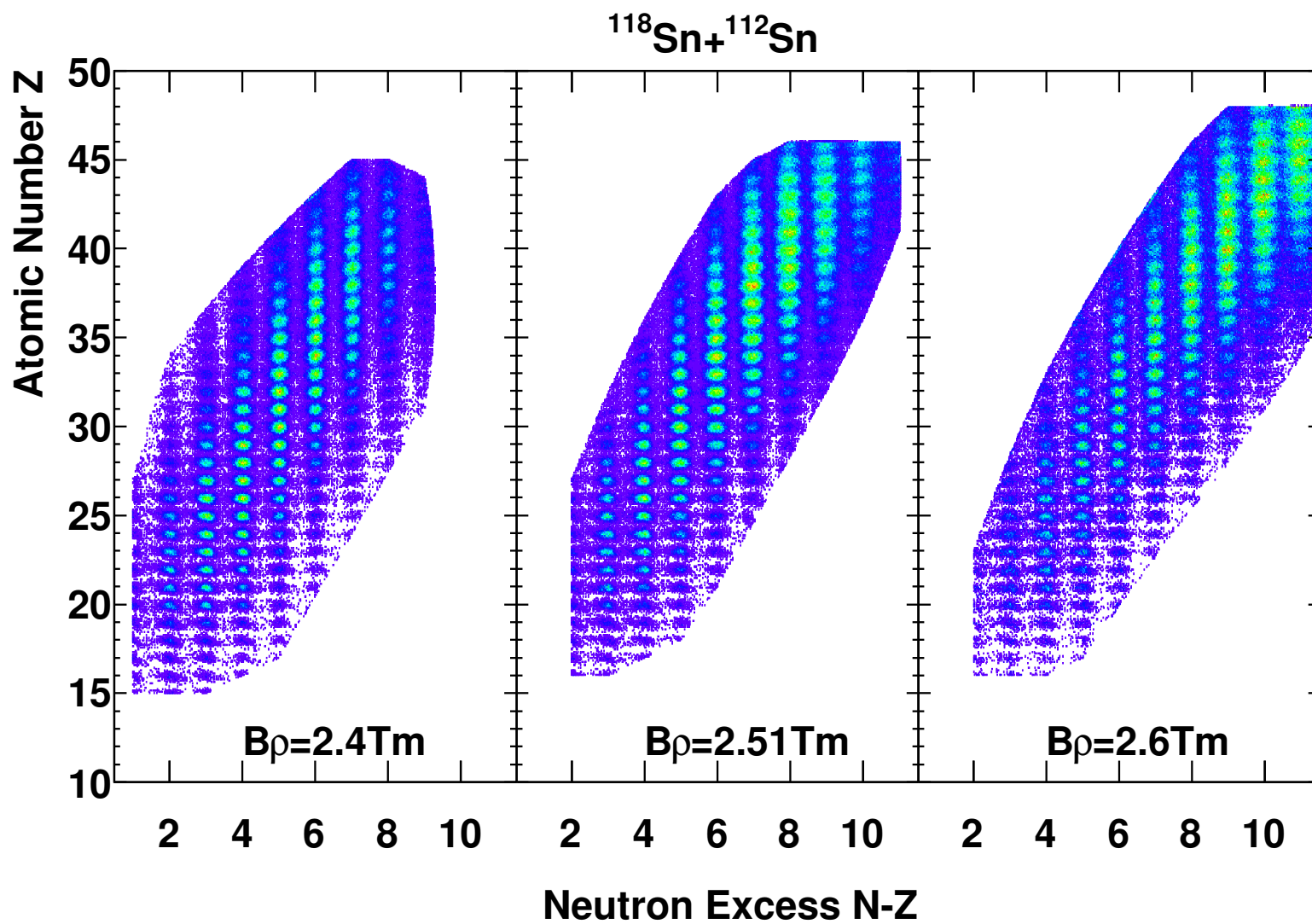


Figure A.3 Particle Identification for the $^{118}\text{Sn}+^{112}\text{Sn}$ reaction. The three panels show the three different momentum settings that were measured. See Section 4.2 for details.

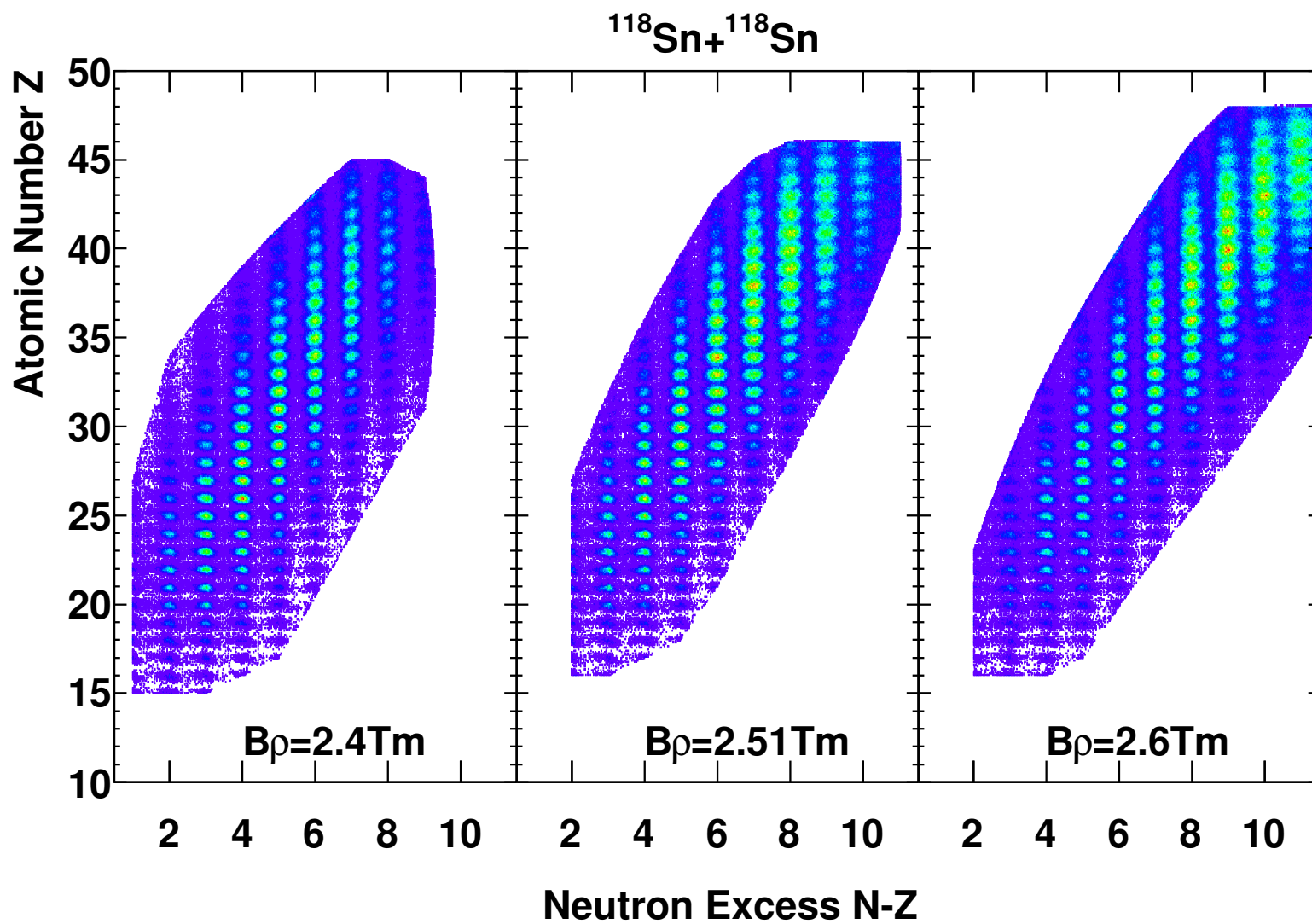


Figure A.4 Particle Identification for the $^{118}\text{Sn} + ^{118}\text{Sn}$ reaction. The three panels show the three different momentum settings that were measured. See Section 4.2 for details.

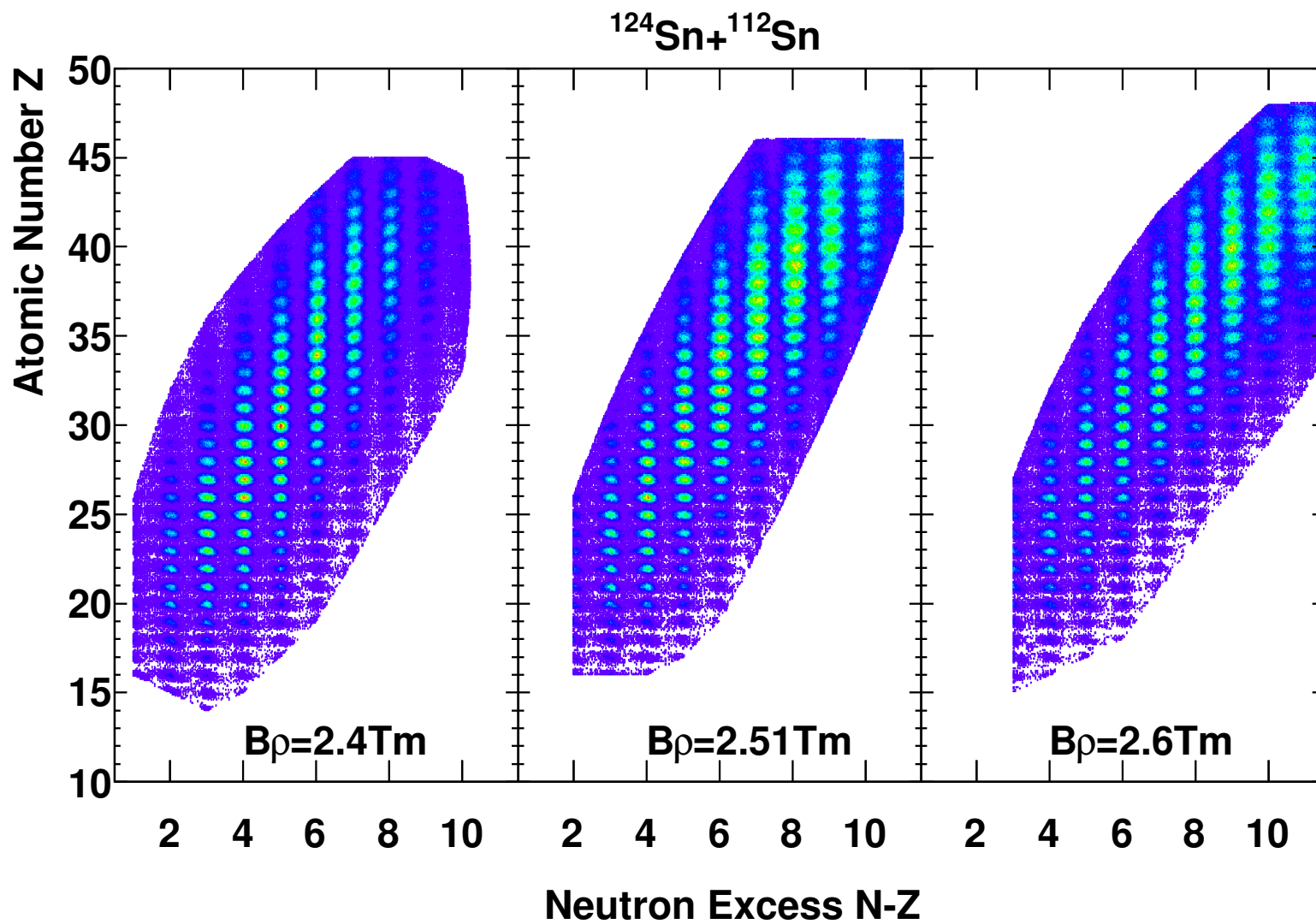


Figure A.5 Particle Identification for the $^{124}\text{Sn} + ^{112}\text{Sn}$ reaction. The three panels show the three different momentum settings that were measured. See Section 4.2 for details.

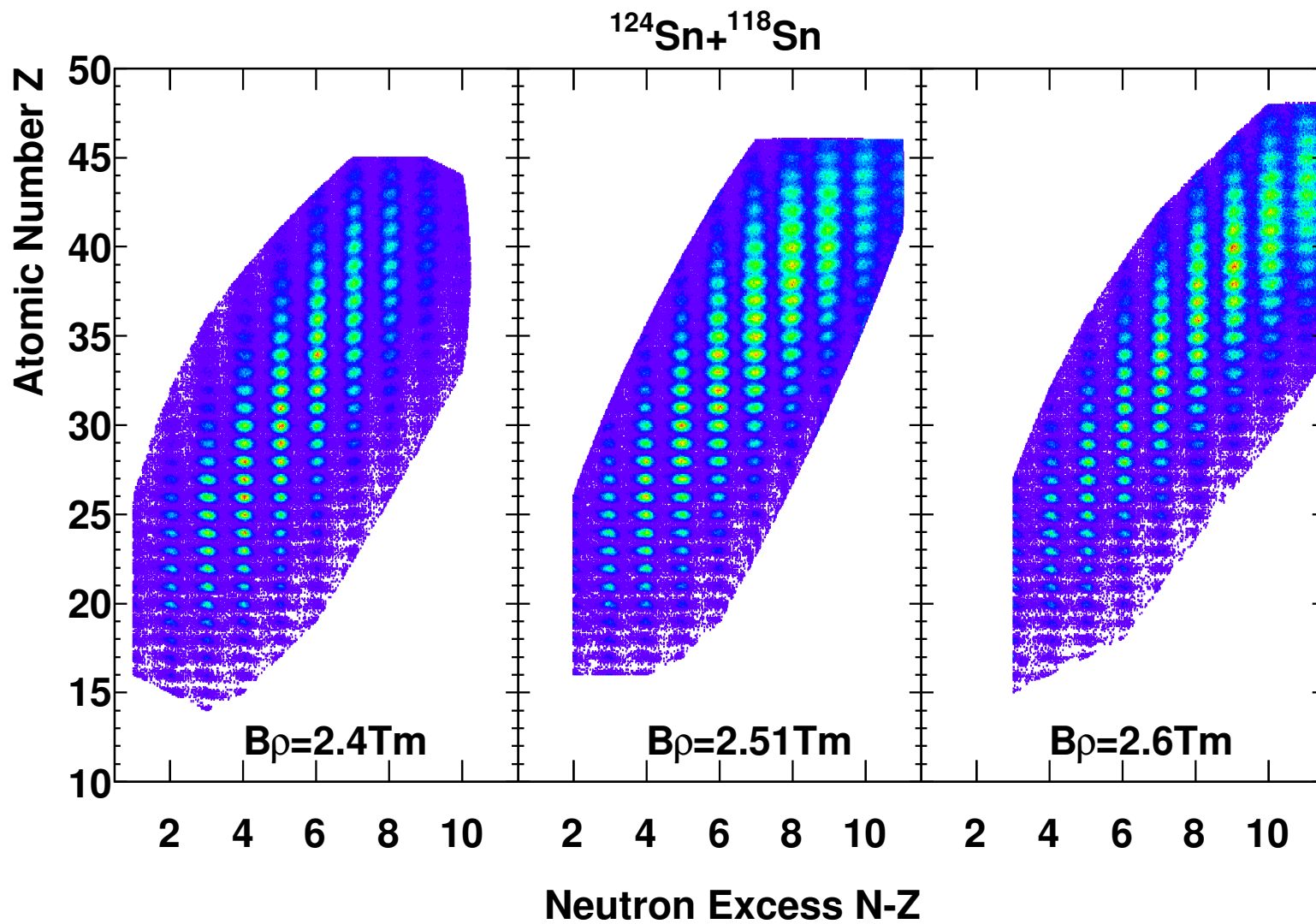


Figure A.6 Particle Identification for the $^{124}\text{Sn} + ^{118}\text{Sn}$ reaction. The three panels show the three different momentum settings that were measured. See Section 4.2 for details.

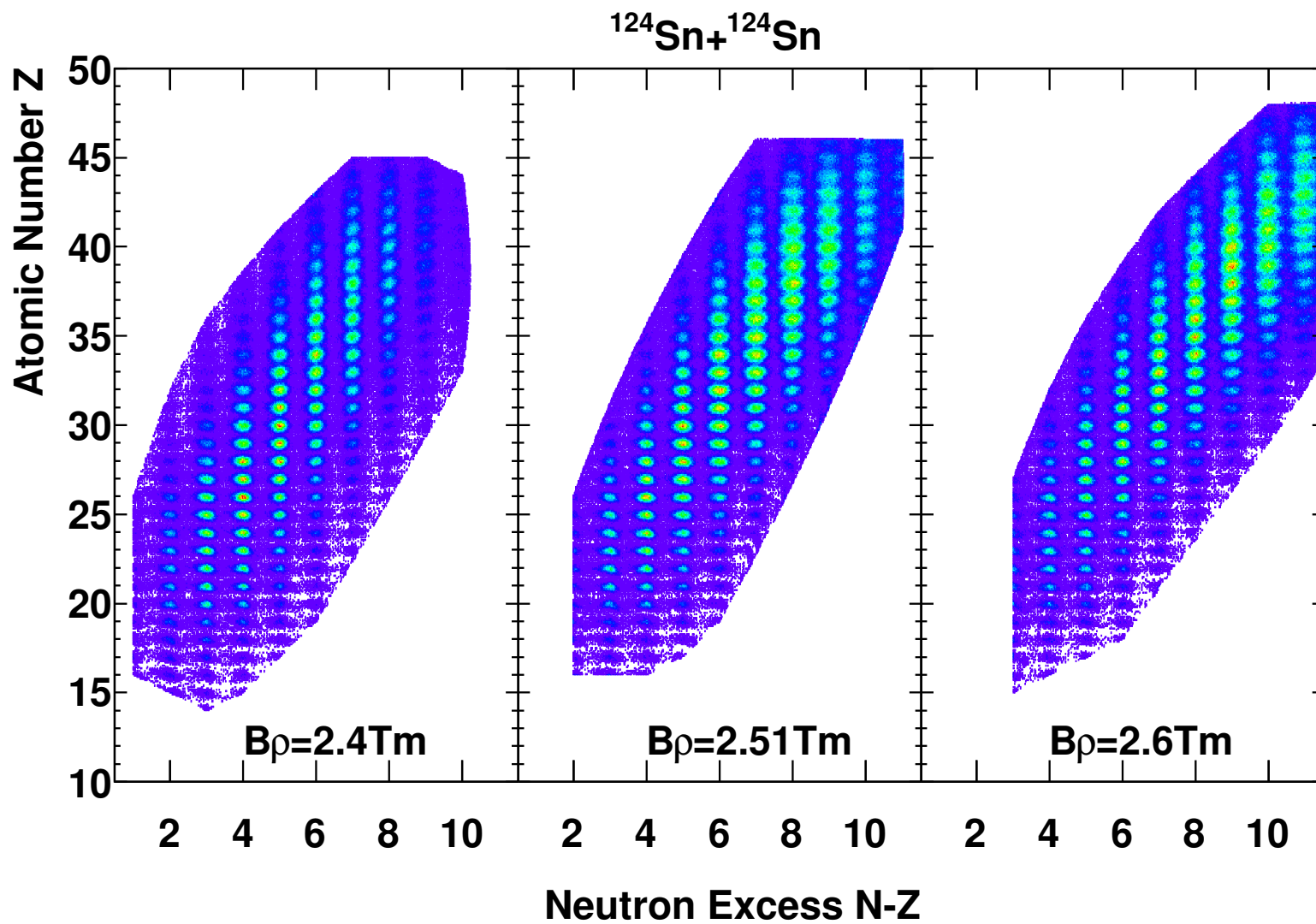


Figure A.7 Particle Identification for the $^{124}\text{Sn} + ^{124}\text{Sn}$ reaction. The three panels show the three different momentum settings that were measured. See Section 4.2 for details.

Appendix B

Hodoscope Analysis

The S800 spectrometer measures time-of-flight, energy loss, and magnetic rigidity in order to extract the charge, mass, and momentum of heavy residue fragments. When fragments enter the S800 with $Z \neq q$ they will be misidentified. A CsI hodoscope to measure the total kinetic energy (TKE) of the fragments was commissioned just prior to this experiment in order to solve this problem. The hodoscope did not exist at the time of the proposal, so the experiment was not optimized to take advantage of it. The energy of the projectile was increased from the proposed energy so that fragments could be detected in the hodoscope. Ultimately, the hodoscope did not provide useful information for this experiment, but the attempted analysis is described here.

Two overlapping isotopes in Figure 4.23, at a fixed $B\rho$, $\frac{m}{q}$, and Z , would enter the S800 with different total kinetic energy (TKE), and the hodoscope would be able to discriminate between these two isotopes. In practice, there are several complications. The first problem is that the fragments must travel through several detectors (the two CRDC's, the ionization chamber, and the timing scintillator) as well as a Teflon covering over the CsI array. The hodoscope was commissioned using a beam of ^{76}Ge ($Z=32$) at 130 MeV/u, or 9870 MeV TKE. [59] In that case, after taking into account all energy losses, the calculated energy at the hodoscope was 8680 MeV. Fragmentation products were also measured using both Au and Be targets, and the hodoscope was characterized over the energy range of 3600 MeV to 7600 MeV TKE for elements from $Z = 17$ to $Z = 33$. [70] In this experiment with Sn beams of 70 MeV/u, the measured energies of fragments from $Z = 20$ to $Z = 45$ are much lower. Table B.1 shows the materials and estimated thicknesses of the detectors in the S800 focal plane. To investigate the effect of energy losses for this experiment, calculations using LISE++ [88, 89] are shown in Table B.2. The calculations are done for an isotope in the middle of the measured isotopic distribution, and the incoming energy is 60 MeV/u for all fragments for simplicity. 60 MeV/u is chosen because it corresponds the $B\rho = 2.51$ setting, in the center of the experimental acceptance. Because there are many uncertain variables such as the gas pressure (which varied throughout the experiment), the E1 timing scintillator thickness, or the exact thickness of the teflon covering of the hodoscope, this is only an estimate of the energy losses.

Because energy loss increases with Z , fragments with $Z > 35$ do not reach the hodoscope. For $Z = 25$, already half of the fragment energy is estimated to be lost before reaching the hodoscope. To see the real effect of the energy losses, Figure B.1 shows the overall efficiency for detecting fragments as a function of Z . This efficiency is calculated as the ratio of events with a signal above threshold in the hodoscope compared to the total number events with a fragment identified in the focal plane for each given Z . Figure B.1 agrees qualitatively with the calculations from Table B.2, but the calculations clearly underestimate the energy loss.

Layer	Material	Estimated Thickness
CRDC1 entrance window	PPTA	12 micron
CRDC1 gas	80% CF ₄ - 20% C ₄ H ₁₀	40 torr
CRDC1 exit window	PPTA	12 micron
CRDC2 entrance window	PPTA	12 micron
CRDC2 gas	80% CF ₄ - 20% C ₄ H ₁₀	40 torr
CRDC2 exit window	PPTA	12 micron
IC entrance window	PPTA + Kevlar	14.0 mg/cm ²
IC gas	P10	300 Torr
IC plates	PPTA	2 mg/cm ²
IC exit window	PPTA + Kevlar	14.0 mg/cm ²
E1 scintillator	polyvinyltoluene	1.0 mm
Teflon hodoscope cover	Teflon	300 μm
hodoscope	CsI(Na)	5 cm

Table B.1 Approximate thicknesses of the S800 focal plane detectors

Fragment Z (N-Z)	E After IC	E After E1	E into Hodo
20 (4)	54.1 MeV/u	42.5 MeV/u	35.3 MeV/u
25 (5)	52.6 MeV/u	37.7 MeV/u	27.8 MeV/u
30 (6)	51.2 MeV/u	32.9 MeV/u	19.7 MeV/u
35 (7)	49.9 MeV/u	28.2 MeV/u	9.94 MeV/u
40 (8)	48.7 MeV/u	23.4 MeV/u	0 MeV/u

Table B.2 Approximate energy loss as a function of Atomic Number Z, Starting from 60 MeV/u (near $B\rho = 2.51$)

For $B\rho = 2.51$, which should be directly comparable to Table B.2, the efficiency drops by 50% by $Z = 28$. Furthermore, the range where charge states become an appreciable effect is for $Z > 30$.

To further understand the effect of energy loss with increasing Z , Figure B.2 shows the hodoscope energy for one crystal as a function of Z , for the $^{112}\text{Sn} + ^{112}\text{Sn}$ reaction system, at $B\rho = 2.51$ Tm. The hodoscope energy quickly drops to zero as Z increases beyond $Z = 25$, which is consistent with the energy loss effects described above. Another effect that may play a role is the light response of the CsI(Na) for these very highly ionizing particles. This effect was described in [70], but that analysis relied on the ability to accurately calculate all energy losses before the hodoscope. Without better calibrations of the material thicknesses, this would be futile for the present experiment.

Another problem, also observed in the commissioning of the hodoscope, is the position dependence of the CsI signals. The array is made up of 32 separate crystals arranged in a 4x8 array. It was found that the energy deposited (by the monoenergetic primary beam) had anomalous behavior near the edges of the crystals. Within about 5mm of each edge of the crystal the light output is enhanced. In that experiment, data from the edges of the crystals were simply removed. In this experiment, the problem is unavoidable. As discussed

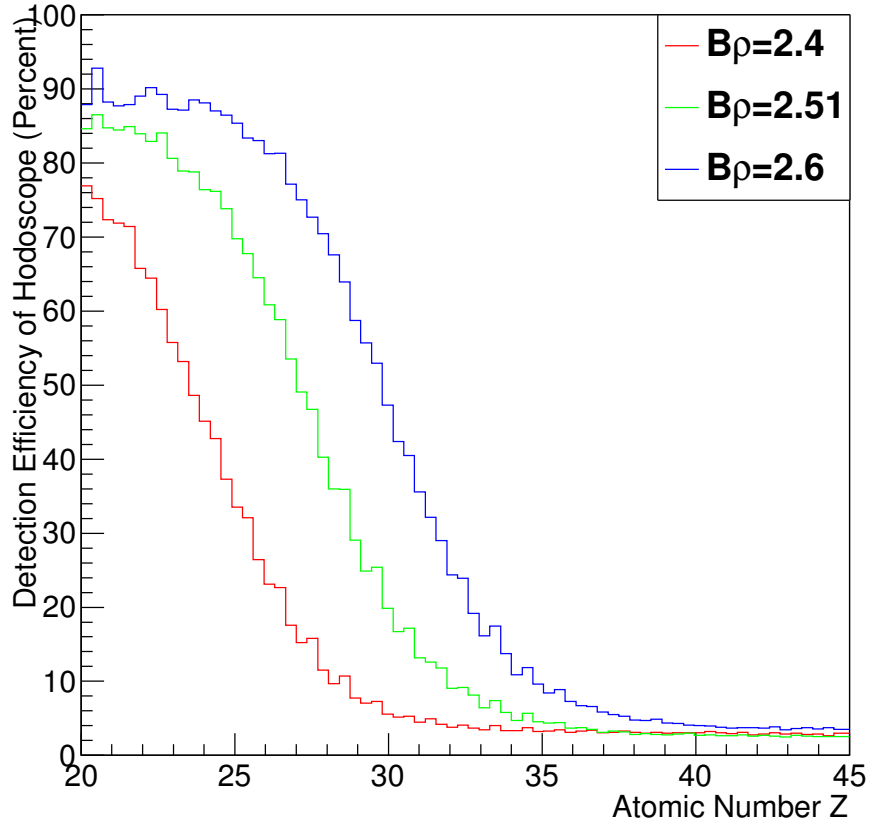


Figure B.1 Overall detection efficiency of the CsI hodoscope for the $^{112}\text{Sn}+^{112}\text{Sn}$ reaction system, at $B\rho = 2.4, 2.51,$ and 2.6 Tm. The efficiency is simply the fraction of particles which are otherwise detected and identified in the focal plane that also leave a signal in any hodoscope crystal.

in Appendix C, due to a problem in the tuning of the S800, the acceptance of the S800 was very limited, especially in the non-dispersive direction. As a result, instead of illuminating the entire middle two columns of crystals, only the seam between these two columns is illuminated. During the first few days of the experiment, in June, the fragments are well spread over the hodoscope, as expected. This is shown in Figure B.3. Based on the energy-position correlation noted in the June segment of the experiment, to remove the edge region would likely mean removing $\pm 5\text{mm}$, which would remove most of the data. To analyze these data would require a careful calibration of the position dependence, which is not done here. To make a correction for this effect, the best case scenario would be to send a monoenergetic beam into the focal plane to scan the crystals. In this case, because the experiment uses beams of Sn, ($Z = 50$), the beam does not reach the hodoscope, due to energy losses. When calibrating the hodoscope crystals, the gas was removed from the ionization chamber and the two CRDC's, so the calibration data has no tracking information. This position dependence is evident in the data from June, although only qualitatively, so it is not shown here.

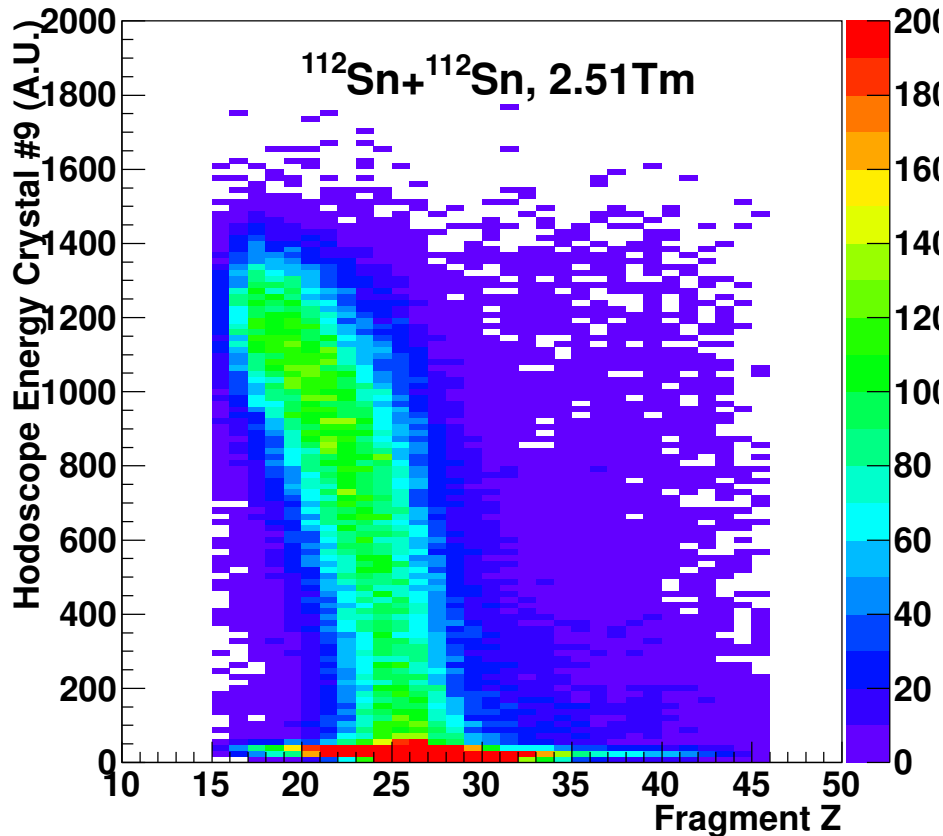


Figure B.2 Energy measured in crystal #9, shown vs. Z , for the $^{112}\text{Sn}+^{112}\text{Sn}$ reaction system, at $B\rho = 2.51\text{ Tm}$. This figure requires that crystal #9 is the crystal with the largest signal amplitude for that event.

Another problem that may affect the resolution of the hodoscope is the possible presence of multiple hits in the hodoscope in a single event. Since higher- Z fragments that are triggered in the timing scintillator are stopped there or in the Teflon cover of the hodoscope, there are many events that do not include a corresponding TKE in the hodoscope. In these events, there are often signals with appreciable amplitude, which must come from either pile-up from other events, multiple hits in a single event, or some other source of background. The signature of these effects is the same: there are signals in hodoscope crystals where there should be none. This can be seen simply from Figure B.1 where, at high Z , all three $B\rho$ settings approach a non-zero value, around 4%. By requiring that the TKE is extracted from the hodoscope crystal that is indicated by the position tracking, some of these spurious signals could be removed, but there may still be a problem of multiple hits in crystals with real events.

Figure B.4 shows the correlation between a signal in a given crystal and the position of that signal. There are several features in this figure worth noting. First, aside from most of the counts inside the dimensions of the crystal, (shown by two dotted lines) there is also a

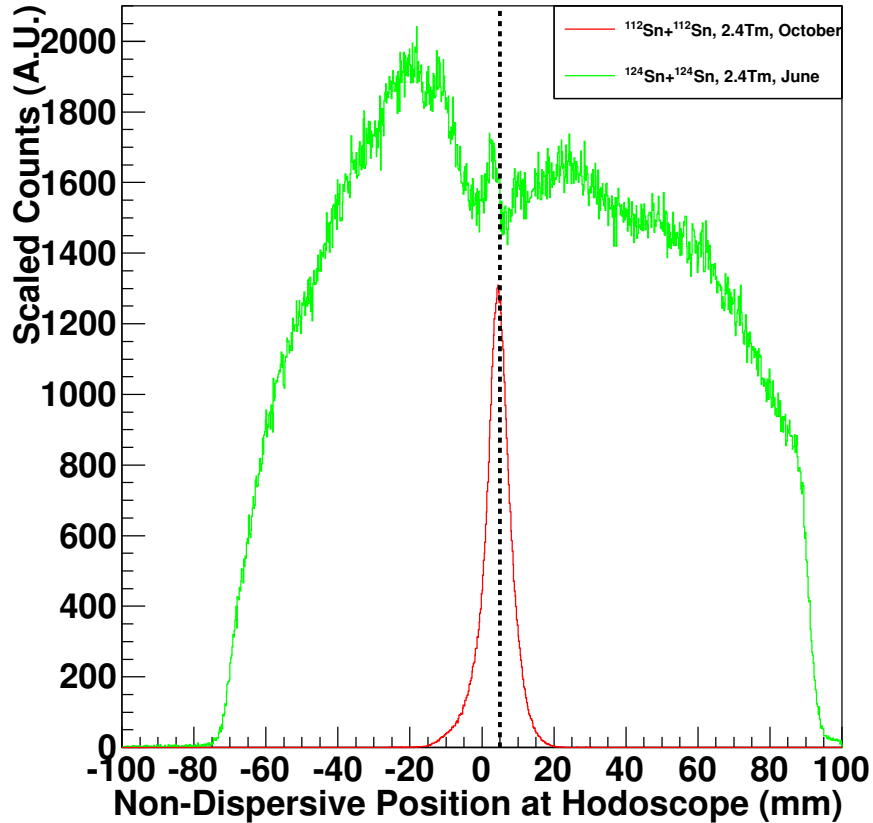


Figure B.3 Non-dispersive position spectra at the hodoscope, shown for the two different segments of the experiment. The dotted line shows the approximate position of the gap between the middle two columns of hodoscope elements. The spectra are arbitrarily normalized to be on the same scale. Because the acceptance was limited to the region near the gap, most of the data is corrupted by the position dependence of the crystal response.

distribution of events that are outside those dimensions, although still correlated spatially. This may be a signature of angular straggling for some low- Z particles. There is also some background that is not spatially correlated, which covers the same energy range as the signals presumed to be from the heavy fragments. These could be pile-up, multiple-hit events, or possibly light particles emitted from the stopped heavy fragments. To better characterize the background due to these effects, Figure B.5 shows the hodoscope spectrum for crystal #9, requiring a high- Z identification from the ionization chamber. Since a high- Z fragment stops before reaching the hodoscope, signals in Figure B.5 must be spurious events.

Figure B.5 shows that the TKE spectrum would contain contaminated signals, even if the particle tracking were enforced. In the low energy portion of Figure B.4, there is an excess of counts as the energy goes to zero. Looking closer at this region shows evidence of the gain shifting near the edges of the crystal, which rules out electronics noise or ADC pedestal values. Since the counts do appear spatially correlated with the crystal, it can be

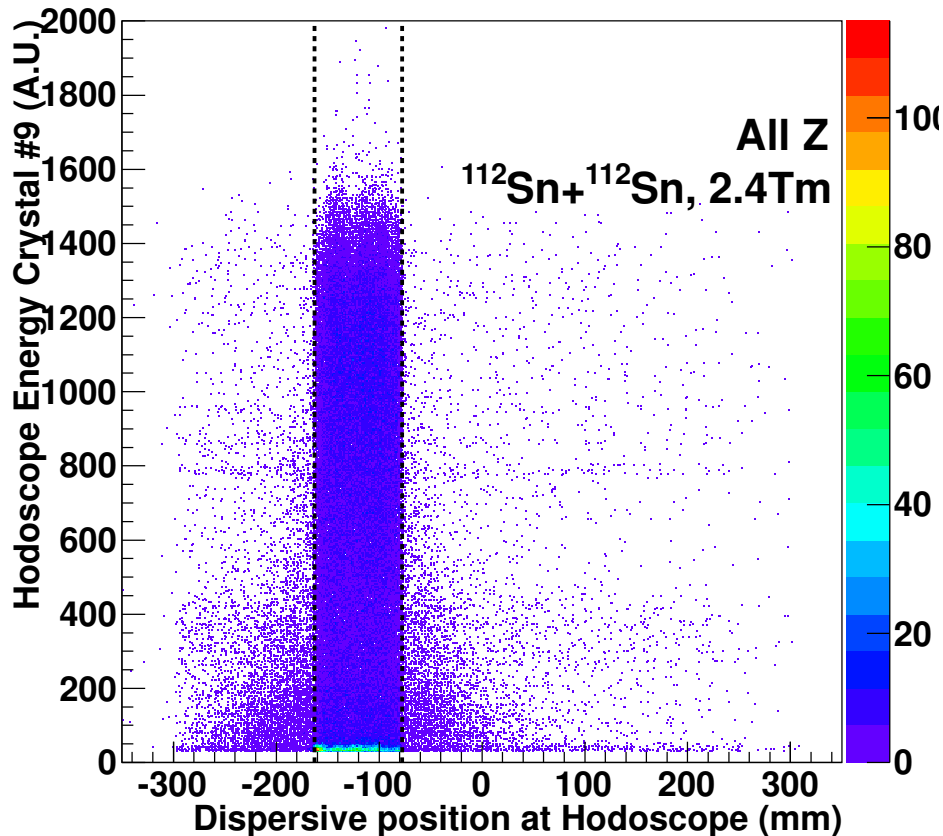


Figure B.4 Hodoscope Energy from crystal #9 vs. Dispersive position spectra at the hodoscope, for the $^{112}\text{Sn}+^{112}\text{Sn}$ reaction system, at $B\rho = 2.4$. The dotted lines show the approximate positions of the edge of crystal #9.

assumed that they come from real particles. If these particles are arriving in coincidence with the heavy fragment in the focal plane, there may be a significant fraction of events where a heavy fragment does leave a real signal in the crystal, but is coincidence-summed with other detected particles, so the hodoscope misidentifies the TKE of the fragment of interest.

After this aggregation of problems, the best case scenario for extracting useful information is the highest velocity, lowest Z fragments that are measured with appreciable statistics. This leaves only the $B\rho = 2.6$ Tm setting, and a Z of 22. Focusing on this isotope, first, the hodoscope energy can be corrected empirically for the momentum (similar to the TOF and ΔE), which allows for a 1-d projection onto the hodoscope energy. This is shown in Figure B.6. Assuming that the energy scale is linear, the resolution for this element may be sufficient to estimate the contribution of charge states, but not to physically resolve them.

Because of the many problems and uncertainties associated with the hodoscope data from this experiment, no useful information is extracted from the hodoscope. The conclusion is that the hodoscope is not a useful tool for measuring the charge states distributions for

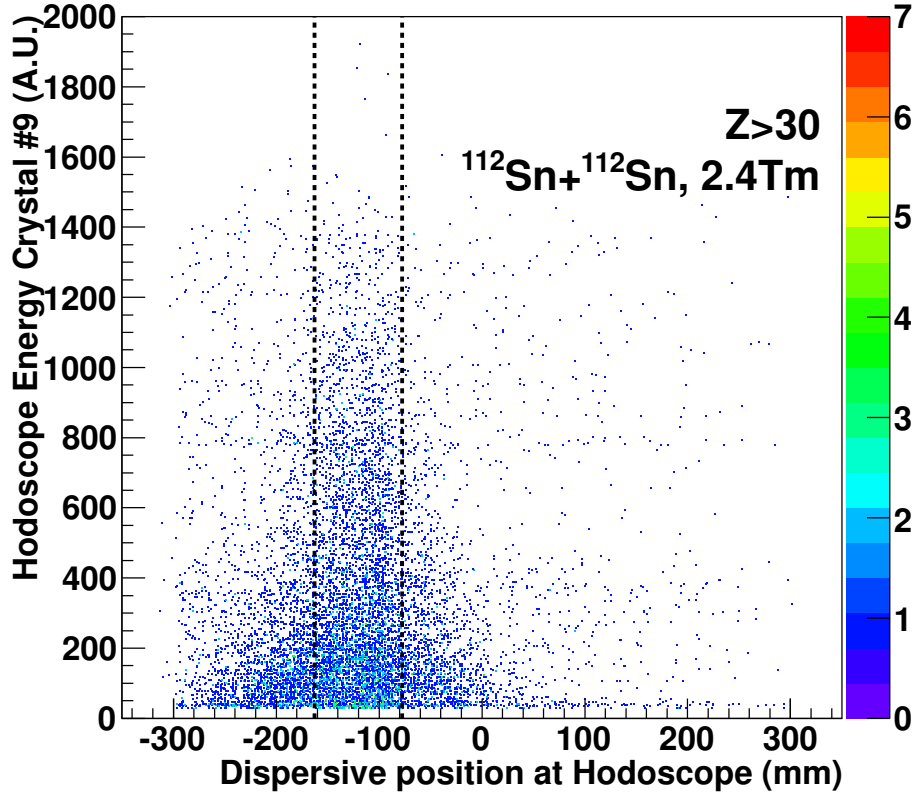


Figure B.5 Hodoscope Energy from crystal #9 vs. Dispersive position spectra at the hodoscope, for the $^{112}\text{Sn}+^{112}\text{Sn}$ reaction system, at $B\rho = 2.4$. The dotted lines show the approximate positions of the edge of crystal #9. Only fragments identified as $Z > 30$ using the normal particle identification spectrum are included this figure, which should not reach the hodoscope. As a result, these signals come from either coincident light fragments or background from multiple hits.

fragments of $Z > 25$ with energies at or below 60 MeV/u. For this type of experiment, some possible improvements would be to decrease the thickness of the E1 scintillator and to minimize and measure the exact thickness of the material covering the front face of the hodoscope crystals. To do precision work with the hodoscope, the non-linearity near the edges of the hodoscope would have to be carefully characterized. In any similar future experiments, the question of multiple hits in the hodoscope would have to be addressed. For this experiment, the contributions from charge states are characterized using empirical models as originally planned, described in the Section 4.3.1.

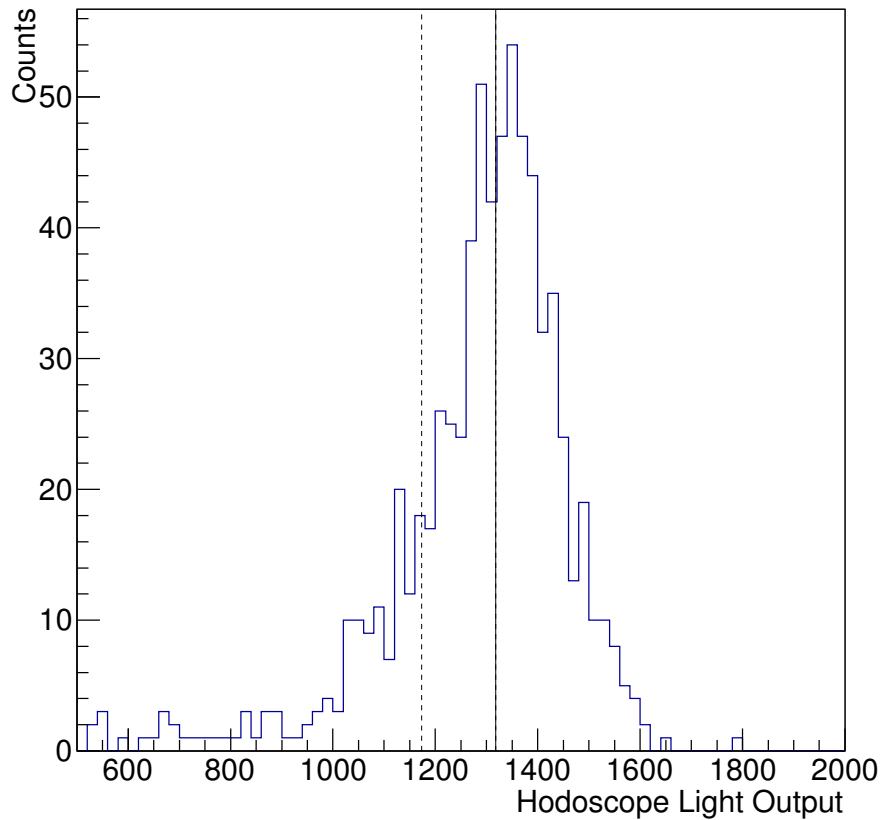


Figure B.6 Hodoscope energy, measured in the $^{112}\text{Sn}+^{112}\text{Sn}$ reaction system, at $B\rho = 2.6$ Tm, empirically corrected for momentum, for $^{46}\text{Ti}^{22+}$. The solid line shows the approximate centroid of this peak, and the dotted line shows the estimated position of the primary contaminant, $^{44}\text{Ti}^{21+}$, when accounting for energy losses and assuming the energy scale is linear.

Appendix C

Acceptance Correction

As with most detector systems, the S800 Spectrometer only accepts a limited range of kinematical variables. In the case of the S800, the situation is complicated, as the detectors are located in the focal plane, after passing through several magnets. As a result, particle trajectories must be traced back through the magnets to reconstruct the reaction at the target position. This process is described in more detail in Section 4.1.4. Tracking through the magnets also introduces a correlation between the angle of a particle and the magnetic rigidity of a particle. To correct for this effect, the acceptance must be simulated using a Monte Carlo algorithm. This experiment was designed to measure ratios of particle yields, specifically to avoid this type of problem with acceptance. If the spectrometer acceptance was unchanged from one reaction system to another, the acceptance correction would cancel in the ratio. During the experiment, there were several problems that led to having different acceptance corrections in the different reaction systems, and these are accounted for in the calculation of the acceptance.

The largest problem affecting the acceptance was the result of an error in the device tuning for the S800 itself. To accommodate the large volume of the miniball detectors around the target position, the target was placed about 50 cm upstream of the normal focal point of the S800. This requires a simple scaling of the fields in the quadrupole magnets after the target, to optimize the acceptance for the new target position. While this was done correctly during the first portion of the experiment in June 2011, when the experiment was resumed in October 2011 this step was accidentally omitted from the beam-tuning checklist. The problem is shown schematically in Figure C.1. While it was observed that the S800 was working normally in the beginning of the experiment in June, this problem was not noticed in October and persisted through all three beams used in the experiment. Fortunately, because of the possibility of changes in detector gains or thresholds, the ^{124}Sn beam measurements were repeated when the experiment resumed in October, so comparable data was taken for all beams. After mapping the angles to the target position, the differences are obvious, as shown in Figure C.2. The end result is that the angular acceptance is about 25% of the nominal acceptance, and this reduced efficiency magnifies other changes in the acceptance.

Figure C.2 shows that the acceptance at very small angles (near $afp = 0, bfp = 0$) is reduced by a cutout in the scintillator placed after the target. This scintillator was required to measure the start time of the time-of-flight from the target position to the focal plane. Because the expected beam rate was larger than 10 MHz, and the stable beams used were highly focused, the plastic scintillator material would be rapidly degraded if the full beam rate was impinged on it. A square hole was cut into the scintillator, which would allow the unreacted beam to pass through it. The light-guide for the scintillator was then designed with two photomultiplier tubes to collect light from particles hitting either side of the hole.

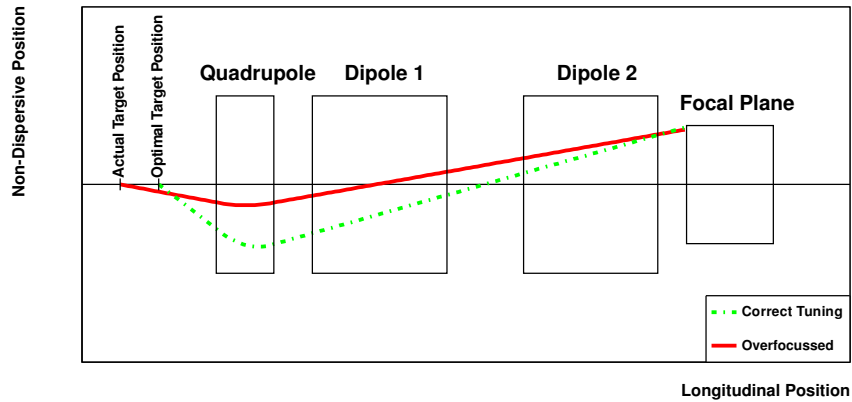


Figure C.1 Schematic diagram showing magnetic elements of the S800. Only the Optics in the Non-Dispersive Direction are shown. The S800 was tuned assuming the reaction target was at the normal target position (the pivot point), which resulted in over-Focusing the fragments from the actual target position. The dashed green curve represents the track of a fragment emitted at the maximum scattering angle from the optimal target position. The solid red curve represents the track of a fragment emitted at the maximum scattering angle from the actual target position, upstream of the pivot point.

Figure C.3 shows an image of the scintillator after the experiment, with one of the two photomultiplier tubes still attached. This scintillator hole modifies the acceptance between reaction systems because of a faulty mechanical target drive that was used to adjust the position of the start timing scintillator. It was discovered part-way through the experiment that the drive did not hold its calibration reliably. The uncertainty in the scintillator position was minimized by recalibrating the drive before each movement. The largest miscalibration occurred during the ^{112}Sn beam, which is shown (for the worst case, when comparing to the ^{124}Sn beam) in Figure C.4. Because these changes in acceptance can make an impact on the resulting fragment yields, a careful calculation of the acceptance was done, and is described in further detail in this section.

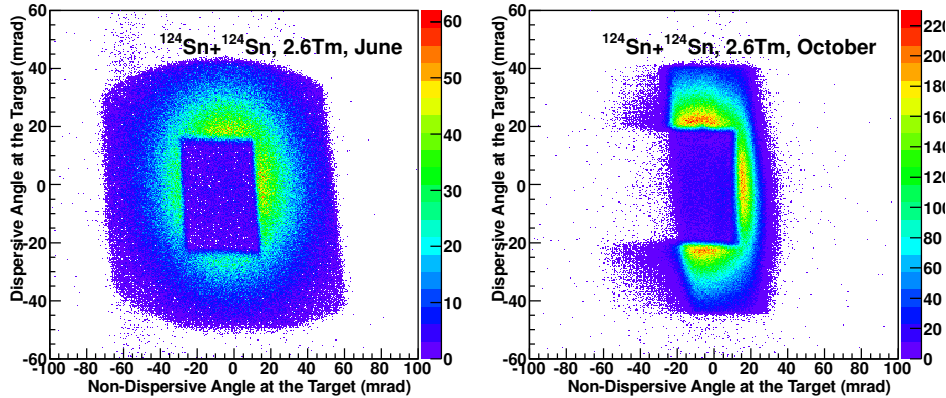


Figure C.2 Scattering angles at the target position. The left panel shows the $^{124}\text{Sn}+^{124}\text{Sn}$ reaction at the 2.6 Tm magnetic rigidity setting as measured in June 2011 with the proper beam tuning. The right panel shows the $^{124}\text{Sn}+^{124}\text{Sn}$ reaction at the 2.6 Tm magnetic rigidity setting as measured in October 2011 with the incorrect beam tuning. Neither histogram requires a particle identification gate, but both require a timing signal in the timing start scintillator, which causes the square cut out in the center. (See Figure C.3)

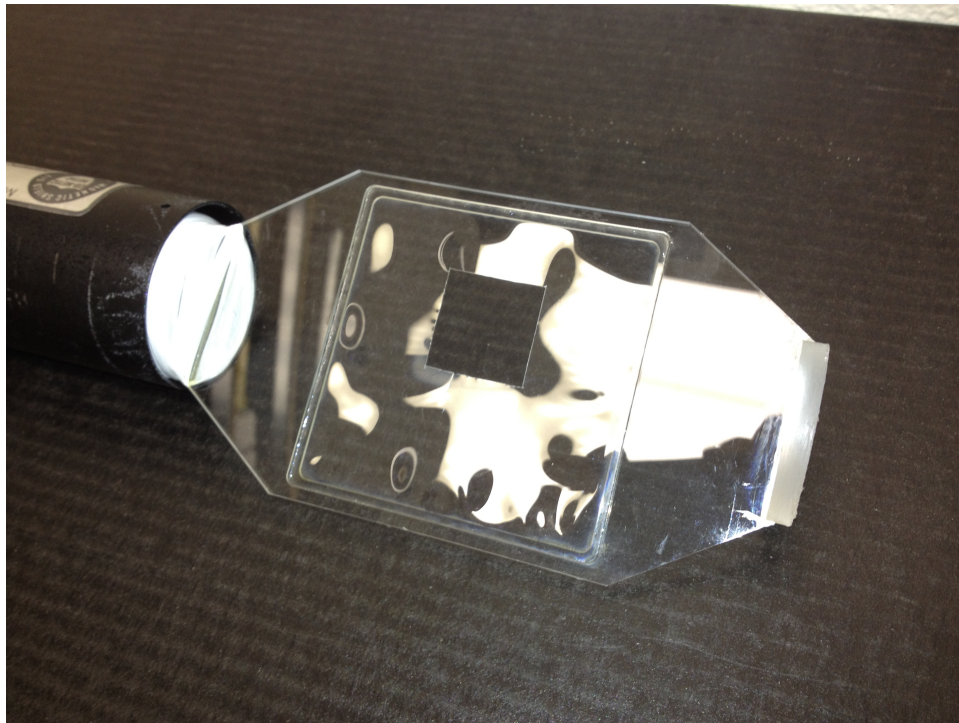


Figure C.3 Scintillator used to measure the start time of the heavy fragments that are detected in the S800 focal plane. Notice the square hole cutout, which allows the unreacted beam to pass through.

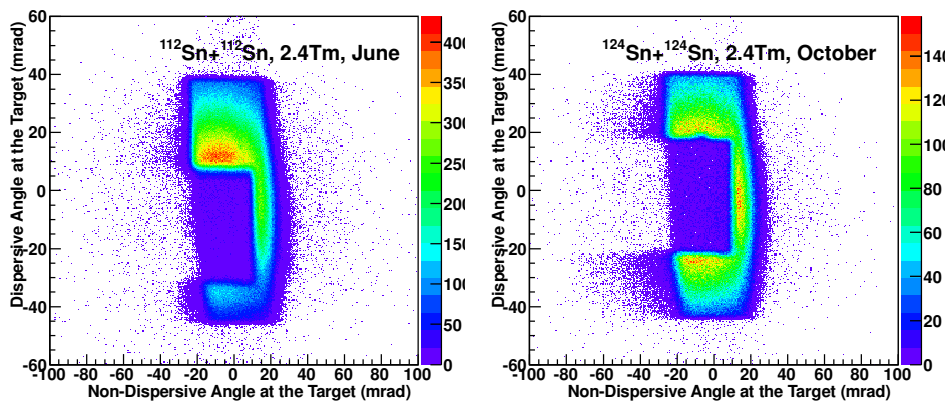


Figure C.4 Scattering angles at the target position. The left pane shows the $^{112}\text{Sn}+^{112}\text{Sn}$ reaction at the 2.4 Tm magnetic rigidity setting. The right pane shows the $^{124}\text{Sn}+^{124}\text{Sn}$ reaction at the 2.4 Tm magnetic rigidity setting. The significant vertical offset in the left panel is due to miscalibration of the mechanical target drive used to move the scintillator.

C.1 Monte Carlo Acceptance Calculation

While the S800 has a complex geometric acceptance, the ability to track particles from the focal plane to the target position allows for an accurate calculation of the acceptance correction. A comparable procedure has been used multiple times to make corrections at large scattering angles when using the normal acceptance of the S800. [90, 91] In this experiment, the distributions in energy and in scattering angle are necessary to make comparisons between different beam-target combinations. The goal of the correction is to derive a weighting factor for a given (θ, dta) that can be applied on an event by event basis. The basic steps to do this are as follows: generate a large set of simulated data events, apply the requirements of the experimental conditions, and simply calculate what fraction of the events at a given (θ, dta) would be detected. The procedure assumes that, inside the gates chosen, the efficiency of detecting a particle is 100%, which means that edges must be excluded in the simulation as well as the data.

The first step is to generate a random distribution of (θ, ϕ, dta, yta) . For (θ, dta) , a uniform distribution is used, since the correction is calculated independently for each (θ, dta) . For ϕ , a uniform distribution is used because the reaction should be cylindrically symmetric. Since the S800 measures scattering angle in terms of rectilinear variables ata and bta , θ and ϕ are transformed accordingly. yta , which is the non-dispersive position at the reaction target, is taken from the data itself, and it simply represents the spread of the beamspot on the target. In this experiment, the beam was well focused at the target position, and is represented in the simulation by a gaussian distribution. The width (FWHM) of the yta distribution is typically 3mm but is extracted for each beam-target-rigidity setting separately, to account for possible offsets in calibrations between settings.

Once the pseudodata is generated, several two-dimensional gates can be applied. The S800 measures four parameters (ata, bta, yta, dta) , and these four variables can have correlations between them. In previous studies, 2 dimensional boundaries in the $ata - dta$ plane and the $yta - bta$ plane were applied. In this experiment, because of the square cutout in the timing scintillator, there is also a correlation in the $ata - bta$ plane. Also, as a result of the overfocusing of the S800 quadrupole magnets, there is an appreciable correlation in the $bta - dta$ plane as well.

The first gate, which is the easiest to understand, is in the $ata - dta$ plane. Since the S800 dipoles deflect fragments in the dispersive direction, the range of ata that can be detected becomes smaller as the magnetic rigidity moves away from the central value. This correlation is shown in Figure C.5. The acceptance in the $ata - dta$ plane changes from system to system only because the three different beams impinge on the target with slightly different angles. The incoming beam angle is determined by degrading each beam into the focal plane using varying widths of aluminum.

The next gate that can be applied to the pseudodata is in the $yta - bta$ plane. In this case, with the S800 in focused mode, there is only a small spread in yta . Nonetheless, when bta approaches the edge of the acceptance, the value of yta becomes important. Extracting this behavior is complicated, because of the correlations in the boundaries in the $ata - bta$ plane as well as the $bta - dta$ plane. Since it is impossible to visually determine these boundaries in 3 and 4 dimensions, this multidimensional correlation must be extracted iteratively. To

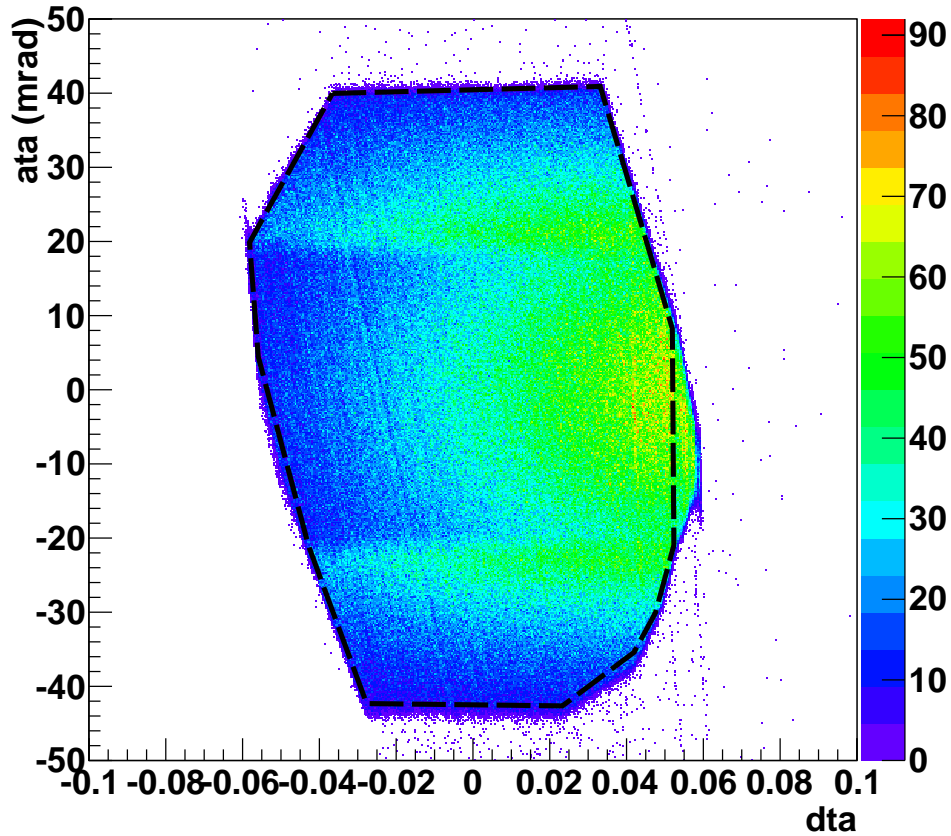


Figure C.5 Dispersive angle at the target position versus fragment energy (dta) measured in the $^{124}\text{Sn}+^{124}\text{Sn}$ reaction at the 2.51 Tm magnetic rigidity setting. No PID gates or other requirements are applied, the sharp cutoffs are simply due to the acceptance of the S800 Spectrometer. The dotted line shows an example of the $ata - dta$ gate used to calculate the acceptance.

understand the boundary in the $yta - bta$ plane, the dependence of bta_{max} on ata and dta should be subtracted, and this must be done separately for bta_{min} (not shown). This correction is shown in Figure C.6. Another correlation that has to be accounted for in the acceptance calculation is between bta and dta . Again, this is shown for bta_{max} in Figure C.7. And finally, the correlation between ata and bta is shown in Figure C.8.

A separate restriction on the acceptance comes from the cutout in the timing scintillator. This effect can be determined by making the same spectra as described above, but requiring a signal from the timing scintillator. These corrections can be seen in Figure C.9, and the same procedure described above to determine bta_{max} is used to determine bta_{hole} .

The pseudodata is filtered by all described gates, and the fraction of the generated particles which are accepted at each dta and θ is calculated. An example of the result from this calculation is shown in Figure C.10.

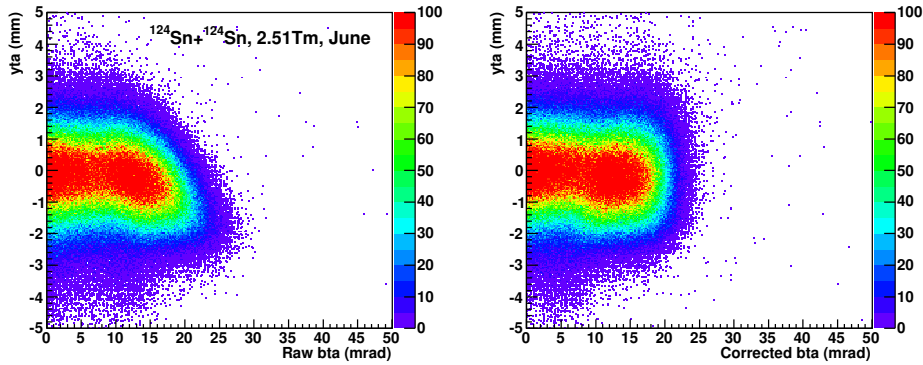


Figure C.6 Non-dispersive position at the target versus Non-dispersive angle, measured in the $^{124}\text{Sn}+^{124}\text{Sn}$ reaction at the 2.51 Tm magnetic rigidity setting, with a gate requiring $-.03 < dta < .03$. The spectrum on the left shows the raw measured parameters, while the spectrum on the right shows bta corrected for the correlations with ata (approximated as quadratic), dta (approximated as linear), and yta (approximated as linear).

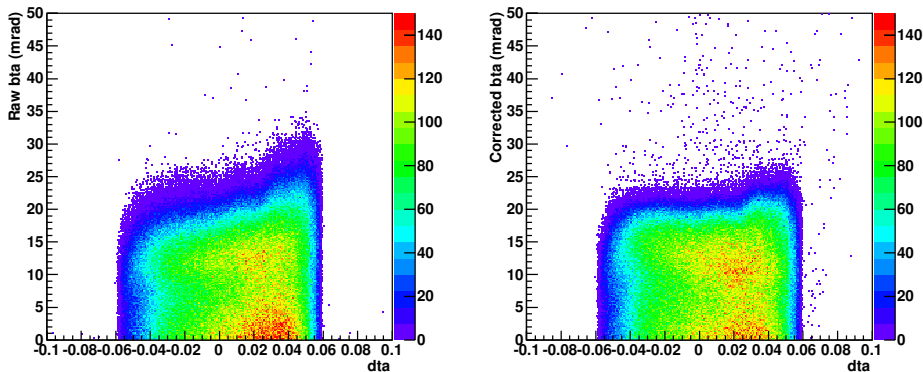


Figure C.7 Non-dispersive angle at the target versus fragment energy, measured in the $^{124}\text{Sn}+^{124}\text{Sn}$ reaction at the 2.51 Tm magnetic rigidity setting. The spectrum on the left shows the raw measured parameters, while the spectrum on the right shows bta corrected for the correlations with ata (approximated as quadratic), dta (approximated as linear), and yta (approximated as linear).

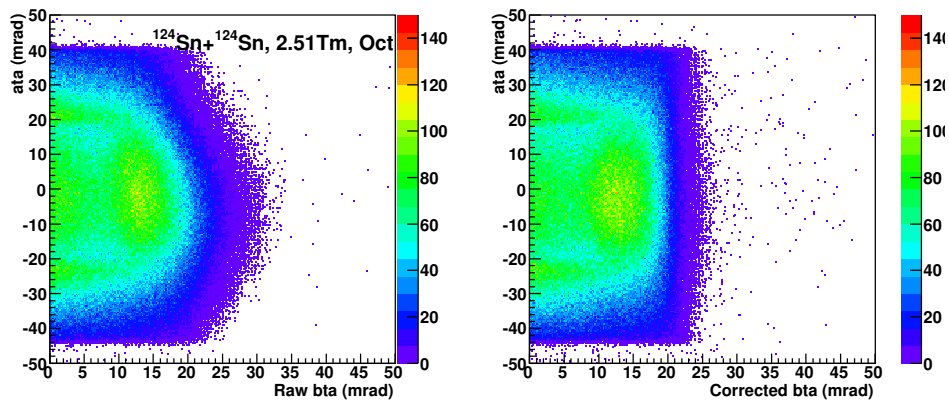


Figure C.8 Dispersive angle at the target versus Non-dispersive angle at the target, measured in the $^{124}\text{Sn} + ^{124}\text{Sn}$ reaction at the 2.51 Tm magnetic rigidity setting. The spectrum on the left shows the raw measured parameters, while the spectrum on the right shows bta corrected for the correlations with ata (approximated as quadratic), dta (approximated as linear), and yta (approximated as linear).

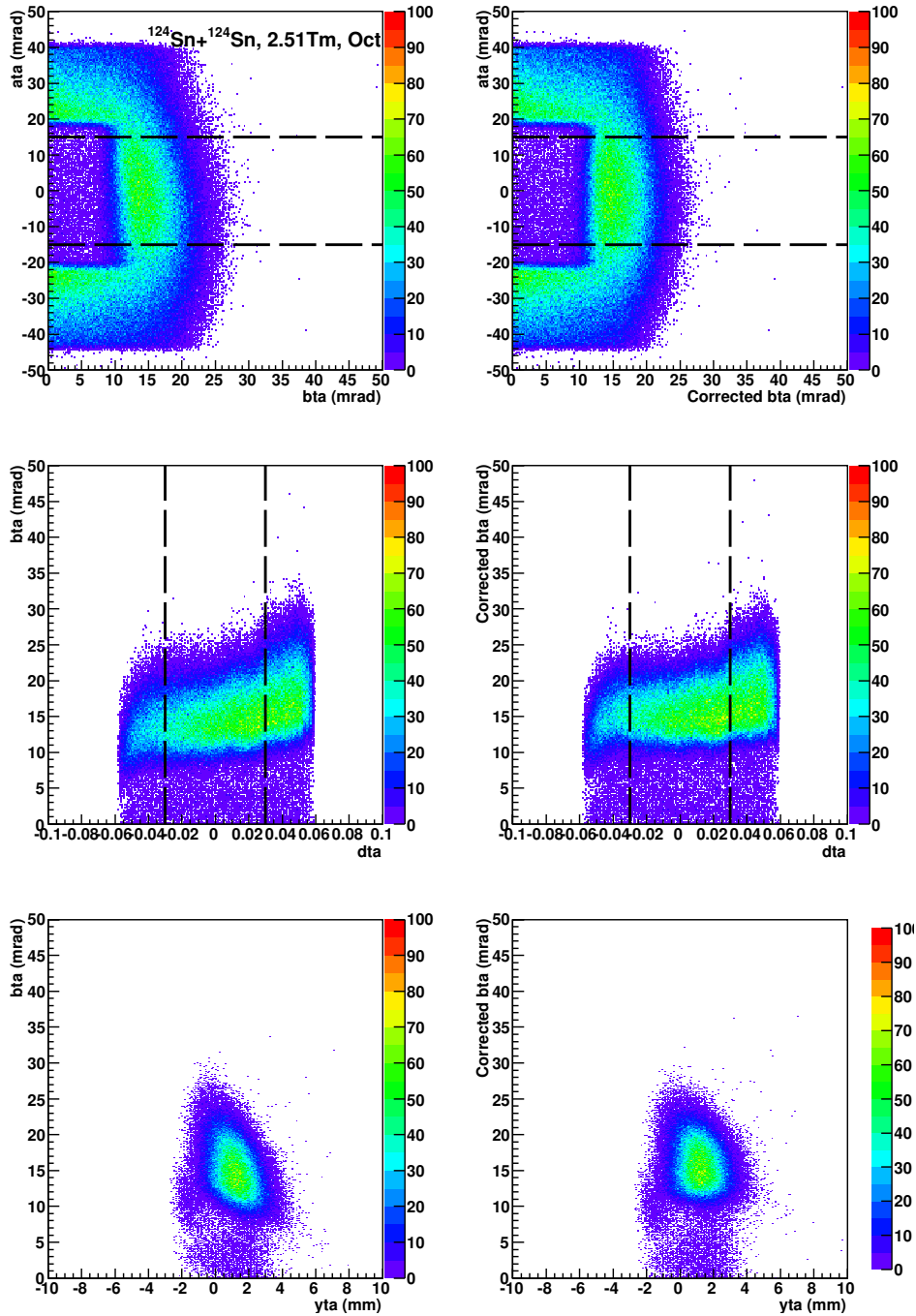


Figure C.9 Corrections for acceptance calculation from cutout in timing scintillator, measured in the $^{124}\text{Sn} + ^{124}\text{Sn}$ reaction at the 2.51 Tm magnetic rigidity setting. Top: Dispersive angle at the target versus Non-dispersive angle at the target; Middle: Non-dispersive angle at the target versus fragment energy; Bottom: Non-dispersive position at the target versus Non-dispersive angle. Spectra on the left show raw measured parameters, spectra on the right show parameters with correlations removed as discussed in the text. Dashed lines indicate cuts applied to the other spectra to demonstrate the boundary clearly.

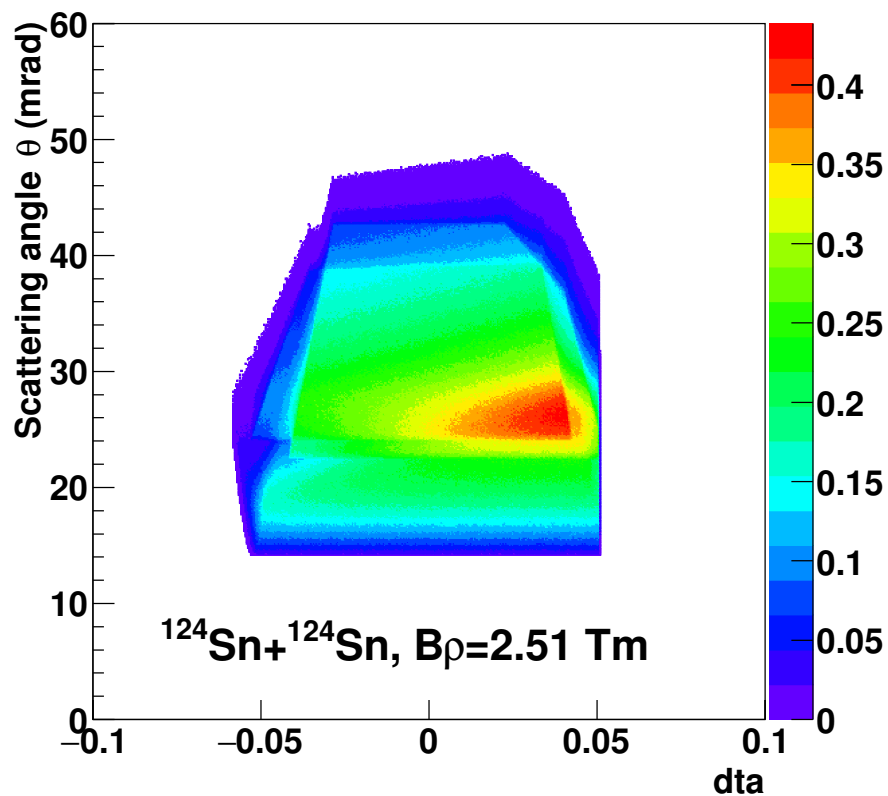


Figure C.10 Monte Carlo efficiency calculated for the $^{124}\text{Sn} + ^{124}\text{Sn}$ reaction, for the $B\rho = 2.51\text{Tm}$ magnetic setting. The efficiency is plotted as a two dimensional function of scattering angle θ and the measured dta . The color scale represents the fractional efficiency for each bin.

C.2 Effect on Experimental Data

The result of the acceptance correction is a two dimensional detection efficiency which is a function of dta and θ . When processing the data, this efficiency is used to weight the results event by event. The weighted results are placed into a corrected velocity distribution which must be fit and integrated. This process is detailed in Section 4.4.

To gauge the accuracy of the acceptance correction, a calculation for two different regions of the acceptance in one reaction system can be compared. Dividing the acceptance into two approximately equal sized regions results in a difference of $\approx 20\%$ in the corrected yields for the same data. Thus, a systematic error of at least $\pm 10\%$ would be introduced by implementing this correction. The source of this inconsistency is possibly due to the intrinsic resolution of the measured tracking information, or because of a miscalibration of the CRDC positions. The acceptance is very small, the continuous coverage in ata or bta only spans at most 20 mrad and the angular resolution of the scattering angles is about 2 mrad. As a result, edge effects likely dominate all regions of the acceptance. Also, the calibration of bta had to be extrapolated from the measured data, which introduced a large uncertainty in the results.

The experiment relies on a precise measurement of yield ratios to get the slope of the logarithm of isotopic yield ratios. This observable is described in more detail in Section 2.3.1. The ratio is expected to follow a simple formula:

$$R_{21}(N, Z) = \frac{Y_2(N, Z)}{Y_1(N, Z)} = C e^{(\alpha N + \beta Z)} \quad (C.1)$$

In practice, 4-5 isotopes are measured for each Z , and a linear function can be fit to the logarithm for each Z . To minimize the effect of the acceptance correction on the yield ratio, a double ratio can be formed for each Z . The integrated yield for each isotope is divided by a reference isotope (N_0, Z) in that same reaction, and this yield ratio is compared between two systems with a “modified isoscaling ratio”:

$$R_{mod,21}(N, Z_0) = \frac{Y_2(N, Z_0)/Y_2(N_0, Z_0)}{Y_1(N, Z_0)/Y_1(N_0, Z_0)} = \frac{\exp(\alpha N + \beta Z_0)}{\exp(\alpha N_0 + \beta Z_0)} = C_{mod} \exp(\alpha N) \quad (C.2)$$

where Z_0 is the atomic number of the chain of isotopes being considered, and N_0 is the reference isotope that would be chosen individually for each Z_0 . The α extracted in this manner is unaffected by this modification, but the sensitivity to the acceptance is cancelled. Because the range of isotopes being compared is small, the angular acceptance of these isotopes is approximately equal. The measured yields are related to the experimental yields by:

$$Y_{exp}(N, Z) = Y(N, Z) \int \int f(N, Z, B\rho, \theta) dB\rho d\theta \quad (C.3)$$

where $Y(N, Z)$ is the total yield of an isotope, $f(N, Z, B\rho, \theta)$ is a detection efficiency function. If the efficiency function is approximately constant as a function of $B\rho$, this equation could be written as:

$$Y_{exp}(N, Z) \approx Y(N, Z) \int_{B\rho_{min}}^{B\rho_{max}} \epsilon_{B\rho} f_{B\rho}(N, Z, B\rho) dB\rho \int \epsilon_{\theta} f_{\theta}(N, Z, \theta) d\theta \quad (C.4)$$

Where $f_{B\rho}$ is the distribution in rigidity and f_θ is the distribution in angle. When Equation C.4 is substituted into Equation C.2, the correction for the angular efficiency would be canceled for isotopes of approximately the same mass. The rigidity efficiency $\epsilon_{B\rho}$ would not be exactly constant, based on the calculations in the previous section. But because the efficiency would be approximately symmetric about $dta = 0$, so averaged over three $B\rho$ settings, the overall efficiency would be smoothed. In fact, Section 4.4 shows that this must be an accurate assumption. If the efficiency depended strongly on dta the velocity distributions would be discontinuous between the three rigidity settings. The velocity distributions are smooth and continuous without any correction. In addition, the systematics of the velocity distributions shown in Section 5.1 indicate that the velocity distributions are similar between reactions and for all isotopes. Consequently, the shape of the uncorrected velocity distribution must be similar to the true velocity distribution.

When extracting the isoscaling parameter α , the modified isoscaling ratio in Equation C.2 is equivalent to subtracting an offset from the normal isoscaling ratio. Because α is the exponent, a multiplicative correction only changes the value of the constant, and not α . In other words, the linear slope of the logarithm is not changed by subtracting a common offset from each point. For these reasons, the acceptance correction does not appreciably affect the results of the isoscaling analysis. The calculated acceptance correction has large systematic errors because the acceptance is quite small, so the acceptance correction is not used in the final analysis. The yield ratios shown in Section 5.3 are not modified in this way, because α would be unaffected regardless.

REFERENCES

REFERENCES

- [1] E. Rutherford. Retardation of the alpha particle from radium in passing through matter. *Philosophical Magazine*, 12:134, 1906.
- [2] J. Chadwick. Possible existence of a neutron. *Nature*, 129:312, 1932.
- [3] M. Goeppert-Mayer. On closed shells in nuclei. *Phys. Rev.*, 74:122, 1948.
- [4] M. Gell-Mann. A schematic model of baryons and mesons. *Phys. Lett.*, 8:214, 1964.
- [5] G. Zweig. An su_3 model for strong interaction symmetry and its breaking. *CERN-TH*, page 401, 1964.
- [6] R. B. Wiringa, V. G. J. Stoks, and R. Schiavilla. Accurate nucleon-nucleon potential with charge-independence breaking. *Phys. Rev. C*, 51:38, 1995.
- [7] S.C. Pieper. Quantum monte carlo calculations of light nuclei. *Nuclear Physics A*, 751:516, 2005.
- [8] M. Bender, P-H Heenen, and Paul-Gerhard Reinhard. Self-consistent mean-field models for nuclear structure. *Rev. Mod. Phys.*, 75:122, 2003.
- [9] T. Niksic, D. Vretenar, and P. Ring. Relativistic nuclear energy density functionals: Mean-field and beyond. *Prog. Part. Nuc. Phys.*, 66:519, 2011.
- [10] T.H.R. Skyrme. The nuclear surface. *Philosophical Magazine*, 1:1043, 1956.
- [11] J. De Boer and H. J. Mang, editors. *Proceeding of the International Conference on Nuclear Physics*, volume 1. North-Holland Amsterdam, 1973.
- [12] Y.K Gambhir, P Ring, and A Thimet. Relativistic mean field theory for finite nuclei. *Ann. Phys.*, 198:123, 1990.
- [13] Pawel Danielewicz, Roy Lacey, and William G. Lynch. Determination of the equation of state of dense matter. *Science*, 298:5598, 2002.

- [14] H.A. Bethe and R.F. Bacher. *Rev. Mod. Phys.*, 8:82, 1936.
- [15] C.F. von Weizsäcker. *Z. Fur Physik*, 96:431, 1935.
- [16] B. Alex Brown. Neutron radii in nuclei and the neutron equation of state. *Phys. Rev. Lett.*, 85:5296, 2000.
- [17] James M. Lattimer, C. J. Pethick, Madappa Prakash, and Pawel Haensel. The direct urca process in neutron stars. *Phys. Rev. Lett.*, 66:2701, 1991.
- [18] R Tolman. Static solutions of einstein's field equations for spheres of fluid. *Physical Review*, 55:364, 1939.
- [19] P. B. Demorest, T. Pennucci, S. M. Ransom, M. S. E. Roberts, and J. W. T. Hessels. A two-solar-mass neutron star measured using shapiro delay. *Nature*, 467:1081, 2010.
- [20] John Antoniadis, Paulo C. C. Freire, Norbert Wex, Thomas M. Tauris, Ryan S. Lynch, Marten H. van Kerkwijk, Michael Kramer, Cees Bassa, Vik S. Dhillon, Thomas Driebe, Jason W. T. Hessels, Victoria M. Kaspi, Vladislav I. Kondratiev, Norbert Langer, Thomas R. Marsh, Maura A. McLaughlin, Timothy T. Pennucci, Scott M. Ransom, Ingrid H. Stairs, Joeri van Leeuwen, Joris P. W. Verbiest, and David G. Whelan. A massive pulsar in a compact relativistic binary. *Science*, 340:6131, 2013.
- [21] C.J. Horowitz and J. Piekarewicz. Neutron star structure and the neutron radius of ^{208}pb . *Phys. Rev. Lett.*, 86:5647, 2001.
- [22] A. Trzcinska, J. Jastrzebski, P. Lubinski, F. J. Hartmann, R. Schmidt, T. von Egidy, and B. Klos. Neutron density distributions deduced from antiprotonic atoms. *Phys. Rev. Lett.*, 87:82501, 2001.
- [23] J. Zenihiro, H. Sakaguchi, T. Murakami, M. Yosoi, Y. Yasuda, S. Terashima, Y. Iwao, H. Takeda, M. Itoh, H. P. Yoshida, and M. Uchida. Neutron density distributions of $^{204,206,208}\text{pb}$ deduced via proton elastic scattering at $e_p = 295$ mev. *Phys. Rev. C*, 82:044611, 2010.
- [24] J. Piekarewicz and S.P. Weppner. Insensitivity of the elastic protonnucleus reaction to the neutron radius of 208pb . *Nuclear Physics A*, 778:10, 2006.
- [25] S. Karataglidis, K. Amos, B. A. Brown, and P. K. Deb. Discerning the neutron density distribution of 208pb from nucleon elastic scattering. *Phys. Rev. C*, 65:44306, 2002.

- [26] The PREX Collaboration. Measurement of the neutron radius of ^{208}Pb through parity violation in electron scattering. *Phys. Rev. Lett.*, 108:112502, 2012.
- [27] The PREX Collaboration. Prex-ii: Precision parity-violating measurement of the neutron skin of lead.
- [28] The PREX Collaboration. Crex: Parity-violating measurement of the weak charge distribution of ^{48}Ca to 0.02 fm accuracy.
- [29] J.P. Bondorf, A.S. Botvina, A.S. Iljinov, I.N. Mishustin, and K. Sneppen. Statistical multifragmentation of nuclei. *Phys. Rep.*, 257:133, 1995.
- [30] Andrea Carbone, Gianluca Col, Angela Bracco, Li-Gang Cao, Pier Francesco Bortignon, Franco Camera, and Oliver Wieland. Constraints on the symmetry energy and neutron skins from pygmy resonances in ^{68}Ni and ^{132}Sn . *Phys. Rev. C*, 81:41301, 2010.
- [31] A. Klimkiewicz, N. Paar, P. Adrich, M. Fallot, K. Boretzky, T. Aumann, D. Cortina-Gil, U. Datta Pramanik, Th. W. Elze, H. Emling, H. Geissel, M. Hellstrm, K. L. Jones, J. V. Kratz, R. Kulesa, C. Nociforo, R. Palit, H. Simon, G. Surwka, K. Smmerer, D. Vretenar, and W. Walu. Nuclear symmetry energy and neutron skins derived from pygmy dipole resonances. *Phys. Rev. C*, 76:51603, 2007.
- [32] V. Baran, M. Colonna, M. Di Toro, V. Greco, M. Zielinska-Pfabe, and H.H. Wolter. Isospin effects in nuclear multifragmentation. *Nuclear Physics A*, 703:603, 2002.
- [33] M. B. Tsang, T. X. Liu, L. Shi, P. Danielewicz, C. K. Gelbke, X. D. Liu, W. G. Lynch, W. P. Tan, G. Verde, A. Wagner, H. S. Xu, W. A. Friedman, L. Beaulieu, B. Davin, R. T. de Souza, Y. Larochele, T. Lefort, R. Yanez, V. E. Viola, Jr., R. J. Charity, and L. G. Sobotka. Isospin diffusion and the nuclear symmetry energy in heavy ion reactions. *Phys. Rev. C*, 92:62701, 2004.
- [34] T. X. Liu, W. G. Lynch, M. B. Tsang, X. D. Liu, R. Shomin, W. P. Tan, G. Verde, A. Wagner, H. F. Xi, H. S. Xu, B. Davin, Y. Larochele, R. T. de Souza, R. J. Charity, and L. G. Sobotka. Isospin diffusion observables in heavy-ion reactions. *Phys. Rev. C*, 76:34603, 2007.
- [35] M. B. Tsang, W. A. Friedman, C. K. Gelbke, W. G. Lynch, G. Verde, and H. S. Xu. Isotopic scaling in nuclear reactions. *Phys. Rev. Lett.*, 86:5023, 2001.
- [36] W.A. Friedman. Isotopic yields and isoscaling in fission. *Phys. Rev. C*, 69:31601, 2004.

- [37] G. A. Souliotis, D. V. Shetty, M. Veselsky, G. Chubarian, L. Trache, A. Keksis, E. Martin, and S. J. Yennello. Isoscaling of heavy projectile residues from the collisions of 25mev/nucleon ^{86}kr with ^{124}sn and ^{112}sn and ^{64}sn and ^{58}sn . *Phys. Rev. C*, 68:24605, 2003.
- [38] M. B. Tsang, C. K. Gelbke, X. D. Liu, W. G. Lynch, W. P. Tan, G. Verde, H. S. Xu, W. A. Friedman, R. Donangelo, S. R. Souza, C. B. Das, S. Das Gupta, and D. Zhabinsky. Isoscaling in statistical models. *Phys. Rev. C*, 64:54615, 2001.
- [39] A. S. Botvina, O. V. Lozhkin, and W. Trautmann. Isoscaling in light-ion induced reactions and its statistical interpretation. *Phys. Rev. C*, 65:44610, 2002.
- [40] G.A. Souliotis, M. Veselsky, D.V. Shetty, and S.J. Yennello. Heavy-residue isoscaling as a probe of the process of n/z equilibration. *Phys. Lett. B*, 588:35, 2004.
- [41] S. Mallik, G. Chaudhuri, and S. Das Gupta. Improvements to a model of projectile fragmentation. *Phys. Rev. C*, 84:54612, 2011.
- [42] M. B. Tsang, Yingxun Zhang, P. Danielewicz, M. Famiano, Zhuxia Li, W. G. Lynch, and A. W. Steiner. Constraints on the density dependence of the symmetry energy. *Phys. Rev. Lett.*, 102:122701, 2009.
- [43] G. A. Souliotis, D. V. Shetty, A. Keksis, E. Bell, M. Jandel, M. Veselsky, and S. J. Yennello. Heavy-residue isoscaling as a probe of the symmetry energy of hot fragments. *Phys. Rev. C*, 73:24606, 2006.
- [44] G. A. Souliotis, P. N. Fountas, M. Veselsky, S. Galanopoulos, Z. Kohley, A. McIntosh, S. J. Yennello, and A. Bonasera. Isoscaling of heavy projectile residues and n/z equilibration in peripheral heavy-ion collisions below the fermi energy. *Phys. Rev. C*, 90:64612, 2014.
- [45] D. D. S. Coupland W. G. Lynch, M. B. Tsang, P. Danielewicz, and Yingxun Zhang. Influence of transport variables on isospin transport ratios. *Phys. Rev. C*, 84:54603, 2011.
- [46] Ning Wang, Zhuxia Li, and Xizhen Wu. Improved quantum molecular dynamics model and its applications to fusion reaction near barrier. *Phys. Rev. C*, 65:64608, 2002.
- [47] Yingxun Zhang and Zhuxia Li. Probing the density dependence of the symmetry potential with peripheral heavy-ion collisions. *Phys. Rev. C*, 71:24604, 2005.

- [48] Yingxun Zhang, M.B. Tsang, Zhuxia Li, and Hang Liu. Constraints on nucleon effective mass splitting with heavy ion collisions. *Phys. Lett. B*, 732:186, 2014.
- [49] G. F. Bertsch, H. Kruse, and S. Das Gupta. Boltzmann equation for heavy ion collisions. *Phys. Rev. C*, 29:673, 1984.
- [50] A. Ono, H. Horiuchi, T. Maruyama, and A. Ohnishi. Fragment formation studied with antisymmetrized version of molecular dynamics with two nucleon collisions. *Phys. Rev. Lett.*, 68:2899, 1992.
- [51] Akira Ono and Hisashi Horiuchi. Antisymmetrized molecular dynamics for heavy ion collisions. *Prog. in Part. and Nuc. Phys.*, 53:501, 2004.
- [52] Massimo Papa, Toshiki Maruyama, and Aldo Bonasera. Constrained molecular dynamics approach to fermionic systems. *Phys. Rev. C*, 64:24612, 2001.
- [53] M. A. Famiano, T. Liu, W. G. Lynch, M. Mocko, A. M. Rogers, M. B. Tsang, M. S. Wallace, R. J. Charity, S. Komarov, D. G. Sarantites, L. G. Sobotka, and G. Verde. Neutron and proton transverse emission ratio measurements and the density dependence of the asymmetry term of the nuclear equation of state. *Phys. Rev. Lett.*, 97:52701, 2009.
- [54] Yingxun Zhang, P. Danielewicz, M. Famiano, Zhuxia Li, W.G. Lynch, and M.B. Tsang. The influence of cluster emission and the symmetry energy on neutronproton spectral double ratios. *Phys. Lett. B*, 664:145, 2008.
- [55] D. Bazin, J.A. Caggiano, B.M. Sherrill, J. Yurkon, and A. Zeller. The s800 spectrograph. *Nucl. Instr. and Meth. B*, 204:629, 2003.
- [56] J. Yurkon, D. Bazin, W Benenson, B.M. Sherrill D.J. Morrissey, D. Swan, and R. Swanson. Focal plane detector for the s800 high-resolution spectrometer. *Nucl. Instr. and Meth. A*, 422:291, 1999.
- [57] K. Meierbachtol, D.J. Morrissey, M. Mosby, and D. Bazin. Evolution of the momentum distribution with mass loss in projectile fragmentation reactions. *Phys. Rev. C*, 85:34608, 2012.
- [58] R. Meharchand. *Spectroscopy of ^{12}Be using the $(^7\text{Li}, ^7\text{Be})$ reaction in inverse kinematics.* PhD thesis, Michigan State University, 2011.
- [59] K. Meierbachtol, D. Bazin, and D.J. Morrissey. New csi(na) hodoscope array for the s800 spectrograph at nscl. *Nucl. Instr. and Meth. B*, 652:668, 2011.

- [60] B. Davin, R.T. de Souza, R. Yanez, Y. Larochelea, R. Alfaro, H.S. Xu, A. Alexander, K. Bastin, L. Beaulieu, J. Dorsett, G. Fleener, L. Gelovani, T. Lefort, J. Poehlman, R.J. Charity, L.G. Sobotka, J. Elson, A. Wagner, T.X. Liu, X.D. Liu, .G. Lynch, L. Morris, R. Shomin, W.P. Tan, M.B. Tsang, G. Verde, and J. Yurkon. Lassa: a large area silicon strip array for isotopic identification of charged particles. *Nucl. Instr. and Meth. A*, 473:302, 2001.
- [61] D.D.S. Coupland. *Probing the Nuclear Symmetry Energy with Heavy Ion Collisions*. PhD thesis, Michigan State University, 2013.
- [62] George L. Engel, Muthukumar Sadasivam, Mythreyi Nethi, Jon M. Elson, Lee G. Sobotka, and Robert J. Charity. A multi-channel integrated circuit for use in low-and intermediate-energy nuclear physics. *Nucl. Instr. and Meth. A*, 573:418, 2007.
- [63] M.S. Wallace, M.A. Famiano, M.J. van Goethem, A.M. Rogers, W.G. Lynch, J. Clifford, F. Delaunay, J. Lee, S. Labostov, M. Mocko, L. Morris, A. Moroni, B.E. Nett, D.J. Oostdyk, R. Krishnasamy, M.B. Tsang, R.T. de Souza, S. Hudan, L.G. Sobotka, R.J. Charity, J. Elson, and G.L. Engel. The high resolution array (hira) for rare isotope beam experiments. *Nucl. Instr. and Meth. A*, 583:302, 2007.
- [64] K. W. Brown, W. W. Buhro, R. J. Charity, J. M. Elson, W. Reviol, L. G. Sobotka, Z. Chajecski, W. G. Lynch, J. Manfredi, R. Shane, R. H. Showalter, M. B. Tsang, D. Weisshaar, J. R. Winkelbauer, S. Bedoor, and A. H. Wuosmaa. Two-proton decay from the isobaric analog state in 8b. *Phys. Rev. C*, 90:27304, 2014.
- [65] R.T. De Souza, N. Carlin, Y.D. Kim, J. Ottarson, L. Phair, D.R. Bowman, C.K. Gelbke, W.G. Gong, W.G. Lynch, R.A. Pelak, T. Peterson+, G. Poggi, M.B. Tsang, and H.M. Xu. The msu miniball 4π fragment detection array. *Nucl. Instr. and Meth. A*, 295:109, 1990.
- [66] C.F. Williams. *Multifragmentation in $^{84}\text{Kr}+^{197}\text{Au}$ Collisions at Beam Energies of $E/A=35$ and 55 and 70 and 100 and 200 and 400 MeV*. PhD thesis, Michigan State University, 1996.
- [67] T.X. Liu. *Isospin Dynamics and the Isospin Dependent EOS*. PhD thesis, Michigan State University, 2005.
- [68] M.D. Youngs. *Using Light Emitted Clusters as a Probe of the Symmetry Energy in the Nuclear Equation of State*. PhD thesis, Michigan State University, 2013.

- [69] H.G. Ritter. Transverse energy and multiplicity distributions in collisions at 60 and 200 gev per nucleon. *Nuclear Physics A*, 488:651, 1988.
- [70] K. Meierbachtol. *Parallel and perpendicular momentum distributions in projectile fragmentation reactions*. PhD thesis, Michigan State University, 2012.
- [71] Martin Berz. Modern map methods for charged particle optics. *Nucl. Instr. and Meth. A*, 363:100, 1995.
- [72] J.R. Winkelbauer, S.R. Souza, and M.B. Tsang. Influence of secondary decay on odd-even staggering of fragment cross sections. *Phys. Rev. C*, 88:44613, 2013.
- [73] S. Piantelli and et al. N and z odd-even staggering in kr+sn collisions at fermi energies. *Phys. Rev. C*, 88:64607, 2013.
- [74] C. Scheidenberg, T. Stohlker, W.E. Meyerhof, H Geissel, P.H. Mokler, and B. Blank. Charge states of relativistic heavy ions in matter. *Nucl. Instr. and Meth. B*, 142:441, 1998.
- [75] M. Mocko. *Rare Isotope Production*. PhD thesis, Michigan State University, 2006.
- [76] T. X. Liu, W. G. Lynch, R. H. Showalter, M. B. Tsang, X. D. Liu, W. P. Tan, M. J. van Goethem, G. Verde, A. Wagner, H. F. Xi, H. S. Xu, M. A. Famiano, R. T. de Souza, V. E. Viola, R. J. Charity, and L. G. Sobotka. Isospin observables from fragment energy spectra. *Phys. Rev. C*, 86:24605, 2012.
- [77] O. Tarasov. Analysis of momentum distributions of projectile fragmentation products. *Nuclear Physics A*, 734:536, 2004.
- [78] D. Bazin, D. Guerreau, R. Anne, D. Guillemaud-Mueller, A.C. Mueller, and M.G. Saint-Laurent. Zero degree measurements of isotopic distributiosn in $44 \frac{MeV}{u}$ ^{86}kr -induced reactions for the production of nuclei far from stability. *Nuclear Physics A*, 515:349, 1990.
- [79] D.J. Morrissey. Systematics of momentum distributions from reactions with relativistic ions. *Phys. Rev. C*, 39:460, 1989.
- [80] A.S. Goldhaber. Statistical models of fragmentation processes. *Phys. Lett. B*, 53:306, 1974.

- [81] G.A. Souliotis, P.N. Fountas, M. Veselsky, S. Galanopoulos, Z. Kohley, A. McIntosh, S.J. Yenello, and A. Bonasera. Isoscaling of heavy projectile residues and n/z equilibration in peripheral heavy ion collisions below the fermi energy. *Phys. Rev. C*, 90:64612, 2014.
- [82] M. Notani, H Sakurai, N. Aoi, H. Iwasaki, N. Fukuda, Z. Liu, K. Yoneda, H. Ogawa, T. Teranishi, T. Nakamura, H. Okuno, A. Yoshida, Y.X. Watanabe, S. Momota, N. Inabe, T. Kubo, S. Ito, A. Ozawa, T. Suzuki, I. Tanihata, and M. Ishihara. Projectile fragmentation reactions and production of nuclei near the neutron drip line. *Phys. Rev. C*, 76:44605, 2007.
- [83] H. Feshbach and K. Huang. Fragmentation of relativistic heavy ions. *Phys. Lett. B*, 47:300, 1973.
- [84] K. Sümmerer. Improved empirical parametrization of fragmentation cross sections. *Phys. Rev. C*, 87:39903, 2012.
- [85] A.B. McIntosh, A. Bonasera, P. Cammarata, K. Hagel, L. Heilborn, Z. Kohley, J. Mabi-ala, L.W. May, P. Marini, A. Raphelt, G.A. Souliotis, S. Wuenschel, A. Zarrella, and S.J. Yenello. Asymmetry dependence of the nuclear caloric curve. *Phys. Lett. B*, 719:337, 2013.
- [86] R.J. Charity. N-z distributions of secondary fragments and the evaporation attractor line. *Phys. Rev. C*, 58:1073, 1998.
- [87] Yingxun Zhang, M.B. Tsang, and Zhuxia Li. Covariance analysis of symmetry energy observables from heavy ion collision. *Phys. Lett. B*, 2015. Accepted and In Press.
- [88] O.B. Tarasov and D. Bazin. Lise⁺⁺: Radioactive beam production with in-flight separators. *Nucl. Instr. and Meth. B*, 266:4657, 2008.
- [89] J.F. Ziegler and et al. *The Stopping and Range of Ions in Solids*. Pergamon Press, New York, 1985.
- [90] C. Guess. *The $^{150}\text{Sm}(t, ^3\text{He})^{150}\text{Pm}^*$ and $^{150}\text{Nd}(t, ^3\text{He})^{150}\text{Pm}^*$ Reactions and Applications for 2ν and 0ν Double Beta Decay*. PhD thesis, Michigan State University, 2010.
- [91] A. Prinke. *Searching for the Origins of Fluorine: A Measurement of the $^{19}\text{F}(t, ^3\text{He})$ Reaction*. PhD thesis, Michigan State University, 2012.
- [92] Ning Wang, Li Ou, Yingxun Zhang, and Zhuxia Li. Microscopic dynamics simulations of heavy-ion fusion reactions induced by neutron-rich nuclei. *Phys. Rev. C*, 89:34603, 2014.

- [93] J.M. Lattimer and M. Prakash. The physics of neutron stars. *Science*, 304:536, 2004.
- [94] M. B. Tsang, J. R. Stone, F. Camera, P. Danielewicz, S. Gandolfi, K. Hebeler, C. J. Horowitz, Jenny Lee, W. G. Lynch, Z. Kohley, R. Lemmon, P. Mller, T. Murakami, S. Riordan, X. Roca-Maza, F. Sammarruca, A. W. Steiner, I. Vidaa, and S. J. Yennello. Constraints on the symmetry energy and neutron skins from experiments and theory. *Phys. Rev. C*, 86:15803, 2012.
- [95] G.C. Baldwin and G.S. Klaiber. Photo-fission in heavy elements. *Phys. Rev.*, 71:3, 1947.
- [96] J.P. Blaizot. Nuclear compressibilities. *Phys. Rep.*, 64:171, 1980.
- [97] F. Rami, J.P. Coffin, G. Guillaume, B. Heusch, P. Wagner, A. Fahli, and P. Fintz. Study of the $^{40}\text{Ar}+^{68}\text{Zn}$ reaction at $27.6 \frac{\text{MeV}}{u}$. *Nuclear Physics A*, 444:325, 1985.
- [98] V. Borrel, D. Guerreau, J. Galin, B. Gatty, D. Jacquet, and X. Tarrago. Peripheral ar induced reactions at $44 \frac{\text{MeV}}{u}$ - similarities and deviations with respect to a high energy fragmentation process. *Z. Phys. A*, 314:191, 1983.